A STUDY OF OPTICAL-FIBRE ELECTRONICALLY-SCANNED WHITE LIGHT INTERFEROMETRIC SENSOR SYSTEMS

by

RAYMOND HUGH MARSHALL

A thesis submitted for the degree of
Doctor of Philosophy

CITY UNIVERSITY

Department of Electrical, Electronic
and Information Engineering

September 1997

Table of Contents

List of Tables

List of Figures

Acknowledgements

The work reported in this thesis was conducted under the supervision of Professor Andrew W. Palmer and Professor Kenneth T. V. Grattan. I wish to express my appreciation and sincere gratitude to Professor Palmer for his excellent supervision of this work and, for the continual help, encouragement and inspiration from him in the course of this study.

I would also like to express my gratitude to Professor Grattan for his stimulating guidance during the course of this study. I am grateful for the continuous encouragement and support that he has offered me, which ranged from the arrangement of my participation of academic conferences, to the reviewing of all of my academic publications during this period of study.

I can hardly express my gratitude to Dr. Ya Nong Ning for his encouragement, help and inspiration, which never ceased during different phases of my studies. I would also like to thank Dr. Igor Sokolov and Dr. X. Q. Jiang for many helpful discussions during different parts of my study. Debts of gratitude are also owed to Mr. Roger Valsler for his expertise in the engineering of optical accessories, which were essential to the development of the work reported. I would also like to thank Joan Rivellini, Linda Carr and Anita Stevenson for all their help and friendly assistance.

I am also grateful for the financial support provided by the Engineering and Physical Sciences Research Council. I would also like to express my gratitude to all the research staff in the Optical Instrumentation Group, all of whom have been very kind in offering their time and expertise. Finally, my deepest gratitude is devoted to my parents and my family. It is only with their tremendous love, guidance and support that has made my research possible.

Declaration

The author hereby grants power of discretion to the University Librarian to allow the thesis to be copied in whole or in part without further reference to the author. This permission covers only single copies made for study purposes, subject to normal conditions of acknowledgement.

Abstract

Starting with a brief review of the development of optical fibre sensors, this thesis comprises work on the study of optical-fibre electronically-scanned white-light interferometers. The theoretical principles of white-light interferometry (WLI) techniques are examined, providing a comparison of these techniques with conventional interferometric methods, highlighting the key advantages of the former. The mechanically- and electronically-scanned WLI methods are also compared and contrasted, highlighting the key advantages of the electronically-scanned method, in that they do not require the use of mechanical phase modulation elements.

An electronically-scanned white-light interferometer (ESWLI) is composed of a sensing interferometer (SI) and a recovery interferometer (RI), operating in tandem. The main part of this work is centred around the design and development of a RI to be employed in an ESWLI. A full theoretical analysis and experimental evaluation of a novel Mach-Zehnder interferometer (MZI) configuration, employed as a RI is presented. The key effects of the SI (which was based upon a modified Fabry-Perot configuration) were also studied, in conjunction with the influence of modal noise in the multimode optical fibre coupler which connects the SI to the RI.

Various methods of enhancing the identification of the central fringe were successfully introduced. These included the method of using dual wavelengths, employing a least-squares curve fitting technique and the use of the centroid method. An investigation of optical dispersion in the dual wavelength configuration was also undertaken.

Examples of the applications of this ESWLI sensing system were also presented. First, the system was employed for the measurement of displacement, which provided an absolute displacement resolution of 40nm. Secondly, the system was studied for the measurement of vibration. Simultaneous measurements of AC and DC stresses were achieved, whereby the system successfully provided information on the direction of the motion associated with the vibration, in addition to its frequency. A photoconductive crystal (PCC) was then used as the detector (rather than a charge-coupled device (CCD) linear array), in a modification of the stress measurement system. Here, the intrinsic non-steady state photo-emf (PEMF) characteristic of the PCC was exploited in conjunction with the MZI to provide higher frequency, smaller amplitude vibration measurements. The system provided mHz sensitivity across a 5kHz range of vibration amplitudes down to the nanometer range.

To conclude this thesis, a cross comparison with previously proposed systems was made with a discussion of the main benefits of this device. A discussion of future work and the further potential of this approach is also presented.

Symbols and Abbreviations

ν	frequency
υ	velocity
ω	angular frequency
λ	wavelength
φ	phase angle
α	Inclination angle of Mach Zehnder interferometer mirror
μ	permeability
ε	permittivity
$\Delta L(x)$	Optical path difference between the two beams at a point x
a	CCD pixel width
b	CCD pixel space
BS	Beamsplitter
CCD	Charge-coupled device
DMA	Direct memory access channel
DSA	Digital storage adapter
ESWLI	Electronically-scanned white light interferometer
f	Frequency of a signal
FPI	Fabry-Perot interferometer
I	Intensity
j	CCD pixel number
$k=2\pi/\lambda$	Wavenumber
L_c	Coherence length
LD	Laser diode
LED	Light-emitting diode
LS	Least squares curve fit

MSWLI	Mechanically-scanned white light interferometer
MZI	Mach-Zehnder interferometer
OPD	Optical path difference
P(x)	Beam intensity profile
PCC	Photo-conductive crystal
PEMF	Photo-electromotive force
p_f	Number of pixels per fringe
ppf	Pixels per fringe
PZT	Piezo-electric transducer
RI	recovery interferometer
SI	sensing interferometer
SNR	Signal-to-noise ratio
t	time
V	Fringe visibility
W	Beam width
WLI	White Light Interferometry
wrt	with respect to
x	axis along linear CCD array

Chapter 1

Introduction and Background

1.0. Introduction

It is almost three decades since the initial concepts of the use of fibre-optic techniques for sensing applications was first debated. During the early seventies, when the technology of optical fibres for telecommunication was evolving, the high sensitivity of these fibres in terms of their transmission characteristics to certain external perturbations like strain, pressure, microbends etc. became evident. A great deal of effort was spent at that time to reduce the sensitivity of signal-carrying optical fibres to such external effects through suitable fibre and cable designs.

Capitalising on this observation of the exceptional sensitivity of optical fibres to external perturbations, an alternative school of thought began to exploit this phenomenon in optical fibres to construct or interrogate a large variety of sensors and instruments. This off-shoot of optical fibre telecommunications quickly led to the emergence of the field of optical fibre sensors.

Prior to the early 1970s, the main application for fiber optic waveguides had been for endoscopic instruments which are still routinely used in medical procedures to look inside the human body. At about the same time, there was a growing interest in the possibility of exploiting optics in communications systems as the potentially large bandwidth would allow significantly more simultaneous users over a single transceiver channel than microwave links. As a result of intense research and

development, the necessary elements to facilitate large bandwidth optical communications were developed. Namely, these were the

a) production of very low-loss single-mode optical fibers;
b) development of high power, single-mode laser diodes capable of direct modulation at gigahertz rates;
c) production of high power, high bandwidth Light-emitting diodes (LEDs);
d) emergence of fast detectors based on silicon and InGaAs.

Throughout this period, the consumer market had also been a major spur to the development of optoelectronic components, such as LEDs, liquid crystal displays, compact disc(CD) players and laser printers. Optical (open air-path) methods for sensor applications were well established before the 1970s. These sensors exploited a range of mechanisms from simple optical switches based upon interrupting an optical beam, through to sophisticated interferometry.

Optical techniques have long played an important role in instrumentation and sensors. A sensor can be classified as a device which has the role of converting a change in the magnitude of one physical parameter into a change in magnitude of a second, different parameter, which can be measured more conveniently and perhaps more accurately. In recent years, the scope of optical techniques used in the area of sensors has made a large jump due to the high availability of low-loss optical fibres and associated optoelectronic components.

1.1. Advantages of optical fibre sensors

Optical fibre sensors offer substantial benefits when compared to conventional electric sensors, mainly as follows:

(i) Immunity to electromagnetic interference (EMI)

Since the materials employed are very good electrical insulators, then they cannot, in principle, introduce electrical shorting paths or electrical safety problems.

Likewise, stray fields cannot induce electrical noise in the fibres, which provides a very high level of immunity to EMI. However, stray electric fields may induce changes in the state of polarization in the fibre.

(ii) Low volume and weight

Due to the use of optical fibres which have an extremely small weight

(iii) Safety

Most fibre optics sensors require no electrical power at the sensing head. They are usually powered remotely by radiation from a light source, and thus they introduce no danger of electrical sparking in hazardous environments. They are chemically inert and can be readily employed in chemical, process and biomedical instrumentation due to their small size and mechanical flexibility.

(iv) Small and versatile

A typical sensing head can be made as small as the diameter of the fibre itself, thus facilitating the use of an extremely small sensor. Also, when used as a point sensor, they can be employed in normally inaccessible regions without perturbation of the transmitted signals.

(v) Remote measurements capability

The sensing head can be easily interfaced to low-loss optical fibre and thus provide remote sensing by locating the controlling electronics for the sources and detectors far away from the sensing head

(vi) Large bandwidth

This offers the possibility of multiplexing a large number of individually addressed point sensors in a fibre network or allows distributed sensing (continuous sensing along the fibre length)

(vii) Good sensitivity

Nanometre measurement resolutions have previously been reported [1,2,3].

These advantages were sufficient to lead to the emergence of a variety of fibre optic sensors for accurate sensing and measurement of many physical parameters, such as displacement, vibration, pressure, temperature, liquid level, refractive index, electric current, rotation, chemical, strain, biomedical parameters and flow.

A fibre-optic sensor may be classified in several ways, but most simply as being either intrinsic or extrinsic. In the intrinsic sensor, the physical parameter to be sensed modulates the transmission properties of the sensing fibre whereas in an extrinsic sensor, the modulation takes place outside the fibre. In the intrinsic case, one or more of the physical properties of the guided light, e.g. intensity, phase, polarisation and wavelength may be modulated by the measurand, while in the extrinsic case, the fibre acts as a channel to transport the light signal from one end to and from the sensor head itself, where the interaction occurs.

Amongst the variety of methods, most fibre-optic sensors are based either on measuring an intensity change in one or more light beams or on looking at phase changes in the light beams by causing them to interact or interfere with one another. Thus sensors in this category are termed either intensity sensors or interferometric sensors. Techniques used in the case of intensity sensors include light spectral transmission changes (i.e., simple attenuation of transmitted light due to absorption), microbending or radiative losses, reflectance changes, and changes in the modal properties of the fiber. The advantage of intensity modulated sensors lies in their simplicity of construction and their compatibility to multimode fibre technology. Interferometric sensors, the subject of this work, have the added benefits of providing orders of magnitude higher sensitivity when compared to intensity modulated sensors. An interferometric optical fibre sensor operates by measuring an environmental change in the delay along a fibre as a change in optical phase.

1.2. White-Light Interferometry

The use of optical interferometric techniques in optical fiber sensor applications allows access to the high resolution and large dynamic range that is associated with these methods. Conventional interferometric fringe counting techniques allow micrometer displacement resolutions and the additional use of phase tracking methods increases the range attainable down to the nanometer scale. Another more sophisticated technique employs the use of low coherence, broadband spectral sources such as LEDs and multimode laser diodes. This technique is known as white-light interferometry or "low coherence" interferometry [4]. Although this technique in optical fibre sensing was not reported until 1983, initially for use with single mode fibers [5] and then with multimode fibers [6], its principle of operation had been demonstrated previously as a potential communication system in 1975 [7].

White-light interferometry is a powerful technique for overcoming the ambiguity problem that limits the dynamic range of conventional interferometers occurs due to the short unambiguous measurement range. These conventional interferometric systems (which employ long coherence length sources), also suffer from the problems of the need to re-initialise the calibrating starting position each time the device is switched on. These problems may be overcome with the use of white-light interferometry.

A typical device is composed of two interferometers operated in tandem, the two interferometers being a sensing interferometer (SI) and a recovery interferometer (RI) [4], as shown in Figure 1.1. The SI is simply the sensing head, which is initially moved "out of coherence" and is further tuned by the measurand. In addition, the RI is used to re-establish interference fringe effects, since it is also preset to an equivalent offset optical-path difference (OPD). Thus, the combination of the two interferometers acts to re-establish overall coherence, thus recovering the interference fringes, whose relative phase is solely due to the measurand. The electronic processing unit is used to detect the optical interference fringes and convert them into an electrical signal for analysis.

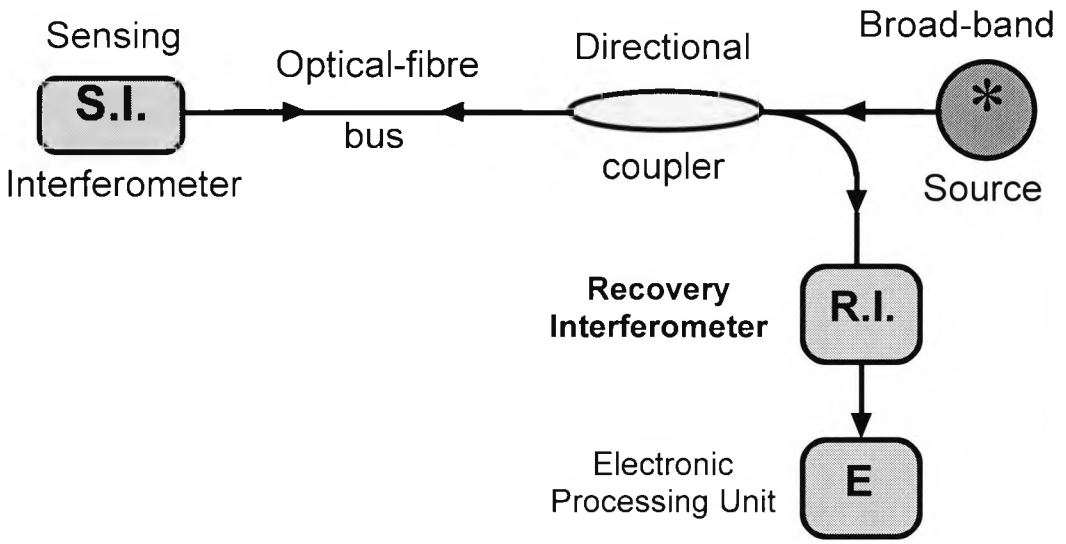

Figure 1.1: Schematic representation of a basic optical fibre sensor configuration using white-light interferometry

A typical white light interference fringe pattern is shown in Figure 1.2. Here, the short coherence length white light source is shown to produce a distinct central fringe (centred at the zero optical-path difference (OPD) position). This feature is one of the most important advantages of white-light interferometric sensing systems [4,5,6], since the direct identification of the central fringe produces the capability to make absolute

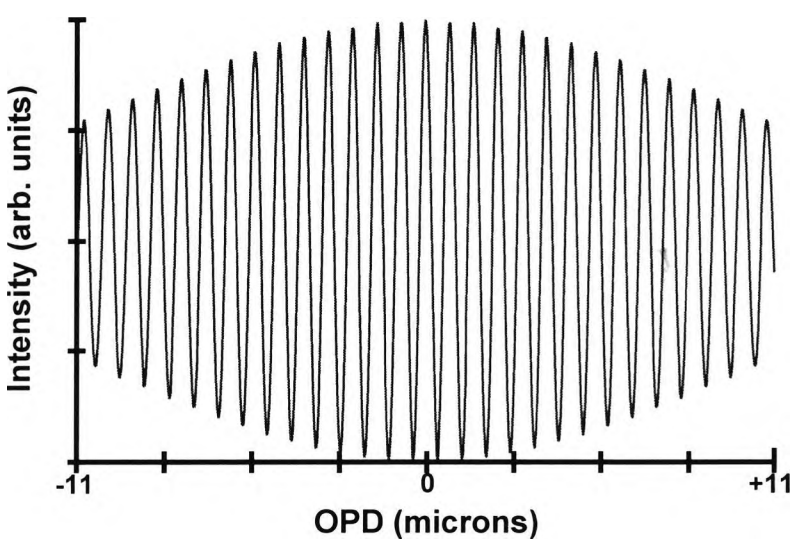

Figure 1.2: Interference pattern from a typical broadband light source, corresponding to a multimode laser diode of wavelength λ=780nm and a coherence length of 20μm.

measurements. In conventional long coherence length interferometers [8] this is not the case since the fringes are of equal amplitude and thus a measurement ambiguity occurs, which limits the systems operating range.

Optical path length changes of the light waves are observed through interferometric fringe pattern analysis. In white-light interferometry, this is more commonly achieved using phase- rather than spectral-domain processing. There are two further sub-divisions employed for the fringe pattern formation, namely temporal and spatial fringe formation. These scanning mechanisms are produced via mechanically-scanned [4] and electronically-scanned techniques respectively [3,4]. In a mechanically-scanned system, a mechanical oscillating phase modulation element is employed in order to provide a changing OPD, and hence yield interference fringes. This is a major disadvantage of these schemes, since the mechanical element will reduce the stability of the system. These problems can be overcome with the use of an electronically-scanned system. Here, the two beams in the recovery interferometer are expanded and overlapped at an angle across a CCD (or photodiode) detector array. Thus, the equivalent spatial interference fringes can be formed without using any moving mechanical parts. Therefore, these so-called electronically-scanned white light interferometer (ESWLI) systems are ideally suited for applications in harsh environments due to their greater mechanical stability.

Thus there is a significant number of techniques in the field available to the sensor designer, and the use of some of these is discussed in the thesis in subsequent chapters.

1.3. Aims and Objectives of this work

The main aims of the work described in this thesis are:

(i) to investigate the use of optical fibre electronically-scanned white-light interferometric (ESWLI) sensing systems.

(ii) to highlight the benefits and disadvantages (if any) of ESWLI sensing systems when compared to mechanically-scanned systems.

(iii) to design and develop a novel electronically-scanned recovery interferometer in order to ascertain the operational conditions, key requirements and specification of such devices. The design methodology will include an evaluation of:

(a) a theoretical analysis

(b) a computer model of the system

(c) comprehensive experimental analysis

(d) signal processing analysis

(e) full experimental results

(iv) to compare and contrast this design with other electronically-scanned schemes in order to review the benefits of a particular configuration for a particular application.

(v) to demonstrate experimentally the use of such ESWLI systems. The requirement is for a generalised rather than a bespoke system which may be readily adapted for different applications. To this end, the complete system will be demonstrated for the purpose of displacement and vibration measurements.

Several other ESWLI systems have been reported. *S. Chen et al.* reported a modified Mach-Zehnder interferometer [9] which was shown to provide displacement measurements with an operating range of 0.3mm with a resolution of 0.5μm, which yields a dynamic range (which is defined as the ratio of the operating range to the resolution [4]), of 600. *S. Chen et al.* also reported an ESWLI configuration that was based on a Fizeau interferometer[10], which provided an operating range of 117μm with a resolution of ~0.5μm. This yields a corresponding dynamic range of only 234. *A. Koch et al.* reported an ESWLI based on a Michelson interferometer [11], which provided an operating range of 75μm and a resolution of 20nm, which yields a dynamic range of 3750, which is a considerable improvement over other reported

schemes. Thus, the results of *A. Koch et al.* [11] was used to define the desired minimum specification for this new system presented in this thesis.

A coherent programme of research, involving new expertise in the field has been developed, the results separated in this thesis and published in the International literature.

1.4. Structure of the Thesis

This thesis comprises a study of the work carried out by the author in the development of the novel extrinsic fibre-optic electronically-scanned white-light interferometer. Beginning with a very brief introduction of the background history of optical fibre sensors, as presented above, the work then explores the theoretical principles of white-light interferometry, which is outlined in Chapter 2. Here, the benefits of white-light interferometry are made with conventional long coherence techniques. The main elements of the white-light interferometer (WLI) are introduced in this chapter and the benefits of employing an electronically-scanned, rather than a mechanically scanned technique is shown.

Chapter 3 contains a review of currently available recovery interferometer (RI) configurations. Based on original work of the author, a coupled theoretical analysis and experimental evaluation of a novel Mach-Zehnder interferometer (MZI), employed as RI is reported. The full implementation of this RI in an ESWLI is provided in Chapter 4. Here, a modified Fabry-Perot interferometer was employed as the sensing interferometer in conjunction with the MZI. Various methods of enhancing the identification of the central fringe were presented, in conjunction with a full analysis of systems constraints. Primarily, the techniques which were reviewed in order to enhance the central fringe identification include the use of curve fitting techniques and/or dual wavelengths.

The MZI was modified in order to provide a higher degree of stability. This new RI design was based upon employing bulk optical components. The system was

implemented for the measurement of displacement, and was shown to achieve absolute displacement measurement resolutions of 40nm, as shown in Chapter 5. This bulk-optical design was also employed for the measurement of vibration, as presented in Chapter 6. In the first experiment described, the system was configured to provide simultaneous measurements of both DC and AC stresses, without the need for polarizers and transmission gratings which are employed in previously proposed configurations. In the second section in Chapter 6, results from an interferometric vibration sensing system are discussed, where the intrinsic non-steady-state photo-electromotive force (PEMF) characteristics of a photoconductive crystal were used in conjunction with the modified MZI. The system was experimentally verified to provide reproducible vibration frequency measurements in the kilohertz region (to ~mHz sensitivity), with the use of a simple signal processing approach.

Finally, a conclusion to the work is presented in Chapter 7, in conjunction with the points of the author's view on aspects of future work and further development of this ESWLI configuration.

1.5. References

1. Bobroff, N.: "Recent advances in displacement measuring interferometry", Meas. Sci. Technol, vol. 4, pp. 907-926, 1993.

2. Ribeiro, A. B. L., Rao, Y. J., and Jackson, D. A.: "Multiplexing interrogation of interferometric sensors using dual multimode laser diode sources and coherence reading", Optics Comms., vol. 109, pp. 400-404, 1994.

3. Koch, A. and Ulrich, R.: "Displacement sensor with electronically-scanned white-light interferometry", SPIE vol. 1267, Fiber Optic Sensors IV, pp. 126-133, 1990.

4. Meggitt, B. T.: "Fiber optic white-light interferometric sensors", Ch. 9, pp. 269-312, In: "Optical Fiber Sensor Technology", Eds. Grattan, K. T. V. and Meggitt, B. T., Chapman & Hall, London, 1995.

5. Al-Chalabi, S. A., Culshaw, B. and Davies, D. E. N. "Partially coherent sources in interferometry", IEE (No. 221), Proc. 1st International Conference on Optical Fiber Sensors, London, pp. 132-5, 1983.

6. Bosselman, Th. and Ulrich, R. "High accuracy position-sensing with fibre-coupled white light interferometers", Proc. 2nd International Conference on Optical Fiber Sensors, Stuttgart, pp. 361-5, 1984.

7. Deslisle, C. and Cielo, P.: "Application de la modulation spectrale a la transmission de l'information", Can. J. Phys., vol. 53, pp.1047-53, 1975.

8. Handerek, V.: "Single mode optical fiber sensors", Ch. 7, pp.197-222, In: "Optical Fiber Sensor Technology", Eds. Grattan, K. T. V. and Meggitt, B. T., Chapman & Hall, London, 1995.

9. Chen, S., Meggitt, B. T. and Rogers, A. J.: "Electronically-scanned white light interferometry with enhanced dynamic range", Electron. Letts., vol. 26, pp. 1663-1665, 1990.

10. Chen, S., Palmer, A. W., Grattan, K. T. V., Meggitt, B. T., Martin, S.: "Study of electronically-scanned optical-fibre white-light Fizeau interferometer", Electron. Letts., vol. 27, pp. 1032-1034, 1991.

11. Koch, A. and Ulrich, R.: "Displacement sensor with electronically scanned white-light interferometer", SPIE vol. 1267, Proc. Fibre Optics Sensors IV, pp. 126-132, 1990.

Chapter 2:

White-Light Interferometry

2.0. Abstract

In this chapter, an overview of the essential theory of white-light interferometry is presented. A comparison of white-light interferometric techniques with conventional techniques is made highlighting the key advantages of the former, where the principal advantage of a white-light interferometer (WLI) is that it overcomes the measurement ambiguity problems of conventional systems with the use of low coherence sources.

The main elements of a WLI are introduced in this chapter, namely the low coherence radiation sources, the sensing interferometer, the recovery interferometer, the optical bus and the detection schemes. The scanning mechanisms in the output are also compared and contrasted, highlighting the key advantages of electronically-scanned systems over mechanically scanned systems, in that they do not require the use of mechanical phase modulation elements.

2.1. Introduction

The use of optical interferometric techniques in optical fibre sensor applications yields the benefits of providing the high resolution and large dynamic range that is associated with these methods. Conventional interferometric fringe-counting techniques [1,2,3] can provide micron displacement resolutions. These resolutions may be further reduced to the nanometer region with the aid of phase tracking techniques [1,2]. However, the use of such fringe-counting techniques has many disadvantages. One of the main constraints on such systems is the requirement to generate a carrier signal in order to provide phase measurements. This carrier signal is usually generated mechanically, which reduces the mechanical stability of the system [2]. This signal is then further modulated by the measurand of interest. In addition these systems suffer from the problems that the measurements are made incrementally, such that if the detection process is interrupted, the measurement will be lost and will require re-calibration, the prime problem with conventional interferometric displacement monitoring systems.

Single mode semiconductor laser diode sources have been used successfully in pseudo-heterodyne sensor systems [1]. They have been used primarily due to their wide frequency tuning capability and they have been successfully widely employed in many sensor systems. In recent years, another more advantageous technique has been employed for optical fibre interferometric sensor applications. This technique uses low coherence, broadband spectral sources such as light emitting diodes (LEDs), multimode laser diodes or halogen lamps. This sensing technique is thus often denoted as "white-light" or "low-coherence" interferometry. This technique was first reported for an optical sensing application in 1983, initially for use with single mode fibres [4] and then with multimode fibres [5]. However, its principle of operation had been demonstrated previously in 1975, albeit for a different application, namely as a potential communication system [6].

As with all interferometric methods, the optical path difference between the waves is detected via interferometric fringe pattern analysis. There are two main methods of fringe pattern observation in optical fibre systems, which are (i) spectral

domain processing, and (ii) phase domain processing. Each of these methods can be further sub-divided into two further classifications, the nature of which is dependent upon the method of fringe pattern restoration. Primarily these are temporal fringe formation and spatial fringe formation.

The most basic optical fibre sensor configuration employed in the low-coherence (or white-light) approach are shown in Figure 2.1. Here, it is shown that in addition to the sensing interferometer, a second 'recovery' (also commonly known as a 'processing') interferometer [2] is also required to extract the required fringe pattern information. The configuration of this additional interferometer is dependent upon the fringe processing mode that is employed. It can take the form of a secondary interferometer or a spectrometer depending upon whether the operation is to be carried out in the phase or spectral domain respectively.

In this work, the optical processing was carried out in the phase rather than the spectral domain since spectral domain processing schemes require the use of additional components such as spectrum analyzers, polarization control mechanisms or diffraction gratings [7,8]. In the phase domain processing scheme, the processing unit (as shown in Figure 2.1), takes on the form of an unbalanced recovery interferometer. In this WLI scheme it is necessary that the sensing interferometer has an optical

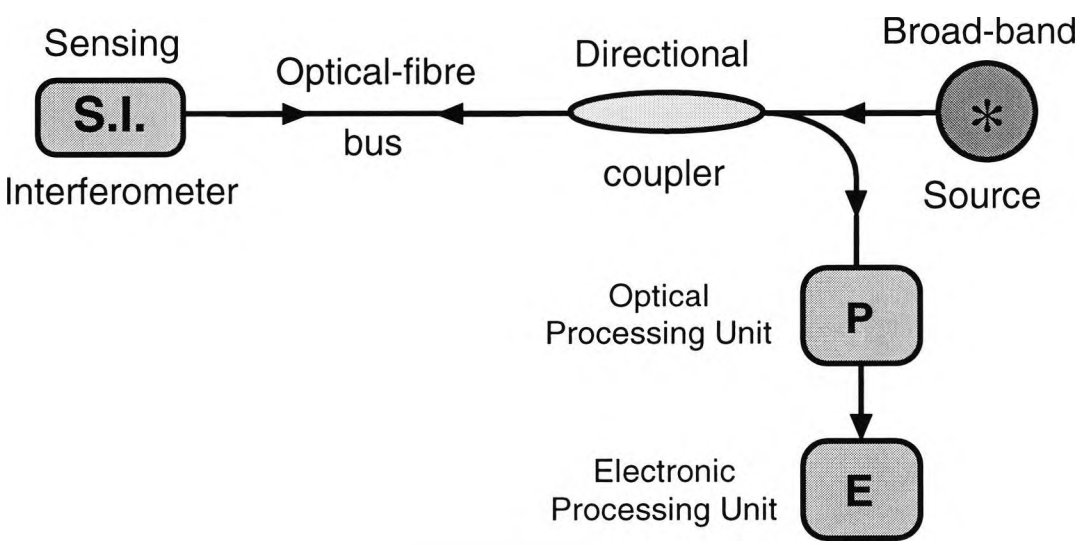

Figure 2.1: Schematic representation of a basic optical fibre sensor configuration using white-light interferometry

pathlength imbalance which exceeds the source coherence length, such that under normal conditions no interference effects are observed at its output. The light waves returned from the sensing interferometer (shown in Figure 2.1), thus are temporally incoherent, and the requirement of the recovery interferometer is to bring the components of the radiation back into temporal coherence, in order to recover the interference fringes generated.

2.2. Advantages in the use of white-light interferometers

White-light interferometry has emerged as a powerful technique for overcoming the ambiguity problem which for many years has severely limited the dynamic range of optical-fibre interferometers. The basic form of a white-light (or low coherence) system reported was first proposed by *Beheim* [9]. Here an unbalanced Michelson reference interferometer was used in conjunction with a Fabry-Perot, temperature-sensing interferometer. By tracking one arm of the reference interferometer, such that zero path difference was maintained between it and the sensing interferometer, ultimately the temperature changes could be determined in a calibrated system. Following this 'temporal-fringe' method, a further modification was proposed by *Chen et al.* [10], whereby one of the mirrors within the reference interferometer was tilted and the coherence profile detected using a CCD array. Using this 'electronically-scanned' technique avoided the need for mechanical ramping of one of the arms of the recovery interferometer, which is a major advantage. However, a design constraint of these systems are that the associated signal-to-noise (S/N) ratio is decreased due to the distribution of the signal over a large number of pixels of the CCD detector.

Fibre-optic sensors remain an active area of research and development, and interferometric-based sensors offer the possibility of achieving high resolution in a simple sensing device. The main limitation in the use of such systems is the short unambiguous measurement range, which is limited by the periodic nature of the optical transfer function [11], and is also further limited by the need to re-initialise the calibrating starting position each time the device is switched on. The use of WLI can

help to overcome these problems through the use of low coherence, broadband sources, with the addition of a secondary recovery interferometer [2, 4, 12].

2.2.1. Limitations of conventional interferometric sensors

In conventional interferometric sensors, due to the periodicity of the output intensity, which occurs as a result of the use of a long coherence length source, a measurement ambiguity will exist. This will lead to the scanning range being limited to one period of the output (which corresponds to $\lambda/2$ in a Michelson interferometer). To overcome this problem, several authors have employed fringe counting techniques [1]. However, in each case, the measurements that are taken are relative, which introduces further problems in that the calibration is lost every time the system is switched off or when the light beam is interrupted, as the fringe count will be lost.

Conventional interferometric sensors usually employ long coherence length sources. The general two-beam output intensity equation derived in Appendix A (Eqn. (A-47)), is repeated here for convenience

$$I = I_1 + I_2 + 2\sqrt{I_1 I_2}\,|\gamma(t)|\cos(\varphi) \tag{2-1}$$

where I is the resultant intensity, φ is the optical phase difference between the two beams, and when $I_1=I_2$, the complex degree of coherence is equivalent to the visibility, $V(\varphi)$, which is the case in the majority of two-beam interferometers. For a long coherence length source, $V(\varphi)\approx 1$, and thus

$$I = 2I_1\left(1+\cos(\varphi)\right) \tag{2-2}$$

This equation is plotted in Figure 2.2, which immediately highlights the problems encountered in using these long coherence systems. Firstly, the sensitivity of the output intensity to small phase changes around zero is itself zero. Optimum sensitivity occurs when $\varphi=\pi/2$. Secondly, phase changes greater than π cannot be unambiguously distinguished from changes less than π because of the periodic response of the system.

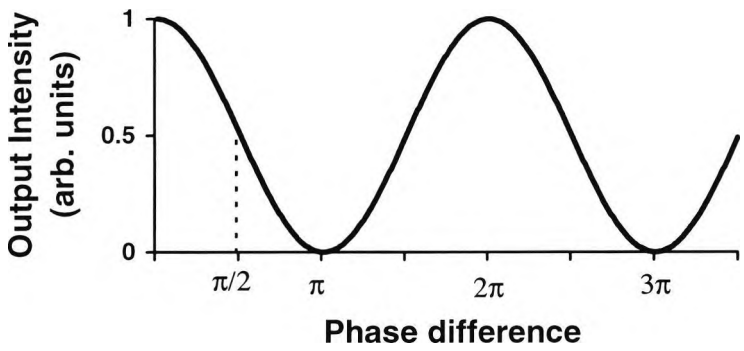

Figure 2.2: Intensity response of a long coherence length, two beam interferometer

To solve this ambiguity problem, a phase bias must be maintained such that $\varphi=\pi/2$, (as illustrated in Fig. 2.2). This is called the 'quadrature condition' [1] because it is equivalent to maintaining a path difference of a quarter of a wave. The dynamic range limitation must also be overcome either by the use of suitable signal processing or by adopting a system architecture which limits the overall OPD to less than $\pm\pi/2$ by means of feedback. This signal recovery may be achieved by the use of feedback, by connecting active components to the interferometer, or without the use of feedback, in which case the system design is arranged to provide a passive bias. The most popular schemes that are employed to achieve this is active and passive homodyne methods and heterodyne techniques [1,3,13].

A popular active scheme is the use of active phase tracking homodyne detection [13]. Here, one of the pathlengths in a two-path interferometer is actively controlled until the relative phase difference is $\pi/2$. Another popular configuration is active wavelength tuning homodyne detection in which the laser source is wavelength-tuned to maintain quadrature, whereby a change in the source wavelength will produce a corresponding change in the relative phase difference between the optical signals propagating in the two arms of an unbalanced interferometer. With semiconductor lasers, the wavelength can be readily tuned by changing the drive current, in an active wavelength tuning homodyne system (AWTH) [14]. Conversely, a passive homodyne scheme may be employed, the aim of which is to recover the signal phase from two output channels of the interferometer which have bias phases which differ by $\pi/2$, such

that, when the signal has faded entirely in one channel, it is a maximum in the other. The two channels are combined into a single output so that the system runs at optimum sensitivity [15,16]. Although these homodyne systems are relatively easy to implement, they have the disadvantage that the dynamic range is often limited by the feedback system.

A. Ezbiri et al. have reported the use of a passive signal processing technique for miniature interferometric sensors [17]. It is based on phase stepping techniques and uses five adjacent axial modes from a multimode laser diode to provide five phase shifted intensity outputs from a low finesse Fabry-Perot interferometer. The use of five measurements reduced the phase errors arising from multiple reflections by two orders of magnitude when compared to techniques using two [18] or three intensity outputs [19].

Heterodyne detection [14,16] provides a different class of technique for recovering phase information from interferometers. The essential difference from homodyne methods is that rather than translating the signal phase directly to a d.c. level, first a beat frequency is generated by shifting the frequency of the optical carrier wave traveling in one arm of the interferometer. The measurand then modulates the phase of this beat frequency, and the signal phase can be recovered by techniques similar to those used in FM radio communications [20]. When the signal shifts the beat signal appreciably, an FM discriminator is used in order to provide a change in output amplitude with a change in input frequency. Alternatively for smaller deviations in the beat signal, the optical beat frequency may be mixed with a signal generated in a local oscillator, known as a phase-locked loop [20]. Popular heterodyne detection schemes are based on synthetic- [21] and pseudo- [3] heterodyne detection schemes. The former avoids the need for a frequency shifter, whilst the latter requires an unbalanced interferometer, and depends on shifting the laser source frequency periodically with time.

The main disadvantages in the use of these heterodyne systems is the relatively complex feedback circuits which need to be employed. In addition, the simple approach of adding a frequency shifter to one arm of a fibre-based device intrinsically

is very difficult to implement, and is practically non-feasible. Although the synthetic- and pseudo- heterodyne techniques can overcome this problem, they still suffer from the use of a local oscillator, which in turn is critically dependent upon the stability of the oscillator.

Another type of interferometric configuration is the polarization interferometer [22,23]. Here, an incident wave is split into measurement and reference beams by a birefringent system (for e.g. a polarizing beamsplitter) [23]. These two beams are orthogonally polarised to each other. The measurand will change the state of polarization in the measurement beam, which is then recombined into a common polarization state by using a polarizer, which causes them to interfere.

Birefringence may be induced in optical fibres from either asymmetric stress induced in the fibre during manufacture, or by external influences (such as bending, twisting or straining). The entire optical system may be constructed using highly birefringent (HiBi) fibre (sometimes called polarization preserving fibre) [24], are specially designed to have a degree of birefringence which is large in comparison with externally induced effects [24]. These HiBi fibre systems have been employed for the measurement of many physical parameters which include displacement [25] and strain[26].

Alternatively, nominally circular core fibre (which has a low intrinsic birefringence), may be employed. Here, externally induced birefringence is compensated by actively controlling the state of polarization of the guided beam [24].

Another common polarization interferometric configuration is based upon a Wollaston prism [26]. These systems have mainly been employed for use as Fourier-transform spectrometers[27] A Wollaston prism produces an angular separation between orthogonally polarized components of the incident light. When it is placed between crossed polarizers and illuminated by a point light source, non-localized straight line fringes are observed after the second polarizer. However, the disadvantage in the use of this and other types of polarization interferometer is that they require the

use of at least two polarizers which have got to be precisely aligned at a set angle of rotation.

2.2.2. The use of White-Light Interferometry techniques

The development and application of the technique of white-light interferometry (WLI) to measurement systems provides the potential to overcome many of the problems that are encountered with conventional interferometers. The advantages of WLI over conventional interferometric sensors are that;

- an increased continuous measurement range is obtained;
- the measurements are absolute;
- the calibration is not lost when the power is switched off;
- the operation is always close to zero optical path difference so the stability requirements on the light source are reduced;
- the optical configuration facilitates the use of signal processing to be more easily incorporated into the optical domain;
- the resolution that is attainable is virtually independent of the wavelength stability of the light source and insensitive to optical fluctuations that occur along the fibre link
- it provides a more practical solution for many measurement problems when compared with an interferometric sensing system that employs single-mode lasers for interrogation, as the lasers have to be highly stabilized.

One of the major advantages of white-light interferometry over conventional interferometric techniques is that the operation of the interferometer is less sensitive to variations in the source wavelength. In a white-light interferometric sensing system, the effective OPD, δ_{wl}, is given by

$$\delta_{wl} = \delta_S - \delta_R \tag{2-3}$$

where δ_S and δ_R are the OPDs in the sensing and recovery interferometers. This effective sensor cavity length of the dual interferometric sensing system, given by δ_{wl}, is the quantity that is sensitive to wavelength fluctuations. Thus, the difference between the OPDs in the two interferometers is sensitive to wavelength changes rather than the actual OPD in each interferometer, which greatly reduces the wavelength sensitivity. To illustrate this difference, consider a wavelength fluctuation, $\delta\lambda$, which has an associated phase noise, $\delta\phi_\lambda$, which is related to source wavelength fluctuations by [2]

$$\delta\phi_\lambda = \frac{2\pi(\delta_S - \delta_R)\delta\lambda}{\lambda_0^2}, \qquad \text{for white light} \qquad (2\text{-}4)$$

whereas, for a pseudo-heterodyne case, the associated phase fluctuation is given by

$$\delta\phi_\lambda = \frac{2\pi\delta\,\delta\lambda}{\lambda_0^2} \qquad (2\text{-}5)$$

where δ' is the sensor cavity length which in practice is typically $\delta' \approx 10$mm. However, for the WLI, typically $\delta_s \approx 50\mu$m with the effective cavity length $(\delta_S - \delta_R) < 10\mu$m. As a consequence this yields a great reduction in phase noise exceeding three orders of magnitude. Thus, stabilization of the source wavelength is much less critical for the WLI method.

In addition to greatly reducing the wavelength stability criteria, the WLI technique also allows the use of much shorter sensing cavity lengths. This factor can be seen from equations (2-4) and (2-5) where the sensor cavity length has been reduced from ~10mm for the pseudo-heterodyne method, to ~50μm for the WLI technique. Hence, the use of the WLI method permits a sensor design whose dimensions approach that of a point sensor.

In addition, the use of optical-fibre white-light interferometry has the added benefits of yielding a more flexible system, since the flexibility of the fibre allows the recovery interferometer to be located in many different locations. Also, the sensing

interferometer may be placed in a hazardous environment whilst the recovery interferometer could be placed several kilometers away in a safe and clean area for processing.

However, there are also disadvantages in the use of white-light interferometers. A WLI may be scanned mechanically [2] or electronically[2]. A mechanically-scanned white-light interferometer (MSWLI) requires the use of a mechanical phase modulation to produce interference fringes, which degrades the mechanical stability of the sensor. In an electronically-scanned white light interferometer (ESWLI), the output beams are expanded across a linear CCD array [2], which distributes the output intensity across a larger area (when compared to a MSWLI). This reduces the optical power across each CCD pixel, which degrades the signal-to-noise ratio.

2.2.3. Essential Theoretical Background for White-Light Interferometry

The basic configuration of a WLI sensor system is a broadband light source (such as an LED or multimode laser diode), and two interferometers connected together via an optical bus. The choice of this optical bus usually dictates the type of light source that is employed. For example, if a single mode optical fibre is used, it would be difficult to couple sufficient power from an LED and thus a multimode laser diode would be the preferable choice. The main WLI source requirement is that the coherence length, L_c, (see Appendix A1.2) is short, such that the intensity, I, of the output interference pattern (from equation (2-1)) is given by

$$I = I_0(1+V(\delta)\cos(k\delta)) \tag{2-6}$$

where I_0 is a constant, $V(\delta)$ is the visibility function of the light source, k is the wave-number and δ is the OPD of the interferometer. A typical interference pattern is shown in Figure 2.3. The visibility can be seen to reach a maximum when the OPD in the interferometer is zero. The coherence length of the source is taken from the 1/e (=0.37) points of the interferogram (as defined in Appendix A1.2), which represents the points

where the interferogram reaches 0.37 of its maximum amplitude. The maximum value occurs at zero optical path difference(OPD), as shown in Figure 2.3.

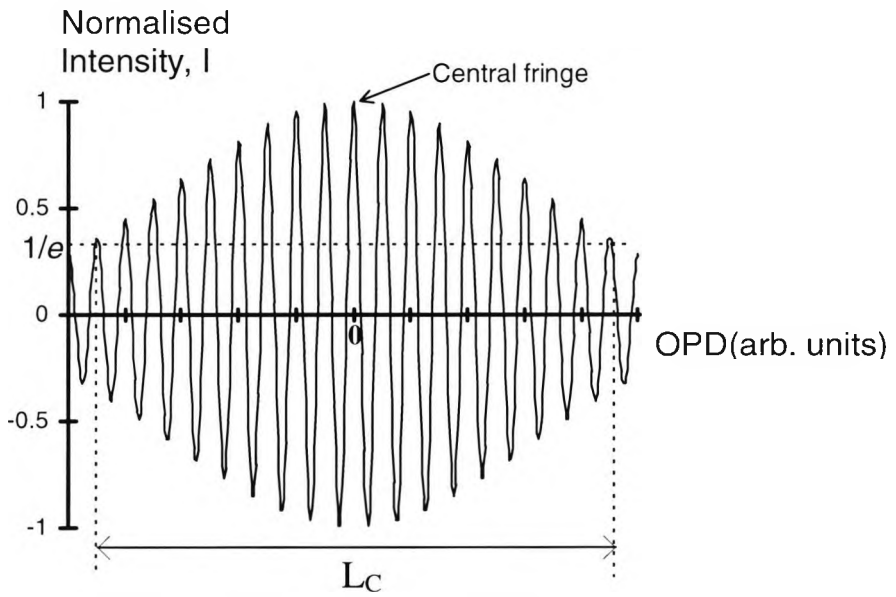

Figure 2.3: Interference pattern from a typical broadband light source, corresponding to a multimode laser diode with a coherence length of L_c.

The OPD in the interferometer is changed by the measurand. By tracking the variation of the position of the central fringe, the variation in the OPD in interferometer can be determined, and thus the corresponding measurand value may be deduced. The position of the central fringe occurs at the zero OPD position, as shown in Figure 2.3. However, when a single source wavelength is employed, the amplitude difference between the central fringe and adjacent fringes may be difficult to distinguish in the presence of noise. To increase the central fringe identification, several authors have reported the use of dual-wavelength techniques. These techniques employ two [28,29] low coherence sources of differing wavelengths, which produces an effective synthesized light source. Due to the beating effect between the two sources, the amplitude difference between the central and adjacent fringes is increased, as shown in Figure 2.4, which greatly increases the measurement accuracy and repeatability. Similar techniques have been extended to multi-wavelength systems to reduce the phase errors in Fabry-Perot sensors [30].

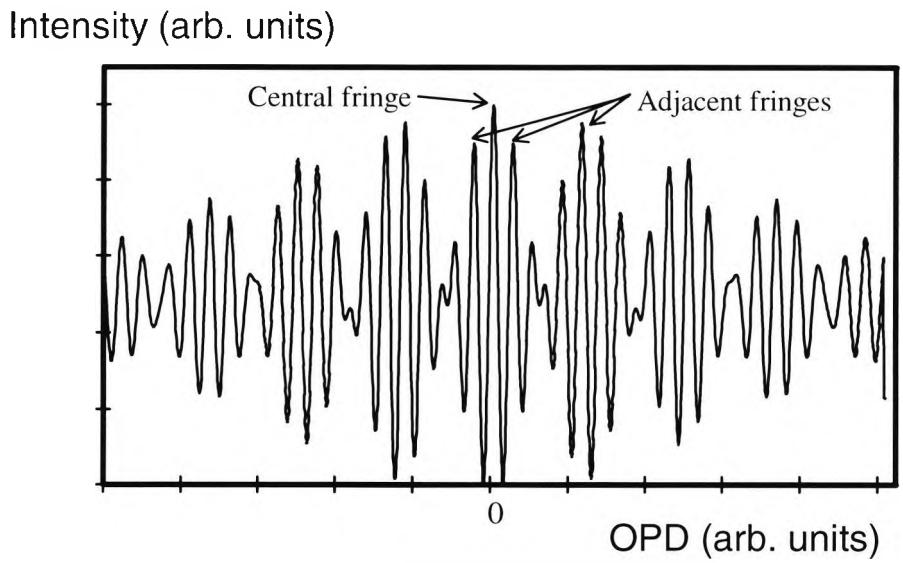

Figure 2.4: Simulated interference pattern from dual low coherence light sources having wavelengths of 635nm and 780nm

A WLI sensor system is comprised of a sensing interferometer and a processing (also commonly called a recovery) interferometer. The OPD in the sensing interferometer may be arranged to be greater than the coherence length of the light source. Thus, no interference will be observed at the output of the interferometer. The sensing interferometer transforms the measurand of interest into a change in the optical path difference. By scanning the OPD in the recovery interferometer, when the combined OPDs of the two interferometers are zero (to within the coherence length) the interference pattern as shown in Figure 2.3 will be observed. Thus, by identifying the OPD of the recovery interferometer corresponding to the maximum visibility of the interference fringes, the OPD of the sensor can be obtained.

The sensor operating range is dependent upon the scanning range of the recovery interferometer, and the measurement resolution is also determined by the resolution of the scan in this interferometer. This implies that the design of the sensing interferometer may be both simple and passive, whilst still achieving high quality measurements. The overall measurement accuracy in WLI systems is determined by both the accuracy with which the central fringe position can be identified, in addition to the precision of the scanning device. The autocorrelation function of the light source

[31] and the signal-to-noise ratio (SNR) of the interferometric output signal determine the resolution required to identify the central fringe position.

The shorter the coherence length of the source, the lower is the requirement for the system SNR. As discussed in detail later in Section 2.4, such short coherence lengths can be achieved using incandescent filament lamps, superluminescent diodes (SLDs), LEDs, or multimode laser diodes. However, incandescent filament lamps have serious disadvantages, such as size, low power launching efficiency into optical fibres, poor reliability and high energy consumption. SLDs are expensive (≈£400), and their use would tend to make the sensor uncompetitive. LEDs can be used, but however they have a low output power and their large relative emitting area leads to inefficient coupling of the light into an optical fibre. Thus, for many applications, the use of a multimode laser diode is the preferential choice. The emission profile of these devices is well matched to the numerical aperture of optical fibres, leading to a high launching efficiency. In addition, the multimode laser diode is relatively inexpensive. The typical coherence length ranges for various short coherence length sources are shown in Table 2.1.

Table 2.1: Typical coherence length ranges for various short coherence length sources

Source	Typical coherence length range (in terms of source wavelength, λ)
White light lamp	5λ-10λ
LED	10λ-25λ
SLD	25λ-64λ
Multimode laser diode (operated just below the threshold current level)	25λ-64λ
Multimode laser diode (operated above the threshold current level)	75λ-120λ

Table 2.1 shows that a multimode laser diode operated at or below its threshold current will yield a coherence length in the range 25λ to 64λ. For a typical laser diode source wavelength of 0.78μm, will yield a coherence length range of 19.5 to 49.9μm, which is sufficiently small for white-light interferometric applications [2].

2.3. Scanning Mechanisms in WLI Systems

A pathlength change in either the sensing or recovery interferometer in a WLI system will produce a modulation in the output signal. Therefore, by modulating the optical path difference (OPD) of the recovery interferometer in a controlled way, a carrier signal can be introduced, the phase of which will then be modulated by the OPD changes in the sensing interferometer. The recovery interferometer in a WLI may be scanned either mechanically or electronically, and the difference between the two schemes lies in the manner in which the OPD is varied.

2.3.1. Mechanically-scanned white-light interferometer (MSWLI)

In a mechanically scanned system [1,2,4,31,32], a mechanical phase modulation element is used in order to provide a changing OPD, and thus produce interference fringes. This modulation is applied in a periodic oscillatory fashion. A simple configuration of a mechanically scanned interferometer is shown in Figure 2.5.

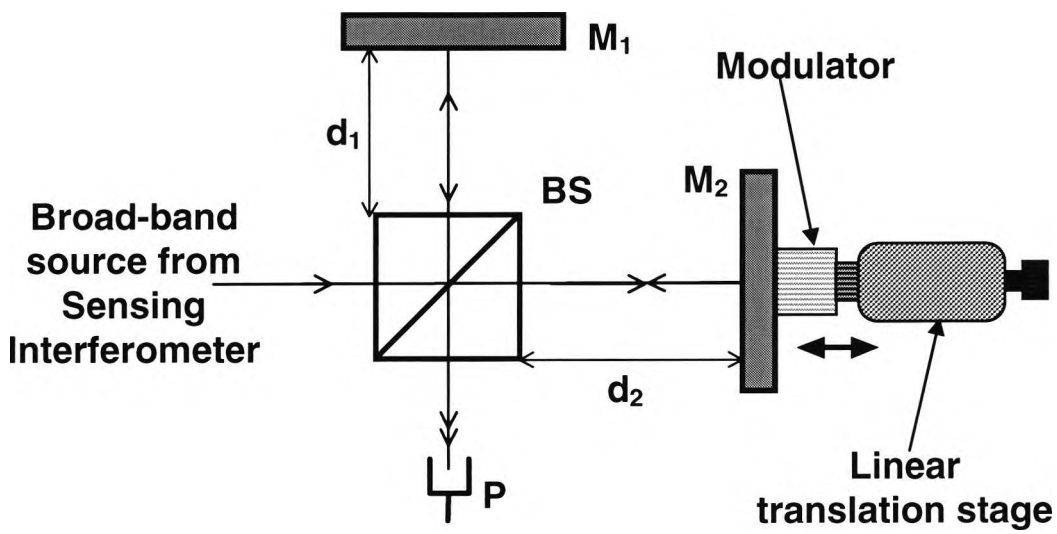

Figure 2.5: Schematic of a mechanically scanned recovery interferometer based upon a Michelson configuration. M_1, M_2 are mirrors and BS is a beamsplitter.

Here, a Michelson interferometer is employed, whereby a linear translation stage is used to control the position of one of the mirrors, which, in turn, controls the OPD in the system.

The main disadvantage of these mechanically-scanned schemes is that they require some kind of mechanical modulation element in order to produce the interference fringes. This is a major problem for industrial applications since this mechanical element will reduce the system stability and increase the alignment sensitivity requirements. In addition, the operational characteristics of mechanical elements will be more liable to drift with time, which necessitates the use of periodic system re-calibration.

2.3.2. Electronically-scanned white-light interferometer (ESWLI)

In order to adjust the OPD in the recovery interferometer, a mechanical scanning device is sometimes used, which offers a large operating range with however, the disadvantage of possessing a relatively large size and with possible mechanical instability associated. In recent years however, the use of the ESWLI approach has attracted a lot of attention [2, 12, 33]. In this technique, the two beams from the recovery interferometer are expanded and collimated to a width of the order of the width of a CCD (or photodiode) detector array. These light beams are overlapped at an angle on this detector array, so that the equivalent spatial interference fringes can be formed without using any moving mechanical parts. Hence, the recovery interferometer may be more compact and stable. In addition, using such an electronic scanner has the added benefits of high accuracy and scanning speed, offers a large operating range and does not require phase modulation and tracing elements, as well as reaping the benefits that are associated with conventional WLIs. These ESWLI systems are ideally suited for applications in harsh environments, such as aerospace sensing due to their compact, rigid and stable structure. However, one disadvantage of this technique is the small operating range and the slightly higher noise level experienced in the detected signal. Nevertheless, these problems can be overcome with the use of appropriate signal processing schemes, as is shown in the work described in the following chapters.

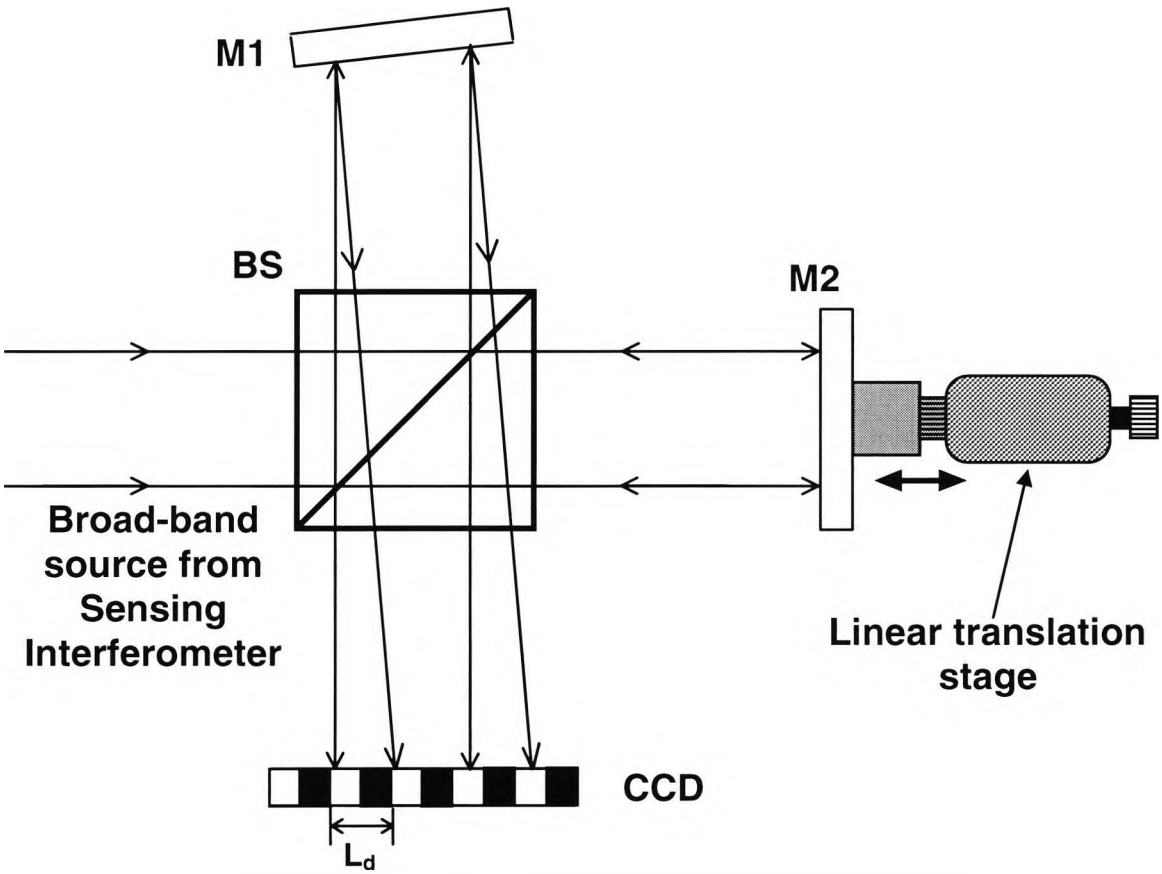

Figure 2.6: Schematic of an electronically scanned recovery interferometer based upon a Michelson configuration. M_1, M_2 are mirrors, BS is a beamsplitter and CCD is a Charge-Coupled Device detector array

By contrast to the techniques employed in the MSWLI, the electronically scanned technique expands the two beams from the interferometer and superimposes them at an angle. A typical ESWLI configuration is shown in Figure 2.6, which is also based upon a Michelson configuration. Here, the interference fringes appear spatially distributed across the beam profile. These fringes are usually detected using a CCD array, hence the term 'electronically-scanned'. This technique has the major advantage that there are no moving parts in the system, thus giving rise to greater mechanical and thermal stability. There are many different ESWLI configurations which have been employed to exploit these advantages [2].

2.4. Sources for Interferometric Systems

2.4.1. Introduction

The mode of operation of an optical fibre sensor, the nature of the signal processing and the degree of spatial and measured accuracy required from it can have a strong influence on the type of source employed in the sensor. Sources for optical sensors tend to vary substantially in price, from a few pounds to tens of thousands of pounds for high power, wavelength-selected lasers. Further important factors in the choice of sources include their size, their associated input and output power, the degree of optical output stability required, the coupling efficiency of the source into optical fibres, the lifetime and maintenance requirements of the source and its spectral characteristics. This last point is especially important for white-light interferometry, which requires the use of short-coherence length sources, thus the coherence length, bandwidth and chromaticity are equally important parameters.

The principal requirements of radiation sources that are employed in optical fibre sensors are that they must provide sufficient radiant energy at a wavelength, or over the wavelength region, of interest and they must maintain a constant or a closely monitorable light intensity over the operational time of the source. Laser sources are employed in ever increasing numbers in fibre optic sensors. Thermal sources (such as white-light lamps) are not used readily for fibre-optic sensors due to the difficulty of coupling sufficient light into the fibre from these sources [34]. Laser sources operate in a completely different manner to thermal and luminescent sources. Primarily, their source characteristics depend upon the energy levels involved in the laser materials, corresponding to different photon transitions, which yield the characteristic colour and monochromaticity of the device. Light emitting diodes (LEDs) have many common features of semiconductor lasers, although their output characteristics differ due to the absence of a laser cavity.

Although there is a wide ranging availability of radiation sources for optical sensors, for the subset of optical-fibre low-coherence sensors, the use of semiconductor lasers and LEDs are the most widely used due to their large availability, coupling

efficiency, output power, small size, spectral output and wavelength range availability. These are just some of the many advantages provided by these sources for optical fibre applications.

2.4.2. Semiconductor Diode Lasers

In recent years, single narrow-stripe semiconductor diode lasers (GaAlAs) operating in a single longitudinal and multi-mode fashion have been used extensively in optical fibre sensors. The rapid increase in availability and choice of semiconductor laser diodes over the last 15 years is due to the need for their use in compact-disc(CD) players. CD players are designed around the 780nm beam of a few milliwatts. With the sale of more than 20 million CD players each year worldwide, this wavelength range is widely available from a range of manufacturers and is the most commonly used diode wavelength for optical sensor applications. Semiconductor laser diodes have become very popular for many applications due to their small size, low cost and high availability. These devices have the advantages of being small and compact, and provide significant output power, a range of wavelengths and possess a low powered drive source requirement.

The energy band structure of a semiconductor laser is essentially similar to that of an LED. The semiconductor laser has a highly populated valence band, a low populated conduction band and a separating energy gap. This energy gap determines the lower limit of the operational wavelength of the laser. The bandgap depends on the

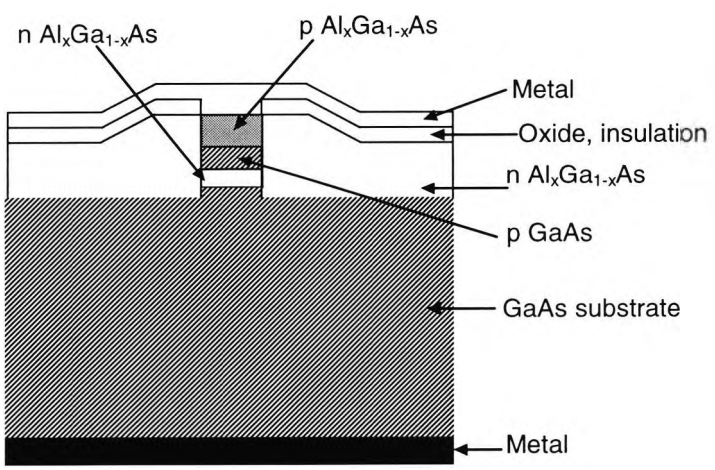

Figure 2.7: Schematic of a buried heterostructure $Al_xGa_{1-x}As$ laser

crystalline structure and chemical composition of the semiconductor material. One of the features of enabling laser diodes to be used in conjunction with optical fibres is the provision of efficient techniques to couple light from the diode into the fibre.

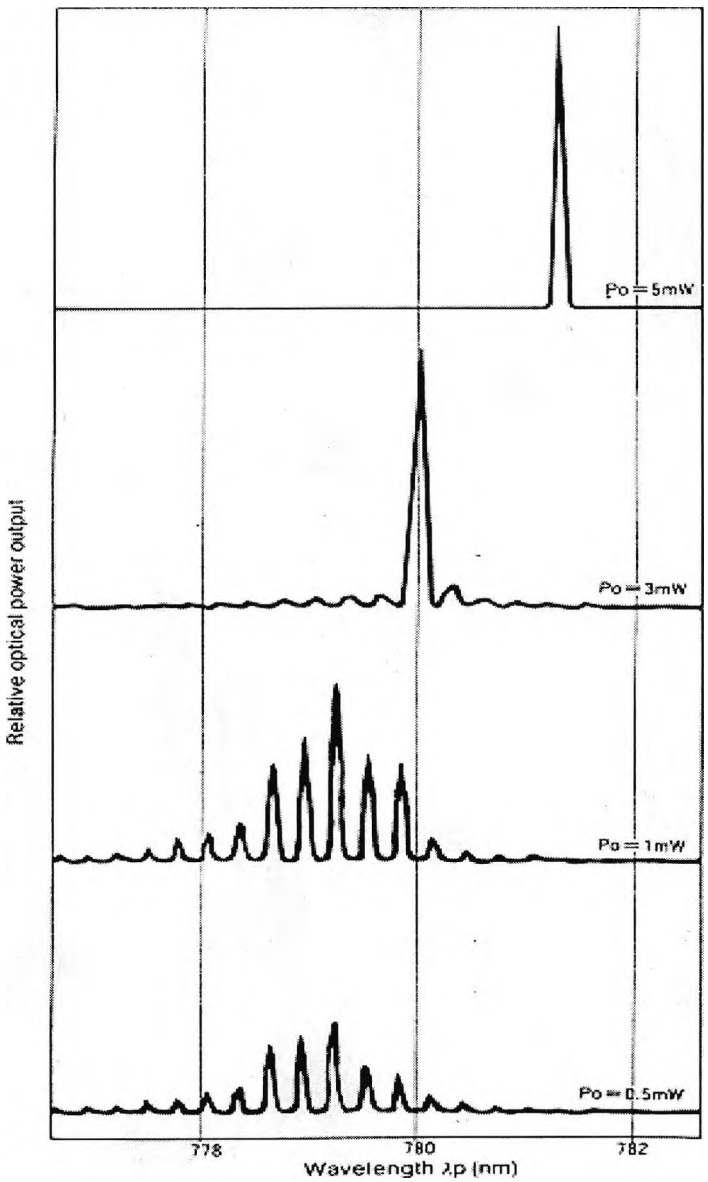

Figure 2.8: Typical optical power output dependence with wavelength, of a Sharp LTO22MD laser diode [35]

Laser diodes typically possess linewidths of 1 to 5nm, considerably smaller than the output spectral width of LEDs. The spectrum of a representative laser diode operating at 780nm is shown in Figure 2.8. The multiple peaks correspond to the longitudinal modes of the device. When the drive current is just slightly above threshold, laser diodes produce multimode spectra, such as that shown in Figure 2.8. This is the desired

mode of operation for white-light interferometry for which short-coherence length, broadband sources are required. Thus, at the threshold current an abrupt increase in the radiance of the emitting region is observed as shown in Figure 2.9. As the current is increased beyond the threshold current, the total linewidth decreases and the number of longitudinal modes diminishes. At a sufficiently high current, the spectrum will contain just 1 mode.

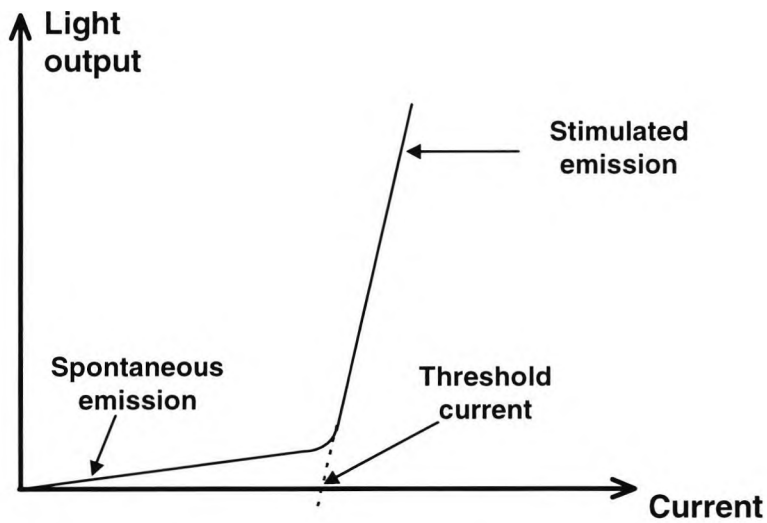

Figure 2.9: Light output-current characteristic of an ideal semiconductor laser [35]

It is shown (in Figure 2.10) that as the temperature of these devices changes, the output power changes as a function of the diode current. Illustrating that the laser diodes are much more temperature sensitive than many other lasers. As the temperature changes,

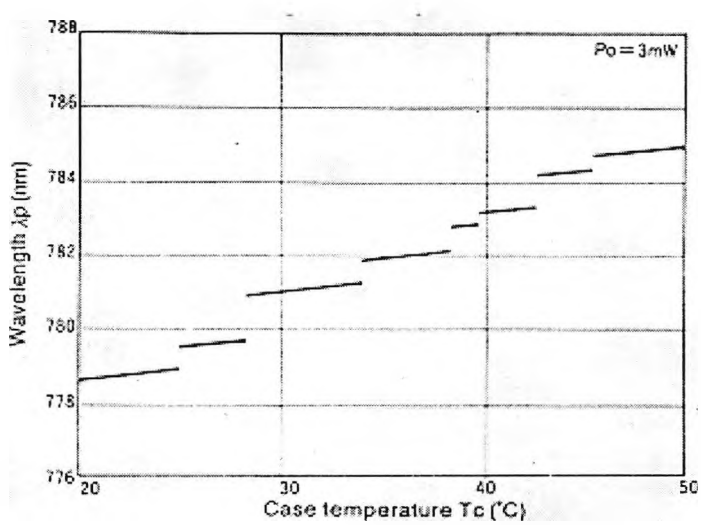

Figure 2.10: Typical wavelength versus temperature characteristics of a Sharp LTO22MD laser diode [35].

a wavelength drift occurs in a typical device, and there are situations that can arise whereby this feature can cause many problems, especially in interferometric sensors. However, temperature tuning may be used to limit 'mode-hopping' [36] and allow the laser to operate on one stable mode, otherwise the laser diode will 'hop' from one mode to another at a specific temperature. This performance characteristic differs from that of an LED where there is a gradual change in wavelength as a result of any change of ambient temperature.

Semiconductor diode lasers have the advantages of being very compact, have a low power consumption, are available in a wide range of wavelengths [37], and a low price. In addition, light from laser diodes is contained in a smaller angular region than that of an LED, facilitating easier and more efficient coupling to a fibre.

2.4.3. Short coherence length sources

There are three main types of sources that are regularly employed in white-light interferometric sensing systems. These are (i) the LED, (ii) multimode laser diode and (iii) interference-filtered halogen lamp. However, the latter is not commonly used in optical fibre based sensors due to the difficulty in coupling sufficient light into the fibre. Thus, the remainder of this section will concentrate on the role of the LED and multimode laser diode in WLI systems. All of these sources have a near-Gaussian spectral intensity distribution in their emitted radiation [37]. Such a distribution can be described by the function

$$i(k) = I_0 \exp\left[-\left(\frac{k-k_0}{\sigma/2}\right)^2\right] \tag{2-7}$$

where k_0 is the central wavenumber and $\sigma/2$ represents the half width of the spectrum $(k_0\text{-}k)$ at which the optical power falls to 1/e of its maximum value at k_0, as shown in Figure 2.11. The light-emitting diode (LED) is usually the preferred choice for simple low coherence sensors using multimode fibre [2,14], except where the higher power capability of lasers is required (i.e. above 3mW). For white-light interferometric

sensors, high radiance broadband sources, such as the superluminescent diode (SLD) [38] or very multimode lasers are advantageous due to their small coherence lengths.

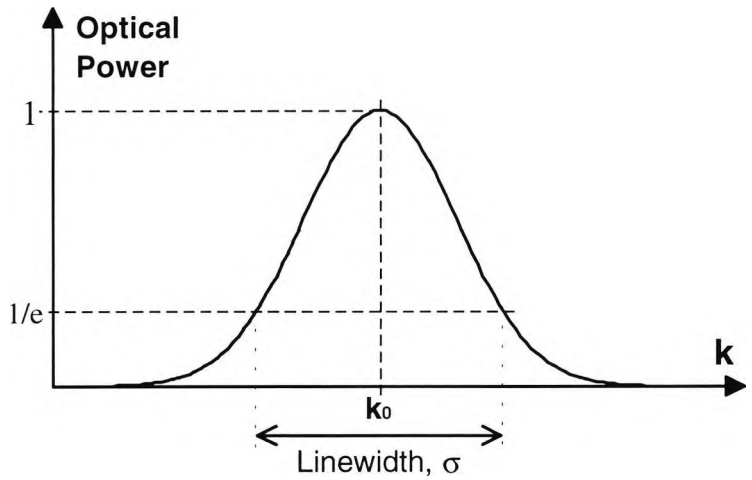

Figure 2.11: Gaussian spectral intensity profile of the optical power versus the wavenumber, k, from a typical low coherence source

2.4.3.1. Light-emitting diode (LED)

The light-emitting diode (LED) has been developed in recent years to produce radiation with a wide variety of spectral characteristics. The operational characteristics of LEDs are well known and have been widely reported elsewhere [34,39,40]. LEDs have the advantages of being inexpensive and widely available, due to their wide use as indicators and thus are widely used in optical fibre sensors [40]. Nevertheless, long term wavelength drifts, in output and source stability due to aging are two important constraints of LED devices. Thus in these instances, monitoring and referencing in actual sensing systems where wavelength stability is critical needs to be employed. In addition, LEDs typically have an emitting diameter in excess of 50μm and therefore couple inefficiently into optical fibres.

2.4.3.2. Multimode Laser Diodes

The most commonly used low-coherence source is the multimode laser diode. The main advantages of a multimode laser diode is that its light output can be more efficiently coupled into an optical fibre when compared to an LED, and typical multimode laser diode has a higher output characteristic with a relatively small emitting area.

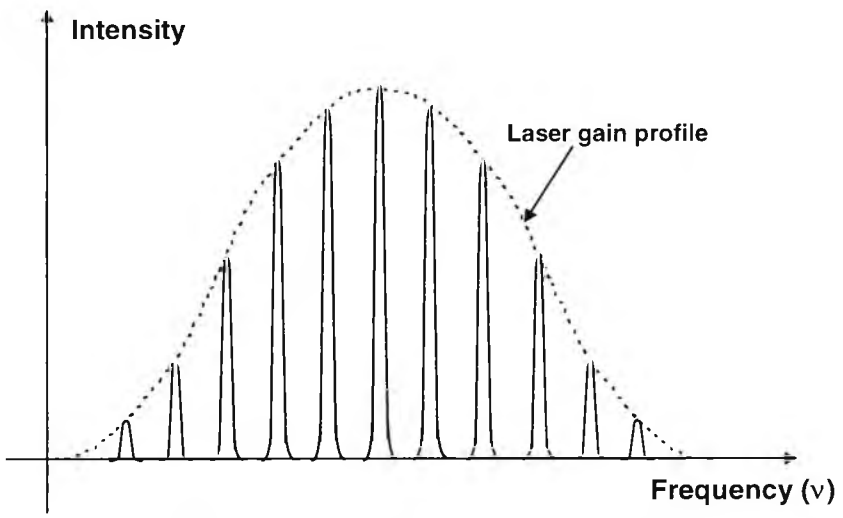

Figure 2.12: A typical mode frequency spectrum for a multimode laser diode, superimposed on the laser gain profile

A laser medium will support lasing over a spectral range that is limited by the natural linewidth of the relevant transition. In practice, the spectral range will be slightly less than this, depending on the cavity losses and the strength of the pumping mechanism. The presence of the optical cavity then serves to limit the oscillating frequencies to certain discrete values within this range, whereby each different frequency is associated with a cavity mode. Figure 2.12 shows a typical mode frequency spectrum for a typical laser diode cavity. The laser medium only exhibits gain over the range of frequencies of the fluorescent emission, which is known as the gain curve. The fluorescent linewidth is the spectral range of the atomic transition giving rise to a laser output and thus, laser modes occupy a spectral range that is approximately equal to the fluorescent linewidth.

In a single mode laser diode, the frequency spread of the laser radiation is reduced to such an extent that only one mode is able to show sufficient gain and thus oscillate. Even if only the TEM_{00} mode is oscillating, several axial (or longitudinal) modes may still be present. The frequency spacing of these longitudinal modes is inversely proportional to the cavity length. Thus, reducing the frequency spacing by increasing the cavity length will result in an increase in the number of longitudinal modes operating, giving multimode operation. In addition, reducing the operational current of a semiconductor laser diode so that it approaches the threshold current, will produce the desired multimode behavioural characteristics. This is shown in Figure 2.10, whereby a Sharp LTO22MD single mode laser diode power output spectrum is shown. However, it only exhibits single mode behaviour at operational powers exceeding 3mW, but at 1mW and 0.5mW operational power levels (which are close to the threshold current level), the output power spectrum is shown to exhibit multimode behaviour, albeit with a slight shift in the central wavelength. Thus, many commercially available laser diodes may be employed in this manner by operating them just above the threshold current level. A thorough analysis of the operational characteristics of multimode laser diodes for interferometric use can be found in the work of *Ning et al.* [31].

2.5. Detectors for Interferometric Measurements

2.5.1. Introduction

An optical sensing system is characterised by an optical signal which is modulated in a reproducible and recoverable manner by a measurand. Although this process is optical, it is necessary to convert the optical signal into electrical form in order that it may be processed. This function may be achieved using a photodetector, which converts optical energy into electrical energy. In general, most photodetectors only produce a low level electrical signal, which must be amplified before it can undergo further processing. The combination of this photodetector and amplifier is called a receiver.

The most basic requirement of any photodetector is the reproducible transfer of optical to electrical energy, ideally with a linear transfer function. Adequate sensitivity is required over the range of power levels and optical wavelengths, with a bandwidth adequate to cover the modulation frequencies present. For simple intrinsic fibre sensors where the optical signal is guided within the sensing element, optical power losses are small. In this case, when readily available sources (such as laser diodes) are employed, then power levels in the milliwatt range are typically present at the output. However, in multiplexed arrays, power is shared between a number of sensing elements, and power levels at the detector are much lower. For extrinsic sensors, the output powers will be even lower, which can severely affect the receiver design.

The three main important detector properties are responsitivity, spectral response, and rise time [41,42]. The responsitivity is the ratio of the output current of the detector to its optic input power. The spectral response refers to the curve of detector responsitivity as a function of wavelength. Due to the rapid change in responsitivity with wavelength, detectors must be matched to the operational source wavelength. The rise time, t_r, is the time required for the detector output current to change from 10% to 90% of its final value when the optic input power variation is a step.

In optical fibre sensing systems, semiconductor photodiodes are employed due to their relatively small size and good operational characteristics. In an ESWLI system, the beams are expanded and as such are detected by using a CCD or photodiode array.

2.5.2. Charge-coupled device (CCD) detector arrays

In an ESWLI system [12, 43, 44, 45], the expanded and collimated light beams from the two arms of the receiving interferometer are overlapped at an angle to produce spatially distributed interference fringes. These spatial fringes may be detected by the use of a CCD or a photodiode array [41,46], so that the equivalent spatial interference fringes can be formed without the use of moving mechanical parts. The use of such an electronic scanner has the added benefits of high accuracy and scanning speed, a large operating range and does not require phase modulation and tracing

elements. A CCD is essentially a series of metal oxide semiconductor (MOS) capacitors [41,46]. CCD arrays are the preferential choice over photodiode arrays due to their higher signal to noise ratio, faster scanning speed, smaller pixel resolution and because of the large dark signals experienced in many photodiode arrays [46,47]. An array of discrete detectors may also be used to convert the optical interferogram signal into an electrical one. However, these techniques have the problems that to obtain a scan requires that the output of each detector to be read out sequentially. Since an array may contain thousands of detectors, then this is not a trivial interconnection problem. A CCD array avoids most of these difficulties. The operational characteristics of a CCD have been reported in depth elsewhere [41,46,47]. For ESWLI applications, one dimensional CCDs suffice since the interference fringes can be detected in one-plane across the incident beams. Typically, line CCD arrays are currently available with up to 4096 pixels and pixel-to-pixel spacings of ~10μm.

2.6. Optical Transmission Medium

2.6.1. Introduction

The use of optical fibres in interferometric sensing systems has many advantages [1,2,44]. Primarily, they possess the advantage of being immune to electromagnetic interference (EMI). They also are highly flexible, such that the fibre probe can be placed in inaccessible areas. Guiding the light in a fibre also reduces the risks of combustion in hazardous environments, such as explosive regions. The fibre itself has the additional benefits that it can often be employed intrinsically as a sensing head. The theoretical background analysis of optical fibres has been widely reported elsewhere [48,49] and is not necessary to describe it here in great detail. Instead, the main implications of their use in white-light interferometers is discussed in the following sections.

The use of optical fibres in a WLI means that the sensing interferometer (SI) and the recovery interferometer (RI) may be separated by a large distance. This facilitates the deployment of the SI in a hazardous industrial environment, whilst the RI

may be located far away in a clean and safe environment. Also, due to its widespread use in and development for optical telecommunication systems, optical-fibre is cheap and readily available. The system can also be connectorized when optical fibres are employed yielding a more convenient system, which can be achieved for example by using SMA connectors [49]. The use of such connectors increases the coupling and guiding efficiency of the light sources and the mechanical stability of the system.

2.6.2 Guidance properties of optical fibres

There are three main factors that affect the light collecting ability of an optical fibre. These are the physical size of the core, the maximum angle between the direction of the incoming light and the core axis and finally the shape of the refractive index distribution within the core. This maximum acceptance angle is limited by the critical angle of incidence at the core-cladding boundary.

2.6.3. Fibre coupling

One of the major considerations in the use of optical fibres in white-light interferometry is the coupling efficiency. Ideally, for both single and multimode fibre, the requirement is to focus the radiation from the source onto the core, and to ensure that the convergence angle of the light is no greater than the fibre will accept. The relatively small core diameters of single-mode fibre (~5μm typically) has significant disadvantages over that of multimode fibre, which has a core diameter ranging from a minimum of 50μm. Thus, in many optical fibre sensors applications [1,2], it is rather difficult to couple sufficient incident light into a single-mode fibre using simple optics. This situation is also increased by the fact that the numerical aperture (NA) profile of the laser diode source is elliptical [35,36,37], whilst the NA profile of the optical fibre is circular [48,49]. A coupling efficiency of approximately 50% can be achieved between a semiconductor laser diode and a single-mode optical fibre, when low cost micro-optical systems are employed [47]. This coupling efficiency may be increased to approximately 80% when a multimode fibre is employed [47]. Figure 2.13 shows the difference between the coupling efficiency of light into a single-mode (Fig. 2.13(a))

and a multimode optical fibre (Fig. 2.13 (b)). Due to the very small core diameter of the single mode fibre, only the rays at or very close to the central ray path will propagate. All of the remaining rays will be lost into the cladding, as shown in the figure. However, in a typical multimode optical fibre, the appreciably larger core diameter facilitates a higher amount of coupling efficiency by trapping more incident rays which are within the NA requirements of the fibre.

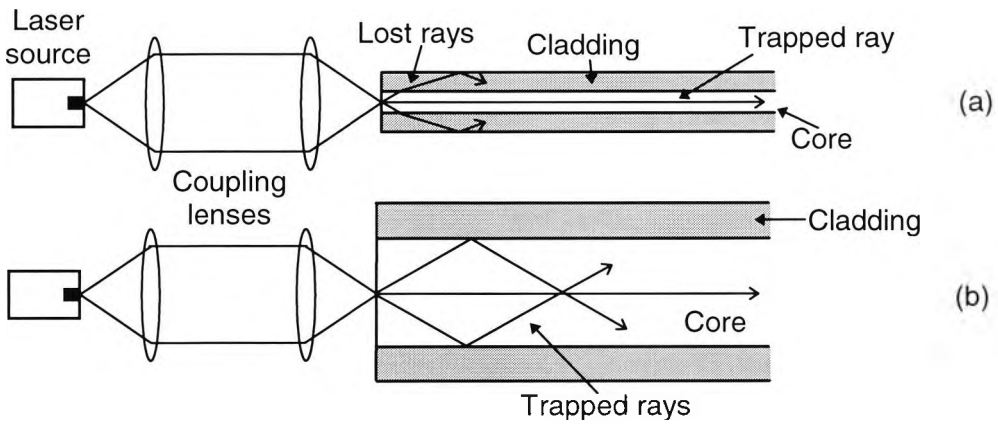

Figure 2.13: Schematic shows the difference in coupling efficiency in a typical single-mode (a) and in a typical step-index multimode optical fibre (b). (Not to scale)

In an ESWLI, the power output requirement is very stringent, so it is more advantageous to employ multimode fibres with their larger core diameters. However, the use of multimode fibres introduces additional problems due to modal noise which must be overcome [51].

2.7. Summary

An overview of the principles of white-light interferometry (WLI) has been provided in this chapter. The main advantages of this technique over conventional interferometric methods has been addressed. WLI have been shown to be capable of providing absolute measurements of a variety of physical parameters with the use of a dual interferometric configuration comprising a sensing interferometer and recovery interferometer in conjunction with a short coherence length source.

The advantages of the use of a CCD array as a detector in an ESWLI have been introduced. Primarily, this scheme can provide accurate measurements without the use of mechanical moving parts, which increases the system stability. All of the elements in this chapter serve as a useful prerequisite to the design and development of a novel ESWLI system introduced in the following chapters.

2.8. References

1. Jackson, D. A., and Jones, J. D. C.: "Fibre Optic Sensors", Opt. Acta, vol. 33, 1469-1503, 1986.
2. Meggitt, B. T.: "Fiber optic white-light interferometric sensors", Ch. 9, pp. 269-312, In: "Optical Fiber Sensor Technology", Eds. Grattan, K. T. V. and Meggitt, B. T., Chapman & Hall, London, 1995.
3. Jackson, D. A., Kersey, A. D., Corke, M. and Jones, J. D. C.: "Pseudo heterodyne detection scheme for optical interferometers", Electron Lett., vol. 18, pp. 1081, 1982.
4. Al-Chalabi, S. A., Culshaw, B. and Davies, D. E. N.: "Partially coherent sources in interferometry", IEE (No. 221) Proc. 1st International Conf. on Optical Fibre Sensors, London, pp.132-5, 1983.
5. Bosselman, T. and Ulrich, R.: "High accuracy position-sensing with fibre-coupled white light interferometers", Proc. 2nd International Conf. on Optical Fibre Sensors, Stuttgart, pp.361-5, 1984.
6. Deslisle, C. and Cielo, P.: "Application de la modulation spectrale a la transmission de l'information", Can. J. Phys., vol. 53, 1047-53., 1975.
7. Velluet, M. T., Graingorge, Ph. and Arditty, H. J.: "Fibre optic pressure sensor using white-light interferometry", Proc. SPIE, vol. 838, Fibre optic Sensors V, pp. 78-83, 1987.
8. Harl, J. C., Saaski, E. W. and Mitchell, G. L.: "Fibre optic temperature sensor using spectral modulation", Proc. SPIE, vol. 838, Fibre Optics and Laser Sensors V, pp. 257-61, 1987.
9. Beheim, G.: "Fibre-linked interferometric pressure sensor", Rev. Sci. Instrum. 58(9), pp. 1655-1659, Sept., 1987.

10. Chen, S., Meggitt, B. T., Rogers, A. J.: "A novel electronic scanner for coherence-multiplexing a quasi-distributed pressure sensor", Electron. Lett., vol. 26, no.17, pp. 1367-1369, 1990.

11. Gerges, A. S., Farahi, F., Newson, T. P., Jones, J. D. C., and Jackson, D. A.: "Fibre-optic interferometric sensor utilising low coherence length source - Resolution enhancement", Electron. Lett., vol. 24, pp.472-474, 1988.

12. Marshall, R.H., Ning Y. N., Jiang, X. Q., Palmer, A. W., Meggitt, B. T. and Grattan K. T. V.: "A novel electronically-scanned white-light interferometer using a Mach-Zehnder approach", IEEE J. Lightwave Technol., vol. 14, No. 3, pp. 397-402, 1996.

13. Jackson, D. A., Dandridge, A., Priest, R., and Tveten, A. B.: "Elimination of drift in a single mode optical fibre interferometer using a piezoelectrically stretched coiled fibre", Applied Optics, vol. 19, pp. 2926, 1980.

14. Digonnet, M. J. F. and Kim, B. Y.: "Fibre optic components", Ch. 7, pp. 209-248, In: "Optical Fiber Sensors: Principles and components", Eds. Dakin, J and Culshaw, B., Artech House, Boston, 1988.

15. Dandridge, A., Tveten, A. B. and Giallorenzi, T. G. "Homodyne demodulation scheme for fibre-optic sensors using phase generated carrier", IEEE J. Quant. Electron., vol. QE-18, pp.1647, 1982.

16. Jackson, D. A.: "Monomode optical fibre interferometers for precision measurement", J. Meas. Sci. and Technol. pp.981-1001, vol. 18, 1985.

17. Ezbiri, A, Tatam, R. P.: "Five wavelength interrogation technique for miniature fibre optic Fabry-Perot sensors", Optics Comms., pp. 62-66, vol. 133, 1997.

18. Wright, O. B.: "Stabilised dual-wavelength fiber-optic interferometer for vibration measurement", Opt. Lett, pp. 56-58, vol. 16, 1991.

19. Ezbiri, A, Tatam, R. P.: "Three wavelength passive homodyne signal processing technique for miniature interferometric sensors", Proc. SPIE, pp. 177-184, vol. 2544, 1995.

20. Handerek, V.: "Single mode optical fiber sensors", Ch. 7, pp. 197-222, In: "Optical Fiber Sensor Technology", Eds. Grattan, K. T. V. and Meggitt, B. T., Chapman & Hall, London, 1995.

21. Cole, J. H., Danver, B. A. and Bucaro, J. A. "Synthetic heterodyne interferometric demodulation", IEEE J. Quant. Electron., vol. QE-18, pp. 694, 1982.

22. Jackson, D. A.: "Monomode optical fibre interferometers for precision measurement", Phys E: Sci. Instrum., vol. 18, pp.981-1001, 1985.

23. Bobroff, N.: "Recent advances in displacement measuring interferometry", Meas. Sci. Technol., vol. 4, pp. 907-926, 1993.

24. Tatam, R. P.: "Optical fiber modulation techniques for single mode fiber sensors", Ch. 8, pp.223-267, In: "Optical Fiber Sensor Technology", Eds. Grattan, K. T. V. and Meggitt, B. T., Chapman & Hall, London, 1995.

25. Weir, K. Palmer, A. W., and Grattan, K. T. V.: "Accurate measurement of small displacement using optical techniques", Intl. J. of Optoelectronics, vol. 9, pp. 449-445, 1994.

26. Bock, W. J., Urbanczyk, W., and Zaremba, M. B.: "Electronically scanned white-light interferometric strain sensor employing highly birefringent fibers", Optics Comms., vol. 101, pp. 157-162, 1993.

27. Courtial, J., Patterson, B. A., Harvey, A. R., Sibbett, W, and Padgett, M. J.: "Design of a static Fourier-transform spectrometer with increased field of view", Applied Optics, vol. 35, pp. 6698-6702, 1996.

28. Wang, D. N. Ning, Y. N., Grattan, K. T. V., Palmer, A. W. and Weir, K.: "Characteristics of synthesized light sources for white-light interferometric systems", Opt. Letts., vol. 18, pp. 1884-1886, 1993.

29. Rao, Y. J. and Jackson, D. A.: "Improved synthesized source for white light interferometry", Electron. Letts., vol. 30, pp. 1440-1441, 1994.

30. Tatam, R. P. and Ezbiri, A.: "Five wavelength interrogation technique for miniature fibre optic Fabry-Perot sensors", Opt. Comms., vol. 133, pp. 62-66, 1997.

31. Ning, Y. N., Grattan, K. T. V., Palmer, A. W., and Meggitt, B. T.: "Characteristics of a Multimode Laser Diode in a Dual-Interferometer Configuration", IEEE J. Lightwave Technol., vol. 8, No. 12, pp.1773-1778, 1990.

32. Weir, K., Grattan, K. T. V., & Palmer, A. W.: "White light interferometric fibre optic measurement systems", SPIE vol. 2248, pp.307-315, Eds. Christophe Gorecki, C., Preater, R. W., Frankfurt, FRG, 1994.

33. Chen, S., Palmer, A. W, Grattan, K. T. V. and Meggitt, B. T.: "Study of electronically-scanned optical-fibre white-light Fizeau interferometer", Electron. Letts, vol. 27, No. 12, pp.1032-1034, 1991.

34. Young, M. "Optics and Lasers", Ch. 3, pp. 39-68, 3rd ed., Springer-Verlag, 1986.

35. Sharp Laser diode user's manual, Sharp corporation, Japan, 1988.

36. Wilson, J., and Hawkes, J. F. B., "Lasers: Principles and Applications", Ch. 3, pp. 90- 127, Prentice-Hall, London, 1987.

37. Hecht, J.: "The Laser Guidebook", 2nd Ed., McGraw-Hill, New York, 1992.

38. Handerek, V.: "Foundations of optical fiber technology", Ch. 2, pp. 11-44, In: "Optical Fiber Sensor Technology", Eds. Grattan, K. T. V. and Meggitt, B. T., Chapman & Hall, London, 1995.

39. Spectra Diode, Laboratories Product Catalog. Palo Alto, CA., 1991.

40. Plessey Research Ltd., "Information sheet on light emitting diodes for sensor applications", Caswell, UK.

41. Wilson, J., and Hawkes, J. F. B.: "Optoelectronics", Ch. 7, pp. 254-304, 2nd ed., Prentice Hall, 1989.

42. Culshaw, B.: "Optical Fibre Sensing and Signal Processing", Ch. 4, pp. 50-61, Peter Peregrinus, 1984.

43. Chen, S., Palmer, A. W, Grattan, K. T. V. and Meggitt, B. T.: "Study of electronically-scanned optical-fibre white-light Fizeau interferometer", Electron. Letts, vol. 27, No. 12, pp.1032-1034, 1991.

44. Chen, S., Rogers, A. J and Meggitt, B. T.: "A large dynamic range electronically scanned "white-light" interferometer with optical-fibre Young's structure", Proc. SPIE vol. 1511 Fiber Optic Sensors: Engineering and Applications, pp. 67-77, 1991.

45. Dandliker, R., Zimmermann, E. and Frosio, G.: "Noise-resistant signal processing for electronically scanned white-light interferometry", Proc. 8th Optical Fiber Sensors Conf., Jan. 29-31, California, No: W3.2, pp. 53-56, 1992.

46. Gasvik, K. J.: "Optical Metrology", Ch. 6, pp. 111-116, 2nd ed., John Wiley, England, 1995.

47. Streetman, B. G.: "Solid State Electronic Devices", section 9.4.3., 2nd ed., Prentice-Hall, Englewood Cliffs, N.J., 1980.

48. Pal, B.P., Thyagarajan, K. and Kumar, A.: "Characterisation of optical fibres for telecommunication and sensors - Part I: Multimode fibres", Ch. 10, pp. 249-279, In: "Fundamentals of fibre optics in telecommunication and sensor systems", Ed. Pal, B. P., John Wiley, England, 1992.

49. Knoblauch, G. and Toussaint, H.: "Connectors for fiber-optic components and systems", In: "Optical Communications", Siemens, vol. 6, John Wiley, 1983.

50. Yurek, A. M. and Dandridge, A..: "Optical sources", Ch. 5, pp. 151-187, In: "Optical Fiber Sensors: Principles and components", Eds. Dakin, J and Culshaw, B., Artech House, Boston, 1988.

51. Ning, Y. N., Liu Y., Grattan, K. T. V., Palmer, A. W., and Weir, K. : "Relation between the coherence length and modal noise in a graded-index multimode fiber for white-light interferometric systems" Optics Lett., vol. 19, No.6, 372-374, 1994.

Chapter 3:

Recovery Interferometer Design

3.0. Introduction

In this chapter, a review of currently available recovery interferometer (RI) configurations employed in electronically-scanned white-light interferometers (ESWLIs) are investigated and contrasted. The key requirements of an RI is investigated as a prerequisite to the specification for the design of an appropriate RI configuration. A theoretical analysis and experimental evaluation of a novel Mach-Zehnder interferometer (MZI), used as a RI in an electronically-scanned white-light interferometer is reported. This modified version of a MZI has the advantages of being very simple and compact, with high stability and does not introduce any spatial "mis-overlapping" of the beams. In addition, since only one beamsplitter is employed in the interferometer (instead of the usual two used in a conventional MZI), the system is relatively easy to implement and at low cost. Furthermore, this configuration can be simply set to cover a wide range of optical path difference values by simply changing the angle and position of one of the mirrors. This gives the interferometer the advantage of being easily adapted for a range of different measurement applications.

A basic electronically-scanned white-light interferometer (ESWLI) [1,2,3] system consists of a low coherence light source, a sensing interferometer which transforms the measurand into an optical path difference (OPD), and a receiving interferometer to recover the signal, as shown in the general schematic representation illustrated in Figure 2.1. However, the OPD in the receiving interferometer is changed "electronically" [1,2,3], rather than using a mechanical scanning device [4,5]. To provide a large operating range with, but however the disadvantage of possessing a relatively large size and possible mechanical instability.

In an electronically-scanned system, the two beams from the receiving interferometer are expanded and collimated to a width of the order of a CCD (or photodiode) detector array. These light beams are overlapped at an angle on this detector array, so that the equivalent spatial interference fringes can be formed without using moving mechanical parts, enabling the receiving interferometer to be more compact and stable. In the subsequent discussion, a series of RI schemes is introduced and discussed.

3.1. Recovery interferometer schemes

3.1.1. Michelson Interferometer

One possible form for the recovery interferometer is that based upon a Michelson interferometric configuration. When employed in an ESWLI, the Michelson interferometer is modified slightly from the classical and familiar version [6]. Here, one of the Michelson mirrors are tilted through a small angle, α, and its midpoint is designed to give the same arm imbalance as the unperturbed sensing interferometer. The two overlapping and slightly diverging output beams from the Michelson interferometer are then directed onto a linear photodetector array, such as a CCD, as shown in Figure 3.1.

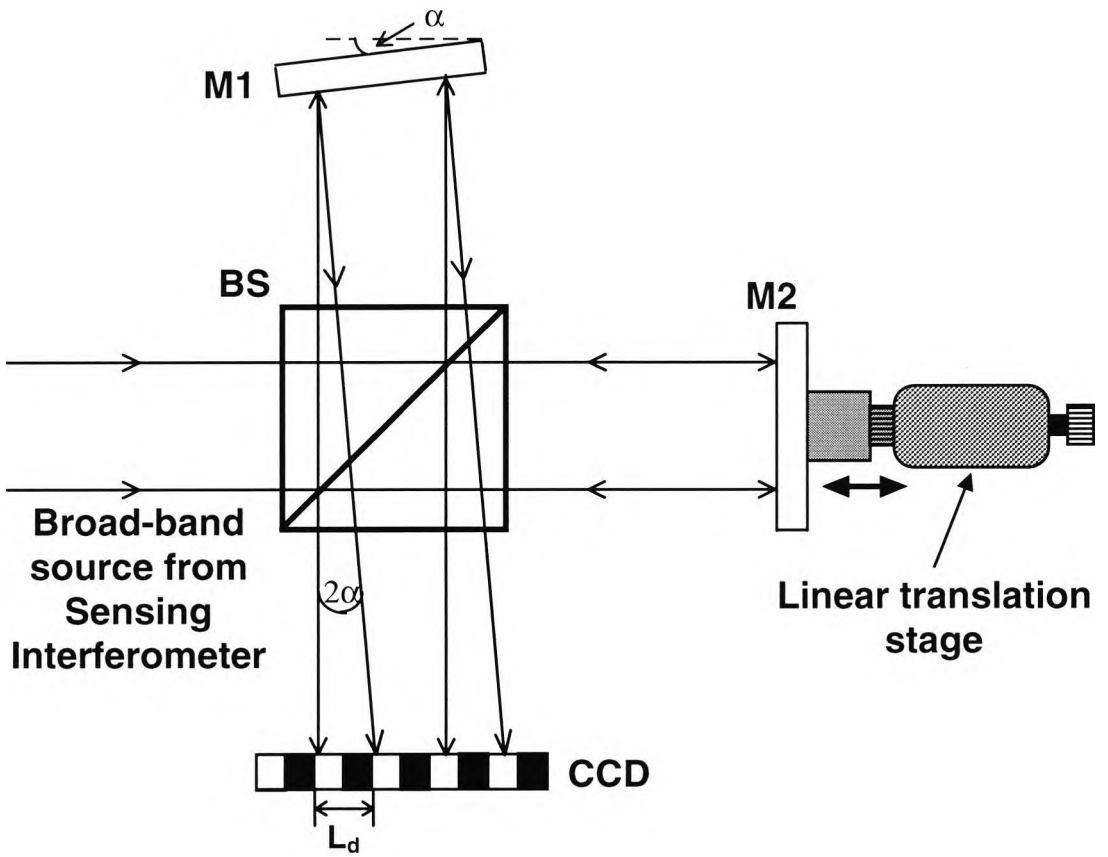

Figure 3.1: Schematic of an electronically scanned recovery interferometer based upon a Michelson configuration. M_1, M_2 are mirrors, BS is a cubic beamsplitter and CCD is a linear CCD detector.

As a result of the presence of a mirror tilt angle, there will always exist a particular path imbalance in the recovery interferometer that exactly matches the OPD of the sensing interferometer, as long as the latter remains within the dynamic range of the recovery interferometer. However, due to the configuration of this Michelson interferometer, there exists a lateral displacement, L_d, between the two beams (as shown in Figure 3.1) since they are diverging slightly with an angle, 2α. This is a major disadvantage of using a Michelson interferometer as an electronically-scanned interferometer. This lateral displacement, L_d, increases with increasing tilt angle, α, and thus reduces the fringe visibility and the operating range. The visibility is diminished due to the mis-alignment (or mis-overlapping of the two beams). Since less of the cross-sectional area of the two beams results in overlap, then this has the added effect of reducing the operation range of the system.

3.1.2. "Basic" Electronically-scanned White-Light interferometer

One of the simplest ESWLI configurations uses only one beamsplitter, BS, and one mirror, M. This interferometer, which shall be denoted as the "Basic" interferometer, is shown in Figure 3.2.

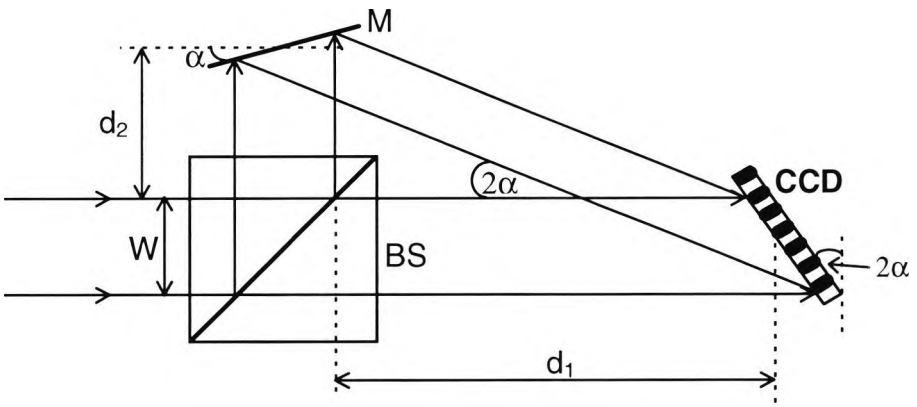

Figure 3.2: Basic ESWLI configuration. M is a mirror, BS is a cubic beamsplitter and CCD is a linear CCD detector array

However, although this configuration employs only one beamsplitter and one mirror, the system is not very practical due to the fact that for practical electronically-scanned interferometers, the inclination angle, α, has a maximum value of approximately 2° [3]. Thus, from Figure 3.2 (which is not shown to scale), for such a small angle, the distance of the CCD detector will be very large. For a typical interferometric sensing system, the beamwidth, W, is ~20mm and for compactness the relative CCD position, d_1, should not exceed ~200mm, to make use of readily available components. From Figure 3.2, the relationship between the parameters governing the use of interferometers may be expressed as

$$\alpha = \frac{1}{2}\tan^{-1}\left(\frac{\frac{W}{2}+d_2}{\frac{W}{2}+d_1}\right) \tag{3-1}$$

In order for the beam to propagate on an unobstructed path to the detector, a minimum mirror position, d_2, of 2cm is required, which would yield an impractical CCD displacement, d_1, of 420cm, for a typical inclination angle, $\alpha \approx 0.2°$. This highlights the fact that it is not a simple task to design an optimum practical ESWLI.

3.1.3 Modified "Michelson/Mach-Zehnder" Interferometer

Chen et al [7] devised a recovery interferometer, denoted as a "modified Michelson/Mach-Zehnder" interferometer, to solve the problem that occurs in the "Basic interferometer". This configuration is shown in Figure 3.3, where an additional mirror is used in order to reduce the size of the interferometer, by increasing the maneuverability of the tilt angle in the interferometer.

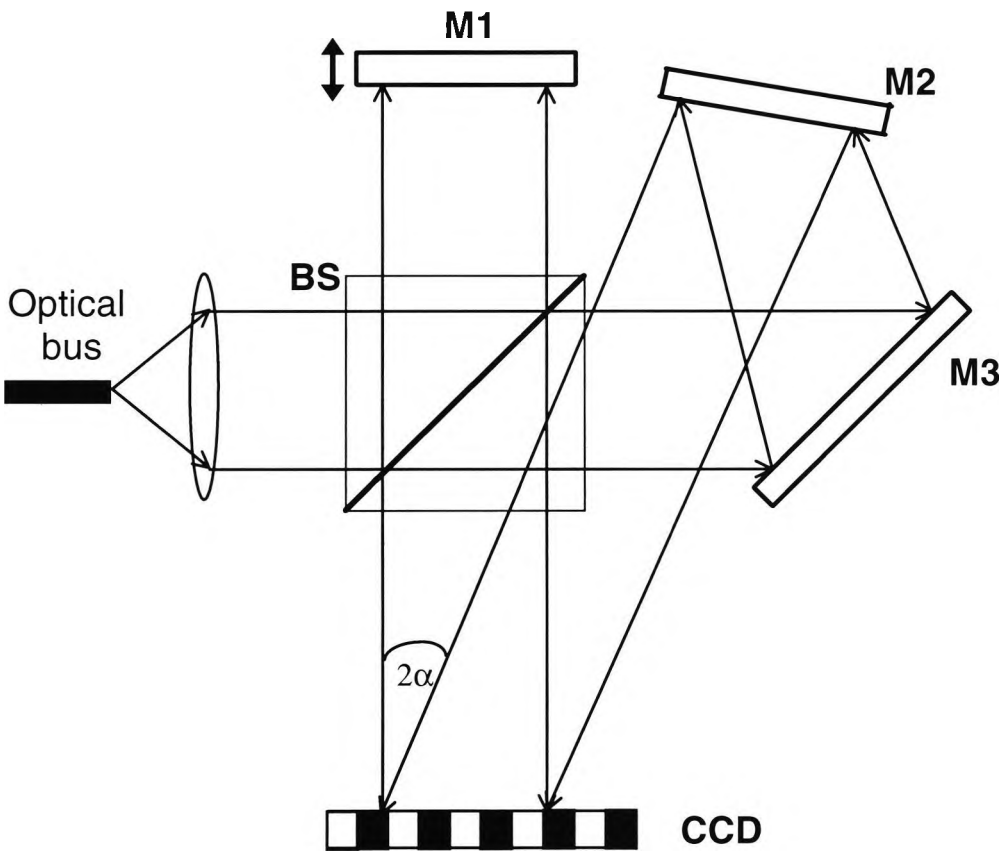

Figure 3.3: Schematic of the Modified Michelson/Mach-Zehnder interferometer [7].
M_1, M_2 and M_3 are mirrors, BS is a cubic beamsplitter and CCD is a linear CCD detector array.

However, this configuration is extremely difficult to align and stabilize since the two mirrors that are employed have to be adjusted precisely to yield the required interference angle between the two beams. In addition, whilst reducing the size of the interferometer somewhat (when compared to the "Basic interferometer"), the interferometer is still rather large, especially when the most desirable small inclination angles are employed [3]. Not surprisingly, the authors have commented that this method is difficult to set up and maintain [1].

3.1.4. Fizeau Interferometer

An early attempt to employ a more practical recovery interferometer was to tackle the requirement for a small, compact configuration. Of all the possible configurations, the Fizeau interferometer could yield the smallest size [1]. The configuration of a conventional Fizeau interferometer consists of a wedge with 2 partially reflective surfaces, P1 and P2, as illustrated in Figure 3.4.

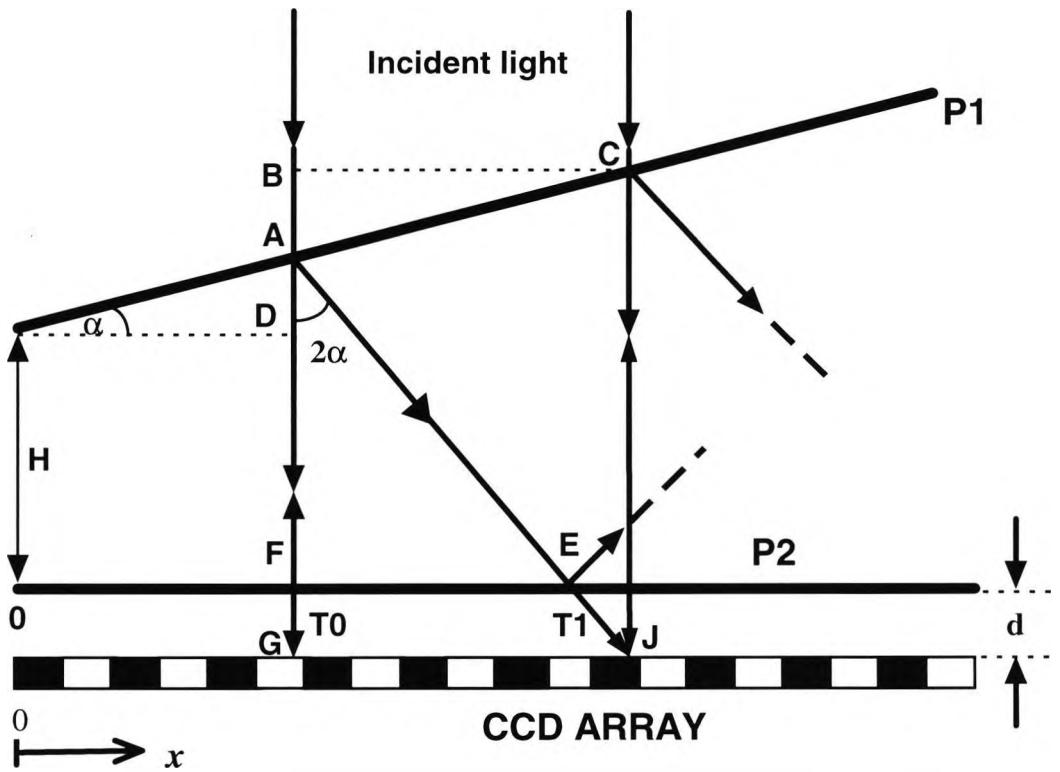

Figure 3.4: Schematic representation of a conventional Fizeau Interferometer producing spatial interference fringes. This configuration shows only 2 significant beams in the interference process. *P1, P2* are mirrors (assumed here to have 50% reflectance and negligible thickness in order to ignore the effects of refraction in this basic model). α is the angle of inclination mirrors P1 and P2.

The collimated incident light (normal to P2) is split into many transmitted (T0, T1,...,) and reflected (R0, R1,...,) beams due to the multiple reflections between the two surfaces. The fringes from the interference between transmitted beams T0 and T1 are detected by a CCD array, and produce the required signal. The full Fizeau analysis can be found in Appendix B. From Equations (B-5) and (B-6), the OPD, ΔL, in the Fizeau interferometer is given by:

$$\Delta L = AD + AE + H + EJ - d \tag{3-2}$$

where;

$$AD = x\tan(\alpha)$$
$$AE = \frac{AF}{\cos(2\alpha)} \equiv \frac{(AD+H)}{\cos(2\alpha)} \tag{3-3}$$
$$EJ = \frac{d}{\cos(2\alpha)}$$

The corresponding intensity (from Appendix B) is given by

$$I = E_0^2[A + 2B\cos(k\delta)]e^{-\left(\delta/L_C\right)^2} \tag{3-4}$$

where

$$A = (1-r_1)^2(1-r_2)^2(r_1^2r_2^2+1)$$
$$B = r_1r_2(1-r_1)^2(1-r_2)^2 \tag{3-5}$$

and L_c is the source coherence length; the OPD between the two beams, δ, is given by $(L_1\text{-}L_2)$; E_0 is the initial electric field amplitude; r_1 is the reflectivity of surface P1; r_2 is the reflectivity of surface P2; and k is the wave-number, given by $2\pi/\lambda$, where λ is the source wavelength.

3.1.4.1. Simulation of the Fizeau Interferometer

From the simulations carried out, it was shown that the Fizeau interferometer produced the required fringe interferogram (see section 2.2.3). However, in a practical ESWLI, there is a need to use a cylindrical lens in order to focus the interfering beams along the linear CCD detector. This lens is required to increase the optical power incident upon the CCD to above its threshold level [3]. Thus, the inclusion of a cylindrical lens implies that the distance, d, between the Fizeau mirror, P2, and the CCD will be ~ 4cm. Thus, the interfering beams will not be exactly spatially coincident, and thus will require a transfer lens to correct this. The use of a transfer lens, in addition to the cylindrical lens, will increase the interferometer size further. In addition, the effects of multiple reflections cannot be totally ignored, even with the use

of low-coherence sources. The interference effects between three beams were also found to have a slight influence (i.e.., between T0 and T2, and T1 and T3,....etc..,) on which produced a slight, but relatively minor reduction in the fringe visibility.

In addition, the Fizeau configuration is difficult to align, since mirrors are in very close contact, as small inclination angles are required in the ESWLI [1] (which are typically < 0.6°). These slight problems with the use of a Fizeau interferometer have led to the development of a novel Mach-Zehnder interferometric configuration. There are several other RI configurations which have been reported, including a Wollaston interferometer [8] and a Young's interferometer [9] among others. The operation of these interferometers will be compared in the following sections.

3.2. Mach-Zehnder configuration

One of the main difficulties with the use of the Fizeau interferometer or a Michelson interferometer in an ESWLI is the so-called spatial "mis-overlapping" of the beams, i.e. the cross-section of one beam cannot be exactly overlapped on that of the other. As a result, the effective scanning range of the system will be reduced over what may otherwise be achieved, whilst, the modified Michelson/Mach-Zehnder interferometer suffers from poor stability, relatively large size and complex alignment requirements. In addition, the Fizeau interferometer cannot be set to yield a zero OPD without the use of an additional sensing interferometer. However, by contrast, the MZI can be set to a zero OPD which is extremely useful during system alignment and calibration, since interference fringes can be observed in the MZI, even when it is operated in isolation.

In this work, a novel Mach-Zehnder Interferometer (MZI) [3] is employed as a recovery interferometer in an electronically-scanned WLI. This modified version of a MZI has the advantages (when compared to previously proposed interferometer configurations for this purpose, such as the Fizeau [10], Michelson and "modified Michelson/Mach-Zehnder" scheme [7]), of being very simple and compact, with high

stability and does not introduce any spatial "mis-overlapping" of the beams. In addition, since only one beam splitter is employed in the interferometer (instead of the usual two beamsplitters used in a conventional MZI), the system is relatively easy to implement, and at low cost. Furthermore, this configuration can be simply set to cover a wide range of OPD values by changing the angle and position of one of the mirrors. This gives the interferometer the advantage of being easily adapted for a range of different measurement applications.

A conventional open-air path Mach-Zehnder interferometer [10,11] consists of two beamsplitters, B_1 and B_2, and two mirrors, M_1 and M_2, as shown in Figure 3.5. The Mach-Zehnder is a two beam interferometer that operates using division of amplitude. The intensity variation of one of the two complementary outputs from a MZI is a function of the OPD between the two arms and may be detected with a photodiode, giving an output changing with time. The first beamsplitter, B_1, divides the beam into two parts, whereas the second, B_2, combines them after reflection from the two mirrors.

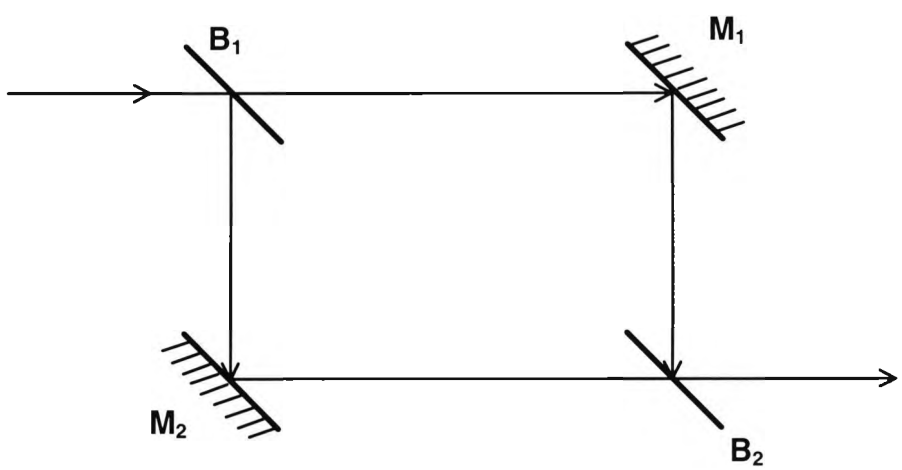

Figure 3.5: Conventional Mach-Zehnder interferometer (B_1, B_2 are beamsplitters; and M_1, M_2 are mirrors)

The configuration of the novel modified MZI used in this work employs only one beamsplitter (BS), as opposed to the two used in the conventional MZI, as shown in Figure 3.6. This modified version of a MZI has the advantages of being very simple and compact, with high stability and does not introduce any spatial "mis-overlapping" of the beams. In addition, since only one beamsplitter is employed in the interferometer (instead

of the usual two beamsplitters in a conventional MZI), the system becomes relatively easy to implement at low cost.

From Figure 3.6, the beam from a low-coherence light source (i.e. a multimode laser diode) may be expanded and collimated. The beam is incident onto the beamsplitter at 45° and then is divided into two by the front-portion of the beamsplitter. After being reflected at mirrors M_1 and M_2, the beams are then recombined through the back-portion of the beamsplitter. The two spots of the beams overlap with each other on the CCD, generating a set of spatially distributed interference fringes along the CCD, which then can be detected using the pixels of the CCD array.

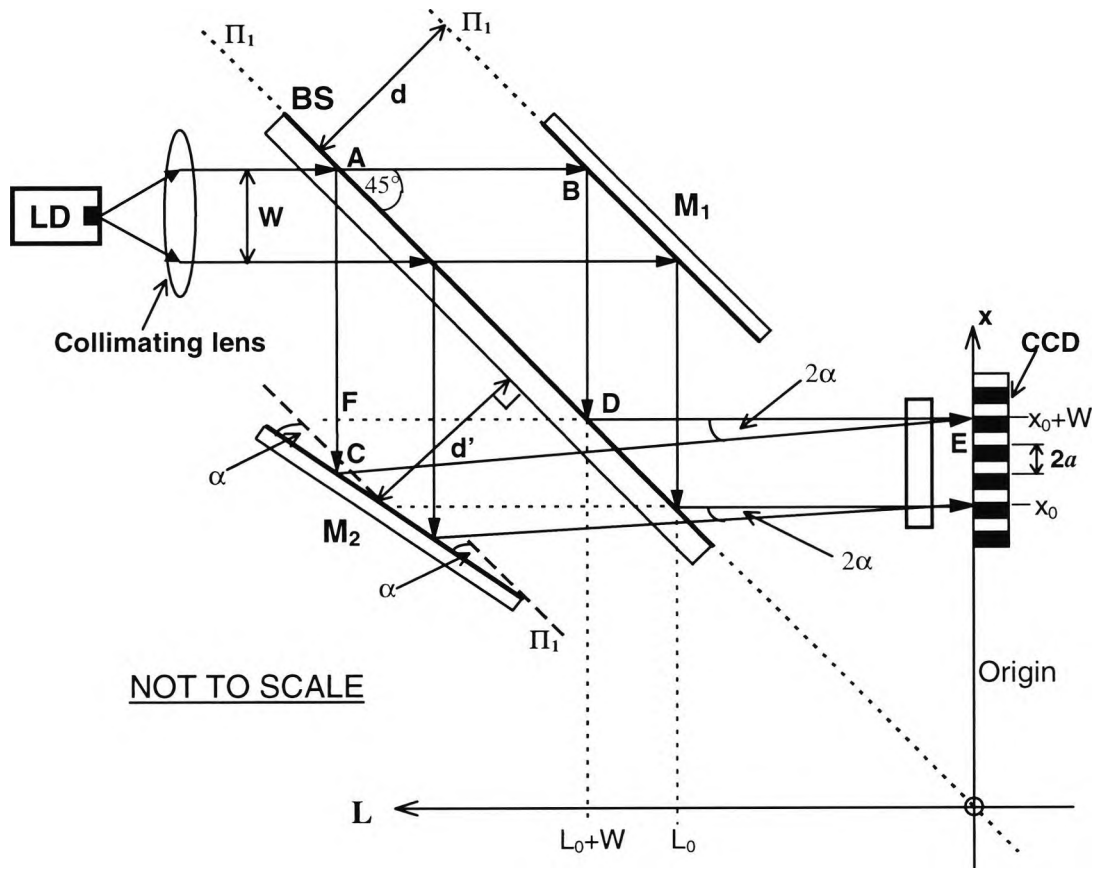

Figure 3.6: Schematic representation of the modified Mach-Zehnder configuration used in this work. LD is a multimode laser diode, W is the width of the incident beam, M_1, M_2 are mirrors, BS is a beamsplitter, CCD is a linear CCD detector array and Π_1 are parallel planes.

3.2.1. MZI Optical Path Difference (OPD)

In order to derive a general expression for the OPD in this MZI, consider the interference observed by the spatial overlapping of the two beams at point E, as shown in Figure 3.6. Here, the OPD, ΔL(x), is given by

$$\Delta L(x) = L_1 - L_2 \tag{3-6}$$

where L_1 is the path taken via ABDE, as shown in Figure 3.6, and is thus represented by

$$L_1 = AB + BD + DE \tag{3-7}$$

Likewise, from Figure 3.6, L_2 is the path taken via AFCE and is given by

$$L_2 = AF + FC + CE \tag{3-8}$$

Such that

$$\begin{aligned} \Delta L(x) &= (AB + BD + DE) - (AF + FC + CE) \\ &= \left(\sqrt{2}d + \sqrt{2}d + x\right) - \left(\sqrt{2}d + FE\tan(2\alpha) + CE\right) \end{aligned} \tag{3-9}$$

Since

$$\begin{aligned} FE &= FD + DE \\ &= \left(\sqrt{2}d + x\right) \\ CE &= \frac{FE}{\cos(2\alpha)} = \frac{\left(\sqrt{2}d + x\right)}{\cos(2\alpha)} \end{aligned} \tag{3-10}$$

equation (3-9) then becomes

$$\begin{aligned} \Delta L(x) &= \left(2\sqrt{2}d + x\right) - \left(\sqrt{2}d + \left(\sqrt{2}d + x\right)\tan(2\alpha) + \frac{\left(\sqrt{2}d + x\right)}{\cos(2\alpha)}\right) \\ &= \left(\sqrt{2}d + x\right) - \left(\left(\sqrt{2}d + x\right)\tan(2\alpha) + \frac{\left(\sqrt{2}d + x\right)}{\cos(2\alpha)}\right) \\ &= \left(\sqrt{2}d + x\right)\left(1 - \tan(2\alpha) + \frac{1}{\cos(2\alpha)}\right) \end{aligned} \tag{3-11}$$

Equation (3-11) may be re-expressed as

$$\Delta L(x) = \left(\sqrt{2}d + x\right)\left(1 - \frac{\sin(2\alpha)}{\cos(2\alpha)} + \frac{1}{\cos(2\alpha)}\right) \tag{3-12}$$

such that

$$\Delta L(x) = \left(\sqrt{2}d + x\right)\left(1 - \frac{1+\sin(2\alpha)}{\cos(2\alpha)}\right) \tag{3-13}$$

Using the trigonometric identities

$$\begin{aligned} \sin(2\alpha) &= 2\sin\alpha\cos\alpha \\ cos(2\alpha) &= 1 - 2sin^2\alpha \end{aligned} \tag{3-14}$$

then the OPD may be expressed as

$$\begin{aligned} \Delta L(x) &= \left(\sqrt{2}d + x\right)\left(1 - \left(\frac{1+2\sin\alpha\cos\alpha}{\cos^2\alpha - \sin^2\alpha}\right)\right) \\ &= \left(\sqrt{2}d + x\right)\left(1 - \left(\frac{\sin^2\alpha + \cos^2\alpha + 2\sin\alpha\cos\alpha}{\cos^2\alpha - \sin^2\alpha}\right)\right) \\ &= \left(\sqrt{2}d + x\right)\left(1 - \left(\frac{(\sin\alpha + \cos\alpha)^2}{(\cos\alpha + \sin\alpha)(\cos\alpha - \sin\alpha)}\right)\right) \\ &= \left(\sqrt{2}d + x\right)\left(1 - \left(\frac{(\sin\alpha + \cos\alpha)}{(\cos\alpha - \sin\alpha)}\right)\right) \\ &= \left(\sqrt{2}d + x\right)\left(\frac{(\cos\alpha - \sin\alpha) - (\sin\alpha + \cos\alpha)}{(\cos\alpha - \sin\alpha)}\right) \end{aligned} \tag{3-15}$$

Such that, the OPD may be re-expressed as

$$\Delta L(x) = \frac{-2\sin\alpha}{(\cos\alpha - \sin\alpha)}\left(\sqrt{2}d + x\right) \tag{3-16}$$

The RI is usually employed with small inclination angles (typically <0.6°), so for small inclination angles, α, the OPD becomes

$$\Delta L(x) \approx -2\sin\alpha\left(\sqrt{2}d + x\right) \tag{3-17}$$

3.2.2. MZI Intensity

From Figure 3.6, the electric field at point E, due to rays L1 and L2, are denoted by E_1 and E_2 respectively. From which, from the principle of superposition (see Appendix A), the electric field, E, at point E may be expressed as

$$\begin{aligned} E &= E_1 + E_2 \\ &= (1-r_1)r_2 r_1 E_0 e^{-j(kL_1-\omega t)} + r_1 r_3 (1-r_1) E_0 e^{-j(kL_2-\omega t)} \\ &= E_0\left[(1-r_1)r_2 r_1 e^{-j(kL_1-\omega t)} + r_1 r_3 (1-r_1) e^{-j(kL_2-\omega t)}\right] \end{aligned} \tag{3-18}$$

Such that

$$\begin{aligned} E &= E_0 e^{j\omega t}\left[(1-r_1)r_2 r_1 e^{-jkL_1} + r_1 r_3 (1-r_1) e^{-jkL_2}\right] \\ E^* &= E_0 e^{-j\omega t}\left[(1-r_1)r_2 r_1 e^{+jkL_1} + r_1 r_3 (1-r_1) e^{+jkL_2}\right] \end{aligned} \tag{3-19}$$

The resultant intensity, I, is given by

$$\begin{aligned} I &= E.E^* \\ &= E_0\left[(1-r_1)^2 r_2^2 r_1^2 + (1-r_1)^2 r_1^2 r_2 r_3 e^{-jk(L_1-L_2)} + r_1^2 r_2 r_3 (1-r_1)^2 e^{+jk(L_1-L_2)} + r_1^2 r_3^2 (1-r_1)^2\right] \end{aligned} \tag{3-20}$$

which may be re-expressed as

$$I = E_0^2\left[(1-r_1)^2 r_1^2 (r_2^2 + r_3^2) + 2(1-r_1)^2 r_1^2 r_2 r_3 \cos\left[k(L_1 - L_2)\right]\right] \tag{3-21}$$

The assumption is made that the light intensity across the incident beam can be uniform and that the incident field assumed to be unity, and thus the intensity, *I(x)*, of the output of the interferometer along the CCD may be given by

$$I(x) = A + 2B\cos(k\Delta L(x))\exp\left(-\left(\frac{\Delta L(x)}{L_c}\right)^2\right) \tag{3-22}$$

where L_c is the coherence length of the source used; k is the wave-number given by $2\pi/\lambda$; λ is the mean wavelength of the source; and $\Delta L(x)$ is the OPD between the two beams at

the point x, where the intensity is detected by the CCD. *A* and *B* are given by $(1 - r_1)^2 r_1^2 (r_2^2 + r_3^2)$ and $(1 - r_1)^2 r_1^2 r_2 r_3$ respectively, where r_n is the reflection coefficient of surface n (n=1,2,3 with surface 1 representing the beamsplitter and surfaces 2,3 representing the mirrors).

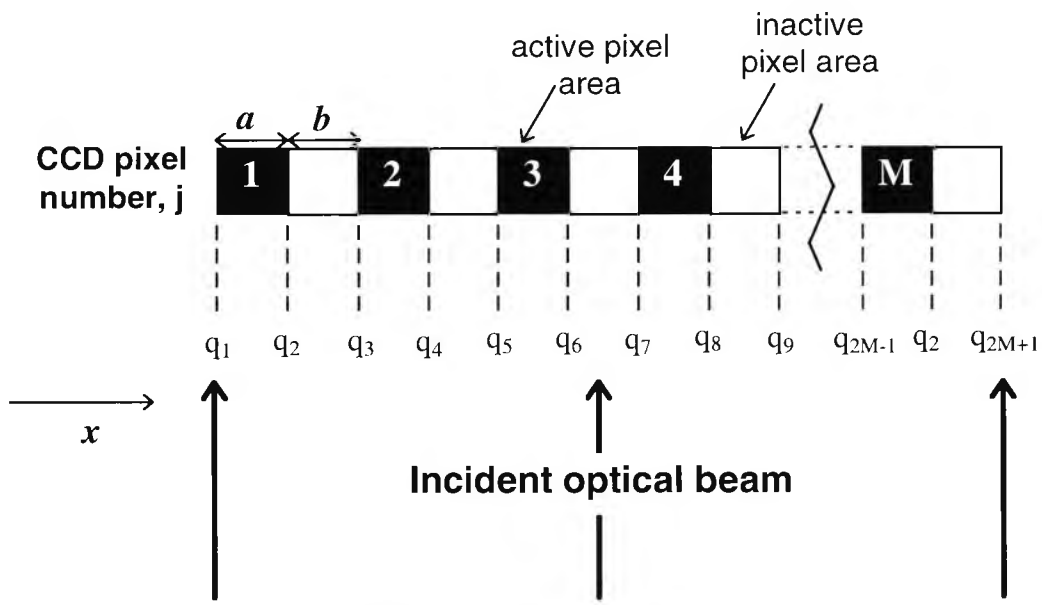

Figure 3.7: Schematic representation of an M-pixel CCD array highlighting the active areas (of width *a*) and the inactive areas (of width b) of the array. Here j is the pixel number, q_k is the kth pixel boundary position and *x* is the propagation direction across the incident beam

3.2.2.1 CCD fringe detection

From the general description of the principle of operation of a CCD array (given in Chapter 2), the incident light falling across each pixel, *I(j)*, is proportional to the sum of the optical power across the active area of the pixel. Each CCD pixel is comprised of an active area, of width, *a*, which can detect the incident radiation; and a pixel spacing, b, which separates the active areas of adjacent pixels. This pixel spacing is present due to the fabrication considerations in the semiconductor material. However, this pixel space yields a sampling rate issue here, since some portions of the incident light cannot be detected. Figure 3.7 shows a schematic representation of a CCD array, which highlights the active and inactive areas of the pixels.

From Figure 3.7, any incident light falling between (q_2 and q_3), (q_4 and q_5) etc...., cannot be detected. Thus, the output power from the jth pixel, *I(j)*, for j=1, 2, ...,M, of the CCD can be related to the pixel boundaries, q_k, by the expression

$$I(j) = \int_{q_{(2j-1)}}^{q_{2j}} I(x)dx \tag{3-23}$$

In most commercially available CCDs, the pixel width is equivalent to the pixel space (i.e. $a \equiv b$), thus equation (3-23) may be transformed into the propagation direction (x domain) as being given by

$$I(j) = \int_{2(j-1)a}^{(2j-1)a} I(x)dx \tag{3-24}$$

where a is the width of each pixel and also the separation between each pixel in the CCD.

3.3 Mach-Zehnder simulation

In order to evaluate the potential performance of the system, its output was simulated by solving equation (3-24). Since an analytical expression could not be obtained for the solution, a FORTRAN program was implemented for this purpose, where a numerical solution (using Simpson's rule) was employed to perform the calculation. The following aspects of the system were considered:

(i) The maximum scanning range (or operating range), of the system, which can be defined by the inclination angle of mirror M2 and the total length of the CCD.

(ii) The use of the CCD pixels to sample the fringes may introduce some level of distortion. Hence it is important to know the variation of the number of pixels per fringe with changing angle of inclination.

(iii) As the inclination angle is changed, the fringe visibility at the central position of the CCD will change accordingly. This should provide an indication of the limitation of the

inclination angle. Whenever the inclination angle is changed, there has to be a corresponding change in the mirror position in order to maintain the overlap of the centres of the two beams.

(iv) If the separation, d', of mirror M2 is fixed, any variation of the inclination angle will result in a positional shift of the central fringe. However, if the inclination angle is fixed, a change in d' will also introduce such a positional shift of the central fringe, and hence it is important to optimize these two parameters for different applications.

A range of typical values of the parameters of interest, was used (as shown in Figure 3.6), in the simulation, these being as follows: λ=0.78μm, L_c=25.0μm, a=13.0μm and d=9500.0μm for M=1024, the total number of pixels.

3.3.1. MZI Operating Range

From Figure 3.6, the overlapping beams along the CCD is shown in more detail in Figure 3.8. The interferometric operating range is a very important parameter that is

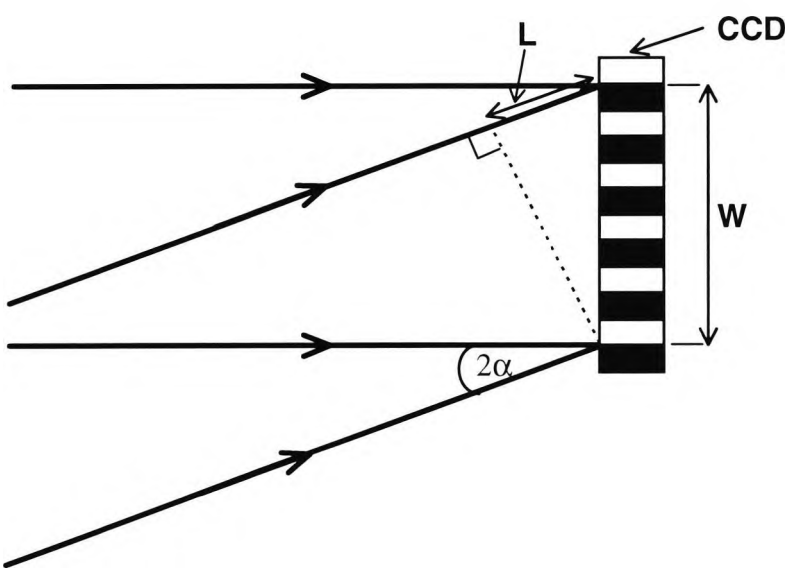

Figure 3.8: Expanded view of the spatial interference of the two beams in the Mach-Zehnder interferometer highlighting the operating range, L

required to be evaluated in order to provide a full system specification. The operating range is the maximum optical scanning range of the interferometer. In an ESWLI, this

operating range, L, is dependent upon the inclination angle, α, and on the beam width, W. Thus, from Figure 3.8, the operating range, L, may be given by

$$L = W\sin(2\alpha) \tag{3-25}$$

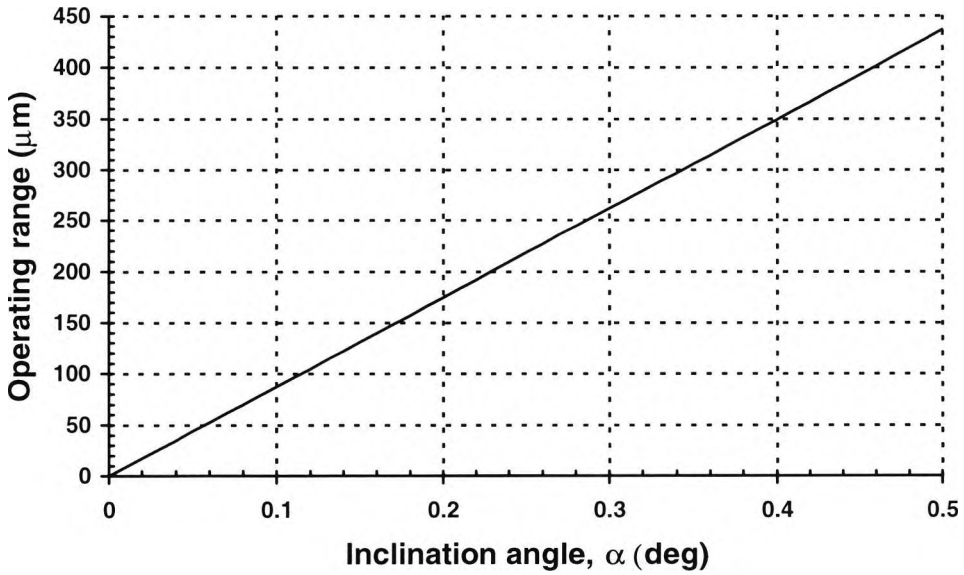

Figure 3.9: Relationship between the inclination angle, α, and the operating range, L, in the MZI

3.3.2. Fringe Visibility

The fringe visibility, V, is a very important consideration in any white-light interferometric sensing system. It is dependent upon many factors, which include the inclination angle, α; the characteristics of the source (see Chapter 2); and the configuration of the interferometer (including the detection scheme). This maximum angle is limited by the fringe visibility and the number of pixels per fringe. In this work the normalized visibility, V, is defined in the usual way as

$$V = \frac{I_{max} - I_{min}}{I_{max} + I_{min}} \tag{3-26}$$

where I_{max} and I_{min} are the maximum and minimum values of the fringe intensity. A simulated visibility plot (Figure 3.10) reveals that the normalized fringe visibility

diminishes to zero at an inclination angle, α, of approximately 1.67°, indicating that the maximum angle used, α_{max}, must be less than this.

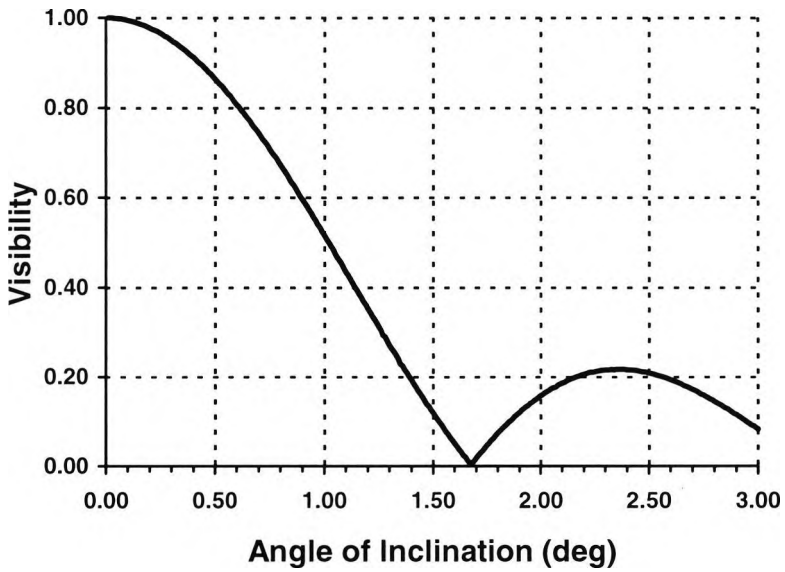

Figure 3.10: Simulated plot of the normalized visibility versus the angle of inclination, α, in the MZI.

3.3.3. CCD sampling rate: the number of pixels per fringe

The use of the CCD pixels to sample the fringes may introduce some level of distortion. Thus, it is important to know the variation of the number of pixels per fringe with changing angle of inclination. In addition, the operating range may be maximized by using the largest permissible angle, α_{max}.

However, according to the Nyquist sampling rate theorem, a fringe must be sampled by at least 2 CCD pixels. As the name suggests, the number of pixels per fringe, p_f, is given by

$$p_f = \frac{T_f}{T_p} \tag{3-27}$$

where T_f is the fringe width and T_p is the pixel width. Figure 3.11 shows a schematic representation of the spatial overlapping of the 2 beams in this MZI. Here, the influence

of the tilt angle, α, on the fringe width is clearly seen, whereby the fringe width is given by

$$T_f = \frac{\lambda}{\sin(2\alpha)} \tag{3-28}$$

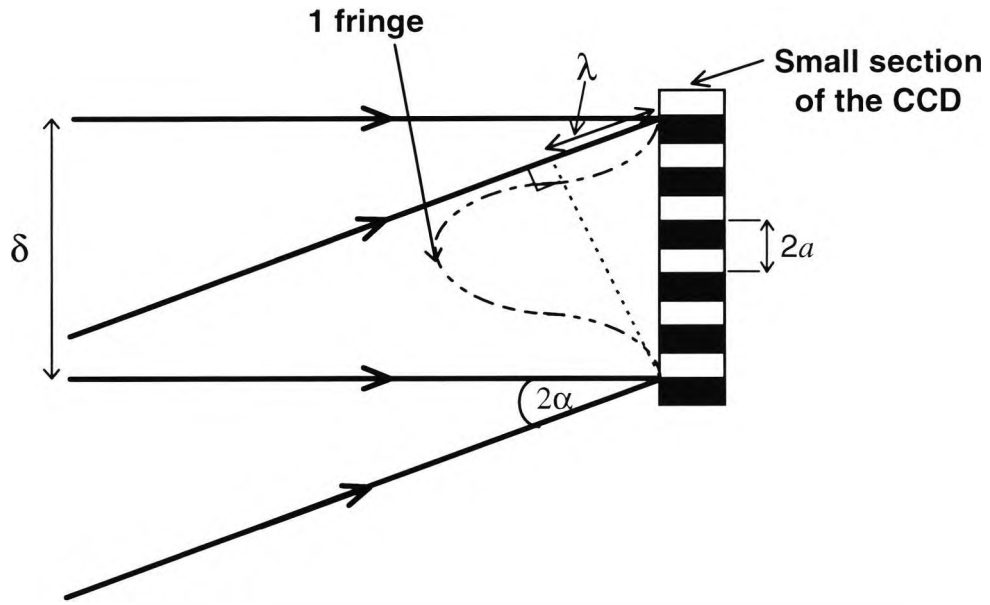

Figure 3.11: Schematic representation of the spatial overlapping of a very small cross-section, δ, of the 2 beams in the MZI which represents one fringe width. Here α is the inclination angle and 2*a* is the effective pixel width (pixel width+pixel space).

Thus, the number of pixels per fringe, p_f, may be expressed as

$$p_f = \frac{\lambda}{2a\sin(2\alpha)} \tag{3-29}$$

where α is the inclination angle, *a* is the pixel width (and the pixel space) as shown in Figure3.11, and λ is the mean source wavelength. Figure 3.12 shows a simulated plot of the number of pixels per fringe versus the angle of inclination, α, which shows that the cut-off point (i.e. at 2 pixels per fringe) occurs at an inclination angle, α, of 0.43°. This shows that the configuration has an effective angular range of $0.0 < \alpha < 0.43°$ under this criterion. The normalized visibility plot (Figure 3.10) shows that the visibility is maintained above 85% in this region, and this is taken as the threshold level.

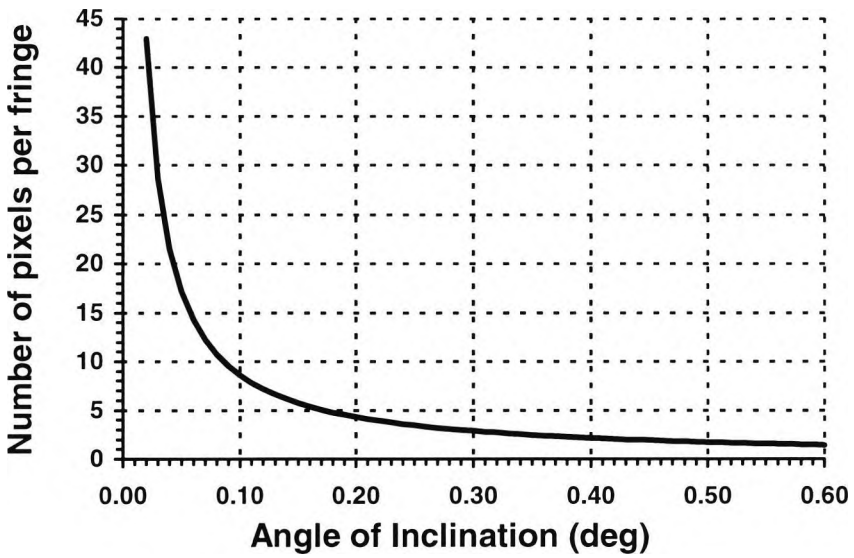

Figure 3.12: Simulated plot of the number of pixels per fringe versus the angle of inclination, α, in the MZI

3.3.4. OPD Balance

It is a very important requirement in the design of the sensing head to compliment this recovery interferometer, to have some indication of the OPD in the MZI under various conditions. The value of the OPD in the recovery interferometer will have a significant bearing on the physical size of the sensing interferometer. This, in turn, may affect the type of interferometer employed in the sensing head. Figure 3.13 shows a plot of the OPD balance with respect to the beam central point, $(x_0+W/2)$, (i.e. the OPD required to balance the Mach-Zehnder interferometer) as a function of α. At this maximum angle, it can be seen that the OPD balance position is $\approx$0.4mm.

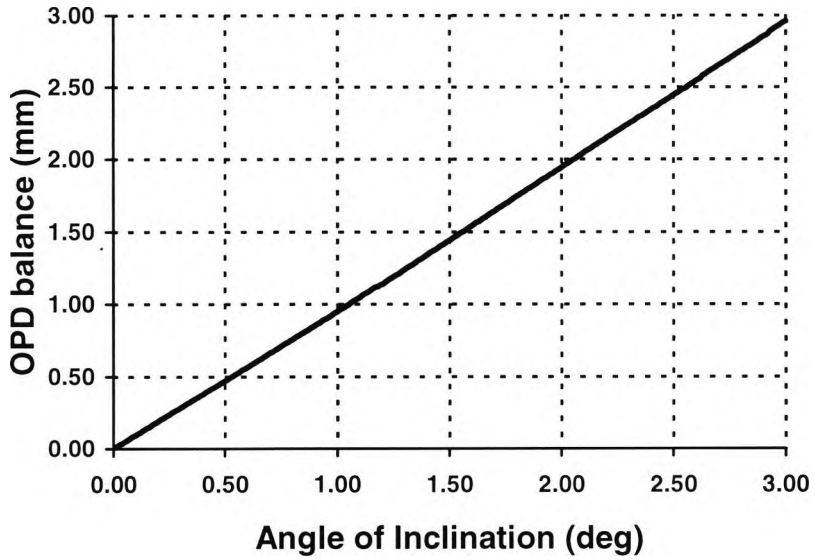

Figure 3.13: Simulated plot of the OPD balance versus the angle of inclination, α.

3.3.5. Simulation Results

Figure 3.14 shows the simulated effects on the visibility profile obtained of changing the separation of the mirrors (d - d'), from the zero OPD position (fig. 3.14(b)); to a value of -30.0μm (fig. 3.14(a)); and then back through to a value of +30.0μm (fig. 3.14(c)), at an inclination angle, α, of 0.11°. As expected, the MZI yields the desired

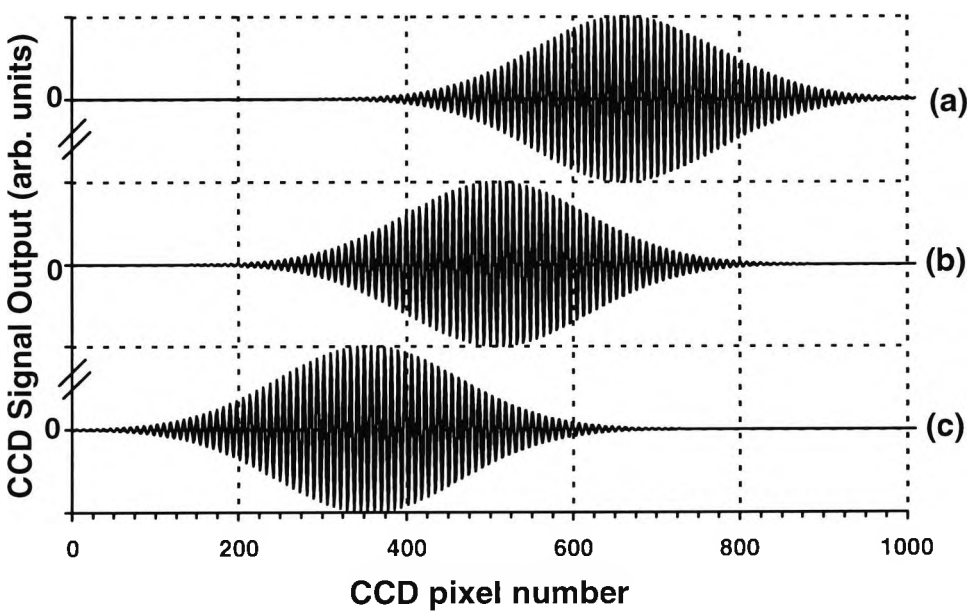

Figure 3.14: Simulated plots showing the effects of changing the OPD in the MZI, at an inclination angle, α, of 0.11°, at relative displacements of (a) -30.0μm; (b) 0.0μm and (c) +30.0μm.

response of providing a scan in position of the central fringe as the relative separation between the two mirrors (i.e. d-d') is altered.

3.4. Methodology of the Experiment

An initial experiment was set up, as illustrated in Figure 3.15. Here, it is shown that a HeNe laser was initially used to aid the alignment of the system. Once the system was aligned correctly, the HeNe and beamsplitter, CBS, were dispensed with. One of the simplest applications of lasers such as the HeNe laser is in producing a visible line which can be used for positioning or for alignment purposes. This method of alignment can be achieved using a conventional 1-5mW HeNe laser, since the beam is visible in an ambient background. In addition, the use of a HeNe laser is especially advantageous in the alignment of white-light interferometric sensors, since the use of low-coherence length sources in white-light systems does not provide interference fringes when the interferometer is unbalanced, which is the operational condition in WLI. Thus, the use

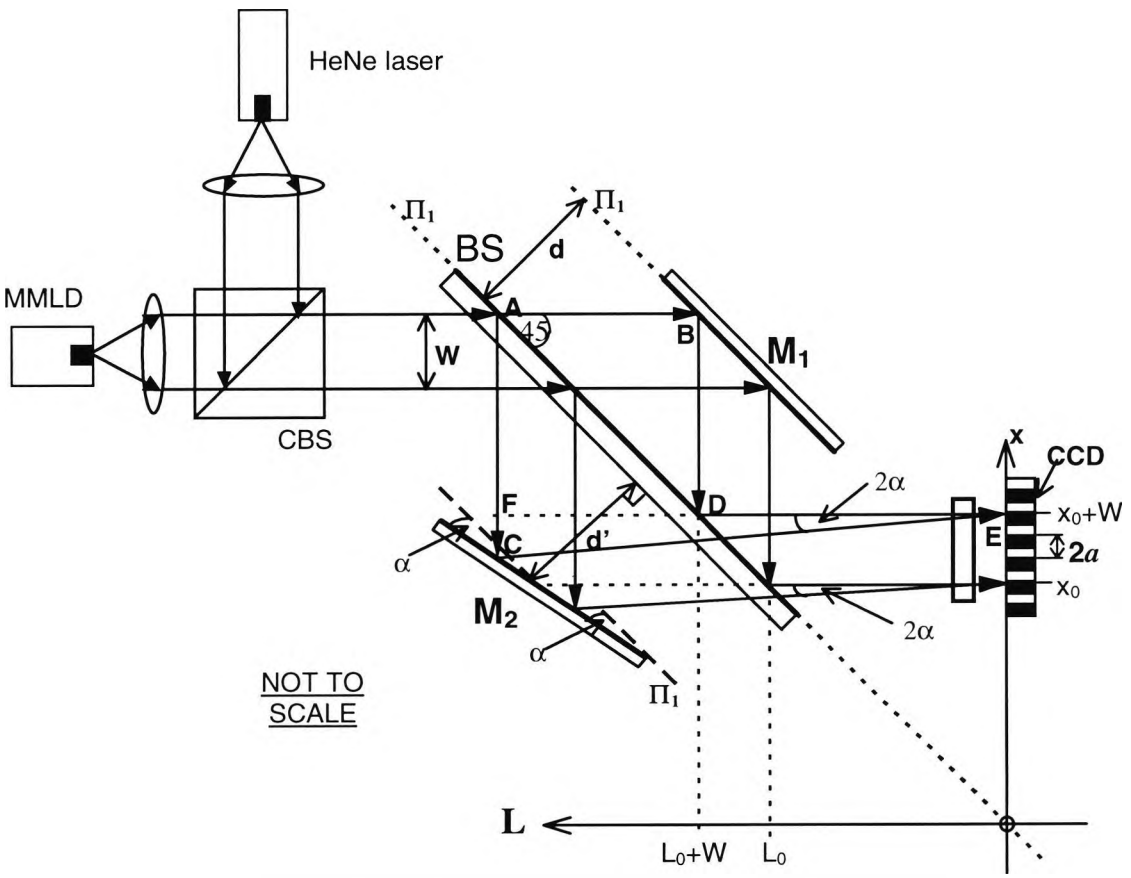

Figure 3.15: Schematic representation of the modified Mach-Zehnder configuration used in this work. MMLD - multimode laser diode; CBS - cubic beamsplitter. M_1, M_2 are mirrors, BS is a beamsplitter, $2a$ is the pixel to pixel spacing, W is the beam width, α is the inclination angle, Π_1 are parallel planes and CCD is a linear CCD detector array.

of long coherence length HeNe sources is very advantageous here in setting up the experimental conditions.

From Figure 3.15, a Sony multimode laser diode (SLD103U) was used as the low coherence source in the system yielding a coherence length of ~ 25μm and a mean wavelength of 780nm. This laser diode was driven below its threshold current in order to produce a very multimode characteristic output and an output power of 1mW. A x5 objective lens was used to collimate and expand the beam to a width, W. The beamsplitter shown, BS, had a reflectance of 0.5, and a Fairchild linear CCD line scan camera (CCD143A) was used, having a maximum of 2048 pixels. However due to the size of the optical components used, the beam was only expanded across approximately one half the CCD width, yielding an effective use of about one thousand pixels of the whole array. The CCD is a high-speed linear model which is capable of being operated upto a scanning frequency of 20MHz which has a low dark signal characteristic. The CCD had a pixel width of 13μm and a pixel spacing of 13μm, and was set to a pixel scanning frequency of 2.0 MHz. This pixel scanning frequency yields a corresponding interferogram frame rate of 1000 frames per second. Also, at this pixel scanning frequency, the minimum incident optical power required to excite the CCD pixels was ~10μW. However, this is at the dark signal noise limit and as such an optical power of ~50μW is required to produce good visibility fringes. The use of the laser diode source at a power output of 1mW, yields an incident optical power of ~450μW, which greatly exceeds the minimum power requirement.

The cylindrical lens was used to focus the incident optical output power onto the detector array. A Thurlby DSA524 digital storage adapter (DSA) was used as a "frame-grabber" in order to store a "frame" of the CCD interferogram. The DSA has an inbuilt 8 bit analogue/digital converter which allows for bi-directional data transfer to/from a computer. A "486" PC was used for this purpose in order to control the DSA and thus read-in and process the interferogram data obtained. The PC was programmed to perform on-line beam profile elimination using a pixel-by-pixel division technique.

3.4.1. System calibration

An initial measurement of the MZI inclination angle, α, was made to confirm the accuracy of the simulation. Here, α was obtained by using the HeNe laser to obtain 'visible' fringes on the CCD plane. Since the MZI has two outputs, the secondary output were observed on a screen, as shown in Figure 3.16.

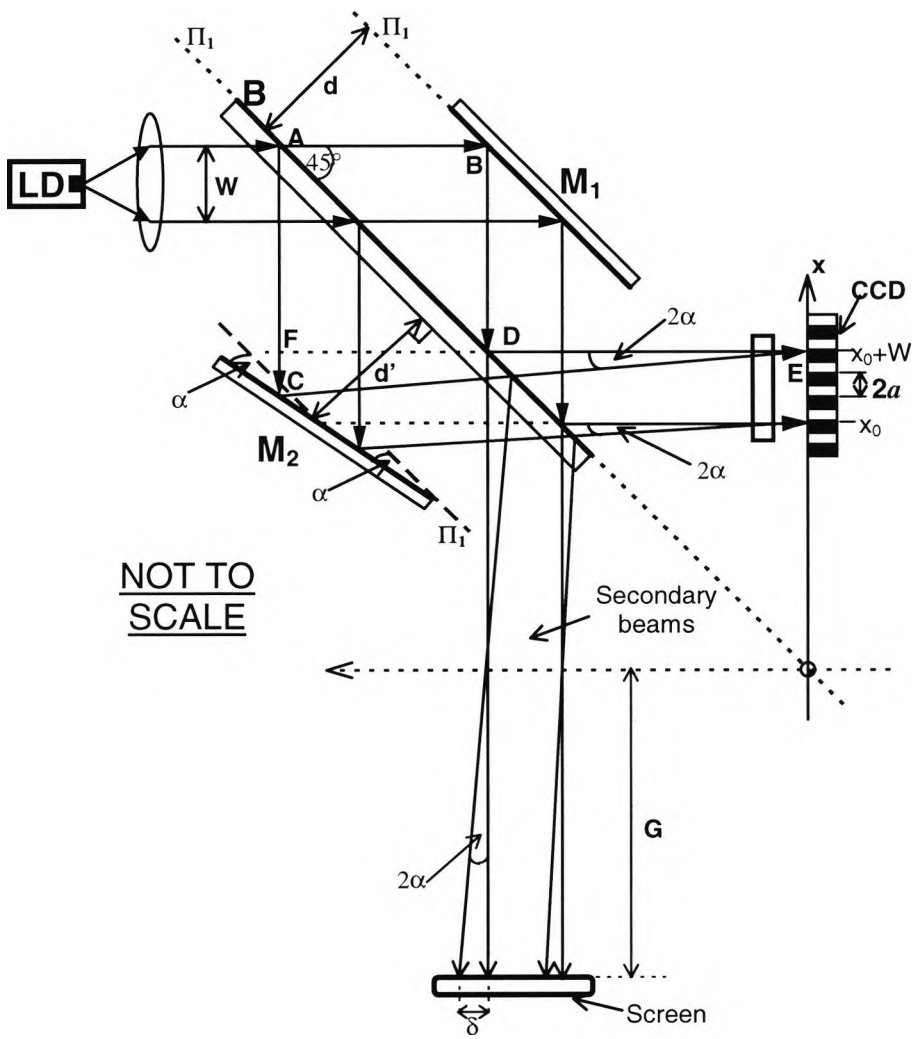

Figure 3.16: Schematic representation of the MZI configuration employed for inclination angle estimation, α. (Notation as Fig. 3.15)

The length, G, and the separation of the beams, δ, may be measured to yield an approximation of the inclination angle, α, which can be cross-referenced against the

theoretical value given by equation (3-29). Thus, the inclination angle, α, could be approximated by

$$\alpha \approx \tfrac{1}{2}\tan^{-1}\left(\frac{\delta}{G}\right) \tag{3-30}$$

The number of pixels per fringe was found by observing an expanded region of the CCD output, as shown in Figure 3.17.

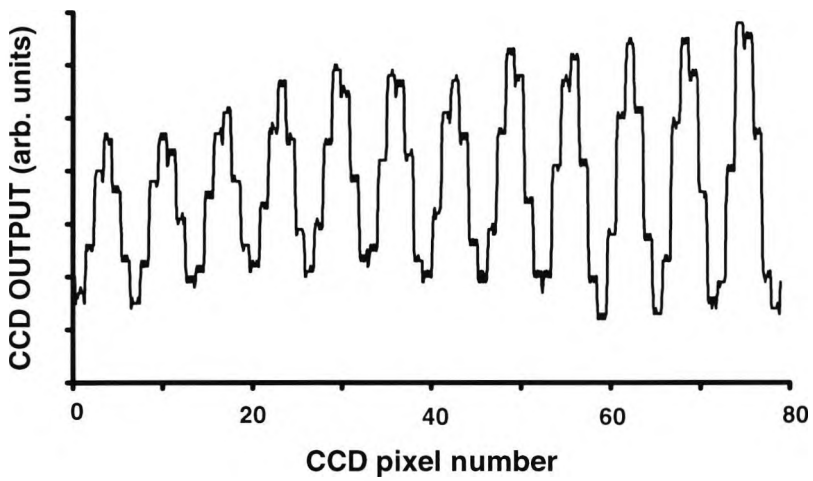

Figure 3.17: Shows expanded view of CCD output across a few fringes

A major cause of poor visibility in the MZI is the degree of flatness of the mirrors. When observed using the red HeNe, it was found that (even when the light was as well collimated as reasonably could be achieved), the observed fringe pattern was not precisely parallel. Instead, the typical fringe patterns observed on the screen are shown in Figure 3.18.

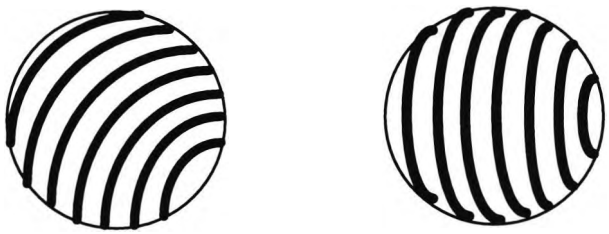

Figure 3.18: Typical fringe patterns observed on the screen from the MZI due to optical "un-flatness" of the mirrors

These "distorted" fringe patterns were observed, and thus when the cylindrical lens was used to focus this information into 1-plane across the CCD, the information was degraded - since the cylindrical lens produces an average of the fringes in the y-direction, as shown schematically in Figure 3.19. Here, the CCD pixel, P, should occur on a "dark fringe" - i.e. at a zero intensity point. However since the fringes are curved, the pixel, P, will also receive some of the "light" fringe signal, such that the pixel will average all the incident light to produce an incorrect non-zero result, as shown in Figure 3.19(b), which degrades the fringe visibility. By contrast, if the fringes are parallel, as shown in Figure 3.19(c), the average signal at pixel, P, will be correctly zero. One method of achieving these good parallel fringes is to use flatter mirrors. Initially, mirrors of flatness $\lambda/2$ were employed which yielded the curved fringes as shown in Figure 3.18. This was improved by using flatter mirrors ($\lambda/10$ flatness) to obtain parallel fringes.

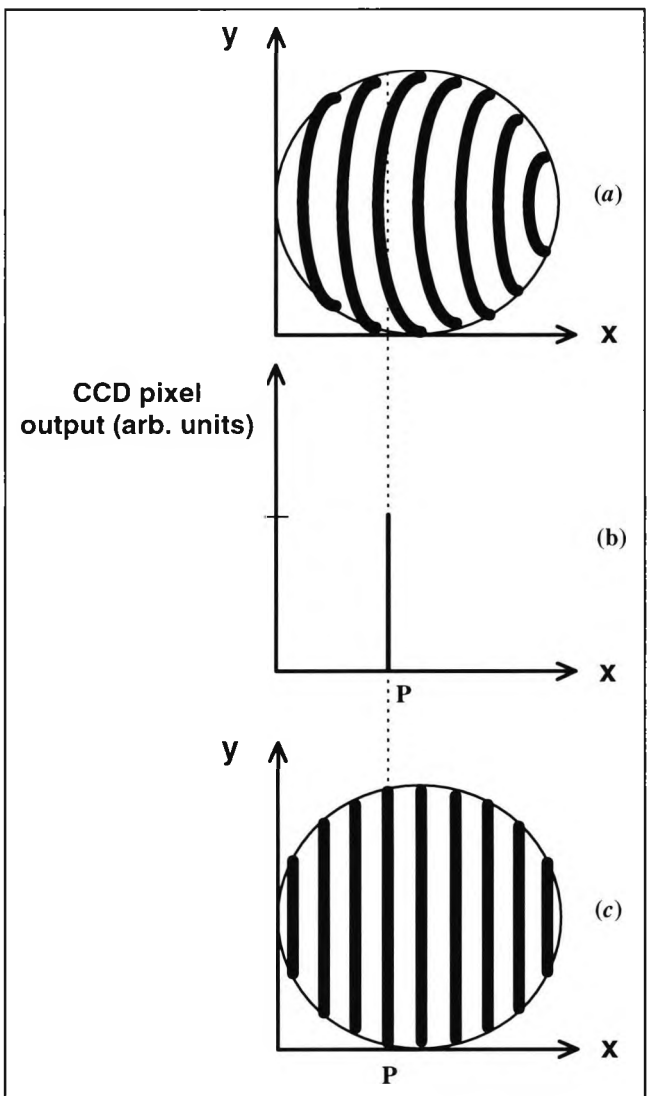

Figure 3.19: Schematic representation of the "distorted" fringe output from the MZI. The output from an arbitrary pixel, P, is shown in (a), highlighting the effects of visibility degradation due to "un-flatness" effects. (b) shows the resultant output power from an arbitrary CCD pixel, P, with the distorted fringes. (c) shows the ideal, parallel fringe pattern from very flat mirrors.

The MZI mirrors were adjusted using flexure mounts to provide rotational positioning about the x, y and z axes in order to align them parallel with respect to one another and perpendicular to the optical bench. In addition, micrometer stages were employed to provide the translational positioning of these mirrors.

The CCD was mounted on a translational stage to provide translation in the x, y and z planes. The CCD also had slight rotational movement in the x-plane, which is a very important movement to give the ideal CCD position for the best visibility. The position of the CCD is critical when aligning the system, as if the CCD is placed too far away from the MZI, then a slight change in the inclination angle, α, or in the mirror position, d, will yield beams which do not overlap correctly. This is highlighted schematically in Figure 3.20.

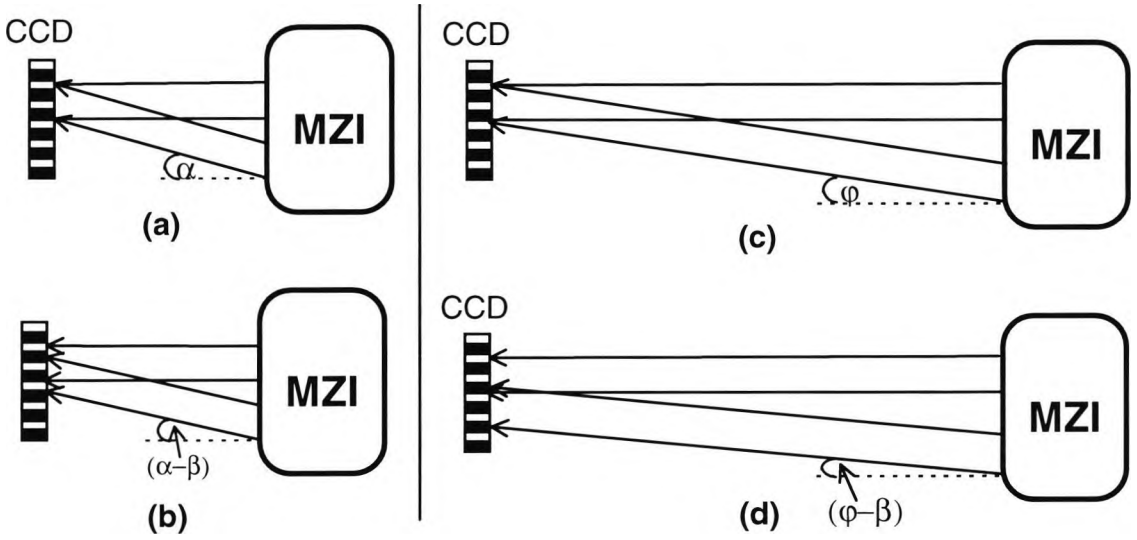

Figure 3.20: Schematic showing the effects of the position of the CCD wrt the MZI. Figs (a) and (b) shows when the CCD is close to the MZI. Figures (c) and (d) shows when the CCD is further away from the MZI. Figures (b) and (d) also show when the MZI is altered by a tilt of β

Here, in Figs. 3.20 (a),(b), the CCD is close to the MZI, such that when the MZI is altered from α to $(\alpha-\beta)$ the beams are still shown to overlap (although not completely). However, when the CCD is further away from the MZI, and the MZI mirror is changed from a tilt of φ to $(\varphi-\beta)$, the effect of the beams mis-overlapping is considerable, as shown in Figs. 3.20 (c), (d). Thus, when aligning the system, it was more desirable to have the CCD as close to the MZI as possible, which also had the added benefit of reducing the size of the system.

3.5. Experimental results

The system was set up as shown in Figure 3.7. Initially, the CCD output was observed using an oscilloscope (CRO). From the theory and subsequent simulation results, the fringe width decreases with an increase in the inclination angle, α. The MZI was set-up with initial values of d~10.5mm and d'~9.5mm. Figure 3.21 shows the effects of changing the inclination angle, α. Here, the photographs are taken from the CRO. Fig. 3.21(a) shows the CCD interferogram for 57 pixels per fringe (ppf) which corresponds to $\alpha \approx 0.015°$. Fig. 3.21(b) shows the interferogram for 23 ppf, which yields $\alpha \approx 0.037°$. Fig. 3.21(c) shows the interferogram for 50 ppf, which yields $\alpha \approx 0.017°$. Fig. 3.21(d) shows the interferogram for 6 ppf, which yields $\alpha \approx 0.143°$.

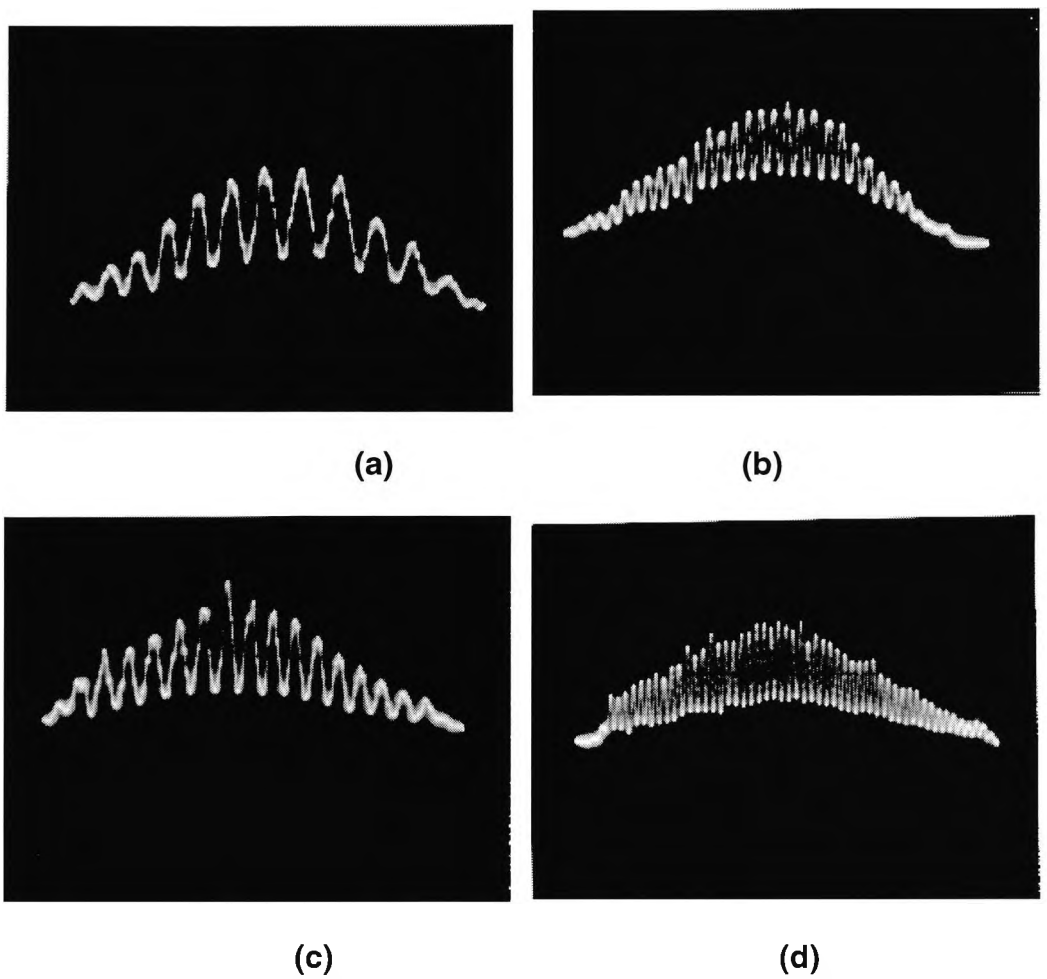

Figure 3.21: Shows the effects of changing the inclination angle, α. Here, the photographs are taken from the CRO. Fig. (a) shows the CCD interferogram for 57 pixels per fringe (ppf) which corresponds to $\alpha \approx 0.015°$. Fig. (b) shows the interferogram for 23 ppf, which yields $\alpha \approx 0.037°$. Fig. (c) shows the interferogram for 50 ppf, which yields $\alpha \approx 0.017°$. Fig. (d) shows the interferogram for 6 ppf, which yields $\alpha \approx 0.143°$.

Figure 3.21 reveals that as the inclination angle is increased, the number of pixels per fringe is reduced, which subsequently represents a reduction in the fringe width. In addition, an increase in α produced a reduction in the fringe visibility, which qualitatively confirms the theoretical simulation results.

3.5.1. CCD interferogram data capture

In order to process the CCD interferogram fringe data some means of capturing the analogue interferogram signal had to be devised. A Thurlby DSA524 digital storage adaptor (DSA) was employed to capture each frame from the CCD array, using the DSA as a "frame-grabber" in order to store a "frame" of the CCD interferogram. A computer program was written in Turbo Pascal in order to perform on-line beam profile elimination using a pixel-by-pixel division technique. Thus, the complete data capture and processing configuration used is shown in Figure 3.22.

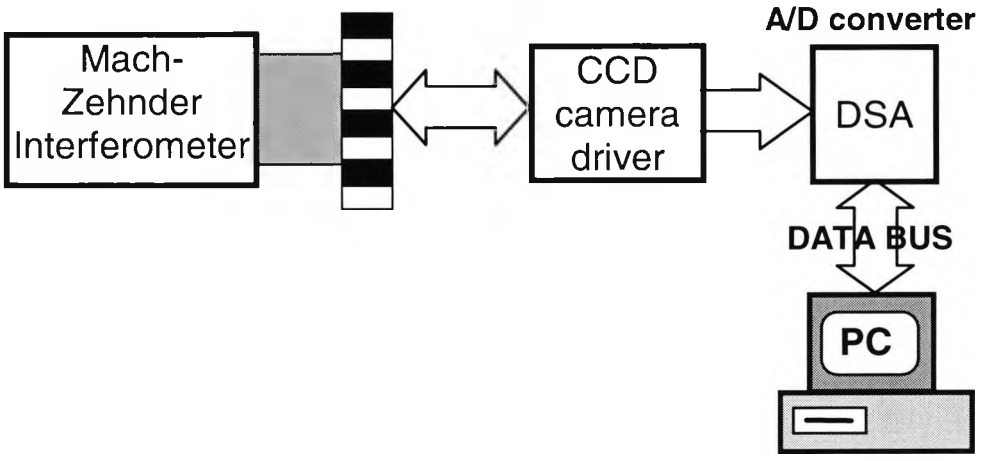

Figure 3.22: Complete experimental arrangement. DSA is the digital storage adapter

3.5.2. Signal processing scheme

In an electronically-scanned WLI system, the interferometric fringe pattern obtained was distorted by the beam intensity profile of the expanded light-beam (see Appendix A). Hence under these circumstances, equation (3-22) can be expressed in the form of:

$$I(x) = P(x)\left[A + 2B\cos\left(k\Delta L(x)\right)\exp\left(-\left(\frac{\Delta L(x)}{L_c}\right)^2\right)\right] \qquad (3\text{-}31)$$

where $P(x)$ is the beam intensity profile, and the other terms are as were given before. After A/D conversion, $I(x)$ and $P(x)$ could be represented as two data sets $I[j]$ and $P[j]$, which were stored in the computer, where j $(=1,2,..,M)$ is the pixel number along the CCD array, and M is the total number of pixels, as before.

From equation (3-31), the corresponding fringe pattern, $F[j]$, can then be restored using pixel-by-pixel division and thus:

$$F[j] = \frac{I[j]}{P[j]} \qquad (3\text{-}32)$$

The effect of the beam intensity profile was successfully eliminated from the fringe data using the pixel-by-pixel division techniques, and the results of this are shown in Figure. 3.23, where Fig. 3.23(a) shows the pre-processed fringe data obtained using ≈8 pixels per fringe (i.e. with $\alpha \approx 0.11°$). Fig. 3.23(b) shows the background beam intensity profile which was obtained by moving mirror M2 out of the coherence region of operation, and further, Fig. 3.23(c) shows the results of pixel-by-pixel division, yielding the final processed fringes. Alternatively, the beam profile intensity could have been recorded by simply blocking off the path of each mirror in turn to yield the beam profile from each mirror, M_1 and M_2, denoted by $P_1(x)$ and $P_2(x)$ respectively, from which, the combined beam profile, P(x), can be obtained and is given by $(P_1(x) + P_2(x))$. However, for practical applications, it is more advantageous to use the method of scanning the mirror "out of coherence."

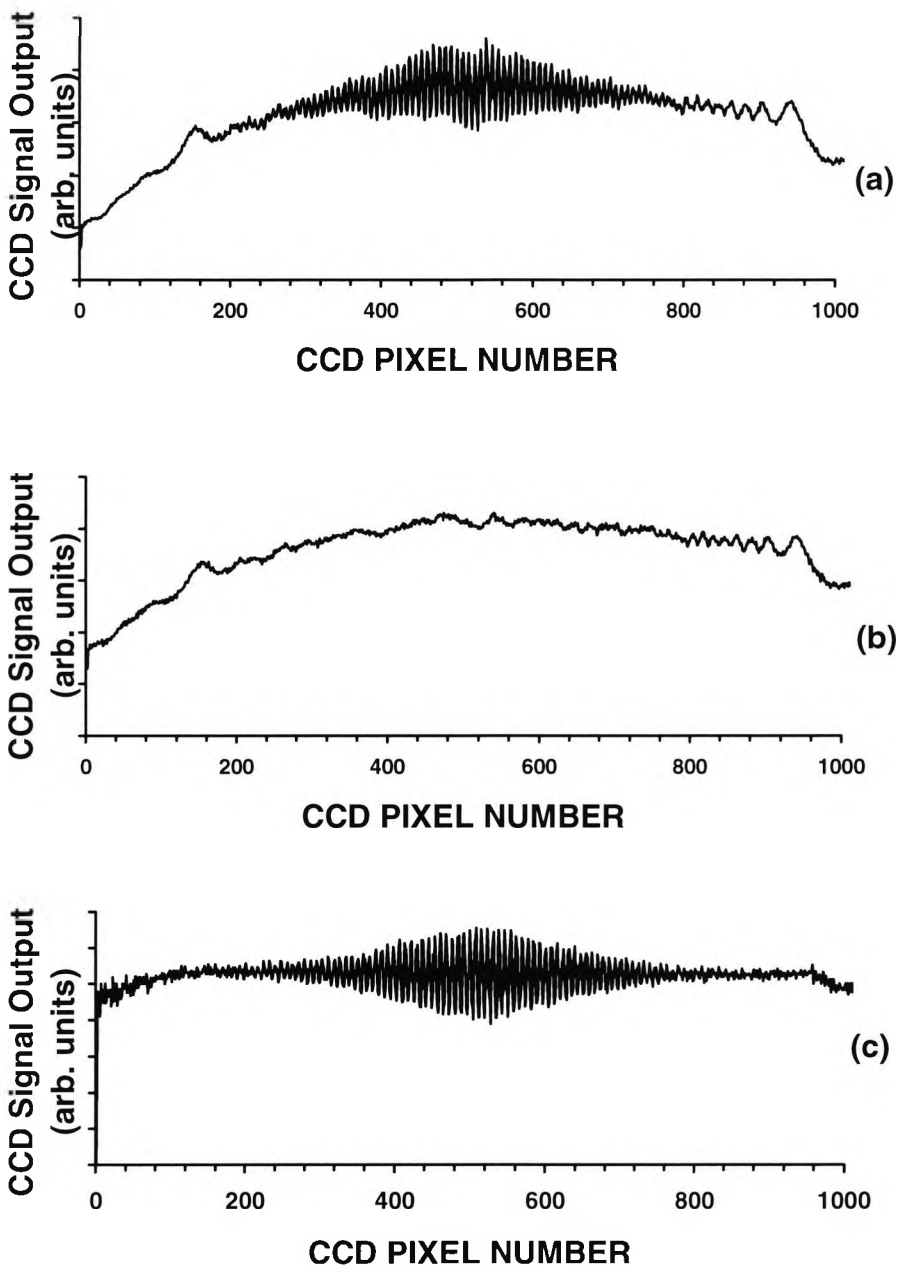

Figure 3.23: Experimental results of the CCD output (arbitrary units) versus the CCD pixel number, highlighting the beam profile intensity elimination using a pixel-by-pixel division technique for an interferogram obtained using ≈8 pixels per fringe, at an inclination angle, α, of ≈0.11°. Fig. (a) shows the pre-processed fringe data. Fig. (b) shows the pre-recorded background beam intensity profile. Fig. (c) shows the results of the pixel-by-pixel division.

3.5.3. Data capture and processing

A computer program created to read in and process the CCD data from the DSA was written in Turbo PASCAL. The program could directly control all of the major functions of the DSA in order to provide bi-directional data flow. The DSA was connected to the PC COMS port via the RS232 connection. The DSA baud rate could be changed from a range of 300 to 38,400. The computer program was relatively extensive (~800 lines of code), and thus its operation is summarized using a simplified flowchart, as shown in Figure 3.24. The computer program listing is shown in Appendix C.

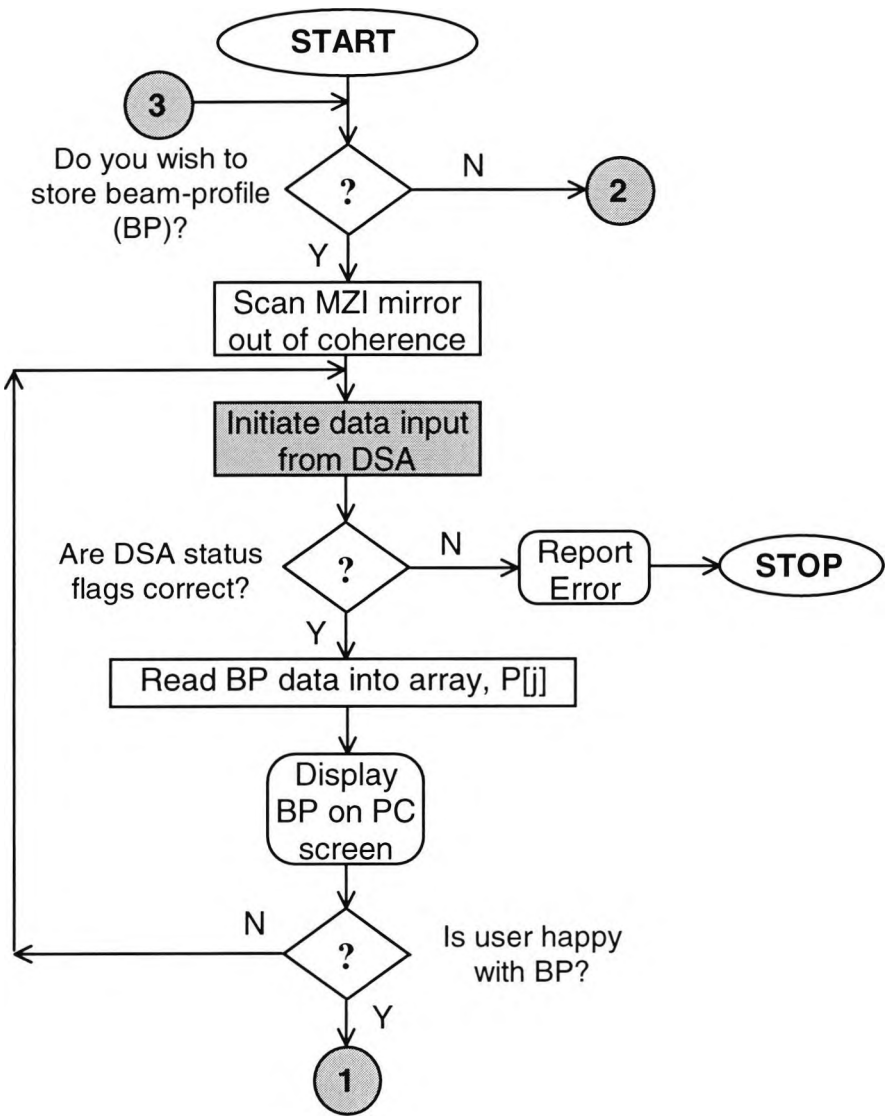

Figure 3.24(a): First section of flowchart of computer program for data capture and processing

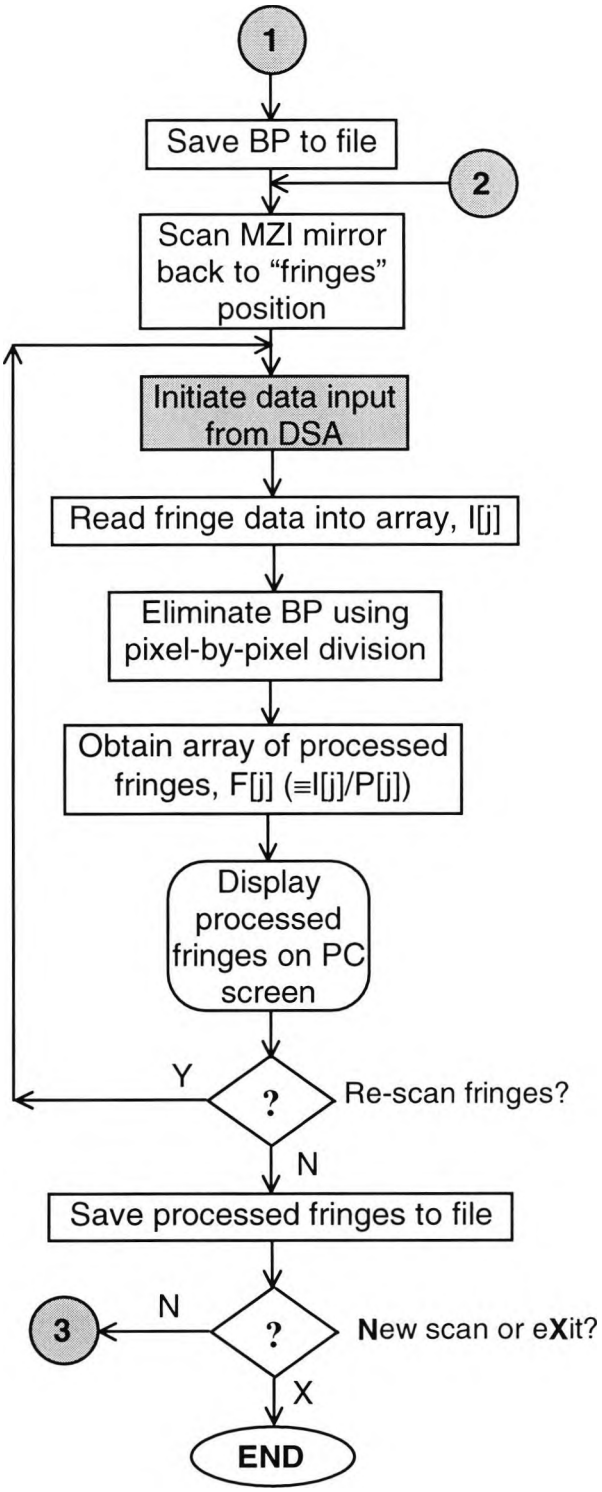

Figure 3.24(b): Final section of flowchart of computer program for data capture and processing

3.5.4. Fringe visibility

The system was set up as shown in Figs. 3.7 and 3.22 in order to measure the effects of the fringe visibility as a function of the inclination angle, α. Here, the fringe visibility (Figure 3.25) is shown to reduce with increasing inclination angle, α, which is what is to be expected from the results of the simulation.

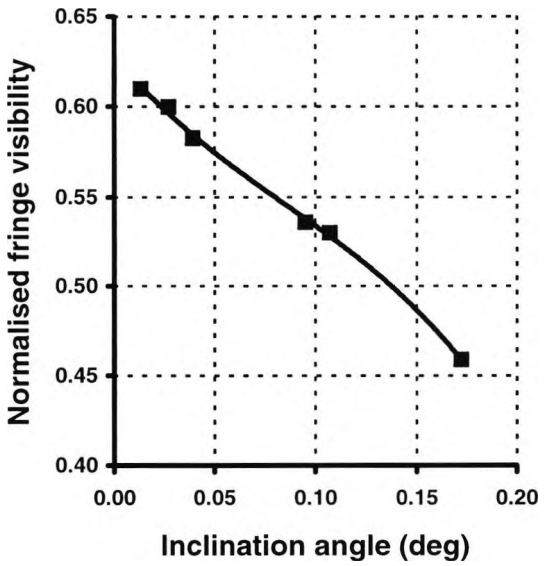

Figure 3.25: Experimental results of the fringe visibility as a function of the inclination angle, α

However, the fringe visibility is shown to be less than the "ideal" simulation values, which approach 100% for very small inclination angles (i.e. $\alpha \rightarrow 0$). This is expected since the simulated visibility function is ideally set for optimised conditions. However in practice, the background beam profile intensity, the reflectance of the mirrors, the quality of the optical components and the CCD dark signal and noise all degrade the fringe visibility.

The MZI used can be set to a variety of different values of OPDs by simply changing the relative angle, α, and the position of one of the mirrors. This versatility allows the scanning range of the recovery interferometer to be altered. An increase in α produces an inversely proportional reduction in the width of the fringes. Hence, the *number of pixels per fringe, p_f,* may be used as a performance index of the angle of inclination, α.

When used as a recovery interferometer, the MZI can be set to produce various OPDs by simply changing the relative displacement (d - d') of the mirrors. This aspect is illustrated in Figure 3.26 which shows the effect of the movement of mirror M2 from the zero OPD position (Fig. 3.26(b)), then to a value of -30.0μm (Fig. 3.26(a)), and finally back through to a value of +30.0μm position (Fig. 3.26(c)). The fringes are shown to be of fairly good quality, however the elimination of the background beam profile was not perfect. This slight interferogram distortion is expected since the recovery interferometer is scanned in isolation. Thus, as it is scanned, it moves slightly out of alignment, even over a relatively short distance. This is not a problem, however, since in an ESWLI, the RI will be fixed, and only the SI will be scanned. At an inclination angle, α, of ~0.11°, the operating range was found to be ~100±5μm which is in good agreement with the theoretical value of 96μm.

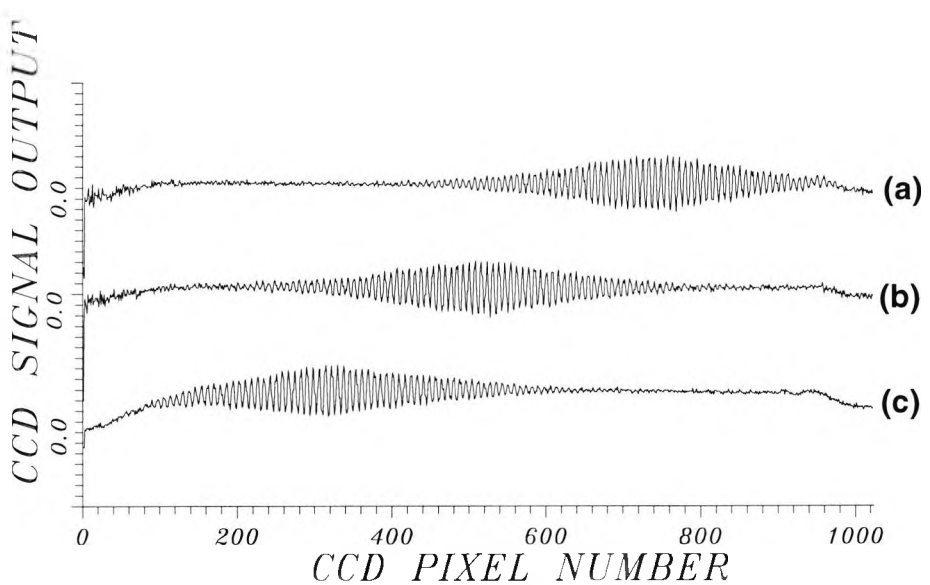

Figure 3.26: Experimental results of the CCD output (arbitrary units) versus the CCD pixel number at an inclination angle, α, ≈0.11°, highlighting the effects of scanning mirror M2 whilst mirror M1 is fixed. M2 is moved from the zero position OPD position (fig.3.26(b)), then to an OPD= -30.0μm (fig. 3.26(a)), and finally back through to the OPD +30.0μm position (fig. 3.26(c)).

3.6. Summary

A novel electronically-scanned white-light Mach-Zehnder interferometric configuration has been introduced [12]. The work shows that the configuration provides absolute "single-pulse" measurements with no moving parts, thus yielding a high scanning speed. This configuration is compact, has a high stability and does not introduce any spatial "mis-overlapping" of the beams, yet operates whilst using only one beamsplitter (instead of the usual two used in a conventional MZI). The MZI also has the advantage of having two complimentary outputs, such that one can be used to calibrate the system without disturbing the detected output to be measured.

The configuration was also shown to be able to be set to a wide range of OPD values by changing the angle and position of one of the mirrors. This gives the interferometer the advantage of being easily adapted for different measurement applications.

A major application of this approach is the implementation of this Mach-Zehnder interferometer (MZI) in a dual wavelength optical-fibre electronically-scanned white-light-interferometric system, by employing a Fabry-Perot interferometer as the sensing interferometer and the MZI as the recovery interferometer. The use of the dual wavelength approach provides a more accurate central fringe identification regime by increasing the relative amplitude between the central fringe and the adjacent fringes. Further developments on this work are reported in the next chapter.

3.7. References

1. Meggitt, B. T.: "Fiber optic white-light interferometric sensors", Ch. 9, pp. 269-312, In: "Optical Fiber Sensor Technology", Eds. Grattan, K. T. V. and Meggitt, B. T., Chapman & Hall, London, 1995.

2. Chen, S., Meggitt, B. T., Rogers, A. J. "A novel electronic scanner for coherence-multiplexing a quasi-distributed pressure sensor", Electron. Lett., vol. 26, no.17, pp. 1367-1369, 1990.
3. Marshall, R. H., Ning Y. N., Jiang, X. Q., Palmer, A. W., Meggitt, B. T. and Grattan K. T. V.: "A novel electronically-scanned white-light interferometer using a Mach-Zehnder approach", IEEE J. Lightwave Technol., vol. 14, No. 3, pp. 397-402, 1996.
4. Jackson, D. A., and Jones, J. D. C. "Fibre Optic Sensors", Opt. Acta, vol. 33, pp. 1469-1503, 1986.
5. Al-Chalabi, S. A., Culshaw, B. and Davies, D. E. N. "Partially coherent sources in interferometry", IEE (No. 221) Proc. 1st International Conf. on Optical Fibre Sensors, London, pp. 132-5, 1983.
6. Francon, M: "Optical interferometry", Ch. 4, pp. 87-100, Academic Press, London, 1966.
7. Chen, S., Meggitt, B. T., and Rogers, A. J.: "Electronically-scanned white light interferometry with enhanced dynamic range", Electron. Lett., vol. 26, No.20, pp. 1663-1665, 1990.
8. Bock, W. J., Urbanczyk, W., and Zaremba, M. B.: "Electronically scanned white-light interferometric strain sensor employing highly birefringent fibers", Optics Comms., vol. 101, pp. 157-162, 1993.
9. Chen, S., Meggitt, B. T. and Rogers, A. J.: "An electronically scanned white-light Young's interferometer", Optics Lett., vol. 16, pp. 761-3, 1991.
10. Chen, S., Palmer, A. W., Grattan, K. T. V., Meggitt, B. T., and Martin, S.: "Study of electronically-scanned optical-fibre white-light Fizeau interferometer", Electron. Lett., vol. 27, No. 12, 1032-1034, 1991.
11. Rogers, A. J.: "Essential optics", Ch. 3, pp. 58-59, In: "Optical Fiber Sensors: Principles and components", Eds. Dakin, J. and Culshaw, B., Artech House, Boston, 1988.
12. Marshall, R. H., Ning Y. N., Jiang, X. Q., Palmer, A. W., Meggitt, B. T. and Grattan K. T. V.: "A novel white-light interferometer using an electronically-scanned Mach-Zehnder interferometer", Proc. SPIE 2594, manuscript number 17, In: "Self-calibrated intelligent optical sensors and systems", Philadelphia, USA, Ed. Wang, A., pp. 159-167, October 1995.

Chapter 4

Electronically Scanned White-Light Interferometer design

4.0. Introduction

In this chapter, the Mach-Zehnder interferometer (MZI) configuration is employed as a recovery interferometer in an Electronically-scanned white-light interferometer (ESWLI) sensing system. Here, a modified Fabry-Perot interferometer (FPI) was employed as the sensing interferometer due to its compact nature and simplicity of operation. The key effects of the operation of this modified FPI are presented in this chapter, along with an analysis of the effects of modal noise in the interconnecting fibre coupler. This 'modified FPI' employs a short coherence length source, thus the common effects of multiple reflections in a conventional FPI does not exist here [1]. Some authors have called this a Fizeau interferometer [2], but in this thesis, it shall be denoted as a 'Modified Fabry-Perot Interferometer'.

Various methods of enhancing the identification of the central fringe were introduced. Here, the benefits in the use of dual wavelengths as a combined synthetic source was discussed. This technique was contrasted with the use of the centroid method and the least squares technique in order to enhance the accuracy of the central fringe identification.

An investigation of the effects of optical dispersion in the dual wavelength configuration was also undertaken. Here, a thorough experimental analysis of these effects enabled quantitative data to be obtained for a range of situations, providing a specification for the use of dual wavelength white-light interferometric sensors.

In an Electronically-scanned white-light interferometer (ESWLI), the sensing interferometer (SI) is initially unbalanced with an optical path difference, δ_S, which is further tuned by the measurand (which has an OPD of δ_m). The SI imbalance, δ_S, is made greater than the coherence length of the source, L_c, such that under normal operating conditions, no interference effects are observed at its output. Thus, the light waves returned from the SI cavity are incoherent. The main function of the secondary recovery interferometer (RI) is to re-establish interference effects by bringing the beams back into mutual coherence. This is achieved by setting the RI to a preset unbalanced position, δ_R, which cancels out the preset OPD in the SI, δ_S. Thus, the SI and RI are both unbalanced, however when operating in combination, their combined OPD, δ_T, is within the coherence length of the source and is given by

$$\delta_T = (\delta_S + \delta_m) - \delta_R$$

$$\begin{aligned} &where \quad \delta_T < L_c \\ &\qquad (\delta_S + \delta_m) > L_c \\ &\qquad \delta_R = \delta_S \ (> L_c) \end{aligned} \tag{4-1}$$

which leaves the desired effect of the resultant OPD in the WLI being equivalent solely to the influence of the measurand, δ_m.

Figure 4.1 shows the effects which would be obtained if the recovery interferometer were scanned. Here, it is shown that the OPD, δ_R, can be made both positive and negative relative to its balance position. Consequently, two positions exist at which the path imbalance matches that of the sensing interferometer, δ_S. There also exists a central fringes region that arises when the recovery interferometer passes through its balanced region. However only the two side fringe regions, at $\delta_R = \pm\delta_S$,

contain phase information on the sensing interferometer. The larger central fringe at $\delta_R=0$ contains no useful information on the SI, and thus the RI is operated at either of the two positions, $\pm\delta_S$.

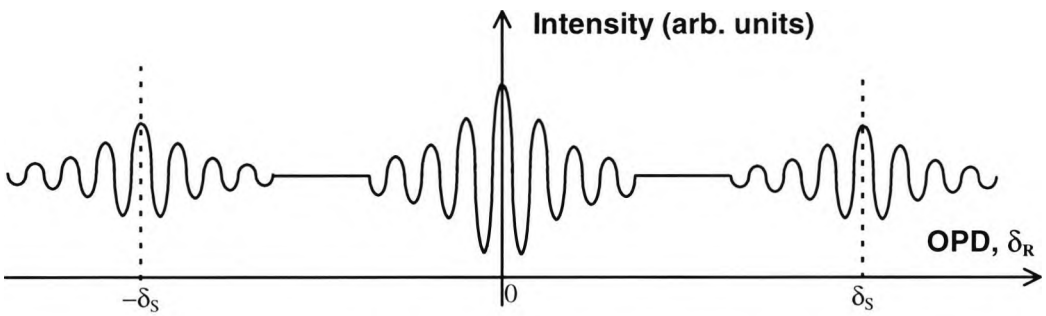

Figure 4.1: White light interferogram showing two signal sidebands at δ_S and $-\delta_S$

4.1. Sensing Interferometer design: The Modified Fabry-Perot Interferometer

A conventional Fabry-Perot interferometer (FPI) consists of two highly reflective mirrors maintained parallel to each other, to a high degree of precision [1]. The FPI is one of the most simple and compact interferometers due to its use of only two mirrors, as shown in Figure 4.2. Here, the incident ray, E, is shown to be partially reflected into many transmitted (E_{t0}, E_{t1}, E_{t2},..,) and reflected rays (E_{r0}, E_{r1}, E_{r2},..,), thus the conventional FPI is a multiple-beam interferometer.

However, in this work a modified Fabry-Perot interferometer is employed, which uses a short coherence length source. The use of a short coherence length source means that the common effects of multiple reflections in a conventional FPI does not exist here [1], since the OPD between the principal and successive reflections will exceed the coherence length of the source [1]. Some authors have called this a Fizeau interferometer [2], but in this thesis, it shall be denoted as a 'Modified Fabry-Perot Interferometer'. This deduction can be made since using the combination of partially reflective mirrors and a short coherence length source, the amplitudes of the reflected vectors quickly becomes negligible. Thus, this FPI can be evaluated in much the same

way as other two-beam interferometers (such as the Michelson), when employed as a SI in a WLI.

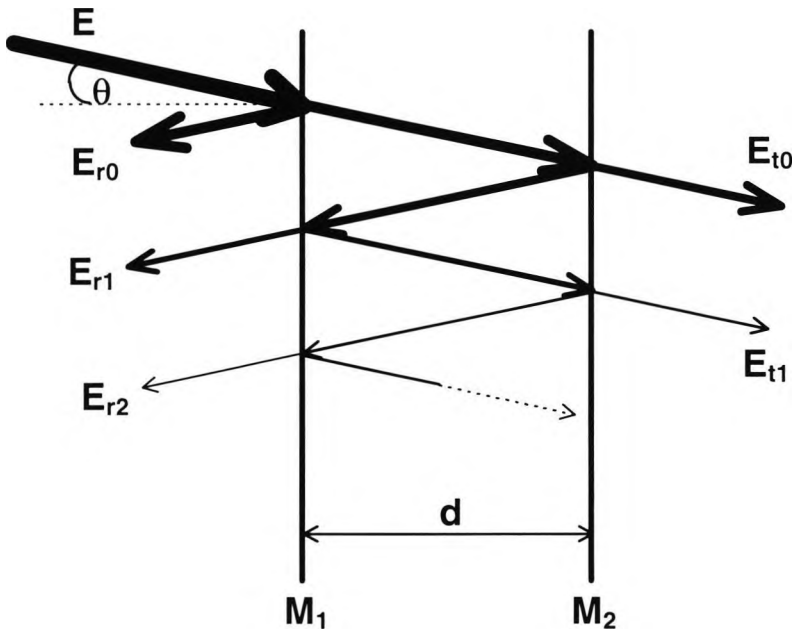

Figure 4.2: Conventional Fabry-Perot Interferometer. M_1 and M_2 are partially reflective mirrors

In an WLI, the FPI is employed as a sensing interferometer operating in the reflective mode. This configuration is employed since it is more advantageous to use the same optical fibre to act as an input to and an output from the FPI, as shown in Figure 4.3. From Figure 4.3, the OPD, δ_S, in the FPI between adjacent reflected beams is given by, $2d$, where d is the separation of the FPI mirrors.

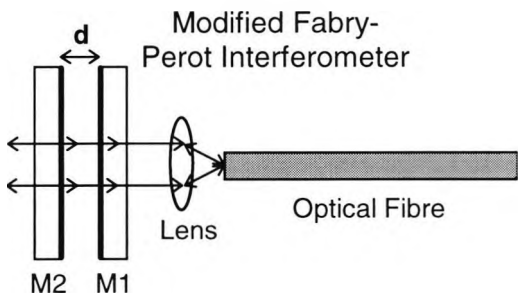

Figure 4.3: Modified FPI configured in the reflective mode as a sensing interferometer. M1 and M2 are partially reflective mirrors

The selection of the reflectance of the FPI mirrors has a direct relationship to the resultant fringe visibility. Plate beamsplitters and mirrors which are currently commercially available, generally have a fixed range of reflectance values [4], which are typically (0.3, 0.5, 0.7, and 1.0). From Figure 4.4, it is shown that by using a mirror, M1, having a reflectance, R1=0.3, yields a slightly higher fringe visibility than a reflectance of 0.5 and a significantly higher visibility than a reflectance of 0.7.

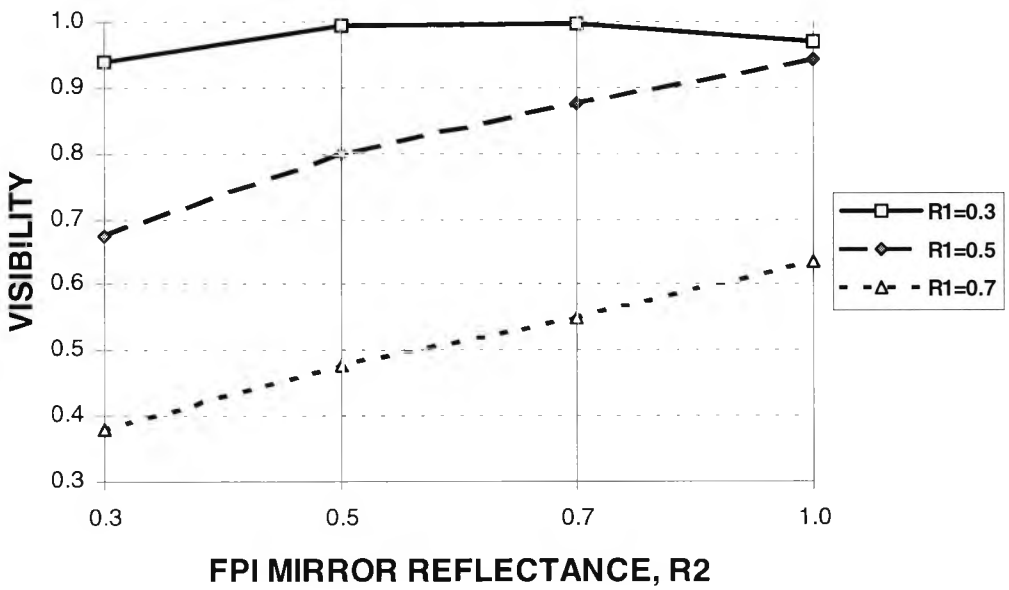

Figure 4.4: Fabry-Perot Interferometer (FPI) fringe visibility as a function of mirror reflectance, R2, for a range of commercial available mirrors reflectances (0.3, 0.5, 0.7, 1.0). Where R1, R2 are the reflectances of the first and second mirror in the FPI respectively.

However, due to the greater availability of 0.5 reflectance mirrors, a 0.5 reflectance mirror was employed in this work, which only has a slightly reduced fringe visibility. In addition, it would have been more advantageous to use a second mirror having a reflectance, R2, of 1.0. However, the physical size of the mirrors which were readily available was too large to be mounted on the PZT. Thus, a mirror M2 of reflectance, R2=0.5, was also employed, which yields a favourable fringe visibility of 0.8.

4.2. Optical bus: Effects of modal noise

In a typical WLI system, multimode fibres may be used to deliver a low coherence light beam from the light source to the sensing element, to collect the modulated light from the sensing element, and then pass it to a detector (via the recovery interferometer), as shown in Section 2.1. There are advantages in using multimode fibres as lead-in fibres, rather than single mode fibres due to the greater coupling efficiency experienced. However, modal noise [5,6] will be induced when these fibres are subjected to environmental perturbations, such as temperature changes or vibrations.

Modal noise in a multimode fibre occurs when three conditions are satisfied. These are firstly, when the high-order modes are excited in the fibre, secondly when the group delay-time induced OPD between each pair of adjacent modes at the far end of the multimode fibre is within the source coherence length, a situation which is known as "intermodal cross-coupling effect" [7]. The third condition is when the fibre-connected interferometer operates around its balanced region, such that the value of its OPD is much less than the coherence length of the source. These modal noise effects will reduce the signal-to-noise (S/N) ratio of the interferometer output [7].

The guided modes supported by a multimode fibre can be represented by a group of allowable rays which will progress down the fibre at a velocity which depends on their angles of injection [3]. Each mode corresponds to a slightly different transit time. Higher angle rays travel longer paths reflecting from side-to-side, and thus they take longer reach the end of the fiber than rays moving along the axis. The differing velocities of the guided modes will lead to varying times of arrival of the modal energy components at the far end of the fibre. The total time delay between the arrival of the axial (fundamental) ray and the slowest ray (highest order) is $\Delta t = t_{max} - t_{min}$, where

$$t_{min} = L/v = Ln_1/c \tag{4-2}$$

where L is the length of the fibre, v is the group velocity of the modes, n_1 is the refractive index of the core and t_{max} is defined below. The highest order mode route, l_h, is at a maximum when the ray is incident at the critical angle, θ_c, and thus in a step-index fibre

$$l_h = \frac{L}{\sin\theta_c} = \frac{Ln_1}{n_2} \tag{4-3}$$

where n_2 is the refractive index of the cladding. Thus the corresponding time, t_{max}, is given by

$$t_{\max} = l_h / v = \frac{Ln_1^2}{n_2 c} \tag{4-3}$$

which yields

$$\Delta t = \frac{Ln_1}{c}\left(\frac{n_1}{n_2} - 1\right) \tag{4-4}$$

which yields a corresponding maximum permissible OPD, ΔL_{max}, between the fundamental mode and the highest order mode, as given by [8]

$$\Delta L_{\max} = L\left(\frac{n_1}{n_2} - 1\right) \tag{4-5}$$

where n_1 and n_2 are the refractive indices of the core and cladding respectively, and L is the length of the fibre used. Thus, the magnitude of the OPD, $\Delta L_{i,k}$, between the *ith* and *kth* mode will increase during propagation and it lies in the range $0<\Delta L_{i,k}<\Delta L_{max}$. Thus, in order to minimise these modal noise effects, it is desirable that $\Delta L_{i,k}>L_c$.

The main factor which determines the efficiency of the modal noise suppression is that the OPDs between each pair of adjacent modes, every second mode, and every third mode inside each modal group at the far end of the fibre exceed the value of the coherence length. Since these OPDs are determined by the length and the diameter of the fibre, for a given coherence length, with a suitable combination of the

fiber parameters, the level of the modal noise induced in the fibre can be reduced. Hence, in this work, a longer length of multimode fibre was fusion spliced onto one arm of the multimode fibre coupler. This fibre used was 50/125 μm, with a 30 metre extension on the recovery interferometer arm. This system is shown in Figure 5.5. The multimode fibre coupler used was a Gould #147619 which uses Corning 50/125 type multimode fibre. Even though a short coherence length source (≈30μm) was employed in this system, the effect of the modal noise present was observed to be significant if the fibre-arm length was less than approximately 10 metres, so a 30 metre extension of 50:125μm fibre was employed.

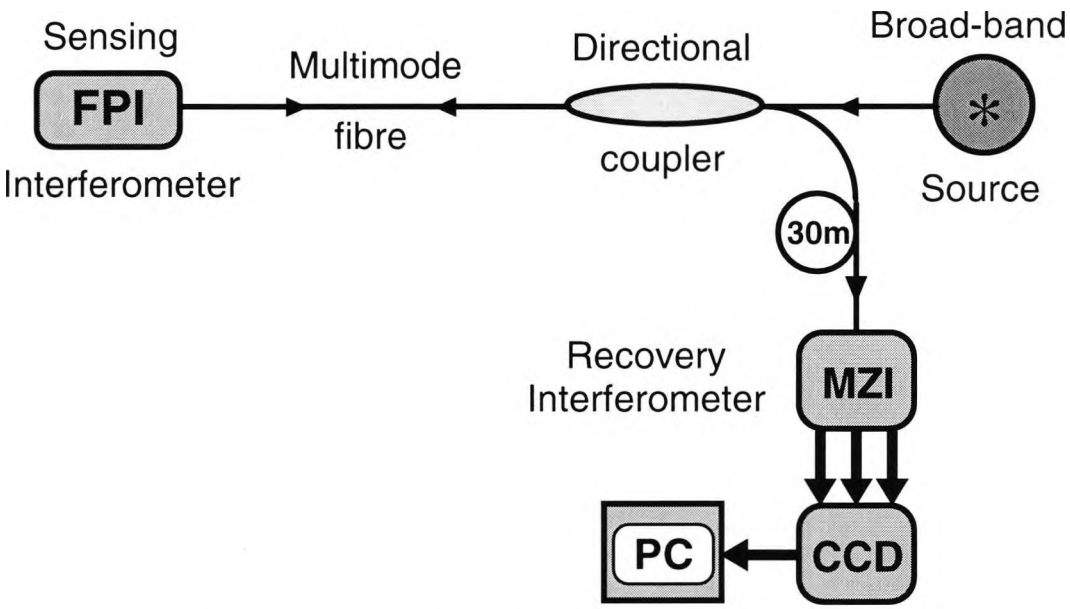

Figure 4.5: Schematic representation of the ESWLI used in this work

4.3. Central Fringe Identification Enhancement

4.3.1. Utilisation of Dual Wavelengths

Multimode laser diodes can provide a larger output power and enhanced coupling efficiency into optical fibers when compared to LEDs. However, in general multimode laser diodes have longer coherence lengths, which can limit their applications in high-precision measurement, because the measurement procedure in a

WLI requires the position of the central fringe to be accurately determined. However, it is often the case that the intensity difference between the central fringe and its adjacent fringes may be too small to be distinguished in the presence of noise that is typically observed in a WLI system.

An efficient technique to overcome this central fringe identification problem is to use two sources of different wavelengths as a single combination source [8,9,10]. For a multimode laser-diode source, the normalized ac signal output intensity can be expressed as

$$I(x) = \cos\left(k\Delta L(x)\right)\exp\left(-\left(\frac{\Delta L(x)}{L_c}\right)^2\right) \tag{4-6}$$

where $\Delta L(x)$ is the OPD and L_c is the coherence length of the source and the visibility function, V, is given by

$$V = \exp\left(-\left(\Delta L(x)/L_c\right)^2\right) \tag{4-7}$$

Thus, when $\Delta L(x)=0$, the visibility V=1, corresponding to the position of the central fringe as shown in Figure 4.6. From Equation (4-7), the fringe visibility is related to the coherence length of the source. In order to distinguish most readily the central fringe from the adjacent side fringes, the visibility difference between them, ΔV, should be made as large as possible. This difference may be expressed as

$$\begin{aligned} \Delta V &= V(0) - V(\lambda) \\ &= 1 - \exp\left(-\left(\lambda/L_c\right)^2\right) \end{aligned} \tag{4-8}$$

From Equation (4-8), for a given mean source wavelength, λ, if the coherence length of the source, L_c, is large, the visibility difference, ΔV, will be small. This will yield a corresponding increase in the difficulty of identifying the central fringe.

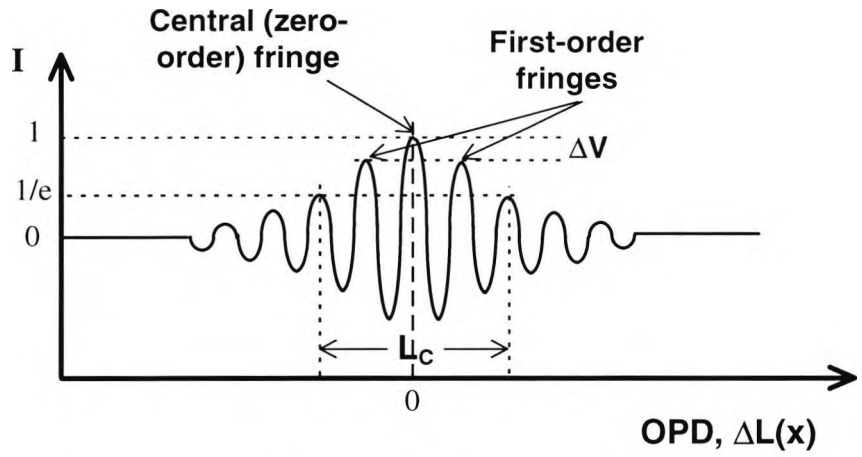

Figure 4.6: Normalized visibility profile of a low coherence source

By employing two differing source wavelengths operating together ΔV can be increased and thus the central fringe identification can be improved. Since light beams of different wavelengths are mutually incoherent, the resultant intensity of the dual wavelength combined source is simply the sum of the individual output intensities from each source. Thus, assuming the interferometer has negligible optical dispersion, the corresponding normalized output ac signal intensity may be expressed as

$$I(x)=\frac{1}{2}\left[\cos\left(k_1\Delta L(x)\right)\exp\left(-\left(\frac{\Delta L(x)}{L_{c1}}\right)^2\right)+\cos\left(k_2\Delta L(x)\right)\exp\left(-\left(\frac{\Delta L(x)}{L_{c2}}\right)^2\right)\right] \quad (4\text{-}9)$$

where $k_1=2\pi/\lambda_1$ is the wavenumber of the first laser diode having a mean wavelength of λ_1; likewise $k_2=2\pi/\lambda_2$ is the wavenumber of the second laser diode source λ_2; and L_{c1}, L_{c2} are their respective coherence lengths.

It is a reasonable assumption that both sources have the same coherence length, $L_c = L_{c1} = L_{c2}$ and with $\lambda_1<\lambda_2$, Equation (4-9) becomes

$$I(x)=\frac{1}{2}\exp\left(-\left(\frac{\Delta L(x)}{L_c}\right)^2\right)\left[\cos\left(\frac{2\pi}{\lambda_1}\Delta L(x)\right)+\cos\left(\frac{2\pi}{\lambda_2}\Delta L(x)\right)\right] \quad (4\text{-}10)$$

Using the trigonometric identity $cos(A+B)+cos(A-B)=2cosAcosB$, then

$$A \equiv \pi\Delta L(x)\left(\frac{1}{\lambda_1}+\frac{1}{\lambda_2}\right) \;;\; B \equiv \pi\Delta L(x)\left(\frac{1}{\lambda_2}-\frac{1}{\lambda_1}\right) \tag{4-11}$$

such that Equation (4-10) becomes

$$\begin{aligned} I(x) &= \exp\left(-\left(\frac{\Delta L(x)}{L_c}\right)^2\right)\left[\cos\left(\pi\Delta L(x)\left(\frac{1}{\lambda_1}+\frac{1}{\lambda_2}\right)\right).\cos\left(\pi\Delta L(x)\left(\frac{1}{\lambda_2}-\frac{1}{\lambda_1}\right)\right)\right] \\ &= \exp\left(-\left(\frac{\Delta L(x)}{L_c}\right)^2\right)\left[\cos\left(\pi\Delta L(x)\left(\frac{\lambda_1+\lambda_2}{\lambda_1\lambda_2}\right)\right).\cos\left(\pi\Delta L(x)\left(\frac{\lambda_2-\lambda_1}{\lambda_1\lambda_2}\right)\right)\right] \end{aligned} \tag{4-12}$$

Thus

$$I(x) = \exp\left(-\left(\frac{\Delta L(x)}{L_c}\right)^2\right)\left[\cos\left(2\pi\Delta L(x)/\lambda_a\right).\cos\left(2\pi\Delta L(x)/\lambda_m\right)\right] \tag{4-13}$$

where $\lambda_a=2\lambda_1\lambda_2/(\lambda_1+\lambda_2)$ is termed the average wavelength and $\lambda_m=2\lambda_1\lambda_2/(\lambda_2-\lambda_1)$ the modulation wavelength. The corresponding fringe visibility function can now be expressed as

$$V = \exp\left(-\left(\Delta L(x)/L_c\right)^2\right)\cos\left(2\pi\Delta L(x)/\lambda_m\right) \tag{4-14}$$

which is a cosine oscillation that is modulated by a Gaussian function. The visibility difference between the central fringe ands its adjacent side fringes becomes

$$\Delta V = 1-\exp\left(-\left(\lambda_a/L_c\right)^2\right)\cos\left(2\pi\lambda_a/\lambda_m\right) \tag{4-15}$$

When compared with the visibility difference, ΔV, obtained with only one source, then ΔV will be greater, provided that the condition

$$\exp\left(-\left(\lambda_1/L_c\right)^2\right) > \exp\left(-\left(\lambda_a/L_c\right)^2\right)\cos\left(2\pi\lambda_a/\lambda_m\right) \tag{4-16}$$

is satisfied. Since $\lambda_2>\lambda_1$, then this implies that $\lambda_a>\lambda_1$, and so this condition can always be satisfied. Thus, the use of dual wavelengths will provide an increase in the visibility difference between the central and adjacent fringes, which facilitates the central fringe identification process.

In order to evaluate these dual wavelength effects, the signal-to-noise ratio was used as a performance index. Here, the minimum signal-to-noise ratio required by the system to identify the central fringe, SNR_{min}, can be defined as

$$SNR_{\min} = 1 / \Delta I_{01} \tag{4-17}$$

which in the electrical domain (in dB) becomes,

$$SNR_{\min}(dB) = -10\log(\Delta I_{01}) = -10\log(1 - I_{01}) \tag{4-18}$$

where ΔI_{01} is the normalized (peak-to-peak) intensity difference between the central fringe and the largest possible side fringe.

A computer generated interference fringe pattern (assuming no noise present) for a single multimode laser diode source is shown in Figure 4.7. Here the mean source wavelength is 635 nm at an inclination angle, $\alpha \approx 0.03°$and L_c is 25μm. It can be seen here that the amplitude difference between the central and adjacent side fringes is very

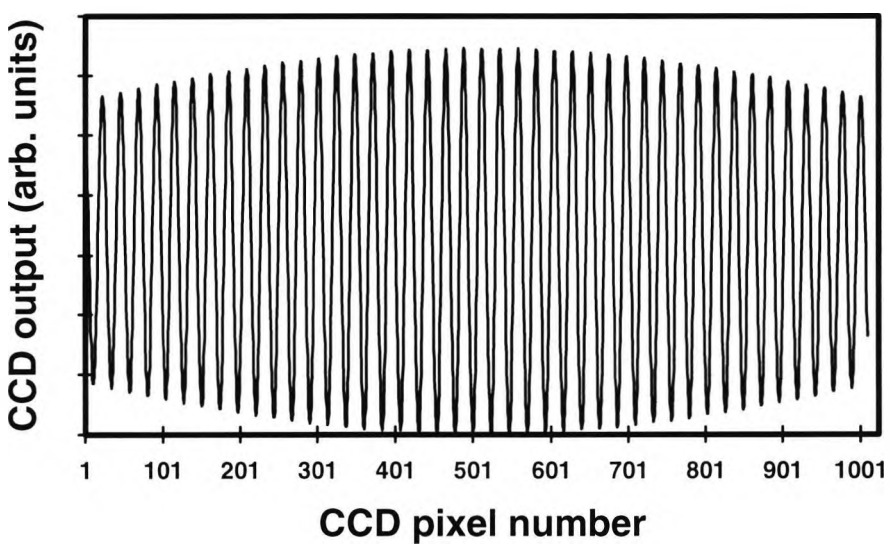

Figure 4.7: Simulated spatial fringe interferogram across a CCD for a source wavelength of 635nm and L_c of 30μm at an inclination angle, $\alpha \approx 0.03°$.

small indeed, and in the presence of a small level of noise would cause some real difficulty in its identification. By using two differing source wavelengths of 635nm and 780nm and keeping the other parameters the same as before, it can be seen that the difference between the central and adjacent fringes is now increased, as shown in Figure 4.8, in a simulation under otherwise similar conditions. When the wavelength pairing is changed, this produces a corresponding change in the beat length between the two wavelengths ($\lambda_m/2$). Figure 4.9 shows the simulated output for a wavelength combination of 635nm and 670nm, which shows that the beat length has been increased as expected. Figures 4.8 and 4.9 also show that, in these examples, the difference between the central and adjacent fringes, ΔV, increases with an increase in the difference between the two source wavelengths, $\Delta\lambda$, which improves the central fringe identification the presence of the system noise expected under typical operating conditions. In addition, the wavelength stability of the two sources (due to the effects of heating of the diodes themselves) is not critical since the sensing and recovery interferometers are close to their balance positions, and thus typical temperature variations of 20°C will produce a negligible effect ($<10^{-3}$ fringe difference in the output phase [11].)

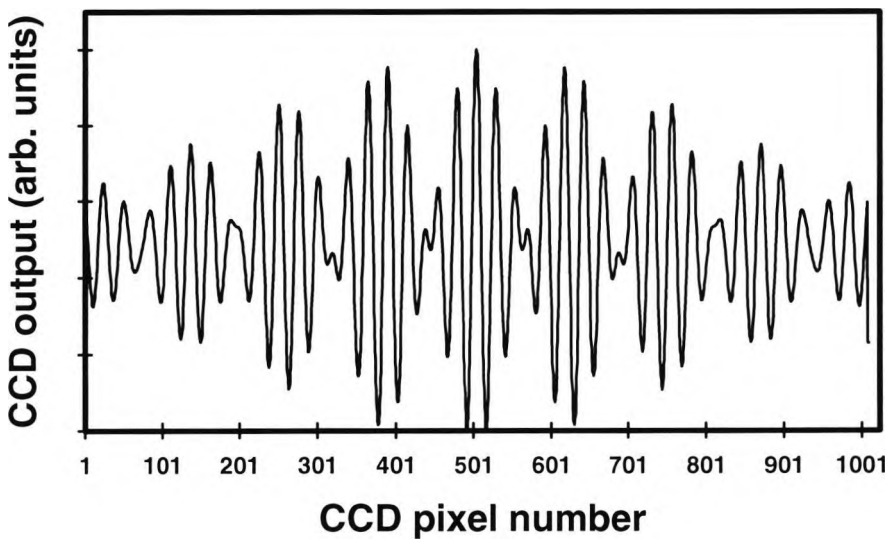

Figure 4.8: Simulated spatial fringe interferogram across a CCD for dual source wavelengths of 635nm and 780nm at L_c of 30μm and an inclination angle, $\alpha \approx 0.03°$.

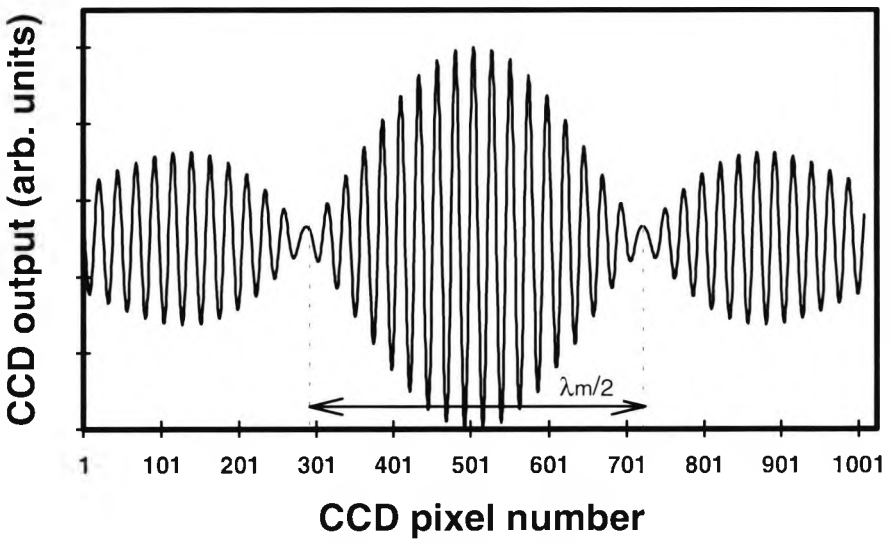

Figure 4.9: Simulated interferogram output for a wavelength combination of 635nm and 670nm

4.3.2. Least squares curve fit

4.3.2.1. Introduction

The use of a least-squares (LS) curve fitting technique has the capability to provide an accurate fit of a function to the data obtained and thus of the central fringe position determination. This technique uses the entire data set to determine the central fringe rather than one single measurement point (when an amplitude thresholding technique is used). Thus, a more accurate estimation of the central fringe position can be achieved, which is more resistant to system noise, than without the use of the method.

4.3.2.2. Construction of the Least squares polynomial

Let $j_1, j_2,..., j_n$ represent the distinct domain points representing the pixel number in the CCD detector and $f_1, f_2,..., f_n$ represent the corresponding processed fringe interferogram values, which are approximated by a polynomial of degree not exceeding m. If m=n-1, the unique interpolating polynomial provides a perfect fit to the data. However, if m<n-1, typically no interpolation polynomial of degree m exists. In these

cases, a polynomial of degree, m, that is the closest, in some sense, to the data set is valuable.

In the least-squares method, the discrepancy of the data points (j_1, f_1), (j_2, f_2),..., (j_n, f_n) and the approximating polynomial, p(j) are measured by the sum of the squared residuals given by [12]

$$Q(f, p) = \sum_{i=1}^{n} \left(f_i - p(j_i) \right)^2 \tag{4-19}$$

where $Q(f,p)$ has to be minimised over the coefficients a_1, a_2,..., a_m of the polynomial $p(j) = a_0 + a_1 j + a_2 j^2 + ... + a_m j^m$. Thus, the polynomial, $p(j)$, minimizing $Q(f,p)$ over all polynomials, p, of degree m or less is called the least-squares polynomial of degree m.

The least-squares fit technique employed here, simply fits a kth order Chebyshev polynomial to the interferogram data.

$$p(x) = \tfrac{1}{2} a_0 T_0(x) + a_1 T_1(x) + a_2 T_2(x) + ... + a_k T_k(x) \tag{4-20}$$

where $T_i(x)$ is the Chebyshev polynomial of the first kind of degree, i (=0, 1, 2 . ,) and where the x range has been normalised from -1 to +1 and is related to the original pixel number variable, j (=0, 1, 2 . ,) by the linear transformation

$$x = \frac{2j - j_{max} - j_{min}}{j_{max} - j_{min}} \tag{4-21}$$

Such a Chebyshev polynomial was chosen since it provides high accuracy and generally yields solutions with lower orders than other schemes (such as the use of power series)[13].

The purpose of using the LS method was to provide a low order fit of the fringe interferogram in order to yield a better estimation of the central fringe position. This method is more resistant to the presence of any noise on the fringe output, since a low

order fit cannot track the variations of high frequency noise. In addition, the use of a curve fitting routine uses the whole data set in order to compute the central fringe position, rather than only using 1 point, which is what is employed in the thresholding technique.

The ESWLI configuration was set up as shown in Figure 4.10, using only a single source wavelength to illustrate this central fringe identification effect. The resultant interferograms were recorded using the PC for ease of data analysis.

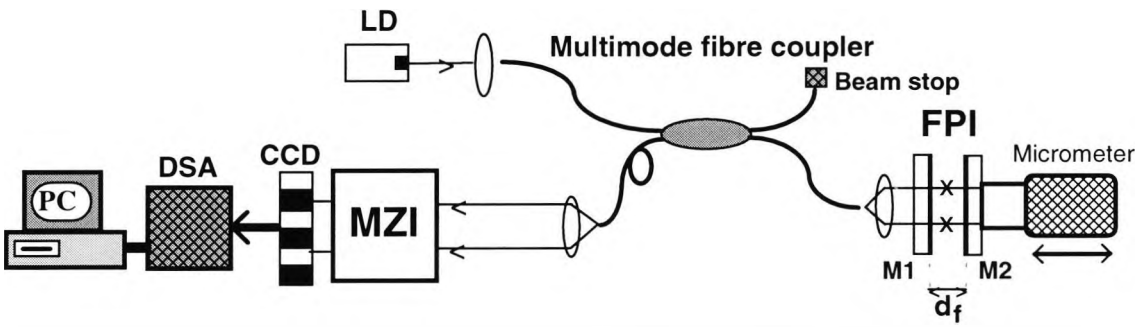

Figure 4.10: Schematic of the experimental arrangement. MZI is the Mach-Zehnder interferometer; M1 and M2 are 50% reflectance Fabry-Perot interferometer (FPI) mirrors, separated by d_f; LD is a multimode laser diode; CCD is a line charge-coupled device detector; DSA is a digital storage adaptor.

Various interferogram traces were recorded as the FPI mirror was scanned. The beam profile intensity was removed from the fringe interferograms as before, followed by the use of a normalisation procedure to yield the resultant fringe interferogram as shown in Figure 4.11(a). Here, the FPI mirror was set at the zero OPD reference position, corresponding approximately to the centre of the spatial interferogram. The MZI was set at an inclination angle, $\alpha \approx 0.14°$ which corresponds to 6 pixels per fringe and at a source wavelength, $\lambda = 0.78\mu m$. Due to the use of a single wavelength, it is shown that the central fringe region is quite flat, even with the use of a low coherence source ($L_c \approx 40\mu m$). Taking this specific example, thus, in error, the central fringe using the maximum amplitude threshold method would be given by pixel number 509.

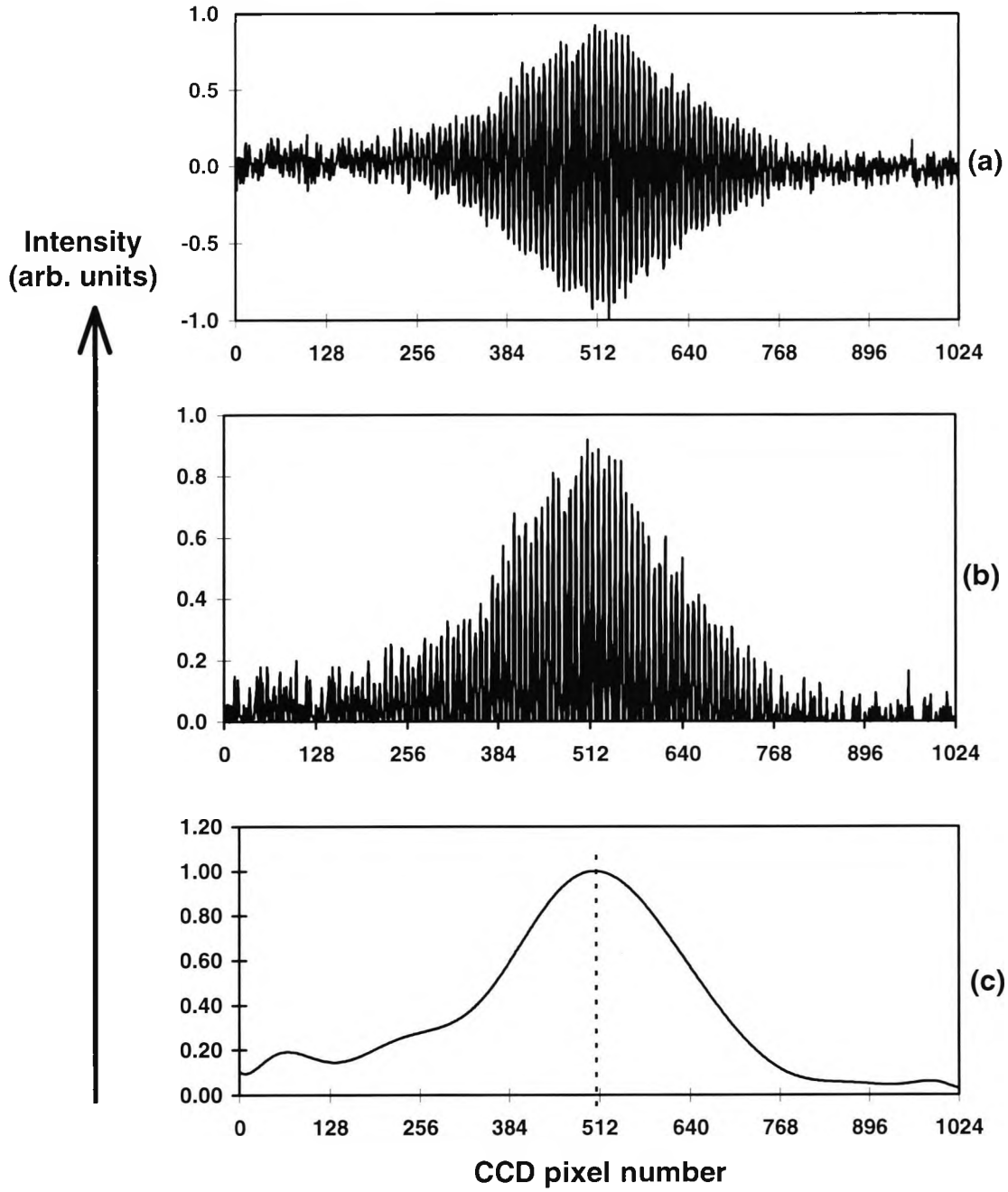

Figure 4.11: Least-squares (LS) curve fitting results. (a) shows the normalised fringe interferogram; (b) Interferogram of the "positive" fringe components showing the upper coherence profile; (c) 15th order LS fit which identifies the central fringe at pixel number 505.

In order to obtain the central fringe position using the least-squares analysis, then initially the interferogram of only those fringe components >0 are considered, as shown in Figure 4.11(b). This is due to the fact that the least-squares fit will fit a line corresponding to a zero mean to the interferogram in its current format. The least squares fitting routine may now be applied to Fig. 4.11(b). The computer program (in

Turbo-PASCAL) automatically selects the desired fitting order, whereby the order, k, which yields the same central fringe position as order (k+1) and (k+2) is chosen to be the desired order. The corresponding LS fit (at k=15) is shown in Fig. 4.11(c), which shows that the central fringe position is, in fact, at pixel number 505.

4.3.3. Centroid method

The centroid method (or centre-of-gravity) technique [14] uses the whole interferogram data set in order to determine the central fringe by locating it as being the centre-of-gravity point at which the summation of the interferogram data on each side of this point is equal. By using the entire interferogram to compute the central fringe position, the effects of the system noise are reduced. The centroid position, C_G, of the processed interferogram, F[j], (where j=1,2,..,M is the pixel number and M is the total number of pixels), is computed in two steps [14]. Firstly, any dc component of the processed fringe interferogram, F[j], is removed, yielding the ac part of the processed fringe signal, $F_{ac}[j]$. Secondly, the centroid position, C_G, is now given by [15]

$$C_G = \frac{\sum_j j.[F_{ac}[j]]^2}{\sum_j [F_{ac}[j]]^2} \qquad (4\text{-}22)$$

The above shows that, the central fringe position can be obtained relatively simply using this expression. In order to compare the effectiveness of this technique, the results from this centroid algorithm were compared with those obtained for the least-squares technique. As the mirror position was scanned, the central fringe position was estimated at various positions, as shown in Fig. 4.12 (for the threshold method), Fig. 4.13 (for the least squares method) and Fig. 4.14 (for the centroid method). Even though a mechanical translation stage was employed, a good measurement accuracy of ±0.1μm was recorded.

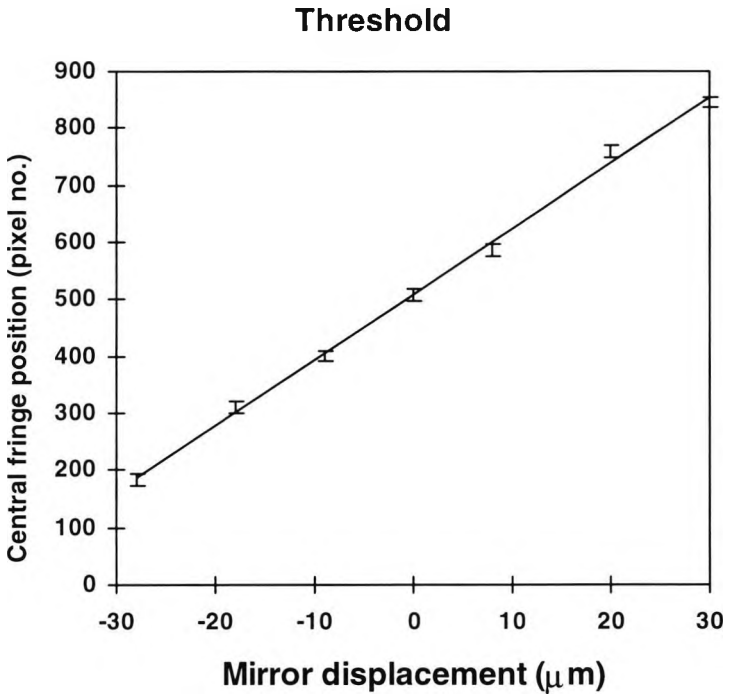

Figure 4.12: Experimental results of the central fringe identification using the threshold method

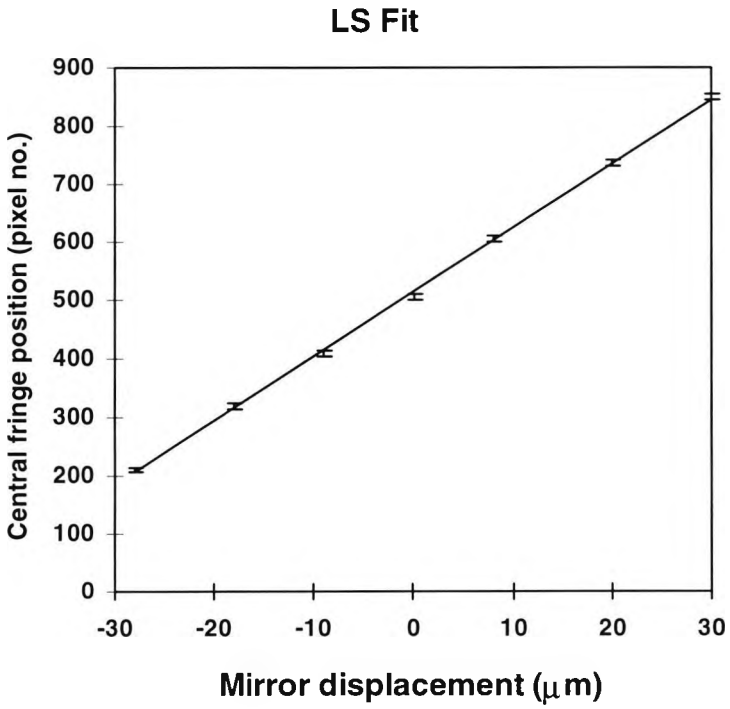

Figure 4.13: Experimental results of the central fringe identification using the least-squares fit method.

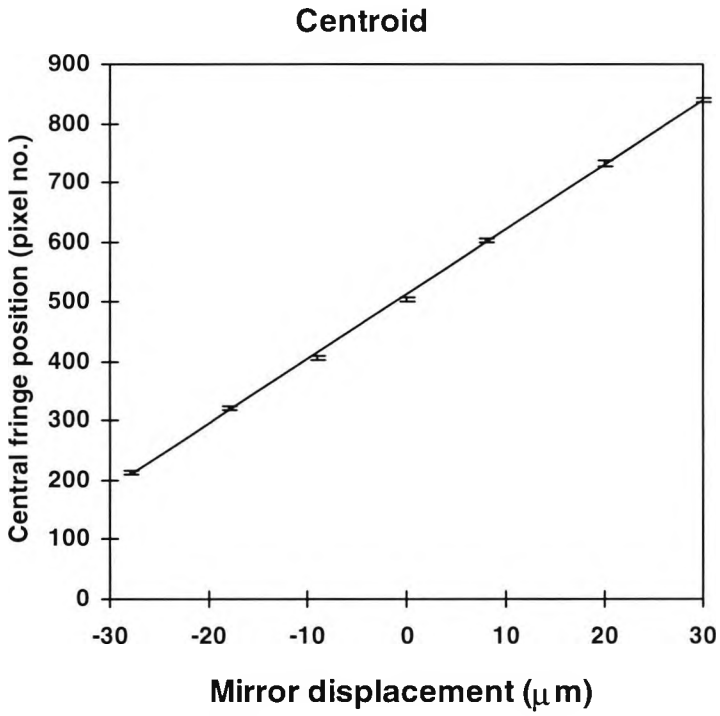

Figure 4.14: Experimental results of the central fringe identification using the centroid method.

From the comparative results shown in Figures 4.12, 4.13 and 4.14, the method of least squares was shown to produce the best results of the methods considered. The centroid method produced good results, albeit with a reduced scanning range, as summarised in Table 4.1, and, as expected, the threshold method produced the worst results. The centroid method has the shortest scanning range (~70μm), as opposed to ~90μm for the other two techniques, under these operational conditions (i.e. at $\alpha \approx 0.14°$). This scanning range limitation with the centroid method is due to the fact that the entire fringe interferogram has to be visible in order to compute the centroid, whereas the other two methods require only the central fringe region to be visible, which extends the scanning range slightly. Other authors have employed adaptive filtering schemes [14,16] in order to identify the central fringe. Although these techniques provide similar results to those employed here, they have the disadvantage of requiring greater computational complexity. In addition, like all adaptive filtering schemes, they occasionally do not converge to an optimum solution, if they are not initialised correctly.

Table 4.1: Experimental results of central fringe identification performance under various techniques		
Method	Error (max) μm	Operating Range (μm)
Threshold	1.8±0.1	90
Centroid	0.3±0.1	70
Least-squares	0.21±0.1	90

To summarise, the use of least-squares and centroid curve fitting techniques are shown to produce sufficiently accurate results for practical use when employed to identify the central fringe, even in the presence of significant amounts of system noise. The centroid method is computationally more simple and fast. However, the LS method yields slightly better results and has a larger operating range when compared to the centroid method.

4.4. Effects of Optical Dispersion

4.4.1. Introduction

An experimental evaluation, coupled with an appropriate theoretical analysis, of a dual-wavelength WLI experiencing dispersion effects, is reported. The dual wavelength arrangement, typical of practical optical sensing systems that were employed, utilized an electronically-scanned WLI configuration with a Fabry-Perot interferometer as the sensing interferometer, and a modified Mach-Zehnder configuration as the recovery interferometer.

The results may be used to analyze the situation that may be experienced where either the sensing or recovery interferometer is dispersive, showing that the central fringe in the visibility profile due to each wavelength will no longer result at the same position as would otherwise occur in the absence of dispersion on the sensing CCD. In view of the importance of the well-known dispersion effects for practical remote sensors using low coherence techniques, the extreme case is highlighted where the fringe patterns of each wavelength do not overlap at all with each other, reflecting real problems in the use of such apparatus in sensor applications, and offering a means to solutions for actual measurements.

If either the sensing interferometer or the recovery interferometer is dispersive, the resultant interferograms due to each of the individual wavelengths used will no longer overlap completely the one with the other, resulting in the central fringe position corresponding to each wavelength no longer occurring at the same position, and thereby causing real problems in any measurement applications of the sensor system.

In this work [17], an experimental analysis of this effect on a very practical, low cost sensor system was investigated and the output compared with supporting theory to enable the results to be validated, for the extreme case where the fringe patterns of each wavelength do not overlap at all with each other.

4.4.2. Theoretical considerations

4.4.2.1. Non-dispersive interferometer case

In this work to illustrate the effect, a Fabry-Perot interferometer (FPI) is considered to be the sensing interferometer, and a Mach-Zehnder interferometer (MZI) (shown in Figure 3.6) the recovery interferometer. For a two wavelength combination source, since the light beams from the two laser diode sources are mutually incoherent, the resultant output signal intensity is simply the sum of the two output signal intensities generated by each laser diode. This resultant output signal intensity, I(x), of the dual wavelength system can be expressed as

$$I(x) = P(x)\left\{A + 2B\left\{\cos\left[k_1\left(\Delta L_P(x) - \Delta L_S\right)\right]\exp\left[-\left(\frac{\Delta L_P(x) - \Delta L_S}{L_{c1}}\right)^2\right] + \cos\left[k_2\left(\Delta L_P(x) - \Delta L_S\right)\right]\exp\left[-\left(\frac{\Delta L_P(x) - \Delta L_S}{L_{c2}}\right)^2\right]\right\}\right\} \tag{4-23}$$

where P(x) is the beam intensity profile; $\Delta L_P(x)$ is the optical path difference (OPD) induced in the MZI between the two beams at the point x, where the intensity is detected by the CCD; and ΔL_S is the OPD induced in the FPI (as shown in Figure 4.15), given by $2d_f$ where d_f is the separation of the FPI mirrors; $k_1=2\pi/\lambda_1$; λ_1 is the

first source wavelength; $k_2=2\pi/\lambda_2$; λ_2 is the second source wavelength; L_{C1} is the coherence length of source 1; L_{C2} is the coherence length of source 2; and A and B are given by $(1-r_1)^2 r_1^2 (r_2^2 + r_3^2)$ and $(1-r_1)^2 r_1^2 r_2 r_3$ respectively, where r_1 is the reflection coefficient of beamsplitter BS, r_2 is the reflection coefficient of mirror M1, and r_3 is the reflection coefficient of mirror M2 in the MZI.

A detailed representation of the MZI used is shown in Figure 3.6. The interferometer is shown to operate without the use of a compensating plate, and thus it is defined for use at a known (room) temperature, or over a limited temperature excursion where the temperature dependence of the refractive index is small enough to be ignored. In addition, the optical fibre coupler of the set-up was initially replaced with an open-air-path in order to exclude any dispersive effects in the fibre.

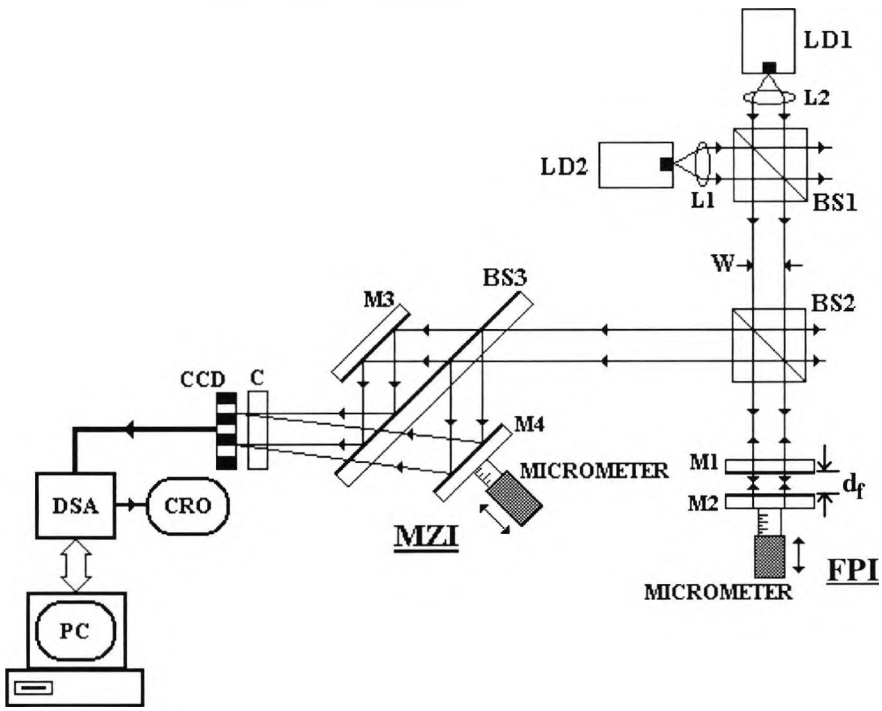

Figure 4.15: Schematic representation of the complete experimental arrangement used to observe the results. Where M1, M2 are Fabry-Perot interferometer (FPI) mirrors; BS1, BS2, BS3 are beamsplitters; L1, L2 are lenses; LD1, LD2 are laser diodes of wavelength λ_1 and λ_2 respectively; and C is a cylindrical lens

From equation (3-16), the OPD in the MZI, $\Delta Lp(x)$, between the two beams at a position x, with respect to an arbitrary origin, is given by

$$\Delta L_p(x) = \frac{2\sin(\alpha)}{[\cos(\alpha) - \sin(\alpha)]}\left(\sqrt{2}d + x\right) \tag{4-24}$$

where d is the perpendicular distance from mirror M1 to the beamsplitter (BS3), x is the value of the x-axis along the CCD array, and α is the angle of inclination of mirror M2 with respect to BS3, as shown in Figure 3.6.

4.4.2.2. Dispersive interferometric case

By contrast to the previous situation, if either the sensing interferometer or recovery interferometer is dispersive, this produces a change in the OPD in the appropriate interferometer. For this dispersive case, the signal intensity output, I(x), may now be expressed as

$$I(x) = P(x)\left\{A + 2B\left\{\cos\left[k_1\left(\Delta L_1(x,\lambda_1)\right)\right]\exp\left[-\left(\frac{\Delta L_1(x,\lambda_1)}{L_{C1}}\right)^2\right] + \cos\left[k_2\left(\Delta L_2(x,\lambda_2)\right)\right]\exp\left[-\left(\frac{\Delta L_2(x,\lambda_2)}{L_{C2}}\right)^2\right]\right\}\right\} \tag{4-25}$$

$$\begin{aligned} where\ \ \Delta L_1(x,\lambda_1) &= \left(\Delta L_p(x) + OPD_{rn1}\right) - \left(\Delta L_s + OPD_{sn1}\right) \\ \Delta L_2(x,\lambda_2) &= \left(\Delta L_p(x) + OPD_{rn2}\right) - \left(\Delta L_s + OPD_{sn2}\right) \end{aligned} \tag{4-26}$$

OPD_{rn1} and OPD_{rn2} are the dispersion induced OPDs by wavelengths λ_1 and λ_2 respectively in the recovery interferometer and OPD_{sn1} and OPD_{sn2} are the dispersion induced OPDs by wavelengths λ_1 and λ_2 respectively in the sensing interferometer.

All optical glasses have an index of refraction which changes with changing wavelength. The refractive index of a glass, n_t, in the wavelength range of 365 to 1014nm can be calculated from the following formula [18]

$$n_t^2(\lambda) = A_0 + A_1\lambda^2 + A_2\lambda^{-2} + A_3\lambda^{-4} + A_4\lambda^{-6} + A_5\lambda^{-8} \tag{4-27}$$

Here, λ, the wavelength, must be in microns, and the constants A_0 to A_5 are given by; A_0=2.271829, A_1=-1.0108077×10^{-2}, A_2= 1.0592509×10^{-2}, A_3=2.0816965×10^{-4}, A_4= – 7.6472538×10^{-6}, and A_5= 4.9240991×10^{-7}; for BK7 crown glass [18]. This equation yields a value for the refractive index that is accurate to ±3×10^{-6} between 400 and 750nm, and accurate to ±5×10^{-6} from 750 to 1014nm.

4.4.2.3. Effects of optical dispersion in the MZI

The effects of the dispersion in the MZI (Figure 3.6) are shown in detail in Figures 4.16(a),(b), which show the upper and lower portions of the beamsplitter, BS3. From Figure 4.16, the additional OPD, OPD_{m1}, induced solely by the refractive index difference of source 1 (λ_1) in the MZI is given by:

$$OPD_{m1} = n_t(\lambda_1)[(EF + FG + HJ) - EF] \tag{4-28}$$

Such that

$$OPD_{m1} = n_t(\lambda_1).t_m\left(\frac{1}{\cos[\theta_{t1}(\lambda_1)]} + \frac{1}{\cos[\theta_{t2}(\lambda_1)]}\right) \tag{4-29}$$

where $n_t(\lambda_1)$ is the refractive index of the BK7 due to wavelength λ_1; t_m is the thickness of the MZI beamsplitter mirror and from Snell's Law;

$$\theta_{t1}(\lambda) = \sin^{-1}\left(\frac{n_i}{n_t(\lambda)}\sin(\theta_{i1})\right), \quad \theta_{i1} = \pi/4 \tag{4-30}$$

$$\theta_{t2}(\lambda) = \sin^{-1}\left(\frac{n_i}{n_t(\lambda)}\sin(\theta_{i2})\right), \quad \theta_{i2} = \pi/4 - 2\alpha \tag{4-31}$$

where the angles are as shown in Figure 4.15.

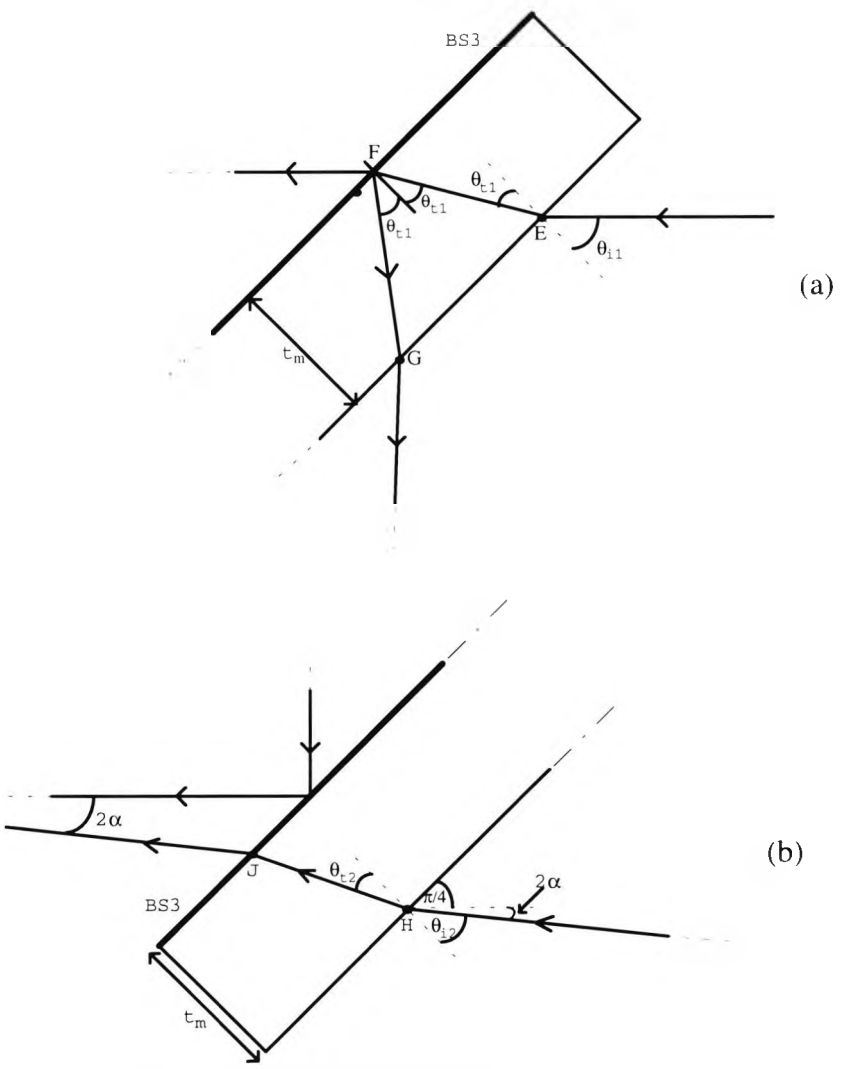

Figure 4.16: Schematic showing the dispersion effects in (a) the upper region, and (b) the lower region of the beamsplitter BS3 in the MZI.

Likewise, the additional OPD, OPD_{rn2}, induced by the refractive index difference of source 2(λ_2) in the MZI may be expressed as:

$$OPD_{rn2} = n_t(\lambda_2).t_m\left(\frac{1}{\cos[\theta_{t1}(\lambda_2)]}+\frac{1}{\cos[\theta_{t2}(\lambda_2)]}\right) \tag{4-32}$$

where $n_t(\lambda_2)$ is the refractive index of the BK7 glass at wavelength λ_2 and t_m is the thickness of the MZI beamsplitter. Thus, the change in the OPD, δ_p, due to the refractive index difference for each wavelength of the dual wavelength source is given by

$$\delta_P = \left| OPD_{rn1} - OPD_{rn2} \right| \tag{4-33}$$

4.4.2.4. Effects of optical dispersion in the FPI

The FPI (as shown in Figure 4.15) contains two 50% reflectance mirrors each having the same thickness, t_f. The effects of the optical dispersion are attributed only to the transit of the light through the first mirror, M1, since the light beam of interest from mirror M2 is reflected from the front surface of M2, and thus this reflected light does not pass through the body of mirror M2. Therefore, the additional OPD, OPD_{sn1}, induced by the refractive index effect at wavelength, λ_1, can be expressed as

$$OPD_{sn1} = 2t_f n_g(\lambda_1) \tag{4-34}$$

Likewise, the additional OPD, OPD_{sn2}, induced by the refractive index effect of source 2, λ_2, in the FPI is given by

$$OPD_{sn2} = 2t_f n_g(\lambda_2) \tag{4-35}$$

where $n_g(\lambda_1)$ and $n_g(\lambda_2)$ are defined as the refractive indices of the mirror M_1 material respectively at λ_1 and λ_2 and t_f is the thickness of the FPI mirror. Thus, the overall change in the OPD, δ_S, in the FPI is given by:

$$\delta_S = 2t_f\left(n_g(\lambda_1) - n_g(\lambda_2)\right) \tag{4-36}$$

4.4.3. Dispersion simulation

In order to evaluate the potential effects of the optical dispersion in the system, a FORTRAN computer program was implemented to evaluate the influence of the induced OPD due to the optical dispersion in the sensing and recovery interferometers. Due to the obvious differences in the geometry of the MZI and the FPI, this refractive index change produces a different OPD change in the respective interferometer. The thickness of the FPI mirror, t_f, is only 2mm, as opposed to the MZI beamsplitter thickness, t_m, of 3mm. Figure 4.17 shows the resultant total induced OPD change due to the dispersion in both the MZI and FPI for a range of commercially available laser diodes. This figure highlights the fact that for widely spaced wavelengths, the induced OPD change between the two wavelength packets can be as large as ~50μm (for λ_1 =0.635, and λ_2 =0.83μm). This would result in the undesired effect of a complete spatial separation of the interferogram due to each wavelength.

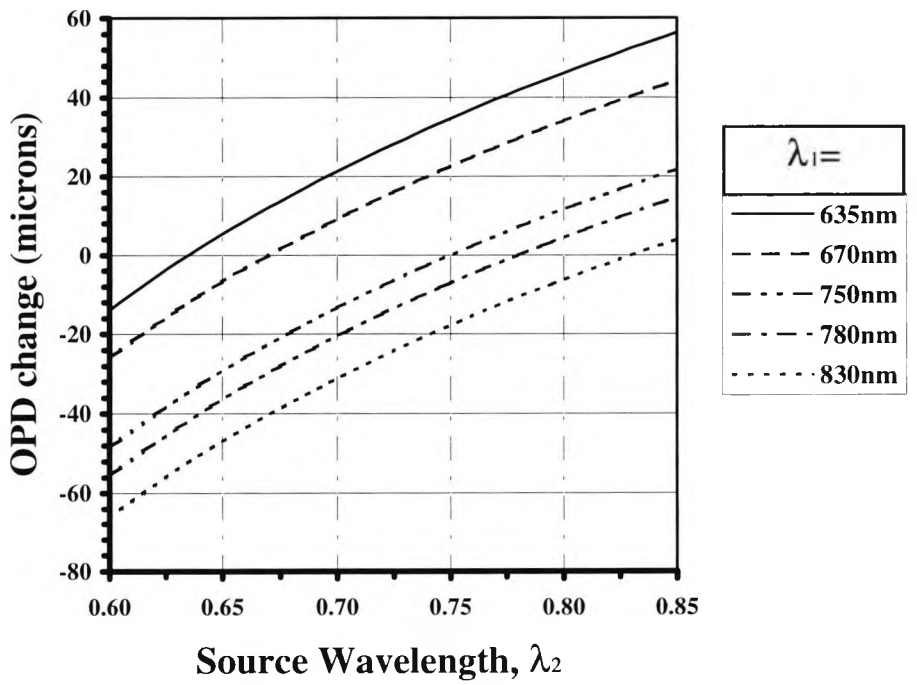

Figure 4.17: Simulated plot of the dispersion induced OPD change in a dual wavelength (λ_1,λ_2) MZI for a series of fixed wavelengths, λ_1, as a function of a varying secondary wavelength, λ_2.

4.4.4. Experimental arrangement

A primary aim of this work is to quantify the effect of the dispersion discussed on a practical sensing system, as shown in Figure 4.15 which illustrates the full dual wavelength, dual interferometer system investigated in this work and widely used for sensing. The configuration used two multimode laser diode sources (LD1 and LD2), providing differing mean source wavelengths of λ_1=635nm and λ_2=780nm respectively, with coherence lengths, $L_{c1}=L_{c2}$=25μm. In previous work, this type of diode laser source, and this combination of wavelengths, had been found to be particularly effective for a sensitive diode wavelength sensor system [9].

Both sources were collimated and expanded to a width, W (in order to expand the resultant beam across the linear CCD), via two ×5 objective lenses, L1 and L2. These beams were then combined through the first beamsplitter, BS1, to form a single light beam before entering the Fabry-Perot interferometer (FPI). The light passes through the second beamsplitter, BS2, and enters the FPI, containing two parallel mirrors, M1, and M2, respectively which have a 50% reflectance, and a thickness, t_f, of 3mm. The two mirrors were separated by a distance, d_f, providing a total optical path difference (OPD) due to the two reflecting surfaces given by $2d_f$. The output of the FPI travels back along the same path and is reflected by 90° via BS2, through to the input of the Mach-Zehnder interferometer (MZI). The operation of this MZI and the associated CCD detection scheme and data capture is given in Section 4.3.

4.4.5. Experimental results and discussion

The experimental arrangement to investigate the situation is shown in Figure 4.15, which shows the extent to which compensation for the dispersion effects is required in a practical sensor system. From simple theory, when a primary source wavelength, λ_1, of 0.635μm, and a secondary source wavelength, λ_2, of 0.780μm are employed, the resultant OPD change induced by the differing wavelengths will be ≈ 42μm, at a typical inclination angle, such as would be used in a sensor, of ≈0.2°.

This implies that the interferogram "packets" of each wavelength will not overlap to produce the desired beating effect, but instead, their central fringe positions will be separated by ≈42μm.

Figure 4.18 shows the resultant interferogram obtained from the use of both sources after beam-profile elimination. Here, an expanded view of these processed fringe interferograms is shown over the CCD pixel number range 180 to 680, revealing the essentially sinusoidal nature of the envelope. Here, the "interferogram packets" were experimentally observed to be separated by a distance of 45±5μm, which is in good agreement with the theoretical result of 42μm. The non-linear shape of the processed interferogram is due to the expected effects of the background beam intensity profile, P(x), which ideally should have a Gaussian profile, but which was distorted further by optical aberrations in the system.

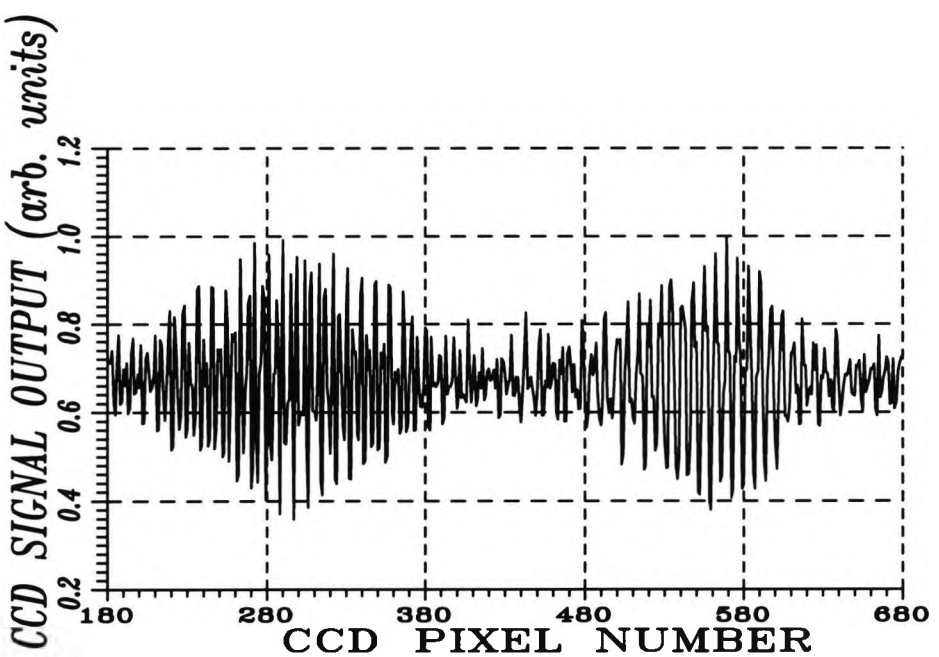

Figure 4.18: Expanded view of resultant processed fringe interferograms over the CCD pixel range 180 to 680, which shows the spatial separation of 45±5μm observed due to the optical dispersion effects.

Equations (4-33) and (4-36), can be used to quantify the intuitive result that a reduction in the dispersion-induced OPD in the system can be achieved by reducing the thicknesses of the optical components in the MZI and the FPI, denoted by t_m and t_f respectively. It is extremely difficult to deduce quantitatively a single figure which represents the maximum permissible dispersion-induced OPD and yet achieve an

acceptable fringe pattern from which the central fringe can be readily identified. This difficulty exists because this maximum value is dependent upon a series of interrelated factors. These include the source wavelengths, (λ_1,λ_2) and their linewidths, the thicknesses of the MZI and FPI beamsplitters (t_m and t_f respectively), the coherence lengths of the sources (L_{c1} and L_{c2}) and to a lesser extent, the number of pixels per fringe (which in turn is related to the inclination angle, α).

A computer simulation was employed in order to attempt to provide a satisfactory quantitative figure for the maximum permissible dispersion induced OPD, δ_{max}. The effects of dispersion will produce problems when δ_{max} separates the two interferograms to such an extent that the resultant central fringe position of the combined interferogram is significantly and measurably shifted in position. This simulation analysis was performed on the basis of the verification of the effects of various combinations of commercially available multimode laser diode wavelength (i.e. 635, 670, 730, 780, 810 and 830nm).

From the simulations carried out, it was observed that the maximum allowable dispersion induced OPD, δ_{max}, was given by

$$\delta_{\max} \approx \frac{\lambda_m}{10} \tag{4-37}$$

where λ_m is the mean of the two source wavelengths, and is given by $2\lambda_1\lambda_2/(\lambda_1+\lambda_2)$. Outside of this limit, the detected central fringe position (using an amplitude thresholding technique [10]) cannot be guaranteed to be in the "correct" position, where this is defined by a tolerance of $\pm\lambda/20$. Indeed, for the parameters of this system, δ_{max} would have a limiting value of ~ 0.07μm, if the source wavelengths are unchanged at 635 and 780 nm. This stringent condition could only be met with beamsplitters having a thickness of $t_m = t_f = 6\mu m$, (which are commercially available in the form of pellicle beamsplitters). This situation may be improved slightly by using sources whose mean wavelengths are in the infrared region rather than the red region (635 or 670nm). This is due to the higher change in refractive index of the dispersive material when

sources in the red region, rather than in the infra-red are used [7]. In addition, the situation may be further improved by reducing the difference between the two source wavelengths. For example, when this system is used with wavelengths of 780 and 810nm, the maximum dispersion induced OPD (δ_{max}) requirement may be met with beamsplitters having a larger thickness, up to approximately 40μm.

This stringent requirement may be eased slightly by employing central fringe identification techniques (such as centroid or curve fitting methods). Under this regime, the effects of dispersion may be relaxed slightly since the central fringe is then being identified from the whole set of fringes, rather than from one fringe. Under this condition, from simulations carried out, the dispersion induced OPD requirement, δ_{max}, may be relaxed to

$$\delta_{max} \approx \frac{L_c}{4} \tag{4-38}$$

If the original source wavelengths remain unchanged at 635 and 780 nm, then under this criterion, $\delta_{max} \approx 6.25\mu m$, which would yield a maximum beamsplitter thickness requirement of $t_m = t_f = 450\mu m$.

4.4.6. Dispersion Summary

From the experimental work undertaken, in this dual wavelength, low coherence interferometric sensor system, it has been shown that if either the sensing interferometer or the recovery interferometer in a dual-wavelength WLI is dispersive, this effect is large enough that the resultant interferograms obtained due to each wavelength will no longer overlap completely with each other [17]. This particular configuration of interferometers has been set up, with supporting theory established to quantify the nature of the effect and the degree to which it is a problem in the use of such techniques in optical fibre-based systems. The work has shown that the central fringe positions resulting will be separated by a distance proportional to the level of the induced optical dispersion in the system. This has highlighted the extreme case where

this induced OPD was so large that the interferograms attributed to each wavelength source were completely separated, a major problem for practical sensor systems.

Considerable care must be taken in the selection of the thicknesses of dispersive optical components, for a given wavelength pairing (λ_1,λ_2), whose selection is optimized to achieve the best central fringe definition [9] in low coherence interferometry. This shows the value of the use of compensating plates in conventional open-air path interferometry, but which are inappropriate in all-fibre-based systems. The key aspect of the work presented, however, is that it enables quantitative data to be obtained for a range of situations and the degree to which the effect could become a problem in practical systems, such as those using fibres, to be assessed, which is of value to the sensor designer.

This will require resolution of the conflict which occurs between the need to have widely spaced wavelengths, in order to obtain a more prominent central fringe, and the desire to reduce this wavelength difference in order to minimize the effects of the optical dispersion. Again, the experimental and theoretical results enable the optimum "trade-off" in this situation to be assessed in a quantitative manner, supported by the theory presented. An open air path interferometer was originally used here in order to remove the effects of dispersion in the optical fibre. In fact, when the optical fibre was later re-introduced, the dispersion induced OPD change was negligible.

4.5. Chapter Summary

In this chapter, the novel MZI configuration discussed was successfully implemented as a recovery interferometer and a FPI was employed as the sensing interferometer in an ESWLI sensing system. Various design constraints on the use of such systems were experimentally demonstrated and supported by a full theoretical analysis. These design constraints included the analysis of the effects of modal noise in the interconnecting fibre coupler and the effects of optical dispersion in the dual wavelength system. A thorough experimental analysis of the effects of dispersion

provided quantitative data for a range of situations, providing a specification for the use of dual wavelength white-light interferometric sensors.

Various methods of enhancing the identification of the central fringe were introduced. The use of dual wavelengths as a combined synthetic source was shown to be very effective in enhancing the identification of the central fringe. This technique was contrasted against the use of the centroid method and the least squares approach in order to enhance the accuracy of the central fringe identification. Both of these methods have produced very accurate results when used to identify the central fringe position, even in the presence of significant amounts of system noise. The centroid method was computationally faster than that of the least squares (LS) technique. However, the LS method provided more accurate results and had a larger operating range when compared to the centroid method.

In the next chapter, a slight modification to this MZI design is introduced, which is made from bulk-optical components in order to provide a higher degree of stability. In addition, the implementation of this system for the purpose of displacement measurements is presented.

4.6. References

1. Vaughan, J. M.: "The Fabry-Perot interferometer : history, theory, practice and applications.", Ch. 3, Hilger, 1989.
2. Velluet, M. T., Graindorge, P. and Arditty, H. J.: "Fiber optic pressure sensor using white light interferometry", Proc. SPIE vol. 838, Fibre Optic and Laser Sensors V, pp. 78-83, 1987.
3. Hecht, E. and Zajac, A.: "Optics", Ch. 5, pp. 170-176, 2nd ed., Addison-Wesley, 1987.
4. Melles Griot: "Optics Guide 1995/96", Chp. 11, pp. 1-17, Melles Griot Inc., USA, 1995.
5. Mickelson, A. R. and Weierholt, A.: "Modal noise-limited signal-to-noise ratios in multimode optical fibres", Applied Optics, vol. 22, pp. 3084-9, 1983.

6. Ning, Y. N., Liu, Y., Grattan, K. T. V., Palmer, A. W. and Weir, K.: "The relation between the coherence length and modal noise in a graded-index multimode fibre for white light interferometric systems", Optics Letters, vol.19, March 15, 1994.
7. Grattan, K. T. V., Ning, Y. N., Wang, Q., Liu, Y., and Palmer, A. W.: "Considerations in the design of a multimode fibre-linked white-light interferometer", Proc. SPIE vol. 2349, pp. 124-130, Industrial Optical Sensors for Metrology and Inspection, Eds. Kevin G. Harding; H. Philip Stahl, 1995.
8. Jackson, D. A. and Rao, Y. J.: "Improved synthesised source for white light interferometry", Electron. Letts, vol. 30, No. 17, pp. 1440-1, 1994.
9. Wang, D. N., Ning, Y. N., Grattan, K. T. V., Palmer, A. W. and Weir, K.: "The optimized wavelength combinations of two broadband sources for white light interferometry", J. Lightwave Technol., vol. 12, No. 5, pp. 909-916, 1994.
10. Chen, S., Grattan, K. T. V., Meggitt, B. T. and Palmer, A. W.: "Instantaneous fringe-order identification using dual broadband sources with widely spaced wavelengths", Electron. Letts., vol. 29, No. 4, pp. 334-335, 1993.
11. Meggitt, B. T.: "Fiber optic white-light interferometric sensors", Ch. 9, pp. 278, In: "Optical Fiber Sensor Technology", Eds. Grattan, K. T. V. and Meggitt, B. T., Chapman & Hall, London, 1995.
12. Yakowitz, S. : "An introduction to numerical computations", Ch.6, 2nd ed., New York, Macmillan, 1989.
13. Cox, M. G. and Hayes, J. G.: "Curve fitting: a guide and suite of algorithms for the non-specialist user", report NAC26, National Physical Laboratory, Middlesex, 1973.
14. Chen, S., Palmer, A. W., Grattan, K. T. V. and Meggitt, B. T.: "Digital signal-processing techniques for electronically scanned white light interferometry", Applied Optics, vol. 31, No.28, pp. 6003-6010, 1992.
15. Dandliker, R., Zimmermann, E. and Frosio, G.: "Noise resistant signal processing for electronically scanned white-light interferometry", 8th Optical Fibre Sensors Conference, W3.2, pp. 53-56, 1992.
16. Romare, D., Rizk, M. S., Grattan, K. T. V. and Palmer, A. W.: "Superior lms-based technique for white-light interferometric systems", IEEE Photon. Tech. Letts., vol. 8, pp.104-106, 1996.

17. Marshall, R. H., Ning Y. N., Palmer, A. W. and Grattan K. T. V.: "Dispersion in an electronically-scanned dual-wavelength low-coherence interferometer", Optics Comms., vol. 138, pp.136-142, 1997.

18. Schott glass, Manufacturer's Data Sheet #3111e (also partially quoted in Melles Griot :"Optics Guide 5", Ch.3, pp.8-11, 1990).

Chapter 5

Bulk Mach-Zehnder configuration

5.0. Introduction

In this chapter, an experimental and theoretical evaluation of a novel Mach-Zehnder interferometer (MZI) is reported. This MZI is composed of bulk optical components, but yields a higher degree of stability than other configurations of such a system discussed. An appropriate analysis of the operation of this bulk MZI configuration is presented and contrasted with other bulk optical schemes. The system was implemented for the measurement of displacement. In order to provide an accurate displacement measurand, a linear translation PZT stage was employed to scan accurately the mirror position. Various methods of identifying the central fringe were employed in order to achieve absolute displacement measurement resolutions of 40nm.

When employing any sensing system in a practical application environment, a number of important factors have to be considered. Principally, the system has to be capable of operating in an industrial environment, such that the system specification will depend strongly upon the constraints of the application for which it is to be used. Generally, the main requirements are that the system should be compact and robust. A

robust design will have the desirable effect of providing greater mechanical stability, allowing greater sensitivity and requiring less regular re-calibration.

The novel Mach-Zehnder configuration introduced in the preceding discussion has been shown to provide accurate measurements (of displacement). However, the configuration employed discrete optical components, which may provide long-term stability problems, due to the fact that the components are discrete and are individually mounted. In addition, the system suffered from the problems of dispersion, due mainly to the characteristics of the beamsplitter that was employed. However, these dispersive effects only yielded problems when dual wavelength sources were employed, as shown

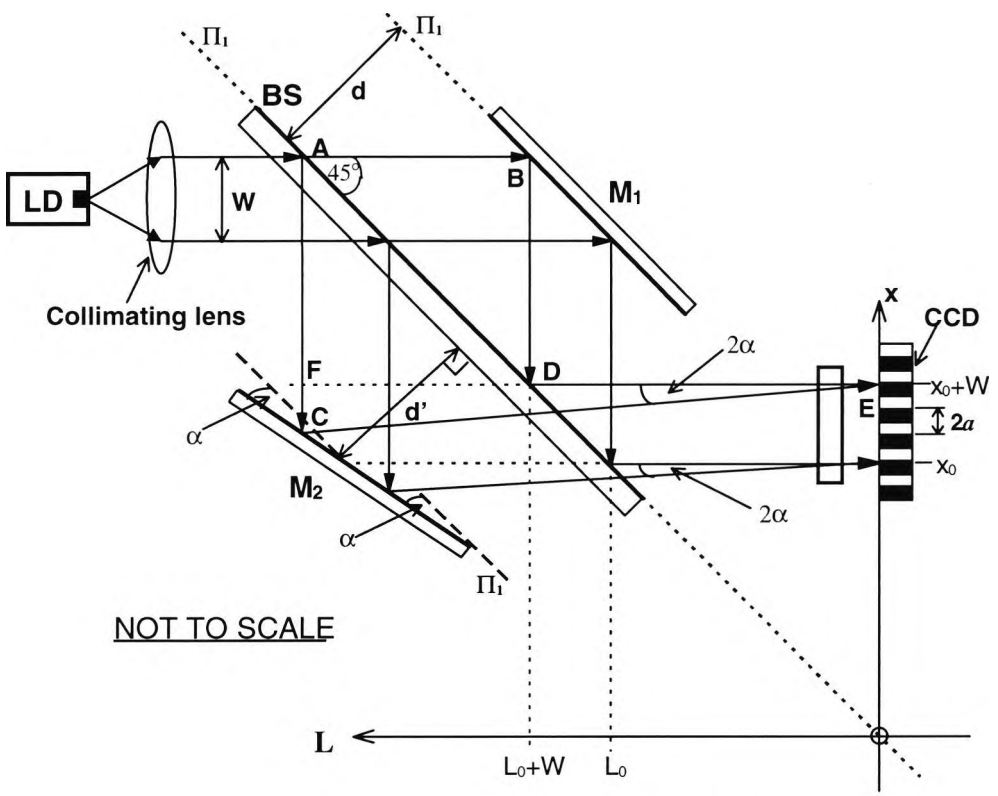

Figure 5.1: Mach-Zehnder interferometric configuration

in Section 4.4. These dispersive effects were exacerbated due to the use of a non-symmetrical beamsplitter, as shown in Figure 5.1. One of the beams passes through the beamsplitter, BS, three times whilst the other beam only passes through it once, which leads to an increase in the dispersion problem. This configuration could have been modified in order to reduce these effects by cutting the beamsplitter, BS, in half

and reversing one side of it, a shown in Figure 5.2. Here, each beam only passes through it once.

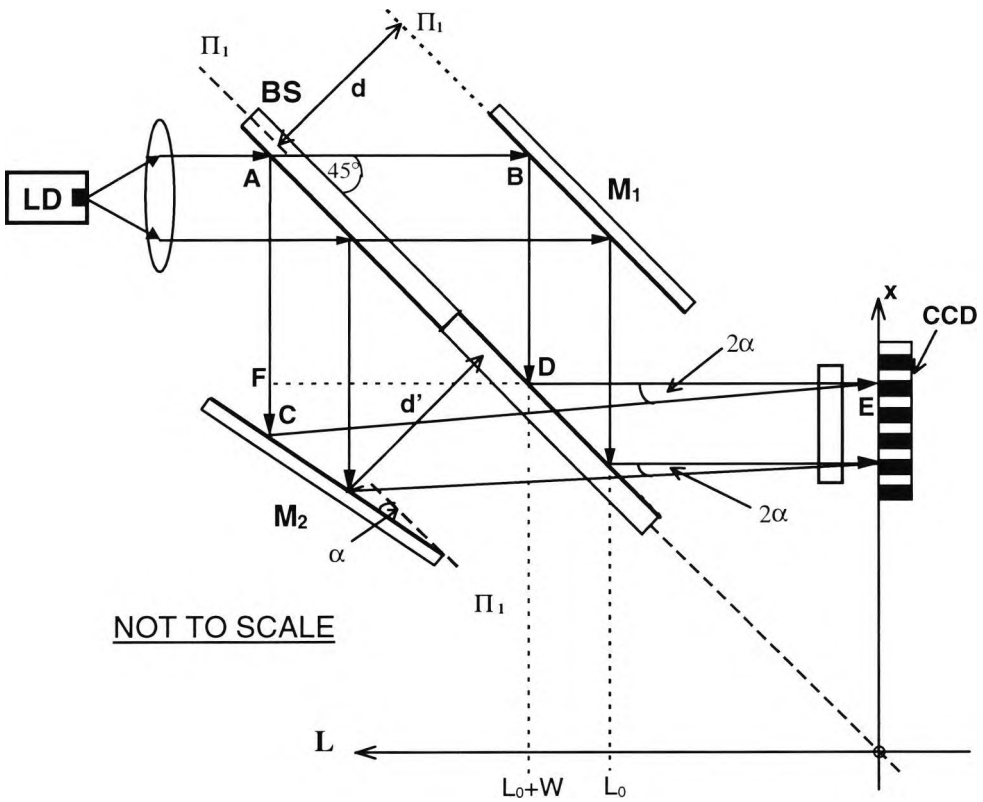

Figure 5.2: Dispersion compensated Mach-Zehnder interferometer

Although this modified MZI reduces the effects of optical dispersion, the relative geometry of the sensor is increased slightly. In many industrial applications, a more compact design is required. One of the major requirements is to have a compact "off-the-shelf" design, based on readily available optical components, such as that using a Wollaston prism [1,2].

A Wollaston interferometer [2,3] is composed of two birefringent wedges with their optical axes at right angles, both to each other and to the optical axis of the prism. Normally incident light is resolved in the first wedge into ordinary (o-ray) and extraordinary (e-ray) components that propagate co-linearly with different phase velocities, as shown in Figure 5.3.

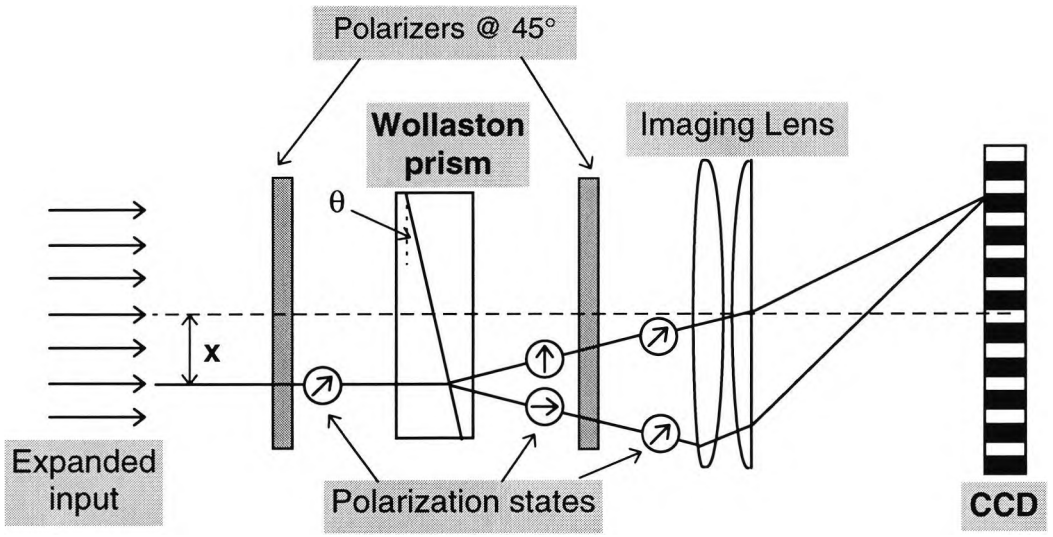

Figure 5.3: Wollaston prism configuration

At the interface between the wedges, the components are interchanged so that the o-ray propagates along the path of an e-ray and vice versa. The effective path difference is dependent on the lateral position within the Wollaston prism. In the centre of the prism, this effective path difference introduced between the orthogonal polarizations in the first wedge is cancelled due to the result of an equal and opposite effective polarization of the beams in the second wedge. Away from the central position, the effective path difference, $\Delta L(x)$, is proportional to the displacement, x, and is given by [4]

$$\Delta L(x) = 2x\left(n_e - n_o\right)\tan\theta \tag{5-1}$$

where n_e and n_o are the ordinary and extraordinary refractive indices and θ is the internal angle of the interface between the two wedges. The two polarization components undergo a symmetrical splitting at the wedge interface. The deviation angle, α, between the two beams depends on θ and the birefringence of the prism material, and is given by [3]

$$\alpha = 2\left(n_e - n_o\right)\tan\theta \tag{5-2}$$

From Figure 5.3, the input light is linearly polarized at 45° to the optical axes of the Wollaston prism, giving equal transmission intensities for the horizontally and vertically polarized components. A second 45° polarizer placed beyond the Wollaston prism analyzes the transmitted light, and the two orthogonal polarizations are permitted to interfere one with the other. The varying path difference across the prism results in the formation of interference fringes localized at a plane within the prism, which is imaged onto a linear CCD detector.

Although this Wollaston-based configuration has the benefits of being compact and robust, it nevertheless requires the use of polarizers which need to be very accurately aligned. Thus, a more practical design amendment to the Mach-Zehnder configuration was made, which was introduced in the earlier chapters. Such a modified Mach-Zehnder interferometer has the advantages of being composed entirely of bulk optical components, whilst not requiring the use of polarizers. Thus this new configuration yields all the benefits of using a bulk-optical based interferometer (i.e., compactness and robustness), without having the penalty of requiring polarizers, which are needed in Wollaston-based schemes. This is a major advantage of this over other proposed systems, such as those described [1,2,3].

A Mach-Zehnder interferometer (MZI) configuration- composed entirely of bulk optical components - employed as a recovery interferometer in an extrinsic fibre-optic electronically scanned white-light interferometer is reported [5]. This so-called "bulk-optical" implementation of a MZI has the advantages of being very simple and compact, inexpensive, operates without introducing any spatial mis-overlapping, and most importantly has a high degree of stability, due to it being composed entirely of bulk optical components.

5.1. Theoretical considerations

This novel MZI configuration consists of two cubic beamsplitters and two right-angled prisms [5], as shown in Figure 5.4. The expanded beam (of width W), is incident onto the beamsplitter (BS1) at 45° and is then divided into two. After being reflected at the hypotenuse face of the right-angled prisms, RAP1, and RAP2, the beams are then recombined via a beamsplitter, BS2. The two spots of the beams overlap with each other on a linear CCD array, generating a set of spatially distributed interference fringes along the CCD, which then can be detected using the pixels of the CCD array.

In this work, a Fabry-Perot interferometer (FPI) was used as the SI and a MZI as the RI. For a dual wavelength combination source, assuming that the system has negligible dispersion, the intensity, I(x), of the dual interferometric configuration along the sensing CCD can be expressed as

$$I(x) = P(x)\left\{A + 2B\left\{\cos\left[k_1\left(\Delta L_R(x) - \Delta L_S\right)\right]\exp\left[-\left(\left(\Delta L_R(x) - \Delta L_S\right)/L_{C1}\right)^2\right] + \cos\left[k_2\left(\Delta L_R(x) - \Delta L_S\right)\right]\exp\left[-\left(\left(\Delta L_R(x) - \Delta L_S\right)/L_{C2}\right)^2\right]\right\}\right\} \quad (5\text{-}3)$$

where P(x) is the beam intensity profile; $k_1=2\pi/\lambda_1$; λ_1 is the first source wavelength; $k_2=2\pi/\lambda_2$; λ_2 is the second source wavelength; L_{C1} is the coherence length of source 1; L_{C2} is the coherence length of source 2; $\Delta L_R(x)$ is the OPD induced in the MZI between the two beams at the point x, where the intensity is detected by the CCD; and ΔL_S is the OPD induced in the FPI, is given by $2d_f$, where d_f is the separation of the FPI mirrors. A and B are given by $(1-r_1)^2 r_1^2\left(r_2^2 + r_3^2\right)$ and $(1-r_1)^2 r_1^2 r_2 r_3$ respectively, where r_1 is the reflection coefficient of beamsplitters BS1 and BS2, and r_2 and r_3 are the reflection coefficients of RAP1 and RAP2 respectively.

The OPD between the two beams along the CCD is introduced by the two right-angled prisms, where the hypotenuse face of RAP1 is parallel to the beamsplitters,

whilst RAP2 is inclined at an angle, α, to the beamsplitters, as shown in Figure 5.4, where the distance p and angle α are defined. Using the crossing point between the beamsplitter, BS2, and the CCD as the co-ordinate origin with the x-axis set along the CCD array, the OPD, $\Delta L_R(x)$, between the two beams at a position x is given by

$$\Delta L_R(x) = (AB + BD + DE) - (AF + FC + CE)$$

$$= (2p + x) - \left(p + (x + p)\tan(2\alpha) + \frac{(x + p)}{\cos(2\alpha)} \right) \tag{5-4}$$

$$= (p + x)\left[1 - \left(\tan(2\alpha) + \frac{1}{\cos(2\alpha)} \right) \right]$$

Thus

$$\Delta L_R(x) = (p + x)\left[1 - \frac{1 + \sin(2\alpha)}{\cos(2\alpha)} \right] \tag{5-5}$$

Using simple trigonometric identities, this may be re-written as

$$\Delta L_R(x) = (p + x)\left[1 - \frac{1 + 2\sin\alpha\cos\alpha}{\cos^2\alpha - \sin^2\alpha} \right]$$

$$= (p + x)\left[1 - \frac{\sin^2\alpha + \cos^2\alpha + 2\sin\alpha\cos\alpha}{\cos^2\alpha - \sin^2\alpha} \right]$$

$$= (p + x)\left[1 - \frac{(\sin\alpha + \cos\alpha)^2}{(\cos\alpha + \sin\alpha)(\cos\alpha - \sin\alpha)} \right] \tag{5-6}$$

$$= (p + x)\left[1 - \frac{(\sin\alpha + \cos\alpha)}{(\cos\alpha - \sin\alpha)} \right]$$

$$= (p + x)\left[\frac{(\cos\alpha - \sin\alpha) - (\sin\alpha + \cos\alpha)}{(\cos\alpha - \sin\alpha)} \right]$$

$$\therefore \Delta L_R(x) = \frac{-2\sin(\alpha)}{(\cos(\alpha) - \sin(\alpha))}(p + x) \tag{5-7}$$

where p is the length, width and height of beamsplitters BS1, BS2; x is the value on the x-axis along the CCD array; and α is the inclination angle of RAP2 with respect to beamsplitters BS1 and BS2.

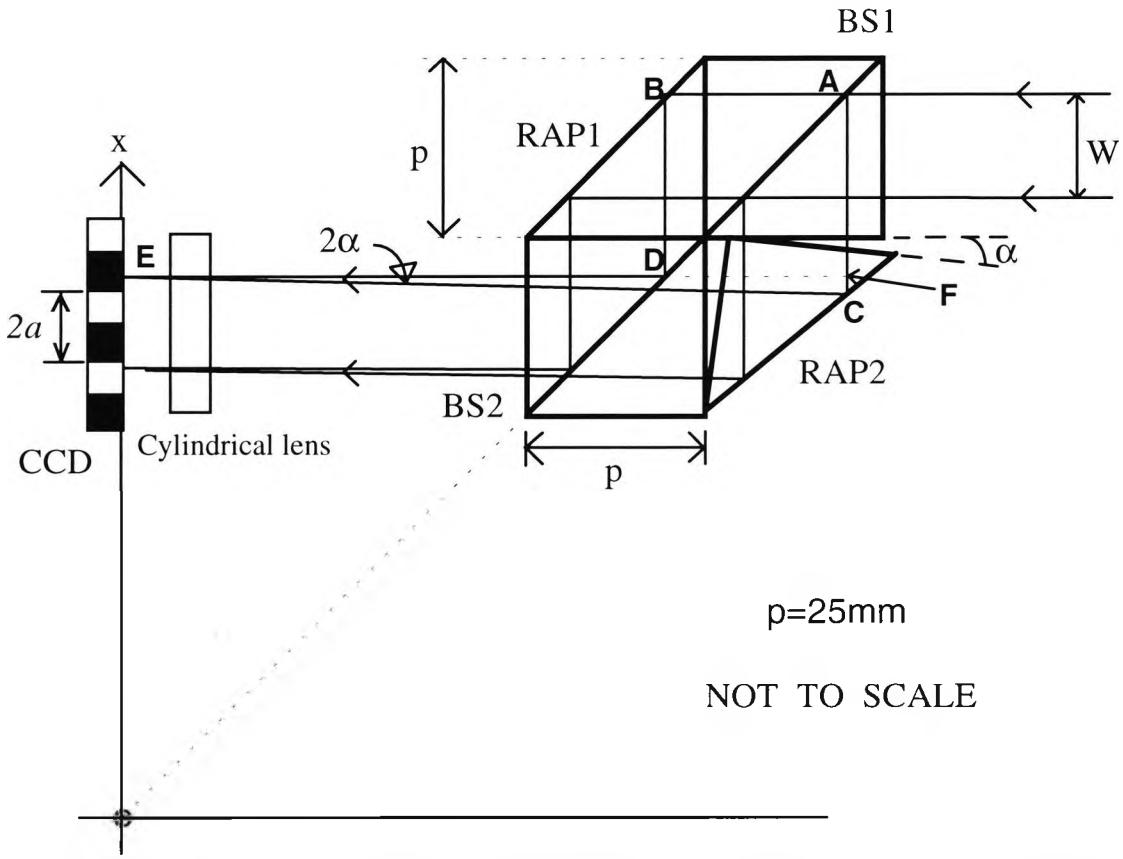

Figure 5.4: The bulk-optic Mach-Zehnder configuration used in this work. RAP1, RAP2 are right-angled prisms; BS1, BS2 are cubic beamsplitters, W is the beam-width, α is the inclination angle and CCD is the linear CCD detector

5.2. Experimental arrangement

5.2.1. FPI Considerations

The alignment and subsequent operation of the modified FPI is a major consideration in achieving good system design. In order to produce high quality, good visibility, electronically-scanned fringes, the visibility of the FPI fringes must be optimised. Apart from the simple alignment considerations, the visibility of the FPI is

highly dependent upon the reflectances of the FPI mirrors need. In order to test the quality of the FPI alignment, without disturbing the MZI setup, the system was modified as shown in Figure 5.5. By using an additional beamsplitter, BS4, and a lens, the quality of the operation of the FPI could be measured without changing the alignment of the MZI. After completion of the FPI alignment, the lens and BS4 are simply removed.

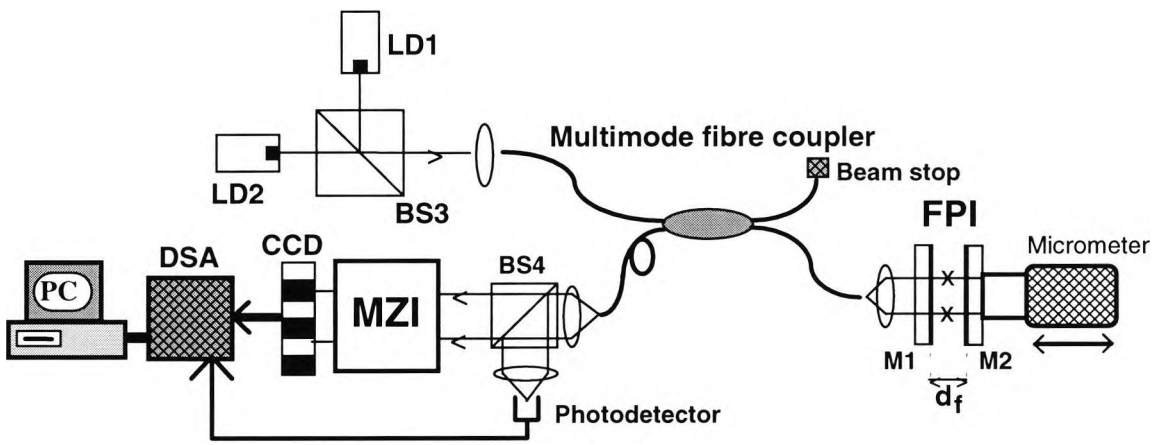

Figure 5.5: Schematic representation of the Fabry-Perot interferometer (FPI) alignment configuration. MZI is the Mach-Zehnder interferometer; M1 and M2 are 50% reflectance mirrors; LD1 and LD2 are multimode laser diodes; BS3, BS4 are cubic beamsplitters; CCD is a line charge-coupled device detector; DSA is a digital storage adaptor and d_f is the FPI mirror separation.

The FPI was configured with both mirrors, M1 and M2 having reflectances, $R_1=R_2=0.5$. For this experiment, the FPI mirrors had to be separated by a distance which would be within the coherence length of the source. This is due to the fact that the operation of the FPI is best observed when the FPI is operating alone, producing interference fringes. At very low drive currents (typically <30mA), the laser diodes will be operating below threshold, yielding a very short coherence length. However at such low coherence lengths (typically <50μm), the FPI mirrors would virtually be in contact with each other, producing erroneous results. For this experiment, the drive current was increased so that the coherence lengths were increased to ~200μm, and hence the mirror separation could be set to be within 100μm. A function generator was used to modulate the PZT in order to modulate the FPI mirror, M2, with a 10Hz sinusoidal modulation. The resultant fringes were observed on the CRO and captured onto the PC via the DSA, as shown in Figure 5.6.

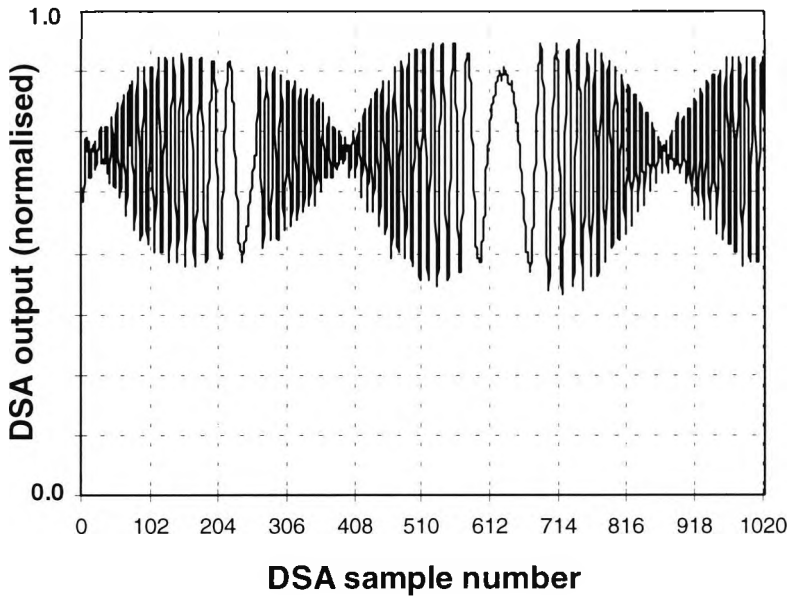

Figure 5.6: FPI fringe profile for $R_1=R_2=0.5$

This produced sufficiently good fringe visibility and this combination of mirrors was adopted for the remainder of this work.

5.2.2. Complete Experimental Arrangement

In order to observe the performance of this new Mach-Zehnder configuration, a careful experimental analysis was performed, as shown in Figure 5.7. The two multimode laser diode sources used, LD1 and LD2, had coherence lengths of ≈50μm. Light from the sources was launched along a 50μm core diameter multimode fibre-optic coupler, via beamsplitter BS3. The light passes through the coupler to the FPI. The two FPI mirrors were separated by a distance, d_f, providing an OPD of $2d_f$. The output of the FPI travels back along the same path through the coupler to the MZI. Again, this arm of the coupler has a 30 metre fibre extension fused onto it in order to reduce the effects of modal noise (as discussed in Section 4.2). This output is expanded to a beam of width, W, and is then incident onto the MZI beamsplitter, BS1, as before. The MZI generates a set of spatially distributed interference fringes along the 1024 pixel CCD, and a cylindrical lens was used to focus the incident optical output power

onto the detector array. The PC used for signal processing was interfaced to the CCD via an 8-bit digital storage adapter (DSA).

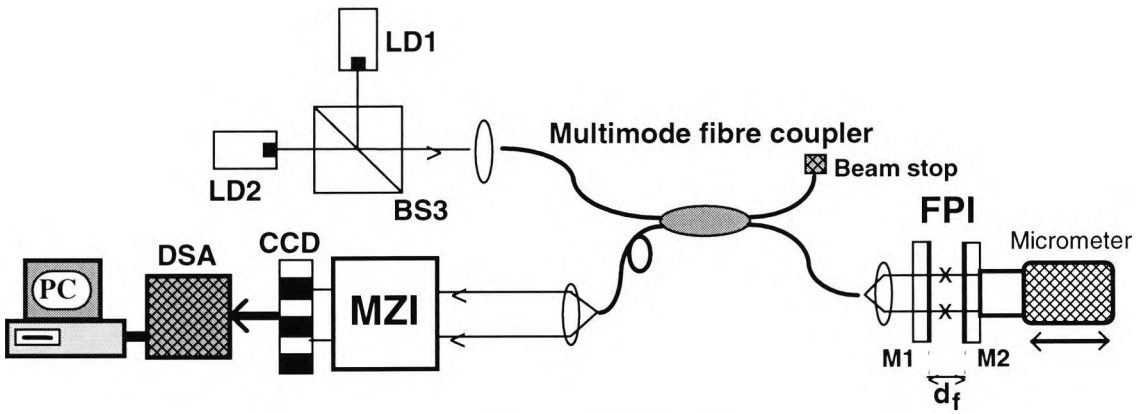

Figure 5.7: Schematic of the complete experimental arrangement. MZI is the Mach-Zehnder interferometer; M1 and M2 are 50% reflectance mirrors; LD1 and LD2 are multimode laser diodes; BS3 is a cubic beamsplitter; CCD is a line charge-coupled device detector; DSA is a digital storage adaptor and d_f is the Fabry-Perot interferometer (FPI) mirror separation.

5.3. Experimental results

The configuration employed two multimode laser diode sources (LD1 and LD2), having mean source wavelengths of $\lambda_1 = 0.685\mu m$ (Toshiba TOLD9140) and $\lambda_2 = 0.780\mu m$ (Sharp LTO23MD) respectively. The two sources can be driven to provide an output power of up to 5mW each. However, the two sources were driven below their threshold currents in order to reduce their coherence lengths (to $\approx 50\mu m$), which in reduced their respective output powers to 1.2mW. However, this source output power was sufficient to provide an incident optical power of 65μW on the CCD detector, which is sufficient to produce good visibility fringes. The relative fringe visibility of the central, with respect to the adjacent fringes, was enhanced by using this combination of the two broadband sources (see Section 4.3.1.). This combination yields a modulation wavelength, λ_m, of approximately 11.24μm. With the reasonable assumption that the coherence lengths of the sources are identical (i.e. $L_{C1} \equiv L_{C2}$), then the average source wavelength, λ_a ($\equiv 2\lambda_1\lambda_2/(\lambda_1+\lambda_2)$) yields a value of 0.729μm, such that λ_m is equivalent to approximately 15.4 fringes.

The operating range is determined by the inclination angle, α, which is mainly dependent upon the number of pixels per fringe and to a lesser extent on the fringe visibility. In order to reconstruct the entire fringe interferogram data with no fringe distortion, a fringe must be sampled by at least 2 CCD pixels. The number of pixels per fringe, p_f, thus may be expressed as

$$p_f = \frac{\lambda_a}{2a\sin(2\alpha)} \tag{5-8}$$

where a is the pixel width (≡pixel space), as shown in Figure 5.4. From equation (5-8), the sampling rate cut-off point (at two pixels per fringe) occurs at an angle, α, of 0.40°, for $\lambda_1 = 0.685\mu m$ and $\lambda_2 = 0.780\mu m$. Hence, the MZI has an effective angular range of $0.0<\alpha<0.4°$. Figure 5.8 shows a plot of the number of pixels per fringe versus the inclination angle for this wavelength pairing.

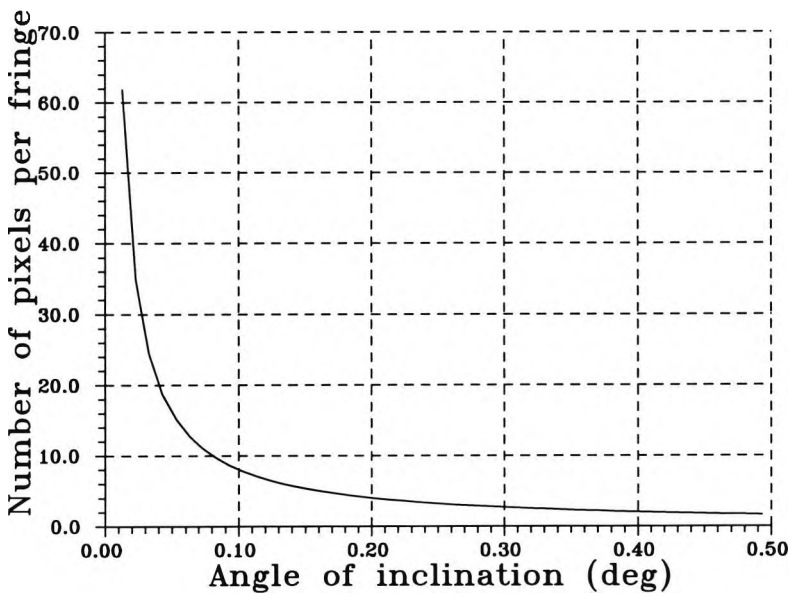

Figure 5.8: Simulation of the relationship between the mean number of pixels per fringe and inclination angle for λ_1=0.685μm and λ_2=0.780μm

The effects of the beam intensity profile were successfully eliminated from the fringe data using the pixel-by-pixel division technique [5], yielding the processed fringe pattern, F[j], as shown before in Section 3.5.2., where j (=1,2,.., M) is the pixel number along the CCD array. The beam intensity profile, P[j], is pre-stored in the computer. Figure 5.9(a) shows the pre-processed fringe data obtained using ≈40 pixels per fringe (i.e. at $\alpha \approx 0.02°$), superposed upon the background beam intensity profile. Figure 5.9(b) shows the results of the pixel-by-pixel division, yielding the processed fringes, which are in good agreement with the simulated fringe interferogram (Fig. 5.10), obtained for a similar set of conditions to these considered experimentally.

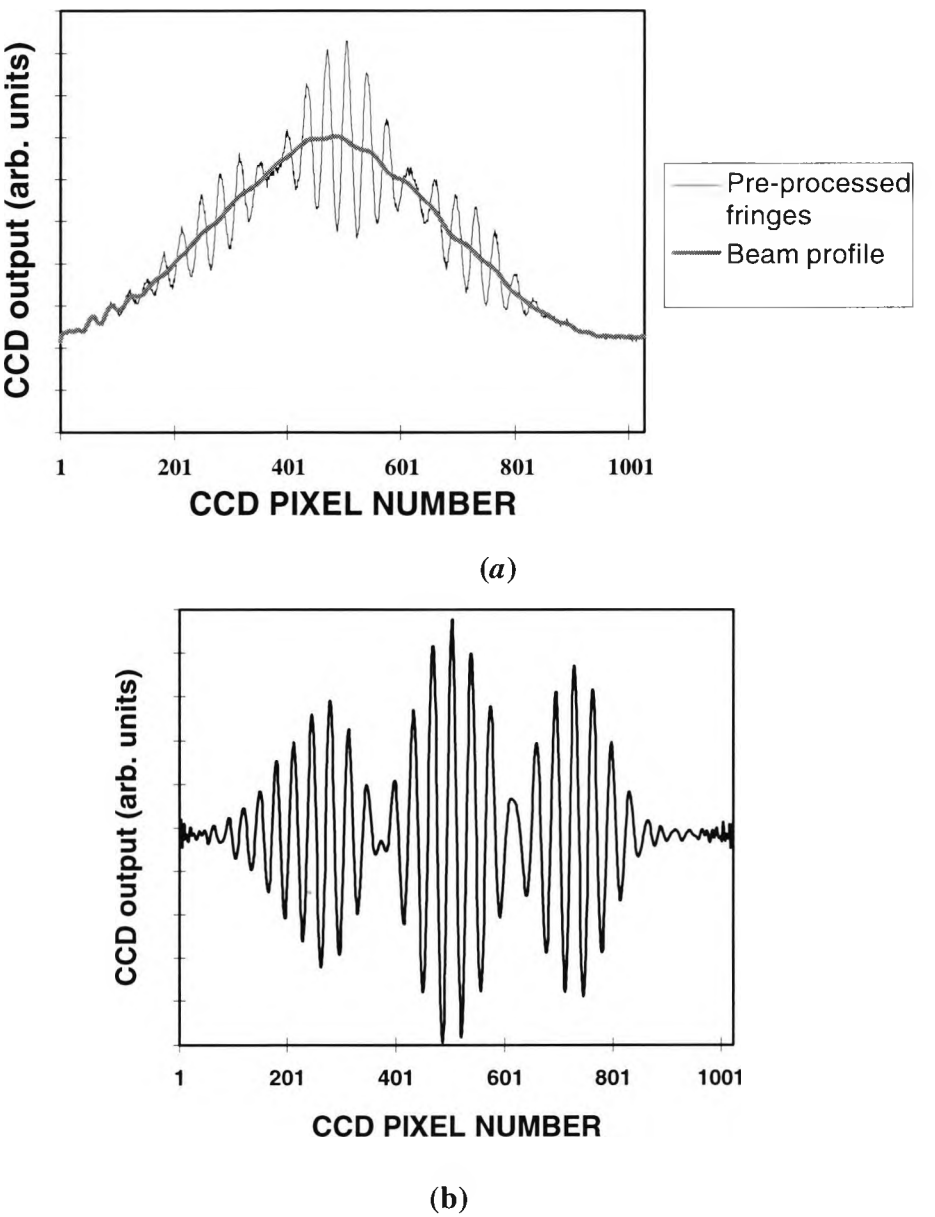

Figure 5.9: Experimental fringe interferograms for λ_1=0.685 μm and λ_2=0.780 μm, at $\alpha \approx 0.02°$; (a) shows the pre-processed fringes and the background beam profile; (b) shows the processed fringes with the background beam profile eliminated using pixel-by-pixel division and the noise reduced using low-pass filtering.

The system "noise" (which includes the effect of optical aberrations and electronic noise and occurred mainly due to noise in the CCD) was reduced by the use of a low-pass filter algorithm, which successfully reduced the effects of these noise sources, as shown in Figure 5.9(b).

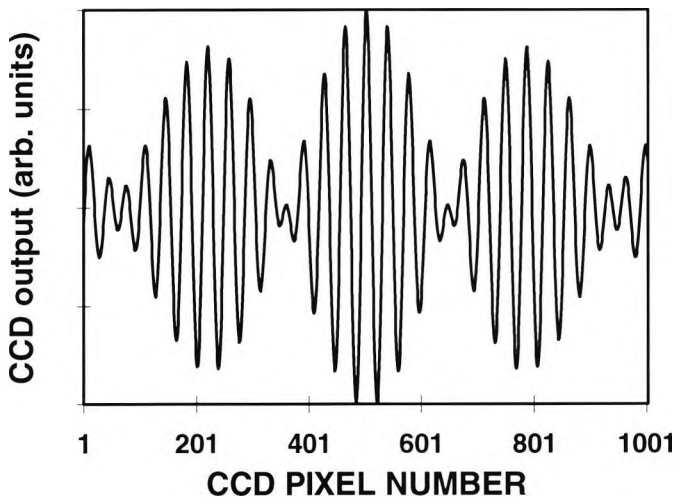

Figure 5.10: Simulated fringe interferogram for λ_1=0.685 μm and λ_2=0.780 μm at α=0.02°.

This low pass filter algorithm was based upon a least squares fitting technique (which was introduced in Chapter 4). A conventional least-squares algorithm could have been employed as an adaptive line enhancer in order to estimate and thus eliminate the noise from the interferogram. Other authors [6,7] have employed such adaptive filtering techniques in order to improve the signal-to-noise ratio. However, these techniques are computationally extensive and are also more sensitive to ill-conditioning [7] which occurs when the initial filter coefficients are not pre-selected correctly, leading to non-convergence of the filter algorithm. This least-squares fit technique employed here, simply fits a kth order Chebyshev polynomial to the interferogram data. The polynomial order is chosen to be sufficient to follow the variations in the fringes and is too low to track the higher frequency noise variations, providing an inherent time-domain low-pass filtering mechanism.

The desired filter order, k, is dependent upon the number of pixels per fringe, as shown in Figure 5.8. In this case, for ~ 40 pixels per fringe, a 100th order fit was employed. The least-squares fit provided a very good approximation of the "noise-free" interferogram. This least squares fitting technique successfully reduced the effects of the system noise, as shown in Figure 5.9(b). However, the comparative simplicity of this technique of noise reduction must be offset against the relatively high order polynomials which need to be used for interferograms having smaller fringe separations. In these instances, more conventional adaptive filtering techniques are more advantageous to use due to their superior performance at smaller fringe separations [6].

5.4. Displacement measurements

It is well known that white-light interferometric sensing systems have been used extensively, in recent years, for the measurement of displacement [8, 9, 10]. In order to obtain accurate displacement measurements, a more sensitive method of translating the FPI mirror had to be employed. Thus, the micrometer (as shown in Figure 5.7) was replaced by an accurate piezo-electric transducer (PZT) stage, in order to obtain an accurate value of the displacement measurand. A Queensgate System 2000 PZT [11] was employed for this purpose. The System 2000 unit employs closed-loop capacitance position measuring technology yielding high linearity and sub-nanometre noise and repeatability. The modules included in the system are nanosensor controllers, translator drive amplifiers, servo modules and PZTs. The PZT (MTP105) provides 105μm full-scale translation. The nanosensors provide non-contact closed-loop control (~0.1nm resolution). The DM100 high voltage amplifier drives the PZT and can be controlled from an analogue or 14-bit digital source. The SM Servo module closes the loop between the Nanosensors and the PZT. Using the SM, a PZT can be positioned to the accuracy to which the Nanosensor can measure, eliminating the hysteresis of the PZT. The position signal generated in the PZT is compared with the required command position in the SM module and the resultant error signal is integrated and output to the DM100 translator module, as shown in Figure 5.11.

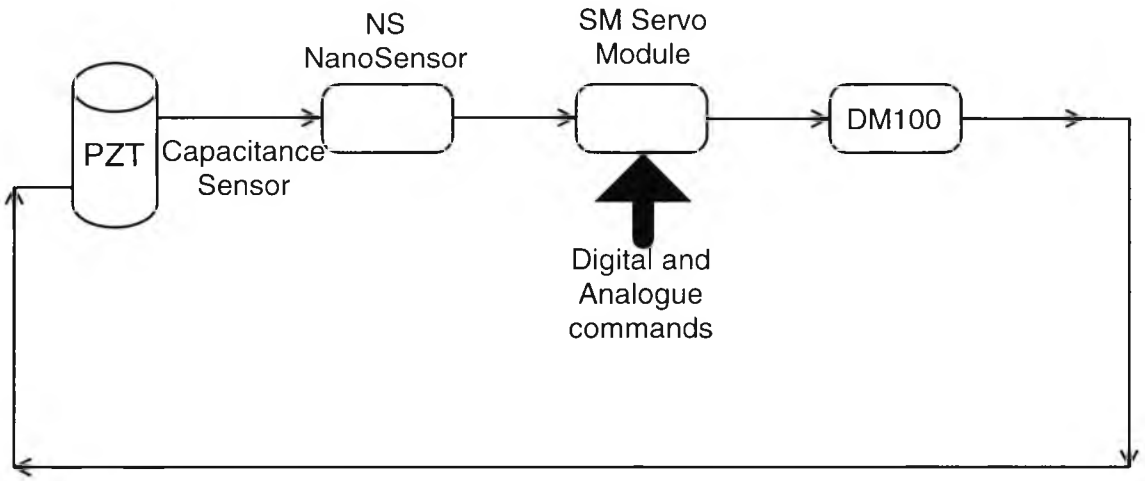

Figure 5.11: Schematic representation of System 2000 servo configuration

5.4.1. Displacement Measurement Results

The PZT was stepped in increments of 1μm across the full-scale range of the system (which was ≈10μm at α≈0.02°). As expected, when the FPI mirror was scanned, the resultant position of the central fringe on the CCD scanned accordingly. The threshold technique was shown to produce larger measurement errors than the LS technique - which is what would be expected due to the fact that the LS technique uses the entire data set in order to determine the central fringe position, whilst the thresholding technique only utilises one data point. From the experimental results, the threshold technique was accurate to within ±0.10μm, whereas the least-squares curve fitting technique produced measurements which were accurate to ±20nm, as illustrated in Figure 5.12. The errors were relatively very small, so no error bars were shown on Figure 5.12 since they would not have been visible on the Figures. The comparative degrees of coupling equality of the outputs of the two laser diode sources into a multimode fibre depends, on the difference in their respective wavelengths. Effects occur due to the presence of chromatic aberration [13] in the lens, arising from the index of refraction variation with wavelength. For example, using λ_1=780nm and λ_2=685nm yields a wavelength difference, $\Delta\lambda$=95nm, where the focal lengths of each wavelength will differ as shown schematically in Figure 5.13.

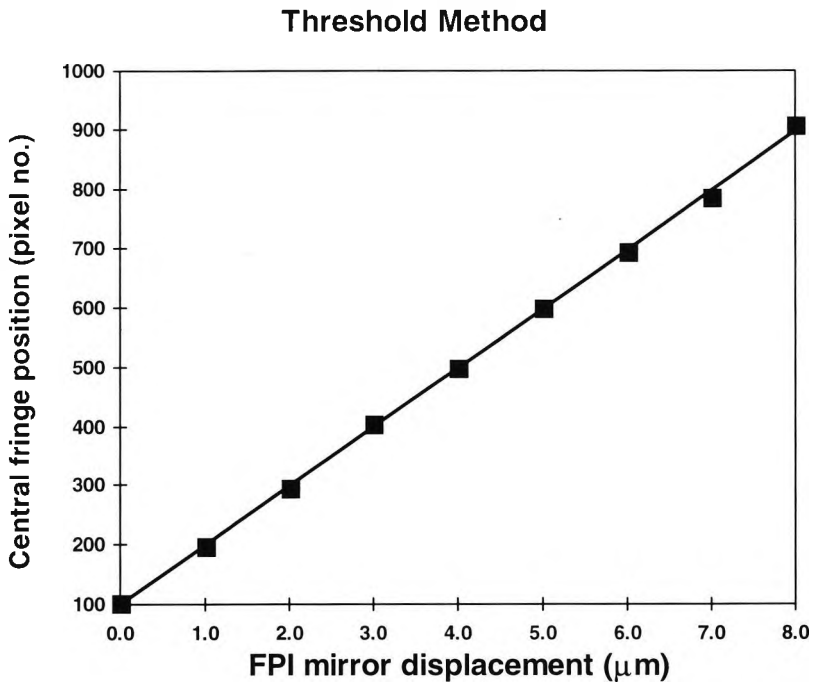

(a)

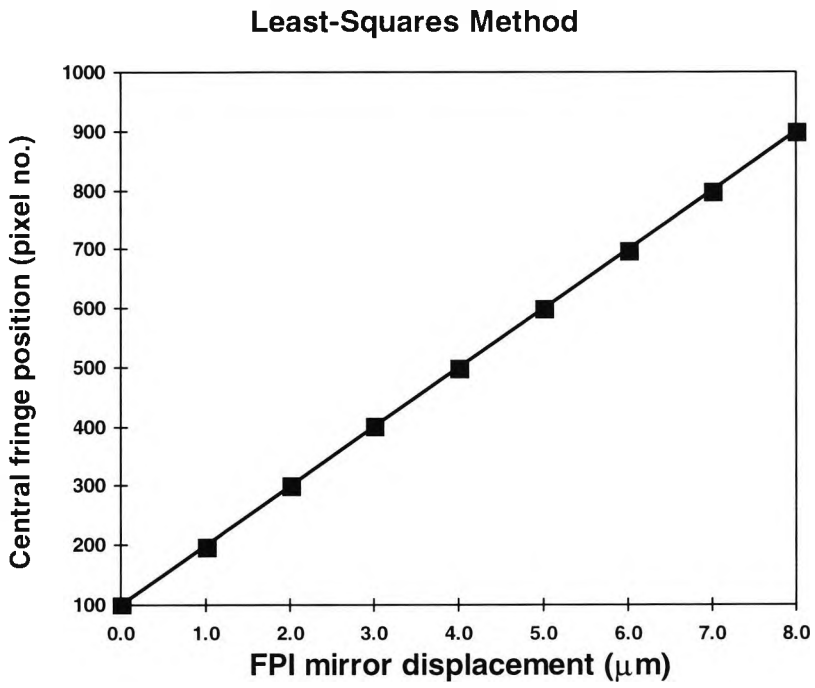

(b)

Figure 5.12: Comparison of the system transfer function for (a) threshold, and (b) least-squares method

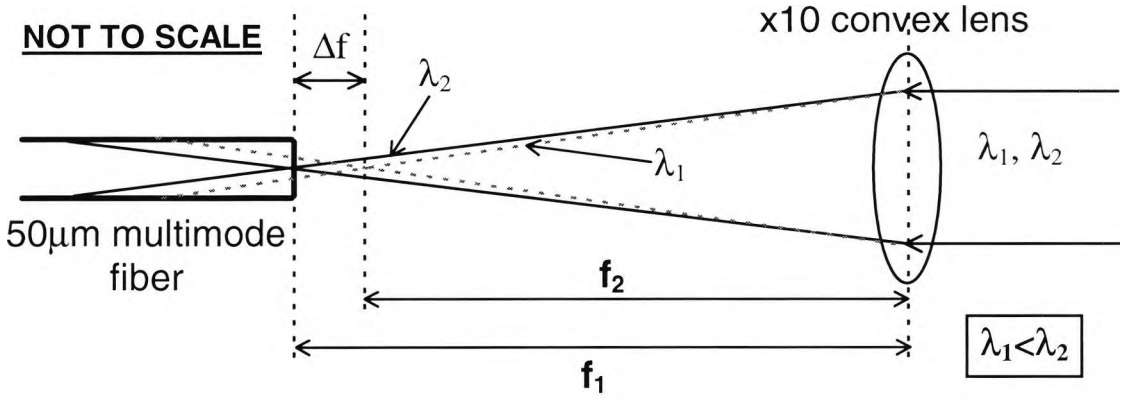

Figure 5.13: Schematic showing the differing focal lengths of each source wavelength

Due to the difference between the two wavelengths, $\Delta\lambda$, there will thus be differing focal lengths, due to the longitudinal chromatic aberration, $\Delta f=f_1-f_2$, such that $\Delta\lambda \propto \Delta f$. Hence, for a wavelength pairing of λ_1=780nm and λ_2=810nm different from that considered above, then $\Delta\lambda$ is reduced from 95 to 30nm, which produces a corresponding reduction in the change in the focal length, Δf, which results in a greater equality of the amount of light being coupled from each source. In addition, a lateral (transverse) chromatic aberration [13] will also be present, which leads to a difference in the image height, and thus this can produce a degradation in the equality of the fringes from each source. The ill-effects of chromatic aberrations may also be improved slightly by using an achromatic doublet [13], which takes the form of two elements with different dispersion characteristics, so that the weaker negative element can balance the effects of the stronger positive element. This compensation method is not readily available with cylindrical lenses [13,14] and hence it was more advantageous simply to reduce the difference between the two wavelengths.

Thus this displacement measurement experiment was repeated, with however, the wavelength pairing being changed. The previous wavelength pairing of λ_1 = 0.685 μm and λ_2=0.780μm provided a modulation wavelength, λ_m, of ~11.25μm, and an average source wavelength, λ_a, of ~0.729μm, such that λ_m is equivalent to approximately 15.4 fringes. In this new experiment, the first mean source wavelength, λ_1, was changed to 0.810μm (Sharp LT010MD), whilst λ_2 remained unchanged. This provided a new average source wavelength, λ_a, of ~0.795μm and a modulation wavelength, λ_m, of ~42.12μm, such that λ_m is equivalent to approximately 53 fringes.

The MZI was set at an inclination angle of ≈0.14°, providing a sampling rate of approximately 6 pixels per fringe. As before, the background beam profile intensity was pre-stored in the computer and was then eliminated on-line from the detected interferograms using pixel-by-pixel division. Figure 5.14 shows the processed fringe interferograms obtained when this beam profile is eliminated.

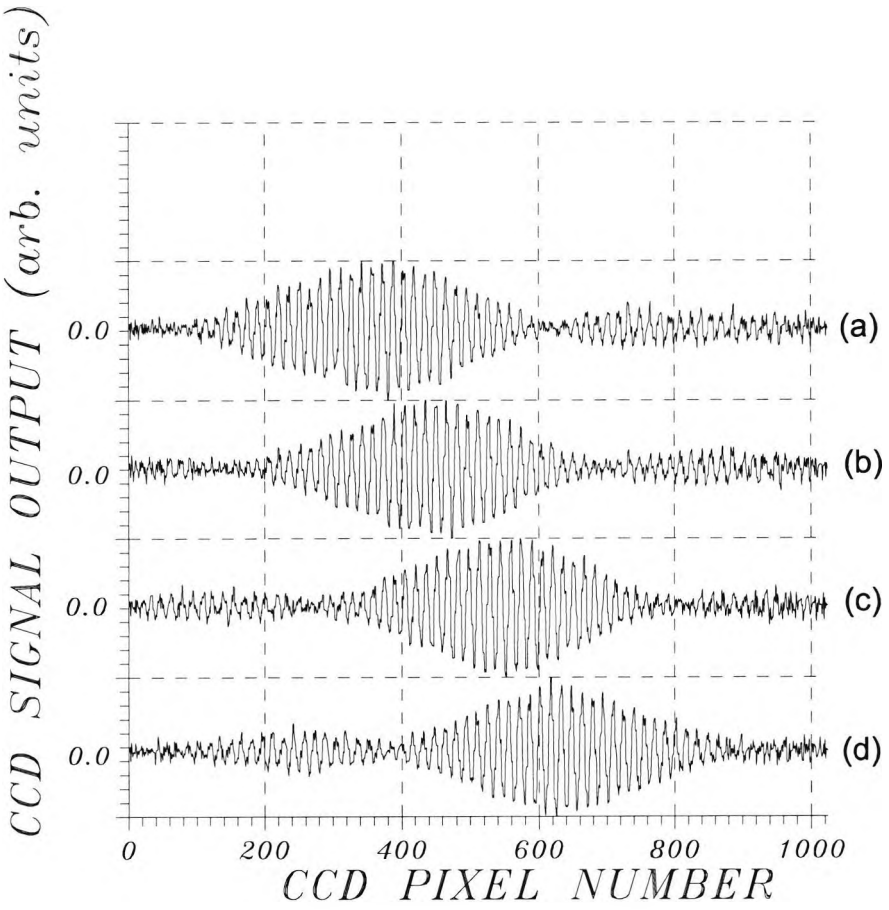

Figure 5.14: Experimental results of the CCD output (arbitrary units) versus the CCD pixel number at an inclination angle, α, ≈0.14°, for λ_1=0.780μm and λ_2=0.810μm, highlighting the effects of scanning the FPI mirror from a -12.0μm mirror displacement position from a zero reference position (**a**); then to a -4.0μm displacement (**b**); to a +4.0μm displacement (**c**); through to a +12μm position (**d**).

One of the FPI mirrors was scanned using the PZT in order to provide the displacement to be measured. The PZT was stepped in increments of 20nm across the full-scale range of the system (which was ≈30μm at α≈0.14°). As expected, when the FPI mirror was scanned, the resultant position of the central fringe on the CCD moved

accordingly. This effect is highlighted in Figure 5.14, which shows the effects of the movement of the FPI mirror from a -12.0μm mirror displacement position from a zero reference position (Fig. 5.14(a)), then to a -4.0μm displacement (Fig. 5.14(b)), to a +4.0μm displacement (Fig. 5.14(c)), through to a +12μm position (Fig. 5.14(d)).

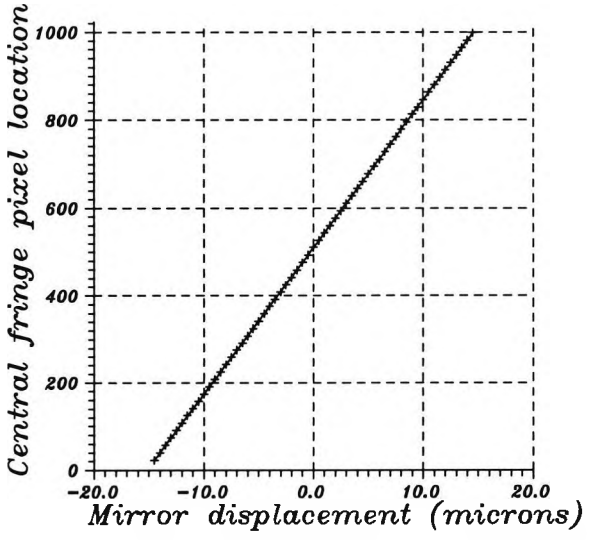

(a)

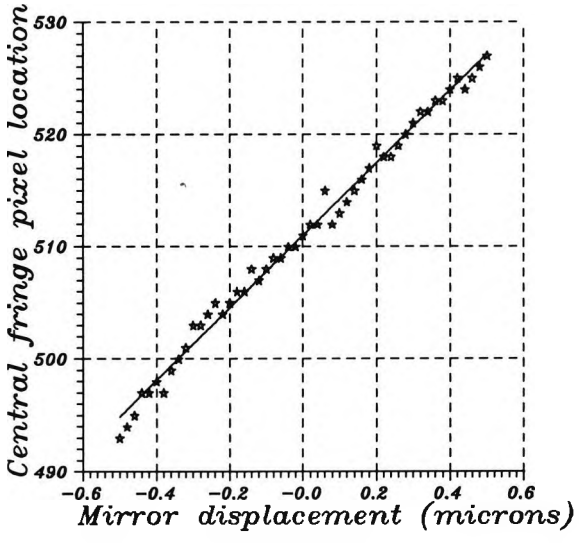

(b)

Figure 5.15:. Transfer function showing the central fringe position using the standard thresholding method versus the PZT mirror position over the full scale range ≈30μm, Fig. (a) and over a small range ≈1μm, Fig. (b).

Even with the use of dual wavelengths, the relatively high levels of system noise that are commonly experienced in all electronically-scanned systems cannot be overlooked. Thus, the system was set up to provide central fringe identification by

using the conventional means of amplitude thresholding and comparing the result of this with the use of the centroid and least-squares methods. The results of identifying the central fringe using the thresholding technique is shown in Figure 5.15. Figure 5.15(a) shows the effects of scanning the PZT mirror over the full scale range (≈30μm). Figure 5.15(b) shows an expanded portion over a smaller range (≈1μm). These results show that this basic central fringe identification technique yields a good linear transfer function response across a large range (fig. 5.15(a)), whilst providing a maximum measurement error of only 80nm over this range. This measurement error was greatly reduced by simply taking 5 interferogram measurements and averaging them. This yielded a maximum measurement error of only 50nm over this range.

The centroid technique was also used to identify the central fringe. As expected, the effects of scanning the PZT over a large range yielded a linear transfer function as before (fig. 5.15(a)). However, now the maximum measurement error was observed to have reduced to only 40nm using this technique (Figure 5.16), at the expense of reducing the measurement range to ≈20μm.

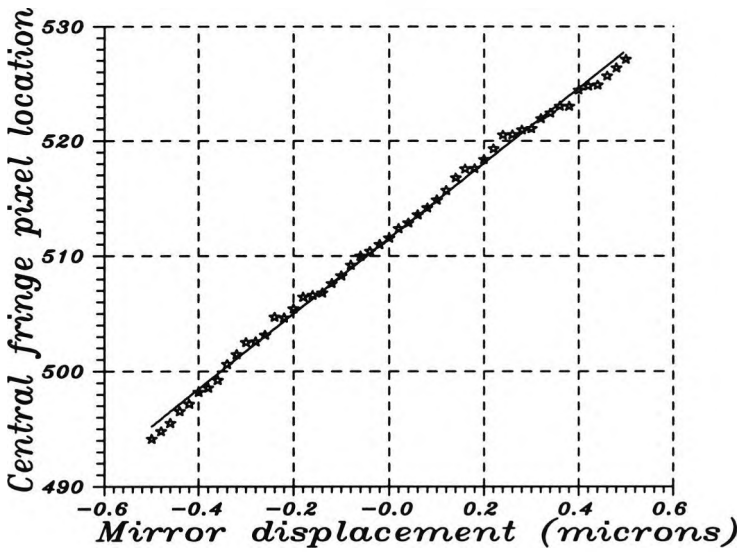

Figure 5.16: System transfer function showing the central fringe position - using the centroid method - versus the PZT mirror position over a small range ≈1μm (Figure 5.15(b)).

The least-squares technique was also used to identify the central fringe. As expected, the effects of scanning the PZT yielded a linear transfer function as was achieved using the centroid method. The linearity is shown over a small range (≈1μm) in order to highlight the resolution which can be achieved, as shown in Figure 5.17. Again, a

maximum measurement error of only 40nm was observed with this technique, but however the measurement range that could be achieved was the full scale range of ~30μm, which is a 50% increase on what was achieved with the centroid method.

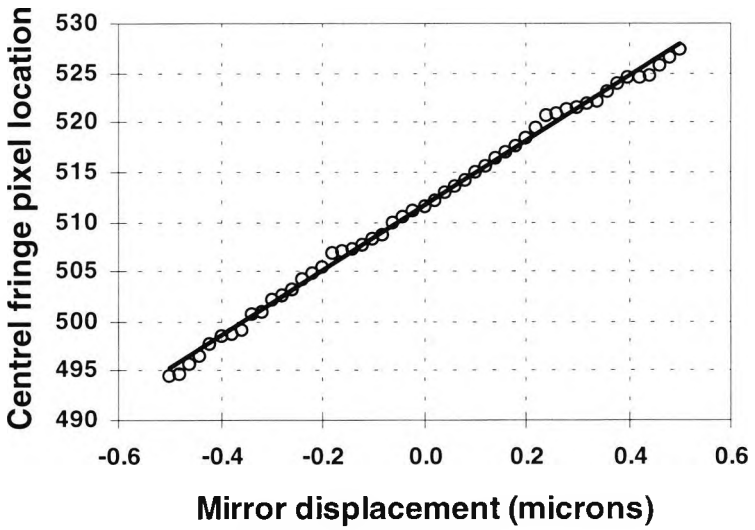

Figure 5.17: System transfer function showing the central fringe position - using the least-squares method - versus the PZT mirror position over a small range ≈1μm.

5.5. Chapter Summary

A novel fibre-optic electronically-scanned bulk optical MZI has been experimentally evaluated. This configuration was shown to yield a higher degree of stability than other proposed configurations [1,2], whilst providing enhanced central fringe identification by using dual wavelengths, without the need for any moving parts. The system was also configured to provide accurate displacement measurements [15]. The work shows that the configuration provides absolute displacement measurements with a high scanning speed [16]. The configuration is compact, has a high stability and does not introduce any spatial "mis-overlapping" of the beams. The use of centroid and least-squares central fringe identification techniques greatly enhanced the central fringe identification accuracy, which was shown to provide repeatable full-scale displacement measurements to an accuracy of 40nm.

In the next chapter, the system will be adapted for the measurement of vibration and results given. The system will be shown to be capable of simultaneously measuring

DC and AC stresses, without the use of polarizers or transmission gratings (which are employed in other proposed systems).

5.6. References

1. Bock, W., Urbanczyk, W., and Zaremba, M.: "Electronically scanned white-light interferometric strain sensor employing highly birefringent fibers", Opt. Comms., vol. 101, pp.157-62, 1993.
2. Jiang, X. Q., Kemp, J., Ning, Y. N., Palmer, A. W., and Grattan, K. T. V.: "Accurate wavelength determination in a Wollaston interferometer for sensing applications", IEEE Photonic Tech. Letts., vol. 8, No. 8, pp. 1055-57, 1996.
3. Padgett, M. J. and Harvey, A. R., "A static Fourier-transform spectrometer based on Wollaston prisms", Rev. Sci. Instrum., vol. 66, No. 4, pp. 2807-2811, 1995.
4. Francon, M. and Mallick, S.: "Polarization Interferometers", Ch. 2, Wiley Interscience, New York, 1971.
5. Marshall, R. H., Ning Y. N., Palmer, A. W. and Grattan K. T. V.: "A novel implementation of a bulk-optical Mach-Zehnder interferometer for enhanced stability in a fibre-optic electronically-scanned white-light interferometric system", Proc. Optical-Fibre Sensors (OFS-11) conference, Sapporo, Japan, In: Interferometry and Polarimetry, paper We3-41, Eds. Y. Ohtsuka, T. Yoshino; pp. 336-339, May 1996.
6. Romare, D., Rizk, M. S., Grattan, K. T. V. and Palmer, A. W.: "Superior LMS-based technique for white-light interferometric systems", IEEE Photon. Tech. Lett., vol. 8, pp.104-106, 1996.
7. Chen, S., Palmer, A. W., Grattan, K. T. V. and Meggitt, B. T.: "Digital signal-processing techniques for electronically scanned optical-fiber white-light interferometry", Appl. Optics, vol. 31, pp.6003-6010, 1992.
8. Koch, A. and Ulrich, R.: "Fiber-optic displacement sensor with 0.02μm resolution by white-light interferometry", Sensors and Actuators A, vol. 25, pp. 201-207, 1991.
9. Bobroff, N.: "Recent advances in displacement measuring interferometry", IOP Meas. Sci. Technol., vol. 4, pp.907-926, 1993.

10. Weir, K., Palmer, A. W., and Grattan, K. T. V.: "Accurate measurement of small displacement using optical techniques", International J. of Optoelectronics, vol. 9, No. 6, pp. 449-455, 1994.

11. Queensgate Instruments Ltd.: "System 2000 Nanopositioning User's Guide"

12. Meggitt, B. T. "Fiber optic white-light interferometric sensors", Ch. 9, In: "Optical Fiber Sensor Technology", Eds. Grattan, K. T. V. and Meggitt, B. T., Chapman & Hall, London, 1995.

13. Hecht, E and Zajac, A: "Optics", 2nd ed., Ch. 6, pp. 220-240, Addison-Wesley, 1987.

14. Melles Griot: "Melles Griot Optics Guide 1995/96", Chp. 1, pp. 15-20, Melles Griot Inc., USA, 1995.

15. Marshall, R. H., Ning Y. N., Palmer, A. W. and Grattan K. T. V.: "Accurate displacement measurement using a novel fibre-optic electronically-scanned white light interferometer", Proc. XIV IMEKO World Congress, P2: Photonic measurements, Tampere, Finland, 1-6 June 1997.

16. Marshall, R. H., Ning Y. N., Palmer, A. W. and Grattan K. T. V.: "High sensitivity displacement measurement using a novel fibre-optic electronically scanned white light interferometer", In: SPIE 1996 International symposium on Optical science, engineering and instrumentation, Denver, USA, Proc: SPIE vol. 2861-08 Laser interferometry VIII : Applications; Eds. Pryputniewicz, R. J., Brown, G. M., Jueptner, W. P.; pp. 52-61, 1996.

Chapter 6

Vibration Measurements

6.0. Introduction

In this Chapter, an experimental and theoretical evaluation of the Mach-Zehnder interferometer (MZI) employed for the measurement of vibration is reported. It is commonly found in many physical systems (such as aircraft wings and tall buildings) that more than one mode of vibration is present. This vibration can be characterised by a slowly varying DC stress which is superposed upon an AC stress. In the first experiment to investigate this, the optical system was configured to provide simultaneous measurements of both the DC and AC stresses, without the need for polarizers and transmission gratings which have been employed in previously proposed configurations.

In the second section in this Chapter, results from an interferometric vibration sensing system are discussed, where the intrinsic non-steady-state photo-electromotive force (PEMF) characteristics of a photoconductive crystal were used practically in a detection system in conjunction with the modified MZI. The system was experimentally verified to provide reproducible vibration frequency measurements in the kilohertz region (to ~mHz sensitivity), with the use of a simple signal processing approach. The system had the added benefits of not requiring external optical components such as optical polarization control, transmission gratings and frequency

shifting modulators, and offers information on the direction of the motion associated with the vibration, unlike many reported schemes.

6.1. Measurement of AC and DC stresses: Introduction

Optical interferometry is a widely used technique for the measurement of the vibration characteristics of a range of industrial components [1,2]. It has a wide dynamic range and a high sensitivity [2,3] However, configurations discussed in the literature require the use of complex frequency shifting modulators [3], polarization control [4] and transmission gratings [2] in order to resolve the vibration directional information.

In addition, it is commonly found in physical systems that more than one mode of vibration is present. This can be characterised by a slowly varying DC stress which is superposed upon an AC stress. These "dual-modal vibration systems" are commonly found in systems such as aircraft wings and tall buildings, whose structural monitoring is important for both safety and commercial reasons.

In this work, the bulk-optical Mach-Zehnder interferometer (MZI) (developed in Chapter 5), is employed as a recovery interferometer in an extrinsic fibre-optic electronically scanned white-light interferometric vibrometer. This implementation of an MZI has the advantages (when compared to previously proposed configurations for this purpose [5]), of being simple and compact, and most importantly can provide simultaneous measurement of DC and AC stresses, without the need for polarizers [6] and transmission gratings [2]. In addition, the polarizer-based configurations also have additional signal processing problems when used in a dual interferometric configuration since they suffer from the problem of having redundant zero-order fringes in the resultant interferogram due to the configuration of the recovery interferometer.

Again, the Fabry-Perot interferometer (FPI) was used as the sensing interferometer (SI) where one of its mirrors was modulated by a combined DC and AC

signal (using the linear PZT stage), in order to provide a vibrating surface on which measurements could be made. The sensing and recovery interferometers were linked in series by a multimode optical fibre. The use of a fibre-optic "probe" at the SI facilitates the provision for non-contact measurements to be made in hostile environments.

The operation of this vibrometer relies upon the interference of light reflected from the vibrating target mixing with a reference beam in the SI. This mixing provides a varying optical-phase-difference (OPD) and this variation in phase is detected via the resultant variation in the position of the fringe interferogram in the electronically-scanned RI. The detected variation in phase of this interferogram can then be related to the initial vibration of the target surface. Such a system was investigated in detail in this work and its performance characteristics will be discussed.

This electronically-scanned fibre-optic vibrometer configuration can provide simultaneous DC and AC stress measurements without the need for polarizers, transmission gratings and moving parts, unlike other proposed configurations for this purpose, thereby yielding a simpler and more convenient device for practical measurements.

6.2. Experimental arrangement

The complete experimental arrangement used is shown in Figure 6.1. The two multimode laser diode sources used, LD1 (780nm) and LD2 (810nm), had coherence lengths of ≈40μm. Light from the sources was launched along a 50μm core diameter multimode fibre-optic coupler, via beamsplitter BS3. The light passes through the coupler to the FPI. The two FPI mirrors were initially separated by a distance, d_f, providing an OPD of $2d_f$ in order to move the FPI out of the coherence region. A Queensgate System 2000 Piezo-electric transducer (PZT) was used to modulate the FPI mirror, M2, in order to provide the vibration measurement. The PZT was modulated externally via a signal generator.

The output of the FPI travels back along the same path through the coupler to the MZI.. This output was expanded to a beam of width, W, and was then incident onto

the MZI beamsplitter, BS1, as before. The angle of inclination of RAP2, denoted by α, was set at ~0.1°, yielding ~9 pixels per fringe.

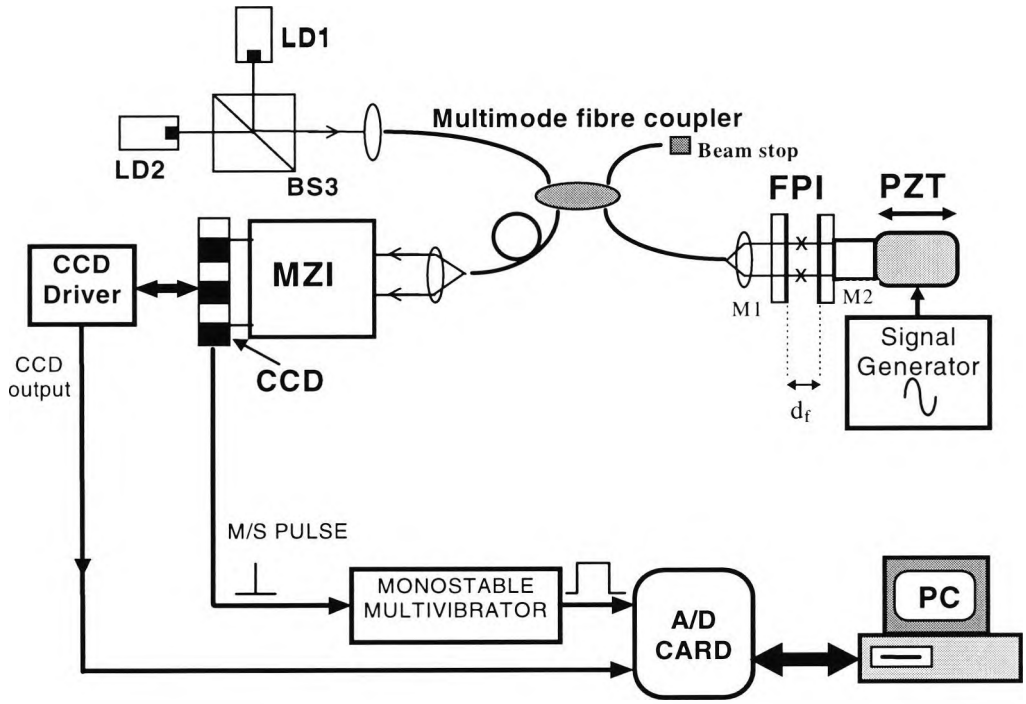

Figure 6.1: Schematic of the complete experimental arrangement FPI- Fabry-Perot Interferometer; MZI- Mach Zehnder Interferometer; LD1, LD2 - Laser Diodes; BS3 - Beam Splitter; A/D Card - 12 bit Analogue-to-digital converter card; M/S pulse - CCD master/start frame synchronisation pulse

A Hamamatsu S5769-1006 linear image line CCD, having 1024 pixels, with a pixel width, *a*, of 12μm, and an equivalent pixel spacing of 12μm was used. However due to the compact nature of the MZI, the beam was expanded across 2/3 of the full CCD width, yielding ~700 effective pixels, which is sufficient for this application. A Hamamatsu CCD was employed, rather than the Fairchild model used previously, due to the fact that the Fairchild CCD has a relatively high scanning rate (a minimum of 0.2MHz). This scanning rate is too fast for the Amplicon A/D card to retrieve (which has a maximum sampling rate of 125kHz), whereas the sampling rate of the Hamamatsu CCD was set to 16kHz. The master/start pulse interval, T_s, of the Hamamatsu CCD was set using the timing switches to 64ms. This master/start pulse sets the repetition rate of each CCD interferogram frame. Thus, for a 1024 pixel CCD, each pixel has a duration, T_p, of

$$T_p = \frac{T_s}{1024} = 62.5\mu s \qquad (6\text{-}1)$$

which yields a pixel rate, f_p, of 1/62.5μs ≡ 16kHz. The Hamamatsu CCD had dimensions of 24.57×1.54mm, but however the active area of each effective pixel was 24μm×24μm.

The MZI generates a set of spatially distributed interference fringes along the CCD. In addition, a Hamamatsu C4074 CCD driver was used in conjunction with a Hamamatsu C4091 pulse generator to amplify and control the frame synchronisation of the CCD output. A cylindrical lens was used to focus the incident optical output power onto the detector array. An Amplicon Liveline PC26AT 12 bit A/D card was used to capture the interferogram data from the CCD array, to facilitate the on-line processing of the interferogram data on a "486" PC. This on-line processing was achieved by writing a program in 'C' to interface directly with the A/D card.

In order to synchronise the capture of each interferogram frame, the master/start (M/S) output pulse from the CCD was used to trigger the PC to capture each frame. Thus, one of the inputs of the A/D card was used for the M/S pulse synchronisation. However, the M/S pulse width (~20ns) was too narrow to trigger the A/D card. The clocks on the A/D card were set in the computer program to provide a sampling rate of 83.3kHz, which corresponds to a minimum sampling interval of 12μs. Thus, a retriggerable monostable multivibrator was used to widen the M/S pulse to a width (~1ms) in order to trigger the PC at the start of each frame, as shown in Figure 6.1. A type 74HC123 retriggerable monostable was selected because of its high speed and short propagation delay (~ns) characteristics and due to the fact that it can be triggered from active high pulses. The output pulse width, t_w, from the monostable multivibrator was changed by the external RC timing components, and was adjusted according to the relation [8]

$$t_w = 0.28 R_{ext} . C_{ext} . \left(1 + \frac{0.7}{R_{ext}} \right) \qquad (6\text{-}2)$$

where t_w is the pulse width in ns; R_{ext} is in kΩ; and C_{ext} is in pF. A pulse width, t_w, of ~1ms was achieved with the use of R_{ext} of 40kΩ, and C_{ext} of 100nF, as shown in Figure 6.2.

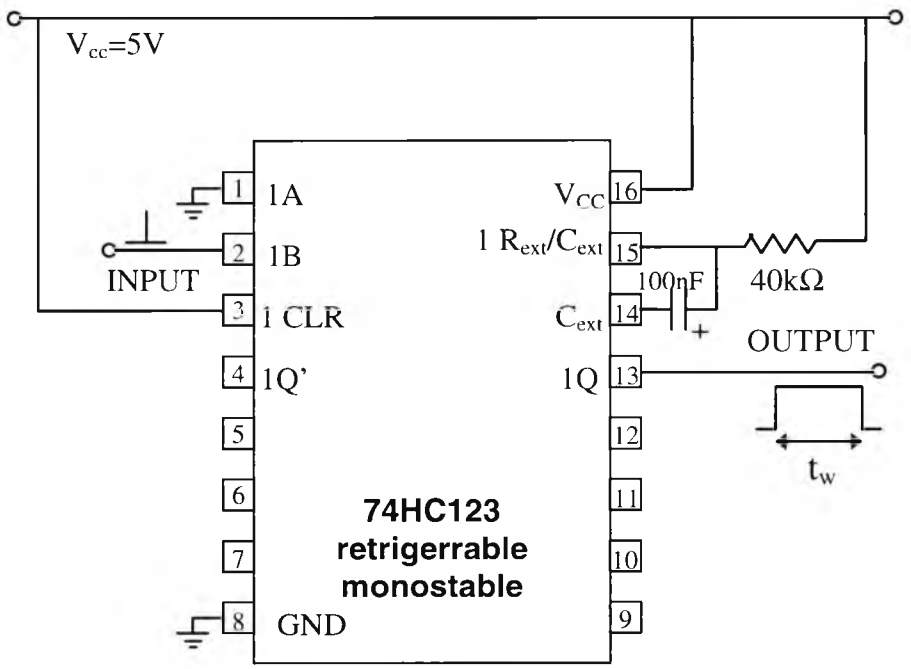

Figure 6.2: Schematic representation of retrigerrable monostable multivibrator used to widen M/S pulse

6.3. Signal Processing scheme

The basic optical principle of operation of this vibrometer is to track the central fringe position of an interferogram which is being modulated spatially along the CCD by the optical phase modulation that is induced by the vibration measurand in the FPI. By tracking the position of this interferogram on the PC, the resultant input vibration may be reconstructed, "on-line".

One of the major system design constraints was the unwanted CCD dark signal characteristics. This was exhibited in the form of a relatively large dark signal which contained no useful CCD fringe information. Since the computer program had to be written efficiently in order to process the data on-line, an efficient and fast means of removing this dark signal had to be realised. The dark signal could not be removed by

filtering due to the obvious phase changes which might result in the interferogram. The typical response of this dark signal is shown in Figure 6.3, for no input signal.

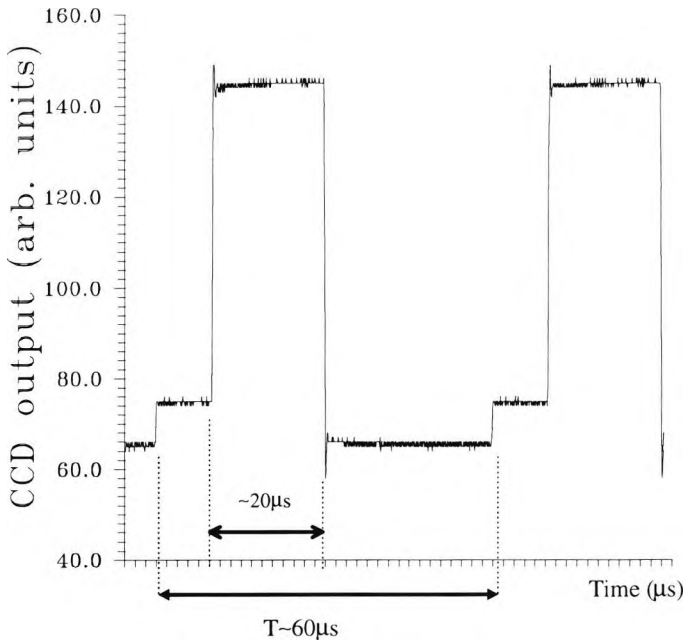

Figure 6.3: Typical dark signal response across 2 pixels

The time period for 1 CCD pixel output was shown to be ~60μs. However, the actual CCD output (shown in Fig. 6.3 as the flat peak region of width ~20μs) contains the useful information. Due to the fact that the A/D card minimum sampling period was ~12μs, then this yields 5 samples per pixel period, which is sufficient from which to extract the CCD pixel value. This was achieved by simply taking every 5 samples and finding the maximum value of this group which will be the useful pixel value. This also has the added benefits of decreasing the dataset size fivefold. This process is highlighted in Figure 6.4. A typical CCD output frame response captured on the PC before the dark signal is removed is shown in Figure 6.4(a). The results of removing the dark signal using this technique are shown in Fig. 6.4(b).

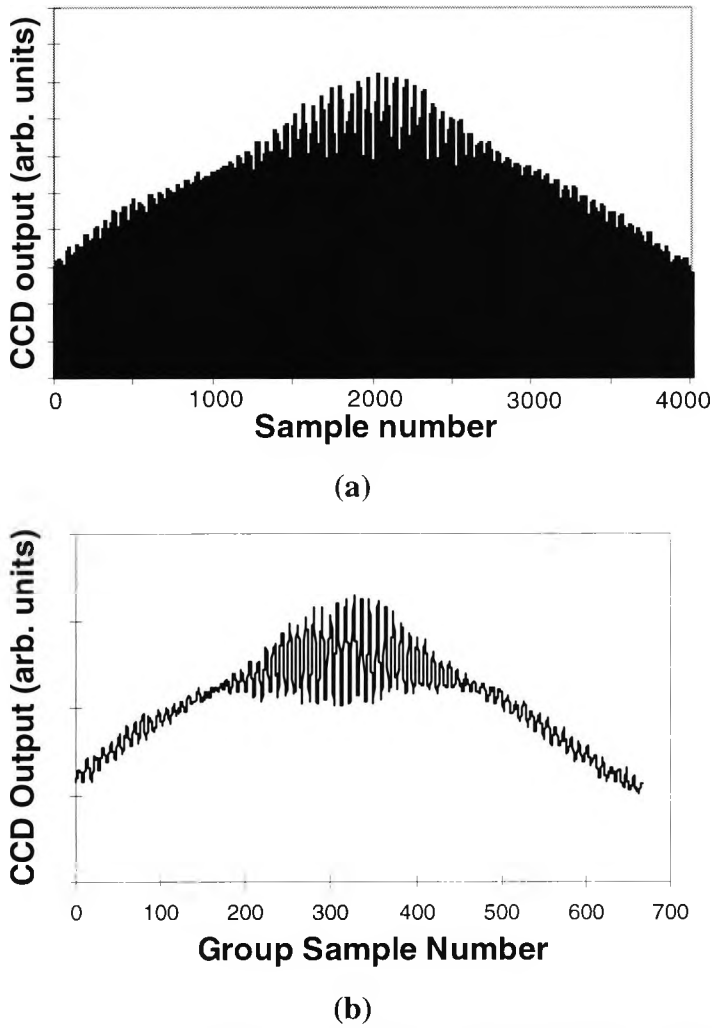

Figure 6.4: **(a)** Typical CCD output frame response captured before the dark signal is removed; **(b)** Typical CCD output frame response captured after the dark signal is removed

A schematic representation of the structure of the computer program used to read in and process the vibration interferogram data is shown in the flowchart in Figure 6.5. The 'C' computer program listing is shown in Appendix D.

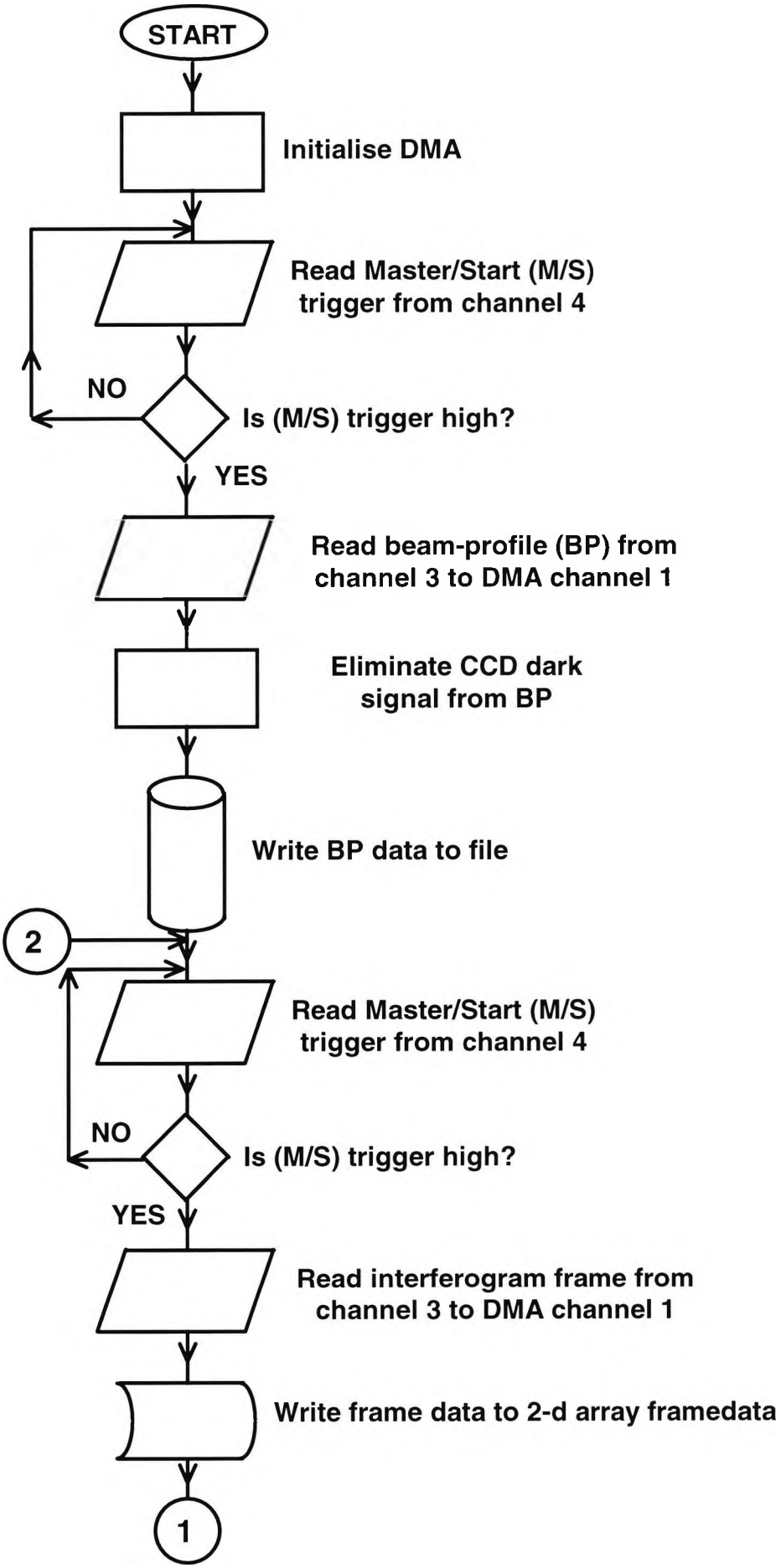
START
Initialise DMA
Read Master/Start (M/S) trigger from channel 4
NO
Is (M/S) trigger high?
YES
Read beam-profile (BP) from channel 3 to DMA channel 1
Eliminate CCD dark signal from BP
Write BP data to file
2
Read Master/Start (M/S) trigger from channel 4
NO
Is (M/S) trigger high?
YES
Read interferogram frame from channel 3 to DMA channel 1
Write frame data to 2-d array framedata
1

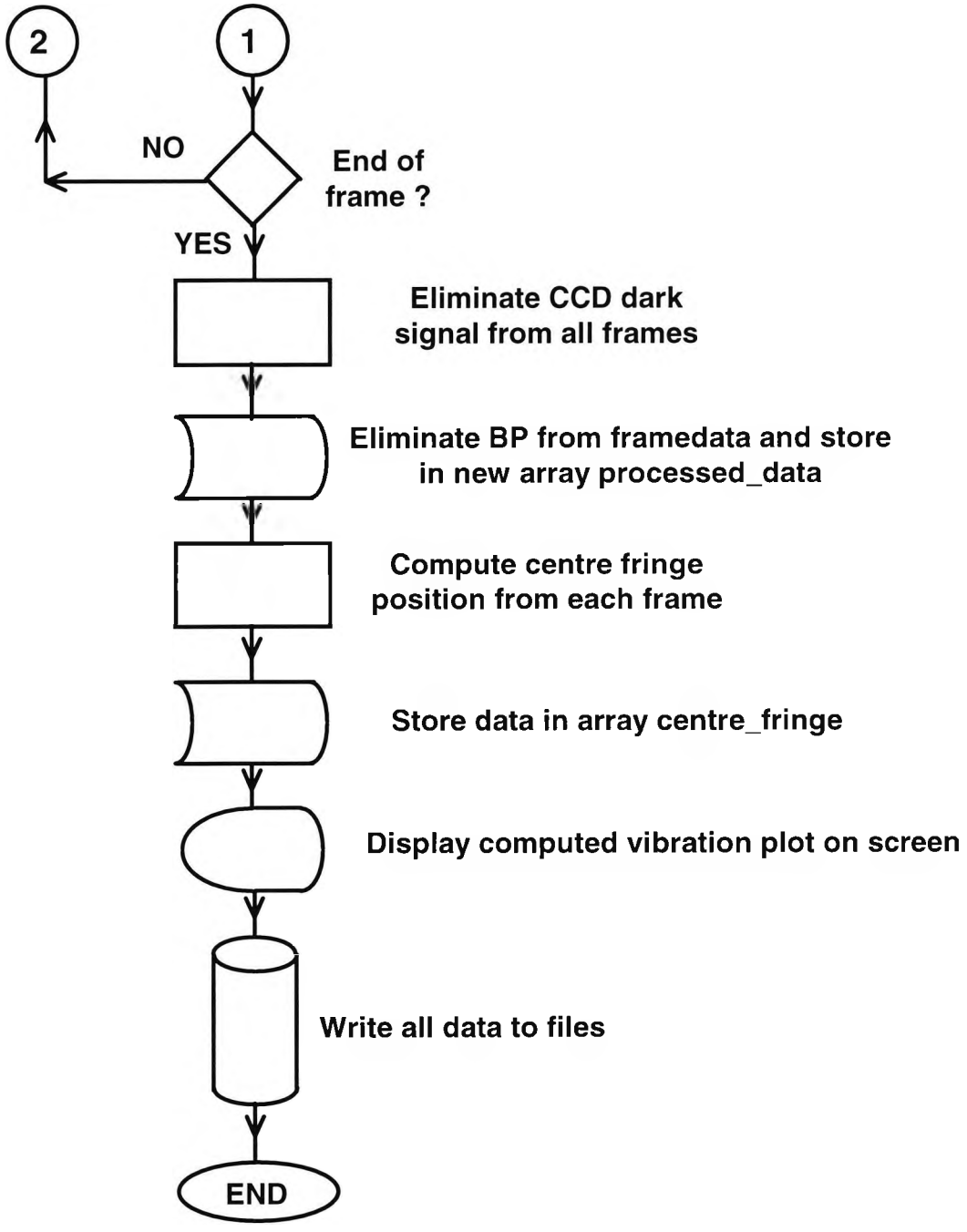

Figure 6.5: Flowchart of 'C' computer program used to read-in and process vibration data. Here, DMA is the Direct Memory Access channel.

6.4. Experimental Results

The system was set up as shown in Figure 6.1, and the PZT mirror, M2, was initially driven by a low frequency 3Hz sinusoidal modulation input, as shown in Fig. 6.6. This modulation produced a corresponding ±5μm shift in the central fringe position of the dual wavelength interferogram. The position of the central fringe from each frame is stored in the PC, in order to yield a reconstruction of the vibration measurand, as shown in Figure 6.7.

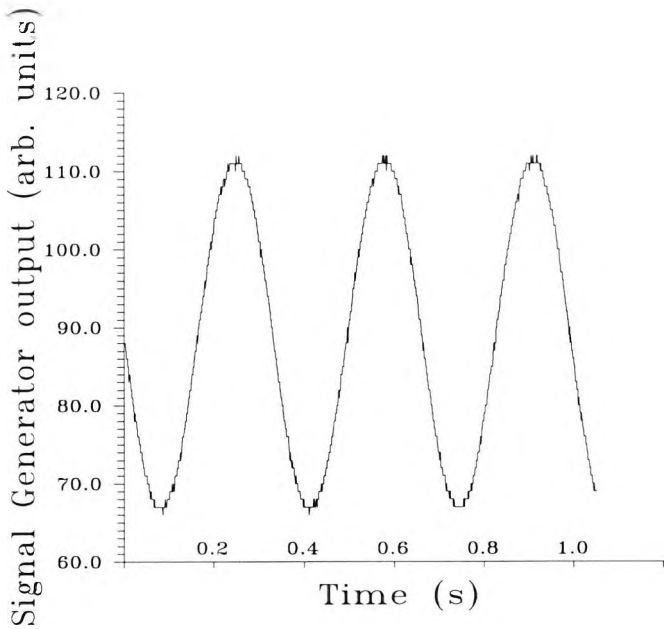

Figure 6.6: Input 3Hz sinusoidal modulation vibration from signal generator, which yielded a ±5μm peak-to-peak vibration amplitude range.

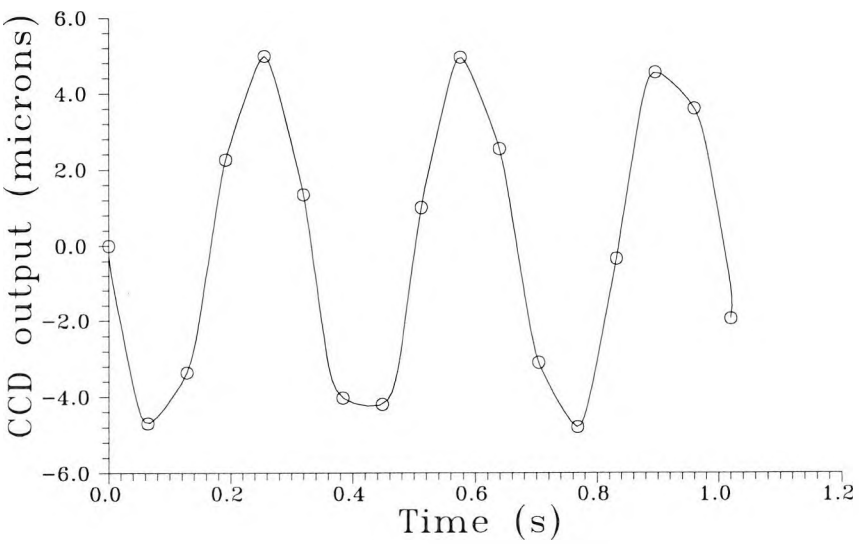

Figure 6.7: Vibration response output to a 3Hz AC sinusoidal modulation yielding a 10μm peak-to-peak vibration amplitude range.

The measurement procedure was extended to produce a simultaneous measurement of AC and DC stresses. This can be achieved due to the fact that the measurement procedure tracks the position of the central fringe which is sensitive to both AC and DC stresses. Figure 6.8 shows the output obtained from a sinusoidal

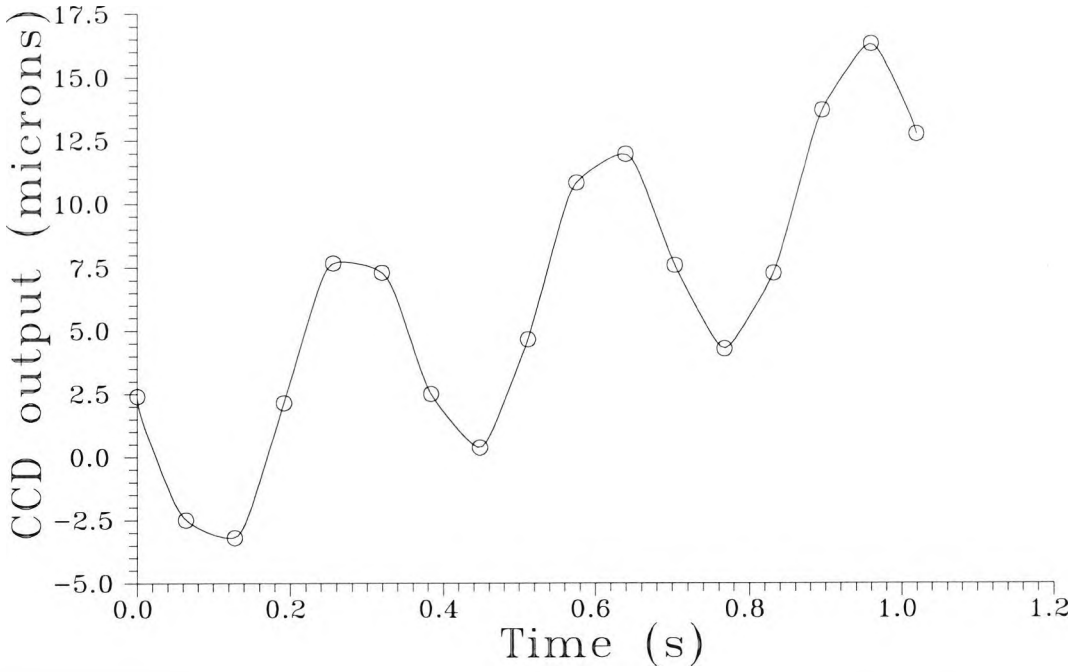

Figure 6.8: Reconstructed vibration response output to a 3Hz AC sinusoidal input modulation stress superposed on an arbitrary slowly changing DC ramp stress.

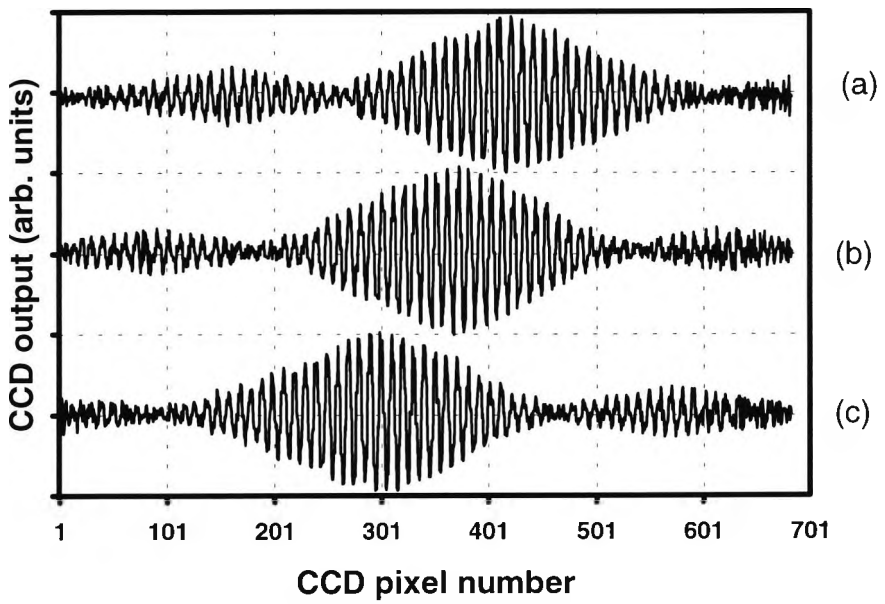

Figure 6.9: Highlighting the effects of the shift in central fringe position with the corresponding changing position of the combined AC. and DC stress measurand. Three arbitrary sampling instants are shown here for sampling instants relating to a mirror displacement of (a) 11, (b) 4, (c) -3 μm.

signal that is superposed on a very slowly varying DC stress. The DC stress was applied using the PZT in the form of a ramp input, which was superposed on the 3Hz sinusoidal input as shown previously in Figure 6.6. The interferogram output taken at 3 arbitrary sampling instants shows the response of the interferogram to this combined DC and AC stress, illustrated in Figure 6.9.

6.5. Discussion and Summary

A novel electronically scanned white light interferometric vibrometer system has been experimentally evaluated to provide simultaneous DC and AC stress measurements of vibration amplitudes spanning a range from ~0.1μm to ~30μm [9, 10]. This provides a major advantage over other reported systems, which cannot simultaneously measure DC and AC stresses [1,2,3,4]. In addition, these preliminary result were achieved without the use of complex frequency shifting modulators, polarization control or transmission gratings, as used in these other reported schemes. This system was implemented on a proof of principle basis, and as such, the system frequency range was limited (~10Hz at the maximum A/D card sampling rate of 125kHz). This limitation was solely due to the relatively slow speed of the CCD and the A/D card, and was not limited in any way by the optical system, which is principally under review in this work. Thus, the frequency response of the system may be increased theoretically to ~kHz, with the use of new commercially available CCDs and A/D cards which can operate up to the 10MHz range.

When employed solely to determine DC stresses, the system provides a measurement resolution of ~0.1μm. However, when simultaneous DC and AC stress measurements are made, the resolution seen is ~0.8μm, due to the "undersampling" rate effects. This occurs due to the fact that the A/D card sampling rate was not sufficiently high to provide optimal performance. With higher sampling rate A/D cards this limitation would disappear and the measurement resolution of ~0.1μm would be achieved in practice. This compares favourably with other reported schemes [2,3]. *K. Weir et al.* [2] reported a vibrometer based upon a Michelson configuration which was capable of kHz vibration frequency measurements of sub-micron amplitude. However,

this device required the use of transmission gratings. *J. R. Baker et al.* [3] reported a vibrometer based upon a Michelson configuration, providing a vibration frequency response ~10kHz. However, their system required the use of signal processing electronics in the form of a gain controlled amplifier and band-pass filters to provide negative feedback control. In addition, both of these other reported systems [2,3] cannot provide simultaneous AC and DC stress measurements.

6.6. Photoconductive crystal vibrometer: Introduction

In this work, results from an interferometric vibration sensing system are discussed, where the intrinsic non-steady-state photo-electromotive force (PEMF) [11] characteristics of a photoconductive crystal were used practically in a detection system in conjunction with the MZI, which was employed to produce interference fringes, which were expanded spatially across an adaptive photo-conductive crystal (PCC) [11]. This PCC is presented as an alternative technique to the white-light interferometric DC and AC stress measurements system, which was highlighted at the beginning of this chapter. This PCC uses its intrinsic non-steady state photo-electromotive force (PEMF) effect properties in order to detect the incident phase-modulated expanded fringe signal, in this practical yet simple application of the technology in detection.

This PCC vibrometer employs a long coherence length source in the form of a HeNe laser. This was employed because the PCC that was available had an absorption spectrum which was designed for optimum sensitivity in the red rather than in the infra-red region. The PCC crystal was produced by *I. A. Sokolov et al.* [11] at the A F Ioffe Physico-Technical Institute. The PCC output response for a typical infra-red multimode laser diode was not sufficient to provide good results. Although this system employs a long coherence length HeNe source, new PCCs have been subsequently produced which are tailored for the infra-red region. These new PCCs can thus be employed in low coherence systems employing multimode infra-red sources. The work described in this section provides an alternative vibrometer scheme using a long-coherence length source, but which has the capability to be used in a full white-light interferometric sensing system.

Basic theoretical analyses of the non-steady state PEMF effect have already been reported [11,12]. In summary, the effect can be observed as an alternating electric current through a short-circuited sample of a photoconductor which is illuminated by an interference pattern, resulting from the presence of the vibration. This electric current arises from a periodic modulation of a phase shift between the spatially periodic distribution of a space-charge electric field and the photoconductivity pattern which is associated with the vibrating light pattern. Such a pattern is generated by the MZI, which is set up to provide spatial interference fringes, and are modulated by the vibration measurand across the beam profile.

This work described here represents a practical advance in the application of the technique in vibrometry, offering a simple system not requiring sophisticated external signal processing. This work shows the efficiency of a straightforward interferometric vibrometer which has the important advantages of providing potentially high resolution, vibration frequency measurements without the use of external components such as polarizers, gratings and complex frequency modulators. In addition, the use of a PCC detector yields the added benefits of not requiring any DC bias voltage and in responding only to non-steady state signals (unlike conventional photodetectors) thus provides an added suppression of slowly varying jamming signals. This system has the valuable characteristics of both providing the vibration frequency output directly with a simple signal processing method and also detecting the direction of the velocity of the target vibration. Thus in contrast to other reported vibrometer schemes [1,2,3], where it represents an advance in the technology in this practical system demonstration.

6.7. Theoretical background

This configuration of this modified MZI used in this work [13] employs only one beamsplitter (BS), as shown in Figure 6.10, where the light from a HeNe source is expanded and collimated, is incident on BS at 45°, and then is divided into two by the front-portion of the BS. After being reflected at mirrors 1 and 2, the beams are then recombined through the back-portion of the BS, and the two spots of the beams overlap with each other on the PCC, generating a set of spatially-distributed interference

fringes across the crystal. In order to review the practical operation of the photo-conductive crystal (PCC) detector in this type of system, a short-circuited, initially homogeneous, photoconductor illuminated by a steady-state light pattern with an arbitrary intensity distribution, I(x), is considered, as shown in Figure 6.10.

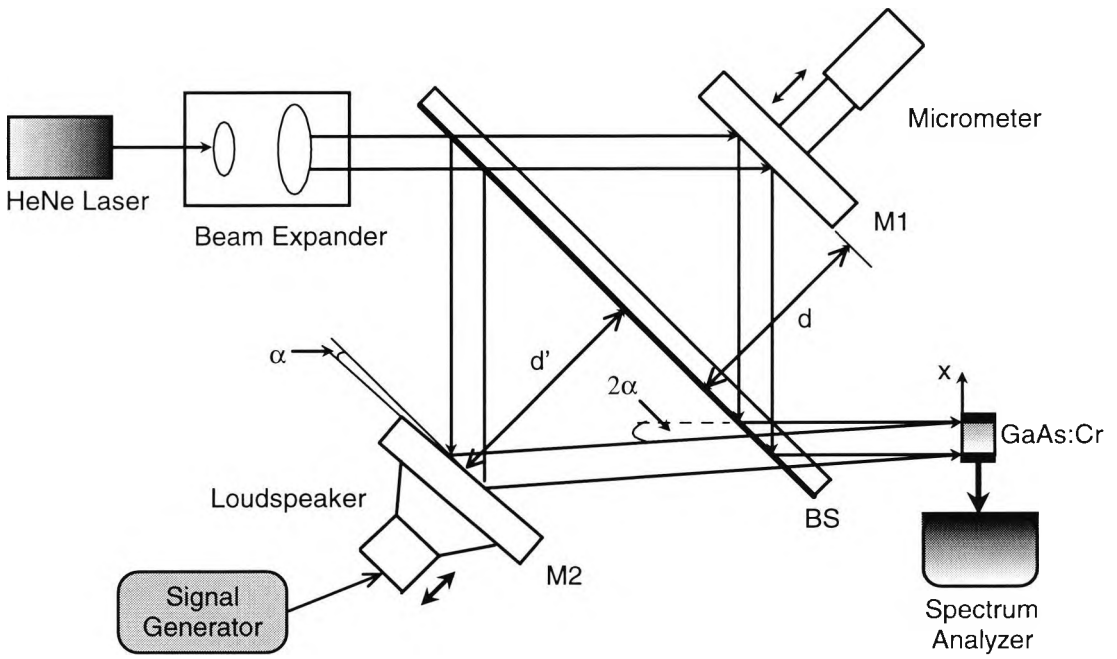

Figure 6.10: Complete experimental arrangement. Highlighting the modified Mach-Zehnder interferometric vibrometer, which employs the GaAs:Cr adaptive detection scheme.

The total electron current through any cross-section of the conductor under steady-state conditions is constant, and may be expressed as [11]

$$j(x) = e\mu n(x)E_{SC}(x) + eD\frac{\partial n(x)}{\partial x} \tag{6-3}$$

Here, n(x) is the steady-state concentration of photoelectrons, of charge e, in the conduction band and μ and D are the mobility and diffusion coefficients respectively. For $j(x) = j_o = \text{const}(x)$, Eq. (6-3) gives an expression for the spatial steady-state distribution of the electric field, $E_{sc}(x)$, in the above as

$$E_{SC}(x) = \frac{j_0}{e\mu n(x)} - \frac{D}{\mu}\left(\frac{\partial n(x)}{\partial x} \Big/ n(x) \right) \qquad (6\text{-}4)$$

Since n(x) is a positively defined function, equation (6-4) can be satisfied only when j_O=0. Hence, it follows that no steady-state current can flow through a short-circuited initially homogeneous photoconductor for any arbitrary light distribution, I(x), and this means that no steady-state PEMF exists. Under non-stationary illumination conditions, the total electron current (Eq. 6-3) can be spatially non-uniform (j(x)≠const(x)), due to local recharging of the photoconductor. The electric field $E_{SC}(x)$ and the spatial distribution of the photoconductivity σ(x) (= eμn(x)) are now shifted by a quarter of a spatial period, Λ/4, with respect to each other to yield a zero mean electron current through the sample [11]. The non-zero current arises when the interference pattern is shifted by this amount to the left or to the right of its initial position. The interference pattern maxima and the corresponding photoconductivity maxima all coincide with the extreme of one sign of the electric field distribution.

This will result in a spatially uniform component of the drift electron current. For an open-circuit sample, a unidirectional current will result in a photo-voltage between opposite faces of the sample, in a time period of the order of the Maxwell relaxation time, $\tau_m = \varepsilon\varepsilon_0/\sigma_0$, (where σ_0 is the average photoconductivity of the sample). The electric field distribution (Eq. 6-4) arrives at its new equilibrium position which is shifted by Λ/4 with respect to the new position of the interference pattern, I'(x), as shown in Figure 6.11.

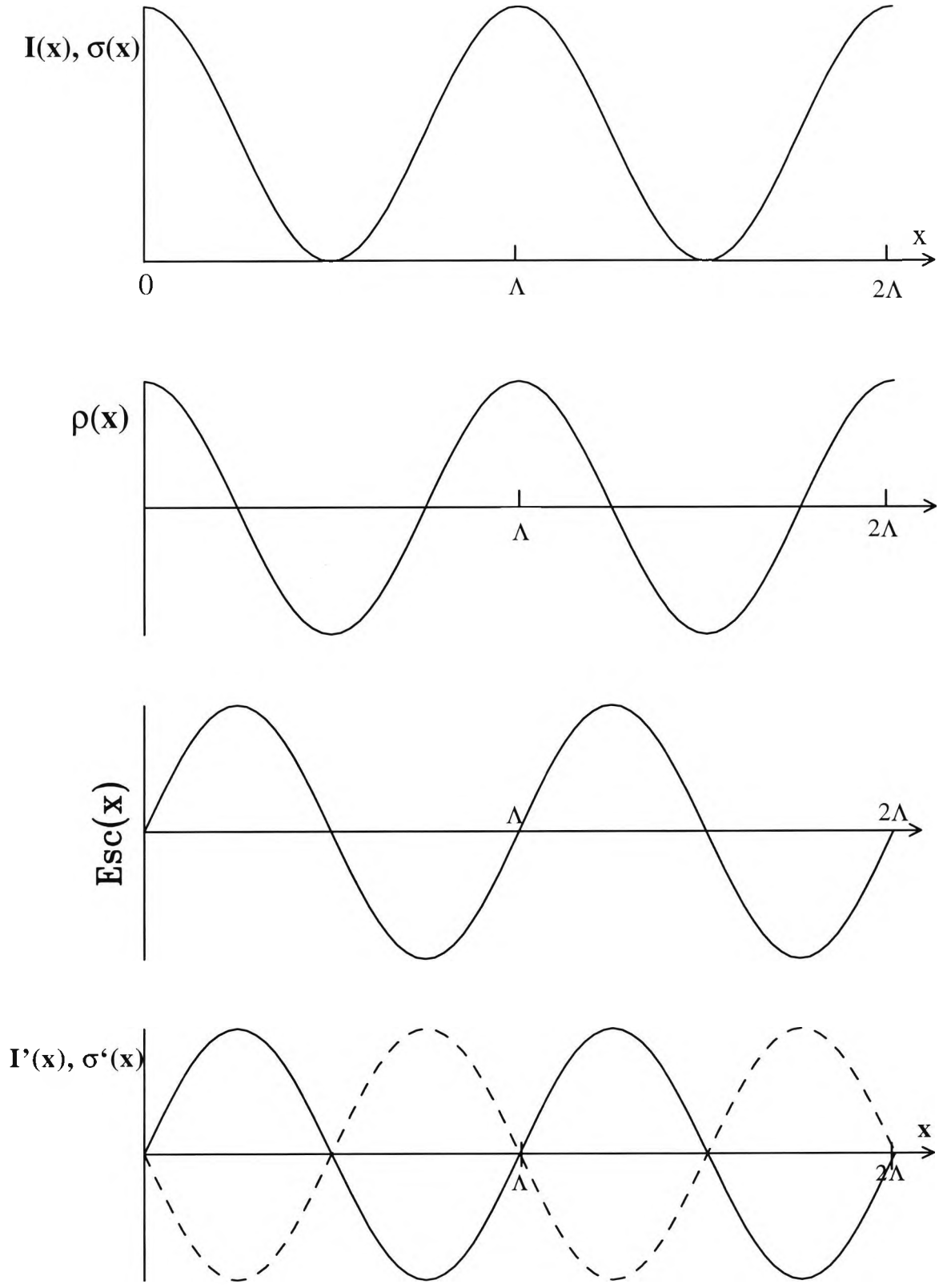

Figure 6.11: Spatial distribution of light intensity, I(x), photoconductivity, σ(x), space charge, ρ(x), and electric field, Esc(x), under steady-state illumination of the PCC illuminated by a sinusoidal interference pattern. I'(x), σ'(x) are spatial distributions of light intensity and photoconductivity just after the pattern shifts by a quarter of a spatial period (Λ/4) to the right (solid line) or to the left (dashed line)

If the light pattern is returned abruptly to its initial position, a non-steady-state current will flow through the short-circuited sample in the opposite direction. When the crystal is illuminated by an interference pattern, I(x), a "frozen-in" electric charge grating, $\rho(x)$, is formed in the PCC, due to the spatial redistribution and subsequent trapping of mobile photoinduced carriers at the impurity centres. The non-steady state photo-emf results from the periodic temporal modulation of a spatial shift between the spatially periodic distribution of the space-charge electric field $E_{sc}(x)$ and the photoconductivity pattern $\sigma(x)$ associated with the vibrating interference pattern.

The model of the volume photoconductive sample (shown in Fig. 6.12) has a donor level, D, and an acceptor level, A, having a lower concentration $N_A << N_D$. This acceptor level does not contribute directly to the photoconductivity, as it only captures a fraction of electrons from the donor level. Thus the negligible effects of this compensating level to the overall photoconductivity can be ignored.

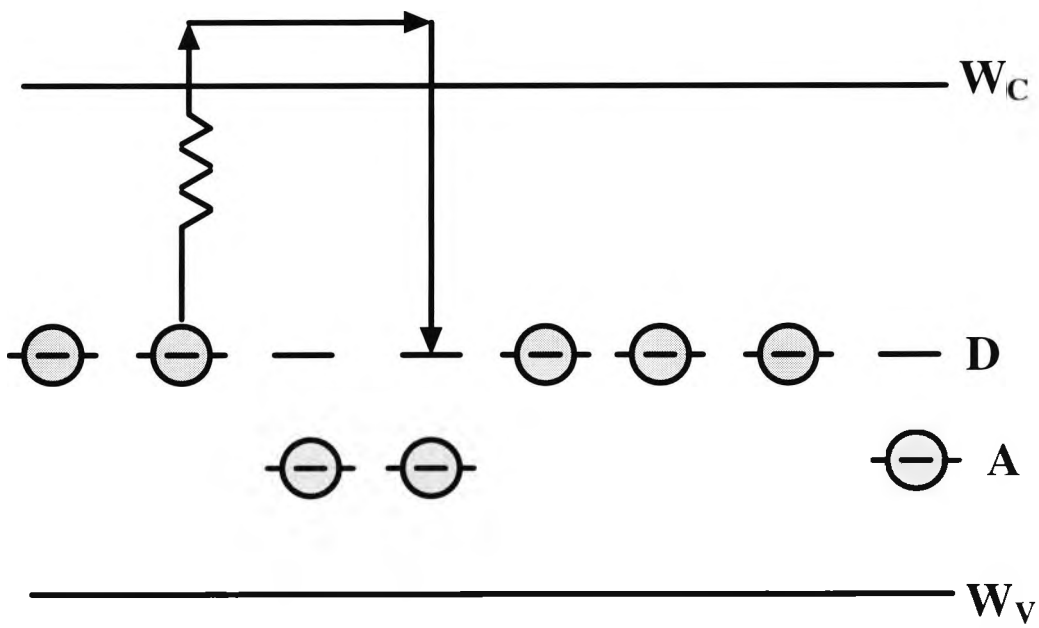

Figure 6.12: Energy-band model of wide-gap partly compensated impurity photoconductor under non-steady state PEMF operation. W_c= conduction band, D = donor level, A = acceptor level, W_V= valence band.

When the donor level is illuminated by a sinusoidal interference pattern vibrating with a frequency ω, the complex amplitude of a short-circuit ac density is given by [12].

$$j^{\omega} = \tfrac{1}{2}\Delta m^2 \sigma_0 E_D \frac{1}{(1+K^2 L_D^2)} \frac{i\omega/\omega_0}{(1+i\omega/\omega_0)} \tag{6-5}$$

where, Δ is the amplitude of the sinusoidal phase modulation of the interferogram signal, m is the average modulation index, $K=2\pi/\Lambda$, is its spatial frequency, Λ is the fringe spacing, $E_D \equiv Kk_bT/e$, is the diffusion field [12], σ_o is the average photoconductivity of the sample, and L_D is the average diffusion length of the photoelectrons. The electric field can follow the shifts of the interference pattern with a characteristic time, τ_{sc}, of the dynamic space-charge grating relaxation

$$\tau_{sc} = \tau_m\left(1+K^2 L_D^2\right) \tag{6-6}$$

Here, $\tau_m=\varepsilon\varepsilon_0/\sigma_0$ is a Maxwell relaxation time, which corresponds to the average photoconductivity σ_0 and the dielectric constant ε of the crystal. As a result the output signal is suppressed at the modulation frequencies lower than some characteristic cut-off frequency that is equal to the inverse recording-erasure time [11] ($\omega_0=1/\tau_{sc}$). It is because of this that the slow phase drifts are efficiently compensated. For high modulation frequencies ($\omega \geq \omega_0$), the short-circuit current proves to be frequency independent and reaches its maximum at

$$j^{\omega}_{\max} = \frac{1}{4}\Delta m^2 \sigma_0 \frac{k_B T}{L_D e} \tag{6-7}$$

for the optimum spatial frequency $K = 1/L_D$. The detailed solid-state physics underpinning the operation of the PCC is given elsewhere [11].

6.8. Experimental arrangement

The experimental arrangement used to investigate the use of the PCC in a practical optical interferometric sensor is illustrated in Figure 6.10. A Helium-Neon (HeNe) long coherence length source, with an output power of 5mW and a mean wavelength of 633nm was employed. A short focal length convex lens (f≈1.5cm) was

used in conjunction with a long focal length convex lens (f≈10cm) to expand the beam from a 0.5mm to a 3.0mm diameter, in order to illuminate completely the full width of the crystal. The incident beam was then launched into the MZI as before, yielding a set of spatially distributed interference fringes across the crystal, with a fringe contrast, m, of ≈0.9.

The MZI mirror, M2, was adjusted to provide an optimum spatial frequency [11]. This occurred at an inclination angle, $\alpha \approx 0.6°$, and thus the two beams were separated by an angle, 2α, equivalent to $\approx 1.2°$ across the crystal. A GaAs:Cr (4.5mm×3.5mm×2.5mm) cubic PCC was used for the detection of the phase-modulated optical signals, the active photoconductive area of which was 2.5mm, yielding an electrode spacing, L, of ~2.5mm. The output from the PCC was recorded using a Hewlett-Packard 3561A dynamic signal analyzer.

6.9. Results and Discussion

With the above configuration of the MZI, initially, the function generator was used to drive the loudspeaker, to which was attached a mirror, with an arbitrary sinusoidal modulation frequency, f, of 999Hz. This was used as a conventional vibration test generator, of known frequency, but in non-laboratory conditions less reflective objects may be interrogated, yielding a lower signal-to-noise ratio. The modulation was adjusted to provide a maximum output, which occurred at an amplitude of vibration spanning a distance of $\sim\lambda/4\pi$. The resultant output from the unbiased crystal was recorded on the spectrum analyzer. Figure 6.13(a) shows the output from the crystal when the MZI mirror was driven by a sinusoidal input of 1kHz (as shown in Figure 6.13(b)). The corresponding spectral output from the unbiased crystal was recorded on the spectrum analyzer, as shown in Figure 6.14, which was obtained by calibrating the loudspeaker over the frequency range to provide an amplitude of $\sim\lambda/4\pi$ for each frequency.

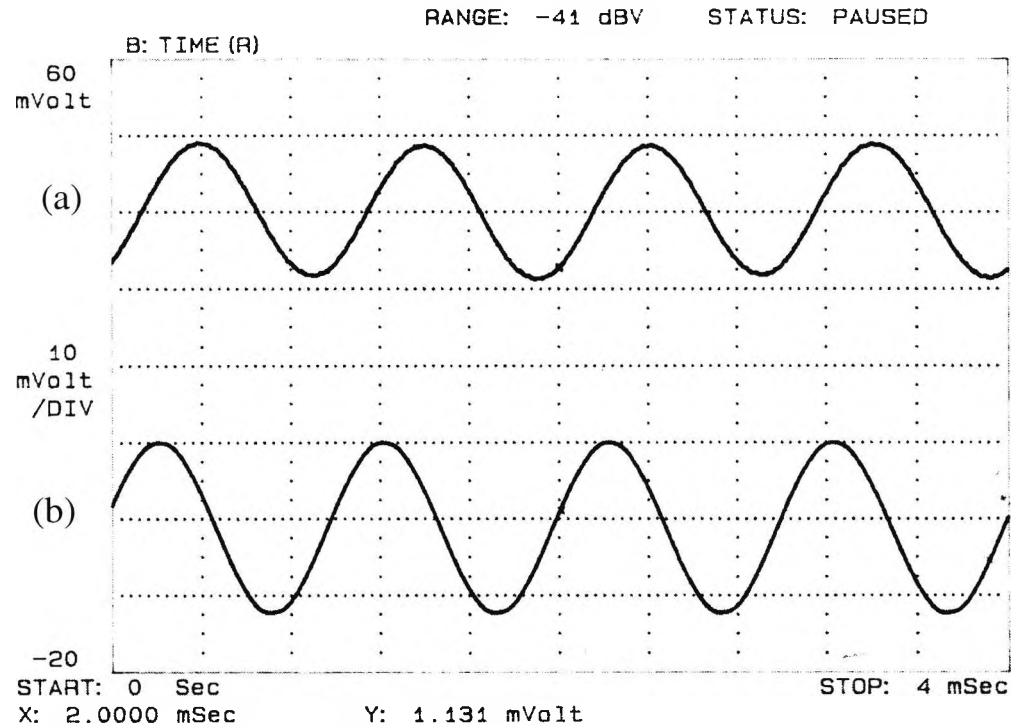

Figure 6.13: Shows the relationship between the crystal output (a) and the input vibration modulation (b) at a sinusoidal input frequency of 999Hz.

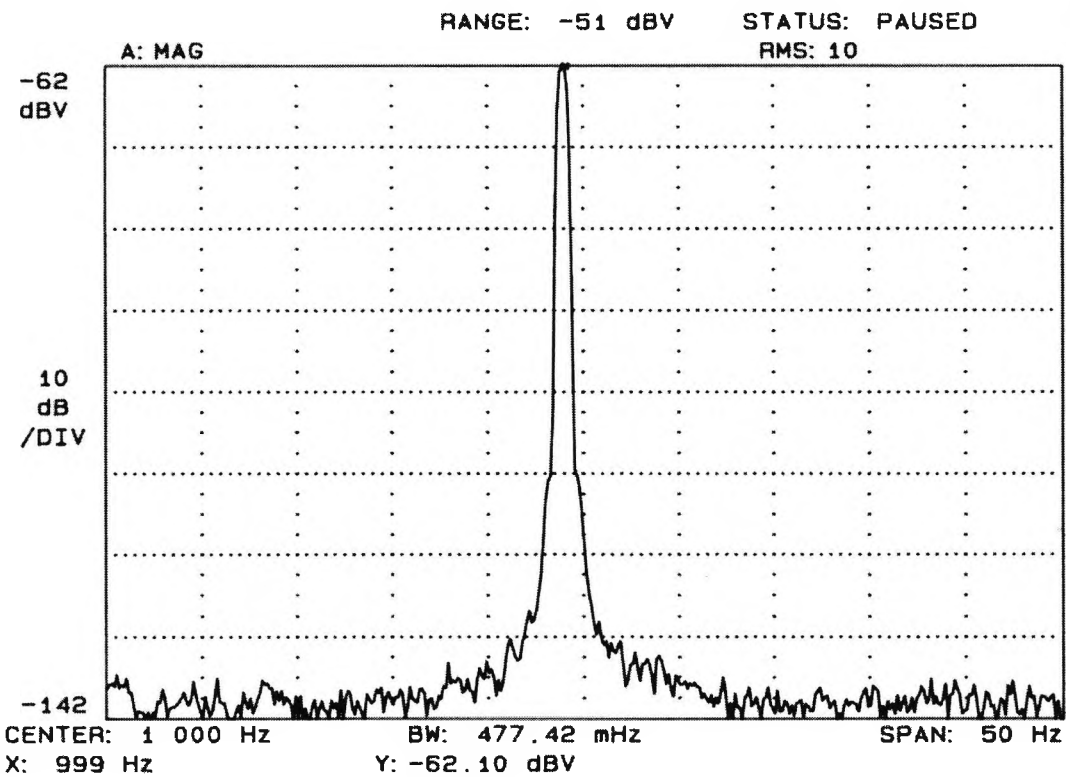

Figure 6.14: The spectral output of the PCC at an arbitrary input modulation frequency of 999Hz.

The PCC output was shown to provide negligible signal distortion over the operational frequency range. Its frequency response, shown in Fig.6.15 shows that the system can provide good quality measurements across a 5kHz range. This response obtained is indicative of the PCC frequency transfer response obtained under similar operating conditions [11] with relatively large modulation amplitudes exceeding $\sim\lambda/4\pi$.

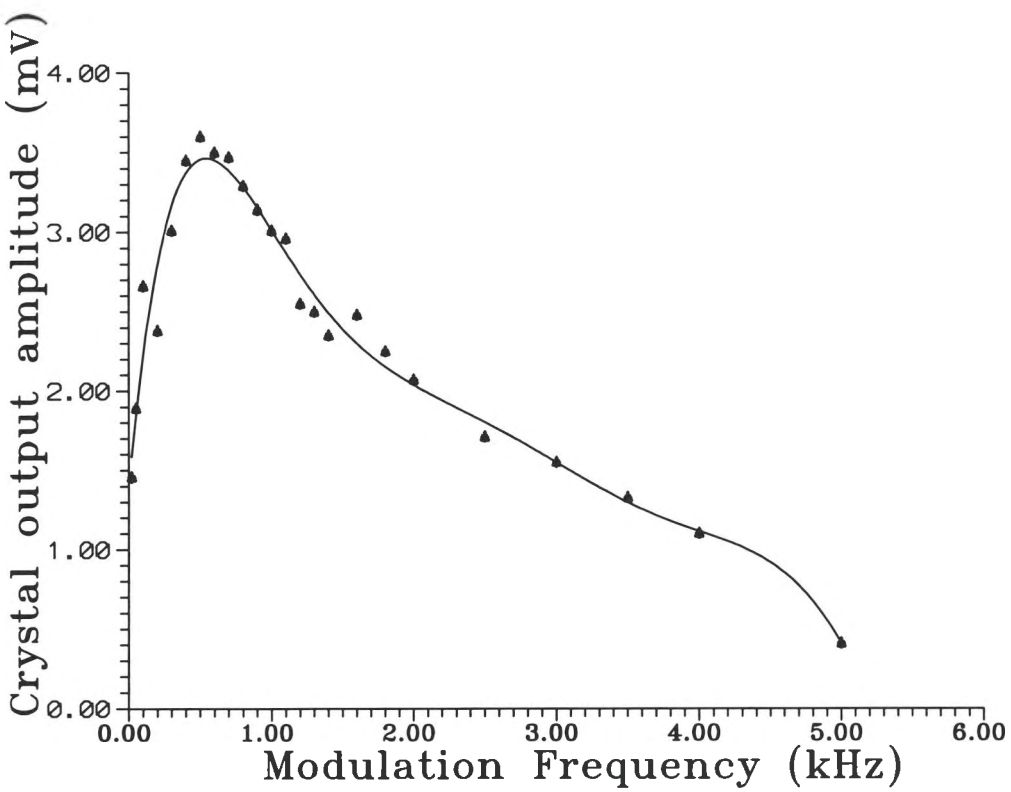

Figure 6.15: The Crystal frequency response for a fixed modulation amplitude of $\sim\lambda/4\pi$.

Even without the use of amplification and filtering of the PCC output, the system signal-to-noise (S/N) ratio was very good, the maximum measured value (73.5 dB), which occurred at a modulation frequency of 700Hz. At a modulation amplitude of $\sim\lambda/4\pi$ and a modulation frequency of ~1kHz (as shown in Figure 6.14), the signal-to-noise ratio was ~ 70dB. For small signal amplitudes a linear relationship between the input modulation and output modulation amplitudes has been shown [11]. It can be seen, from Figure 6.14, that the minimum detectable amplitude can be estimated to be in the picometer range. However, this minimum detectable amplitude is dependent

upon the reflectivity of the target surface. In this experiment a mirror was employed giving a high level of feedback, and thus the minimum detectable amplitude will increase with decreasing reflectivity of the target surface. However, simulations suggest that sub-nanometer vibration amplitudes can be detected even from a relatively low reflectivity object.

The GaAs:Cr crystal used was experimentally verified to provide extremely high resolution vibration measurements of vibration frequencies. Figure 6.16 highlights the linear relationship seen between the PCC output frequency as a function of the input modulation frequency. The crystal was observed to be capable of measuring, directly, vibration frequencies, with a resolution of ~2mHz, limited by the sensitivity of the spectrum analyzer, which was evaluated by locating the central point of the fundamental modulation PCC output on the spectrum analyzer.

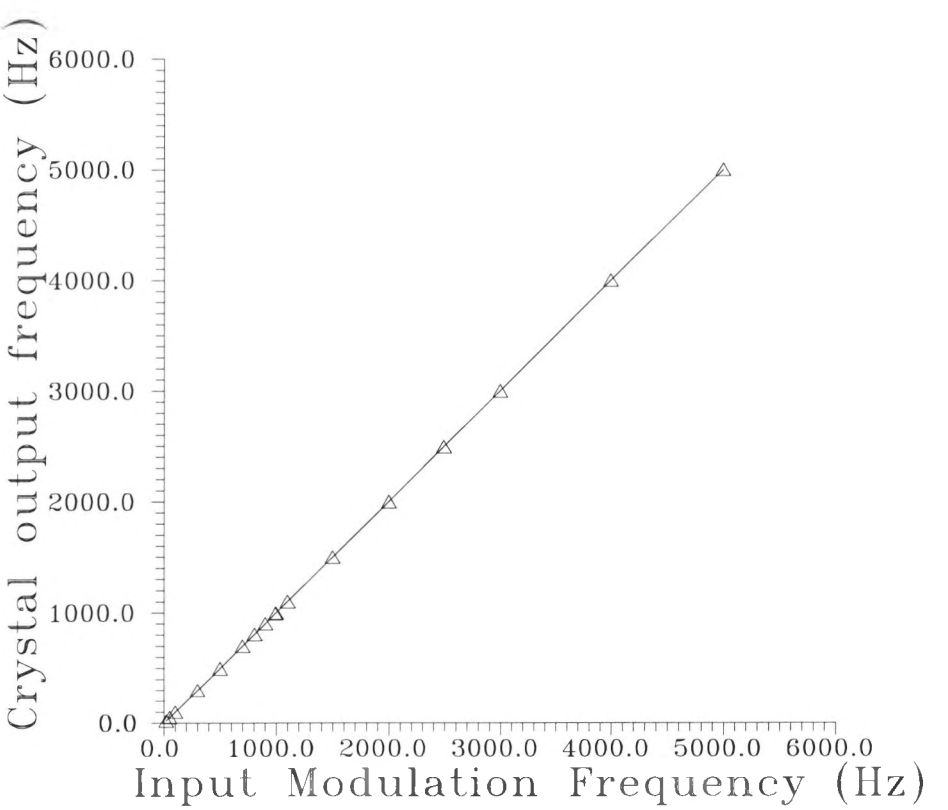

Figure 6.16: The PCC output frequency as a function of the input modulation frequency, for a fixed modulation amplitude of ~$\lambda/4\pi$.

This process was repeated for the input modulation frequency in order to provide a reference frequency measurement. In principle, the system should be capable of

measuring vibration frequencies to a resolution of <1mHz and not limited at this value by the physical characteristics of the PCC. Nevertheless these preliminary results compare favourably with the results of other reported schemes [1,2,3], with the potential of improvement from this simple 'proof-of-principle' test.

The use of this PCC also had the added benefits of providing a 'jamming' of unwanted low frequency signals due to its intrinsic steady state photo-electromotive force properties [11], which yield relatively high cut-off-frequencies in the PCC. This cut-off frequency may be tailored for different applications by the careful selection of the intrinsic PCC parameters [11] (i.e. σ_O, the average photoconductivity of the sample, and L_D the average diffusion length of the photoelectrons), in conjunction with the experimental conditions (i.e. the fringe spacing Λ). A further advantage of the system is that this jamming of unwanted low-frequency signals is not evident in other reported schemes, [1,2,3] which use conventional biased photodetectors that often provide unwanted low-frequency, high amplitude output components.

6.10. Summary

In conclusion, a practical interferometric vibrometer was experimentally demonstrated to provide vibration frequency measurements with ~mHz resolution across a 5kHz range. The system has the advantages of being extremely simple and compact, with limited use of external optical components, unlike many other reported schemes [1,2,3]. The system is also capable of measuring small vibration amplitudes down to the picometer range and can detect the amplitude and direction of the target vibration. It is believed that the frequency response could also be further improved (theoretically to the order of MHz) by the use of selective amplification and filtering of the crystal output.

6.11. References

1. Sheng, S. Y. and Yongdong, J.: "Laser heterodyne vibration measuring method", Opt. and Laser Technol., vol. 20, No.2, pp. 100-102,1988.
2. Weir, K., Boyle, W. J. O., Palmer, A. W. and Grattan, K. T. V.: "A novel adaptation of the Michelson interferometer for the measurement of vibration", J. Lightwave Tech., vol. 10, pp. 700-703, 1992.
3. Baker, J. R., Laming, R. I., Wilmshurst, T. H. and Halliwell, N. A.: "A new, high sensitivity laser vibrometer", Opt. Laser Technol., vol. 22, 1990.
4. Cookson, R. A. and Bandyopadhyay, P.: "Mechanical vibration measurement using a fibre optic laser-Doppler probe",Opt. Laser Technol., vol. 10, pp. 33-36, 1978.
5. Chen, S., Palmer, A. W., Grattan, K. T. V., Meggitt, B. T. and Martin, S.: "Study of electronically-scanned optical-fibre white-light Fizeau interferometer", Electron. Lett., vol. 27, pp. 1032-1034, 1991.
6. W. Bock, W. Urbanczyk and M. Zaremba: "Electronically scanned white-light interferometric strain sensor employing highly birefringent fibers", Opt. Communications, vol. 101, pp. 157-62, 1993.
7. Wang, D. N., Ning, Y. N., Grattan, K. T. V. and Palmer, A. W. and Weir, K.: "The optimized wavelength combinations of two broadband sources for white light interferometry", J. Lightwave. Tech., vol. 12, No.5, pp. 909-916, 1994.
8. Texas Instruments : "54/74 Families of compatible TTL circuits", Ch.6, p.89, 1990.
9. Marshall, R.H., Ning Y. N., Palmer, A. W. and Grattan K. T. V.: "Vibration measurement using a novel fibre-optic electronically-scanned white-light interferometer", Proc. Optical Measurements I: Scientific, In: "International conference on Applications of photonic technology (ICAPT '96)", Montreal, Canada; July 1996.
10. Marshall, R.H., Ning Y. N., Palmer, A. W. and Grattan K. T. V.: "Simultaneous measurement of AC and DC stresses using a fibre-optic electronically scanned white-light interferometer", accepted for publication in Sensors and Actuators in 1997.
11. Petrov, M. P., Sokolov, I. A., Stepanov, S. I. and Trofimov, G. S.: "Non-steady-state photo-EMF induced by dynamic gratings in partially compensated photoconductors", J. Appl. Phys, vol. 68, pp. 2216-2225, 1990.

12. Stepanov, S. I.: "Sensitivity of non-steady-state photoelectromotive force-based adaptive photodetectors and characterization techniques", Applied Optics, vol. 33, pp. 915-920,1994.

13. Marshall, R.H., Sokolov, I., Ning Y. N., Palmer, A. W. and Grattan K. T. V.: "Photo-Electromotive Force Crystals For Interferometric Measurement Of Vibrational Response", IOP: J. Measurement and Science Technol., vol. 7, No.12, pp.1683-1686, 1996.

Chapter 7

Conclusions and Future Work

7.1. Discussion and Conclusions

In this work, the main aims and objectives set out at the beginning of the study have been achieved. The use of a electronically-scanned white-light interferometric (ESWLI) sensing system was investigated theoretically and experimentally. The key benefits in the use of such systems were ascertained and can be summarised as follows (when compared to long-coherence length interferometers [1,2]), in that the systems:

i. provide unambiguous measurements by employing a short coherence length source, which greatly increases the operating range
ii. does not require re-initialisation each time it is switched on
iii. provides absolute measurements due to the use of a short coherence length source
iv. has no moving parts, as opposed to a mechanically-scanned system, which yields greater mechanical stability, and
v. can provide "single-pulse" measurements due to the use of spatial interference fringe detection, which provides a high scanning speed.

In addition to these benefits above, the system also has the additional benefits provided by optical-fibre interferometric sensors. These include, a high measurement resolution (~nanometre range), immunity to electromagnetic interference (EMI), and the provision of remote sensing for example.

A novel electronically-scanned recovery interferometer was successfully designed and developed for use in an ESWLI sensing system. The design methodology included a thorough evaluation of :

i. the theoretical analysis
ii. a computer model of the system
iii. a comprehensive experimental analysis and
iv. a signal processing analysis,

from which the design of a novel bulk-optical Mach-Zehnder recovery interferometer was obtained. The operational characteristics of the recovery interferometer configurations employed in other reported ESWLI sensing systems were analysed and contrasted with this Mach-Zehnder interferometer (MZI) configuration. The benefits of this MZI over these other configurations were presented (see section 3.1). The main advantages in the use of this new system were:

i. it does not require the use of polarizers (unlike other reported schemes such as the Wollaston prism interferometer [4,5])
ii. it had no spatial mis-overlapping of the beams and thus does not require additional correctional optics (unlike other reported schemes such as the Fizeau and Michelson electronically-scanned interferometers [3])
iii. the MZI has two complimentary outputs (rather than one output from the Michelson, Fizeau or Young's interferometer etc.), which facilitates the use of the two outputs in order to increase the sensitivity of the device (see section 7.2.1). In addition, one of the outputs can be employed to calibrate the system without disturbing the detected output to be measured.
iv. the bulk-optical MZI has a small, compact design
v. the recovery interferometer was designed using bulk-optical components which increases the stability of the system.
vi. the MZI configuration can be relatively easily manufactured for mass production from readily available bulk optical components (namely beamsplitters and right-angled prisms, as shown in section 7.2.2)

The original MZI employed (see chapter 3), was a good design, employing only one beamsplitter rather than the two used in conventional systems (saving component costs), but however the benefit of this was offset against the need to reduce the size of the recovery interferometer and to facilitate a design which potentially could operate better in hazardous environments. Hence a design modification was made to produce the more compact and stable bulk-optical MZI (see Chapter 5). Nevertheless, the original MZI still provides very good results, although it has a slightly larger physical size than the bulk MZI.

Various design constraints on the use of this MZI (and other ESWLI) systems were experimentally demonstrated and supported by a full theoretical analysis. These design constraints included the consideration of the effects of modal noise in the interconnecting fibre coupler and of optical dispersion in the dual wavelength system. A thorough experimental analysis of the effects of dispersion provided quantitative data for a range of situations, providing a specification for the use of dual wavelength white-light interferometric sensors. Various methods of enhancing the identification of the central fringe were introduced in Chapter 4. The use of dual wavelengths as a combined synthetic source was found to be very effective in enhancing the identification of the central fringe. This technique was contrasted with the use of the centroid method and the least squares approach in order to enhance the accuracy of the central fringe identification. Both of these methods produced very accurate results when used to identify the central fringe position (40nm sensitivity), even in the presence of significant amounts of system noise. The centroid method was computationally faster than that of the least squares (LS) technique. However, the LS method provided more accurate results and had a larger operating range when compared to the use of the centroid method.

The system was successfully employed for the measurement of displacement and vibration. Displacement measurements were obtained providing repeatable measurement resolutions to an accuracy of 40nm and with a frame read-out rate of only 0.1ms, as shown in Chapter 5. In Chapter 6, the use of the MZI for the measurement of vibration was discussed. The simultaneous measurement of DC and AC stresses

spanning an amplitude range of 0.1 to 30μm was successfully obtained and this provided a major advantage over other proposed systems which cannot simultaneously measure DC and AC stresses (see Chapter 6). In addition, these other proposed schemes also require the use of frequency shifting modulators, polarization control or transmission gratings [6,7]. The system was also implemented for the measurement of higher frequency vibrations. This was successfully achieved using a photoconductive crystal as a detector in conjunction with the MZI. The intrinsic non-steady-state photo-electromotive force (PEMF) characteristics of the photoconductive crystal used had the added benefit of providing an intrinsic discrimination against unwanted DC steady-state signals. The system was experimentally verified to provide reproducible vibration frequency measurements across a 5kHz range (to ~mHz sensitivity), with the use of a simple signal processing approach. The system is also capable of measuring vibration amplitudes down to the picometer range and can detect the amplitude and direction of the target vibration. It is believed that the frequency response of the system can also be further improved (theoretically to the order of MHz) by the use of selective amplification and filtering of the crystal output.

Table 7.1 shows the operational characteristics that were achieved across the full range of the Fairchild CCD143A linear CCD that was used in this work [8] against what could be achieved when a Fairchild CCD191 linear CCD [8] is employed. The table shows various characteristics for various inclination angles, α, which shows that measurement resolutions down to 20nm can be achieved with a dynamic range of $\sim 10^3$. However, with the use of other commercially available, smaller pixel CCDs (such as the Fairchild CCD191), the measurement resolution will be greatly reduced. As shown in Table 7.1, the resolution is reduced by a factor of three (since the pixel-to-pixel spacing is only 10μm, compared with 26μm in the CCD143A). The CCD191 series CCD also has a larger width (6000 pixels) compared to the 2048 pixels in the CCD143A series CCD. This increases the operating range by a factor of two, providing a dynamic range of 6000, which exceeds the dynamic range results of other authors. *S. Chen et al.* reported a modified Mach-Zehnder [9] which was shown to provide a dynamic range of 600. *A. Koch et al.* reported an ESWLI based on a Michelson interferometer [10], which provided an operating range of 75μm and a resolution of

20nm, which yields a dynamic range of 3750. Therefore, by using this MZI with a CCD having a pixel pitch as small as that employed by *A. Koch et al* [10], will yield an enhanced dynamic range of 6000.

Table 7.1: Operational characteristics of the MZI when employed using two different linear CCD detectors

CCD characteristics	Inclination angle, α	Operating Range	Measurement Resolution	Dynamic Range
Fairchild CCD143A	0.02°	21μm	20nm	$\sim 10^3$
2048 pixels	0.1°	94μm	91nm	$\sim 10^3$
26μm pixel pitch	0.6°	565μm	0.54μm	$\sim 10^3$
CCD width 27mm	1.0°	0.94mm	0.91μm	$\sim 10^3$
Fairchild CCD191	0.02°	42μm	7nm	$\sim 6\times 10^3$
6000 pixels	0.1°	210μm	35nm	$\sim 6\times 10^3$
10μm pixel pitch	0.6°	1.26mm	209nm	$\sim 6\times 10^3$
CCD width 60mm	1.0°	2.1mm	0.35μm	$\sim 6\times 10^3$

7.2 Future Work

7.2.1. Dual output Mach-Zehnder interferometer

One additional advantage in the use of this MZI configuration is its dual outputs, as shown in Figure 7.1. Here, one output may be used to calibrate the system without disturbing the detected output. In addition to this, in the vibration experiment conducted in Chapter 6, the experiment could have been extended further by combining the two experiments.

Here, the CCD could be employed to measure large amplitude, slowing varying DC and AC stresses, whilst the second output could be interrogated by the photoconductive crystal (PCC) in order simultaneously to measure smaller amplitude, higher frequency vibrations, as shown in Figure 7.1. Using this combination could theoretically yield a sensor which could detect vibration frequencies up to the kilohertz region with mHz sensitivity, whilst also detecting vibration amplitudes stemming from the picometer to micrometer range.

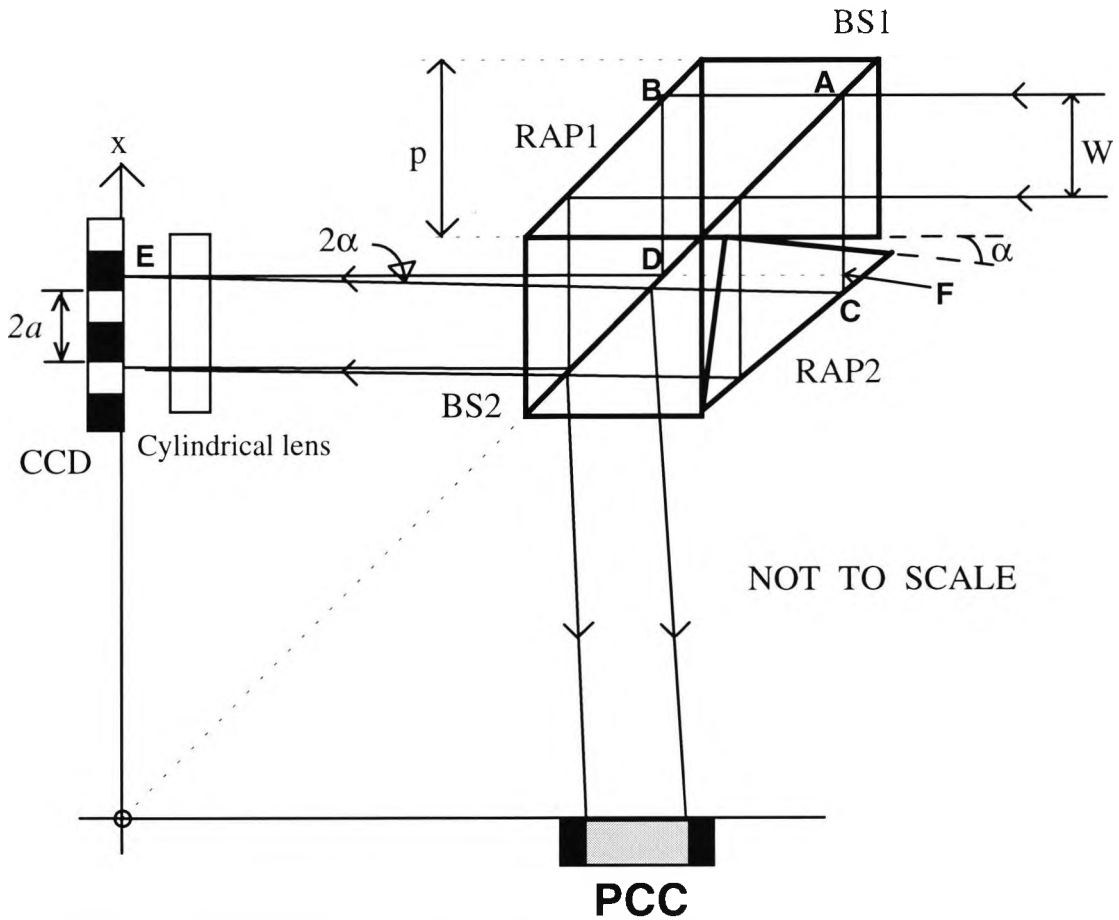

Figure 7.1: Dual output bulk-optic Mach-Zehnder configuration using a CCD detector for one output and a photoconductive crystal (PCC) for the other output. RAP1, RAP2 are right-angled prisms; BS1, BS2 are cubic beamsplitters, W is the beam-width, p=25mm, α is the inclination angle and CCD is the linear CCD detector

7.2.2. Manufacture of the Mach-Zehnder interferometer

The tilt angle, α, in the MZI was made adjustable in this work in order to investigate the effects of this tilt for various applications. Indeed, this angle has a direct effect on the sensitivity and operating range of the sensor (as shown in Section 3.3), whereby an increase in α provides a corresponding increase in the operating range, but however provides an inversely proportional reduction in the sensitivity, and vice-versa.

However, for each particular application, the tilt angle could be fixed, such that a range of MZIs could be manufactured for various applications (preferably in a similar manner to a Wollaston prism [4,5]). This could be achieved by simply using a slightly larger right angled prism, RAP2, as shown in Figure 7.2. This is used to provide the tilt angle, α, simply by polishing its face to a known inclination angle, α. This provides a more solid and stable MZI recovery interferometer unit, which can be manufactured as an "off-the-shelf" unit, as shown in Figure 7.2.

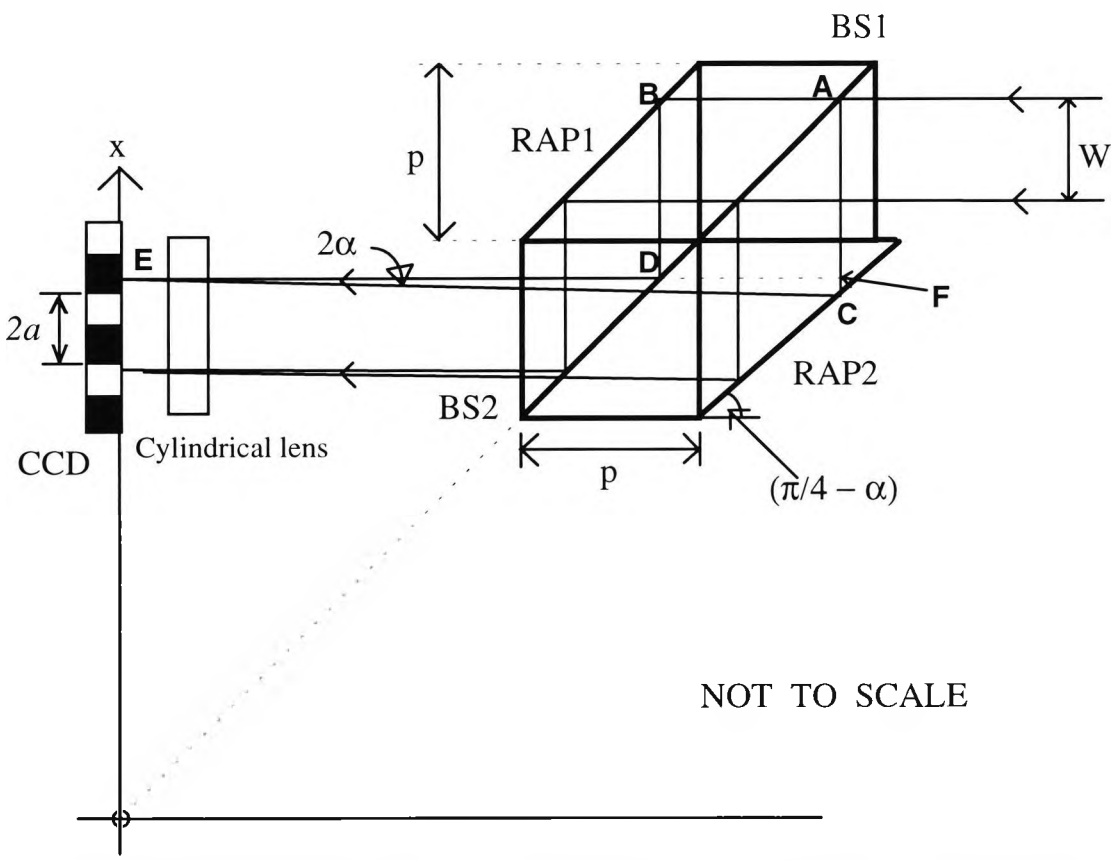

Figure 7.2: The bulk-optic Mach-Zehnder configuration used in this work. RAP1, RAP2 are right-angled prisms; BS1, BS2 are cubic beamsplitters, W is the beam-width, p=25mm, α is the inclination angle and CCD is the linear CCD detector

This ESWLI has been experimentally demonstrated to be adaptable to provide high resolution measurements of displacement and vibration and may also be employed to measure several other physical parameters by simply changing the sensing head. The Mach-Zehnder recovery interferometer may also be manufactured as a single bulk-optical component, which facilitates the mass production of this device. These factors combine to provide a good industrial market potential for this system.

7.3. References

1. Jackson, D. A. and Jones, J. D. C.: "Fibre Optic Sensors", Opt. Acta, vol. 33, pp. 1469-1503, 1986.
2. Jackson, D. A., Kersey, A. D., Corke, M. and Jones, J. D. C.: "Pseudo heterodyne detection scheme for optical interferometers", Electron Lett., vol. 18, pp. 1081, 1982.
3. Meggitt, B. T.: "Fiber optic white-light interferometric sensors", Ch. 9, pp. 269-312, In: "Optical Fiber Sensor Technology", Eds. Grattan, K. T. V. and Meggitt, B. T., Chapman & Hall, London, 1995.
4. Jiang, X. Q., Kemp, J., Ning, Y. N., Palmer, A. W., and Grattan, K. T. V.: "Accurate wavelength determination in a Wollaston interferometer for sensing applications", IEEE Photonic Tech. Letts., vol. 8, pp. 1055-57, 1996.
5. Padgett, M. J. and Harvey, A. R.: "A static Fourier-transform spectrometer based on Wollaston prisms", Rev. Sci. Instrum, vol. 66, pp. 2807-2811, 1995.
6. Sheng, S. Y. and Yongdong, J.: "Laser heterodyne vibration measuring method", Opt. and Laser Technol., vol. 20, No.2, pp. 100-102, 1988.
7. Weir, K., Boyle, W. J. O., Palmer, A. W. and Grattan, K. T. V.: "A novel adaptation of the Michelson interferometer for the measurement of vibration", J. Lightwave Tech., vol. 10, pp. 700-703, 1992.
8. Loral Fairchild: "Loral Fairchild imaging sensors", California, USA, pp. 9-91, 1991.
9. Chen, S., Meggitt, B. T. and Rogers, A. J.: "Electronically-scanned white light interferometry with enhanced dynamic range", Electron. Letts., vol. 26, pp. 1663-1665, 1990.
10. Koch, A. and Ulrich, R.: "Displacement sensor with electronically scanned white-light interferometer", SPIE vol. 1267, Proc. Fibre Optics Sensors IV, pp. 126-132, 1990.

Appendix A

Essential Principles of Interferometry

A1.0. Interference Effects

Light is a transverse electromagnetic wave, characterised by time varying electric and magnetic fields. It is usually sufficient to consider either one and ignore the other in simple analysis. It is conventional to retain the electric field, mainly because its interaction with matter is in most cases far stronger than that of the magnetic field [1,2].

For an electric field, $\overline{E}$, the differential wave equation is given by [1,3]

$$\nabla^2 \overline{E} = \frac{1}{\upsilon^2} \frac{\partial^2 \overline{E}}{\partial t^2} \tag{A-1}$$

where ∇ is the Laplacian operator given by

$$\nabla^2 \equiv \frac{\partial^2}{\partial x^2} + \frac{\partial^2}{\partial y^2} + \frac{\partial^2}{\partial z^2} \tag{A-2}$$

and υ is the velocity of the electromagnetic wave, which in free space is given by $\upsilon = 1/\sqrt{\varepsilon_0 \mu_0}$.

The term interference applies to the phenomenon through which waves, under certain conditions, intensify or weaken each other. Expressions such as "constructive" and "destructive" are referred to in many texts [1, 2, 3], however these terms strictly should not be used because they imply that there could somehow be a "destruction of light". This does not occur, since if less light reaches a given point, more light reaches some other point, so that interference merely causes a redistribution of light across a spatial pattern.

The prerequisite of interference is the superposition of waves. The problem of finding the resultant wave produced when several waves act together at a point in space is a common one in many optical systems. In these situations, the principle of superposition applies, whereby when two light waves are superimposed on each other, the resultant is obtained by constructing their vector sums at each point in time and space.

A1.0.1. Superposition of waves of constant phase difference

In an analysis of such a situation, it is useful to consider two waves that have the same frequency but have a certain constant phase angle difference between them [1,2]. Initially, the electromagnetic wave will be expressed as a scalar solution of the differential wave equation (equation A-1) in the form

$$E(x,t) = E_0 \cos[\omega t - (kx + \varepsilon)] \tag{A-3}$$

where E_0 is the amplitude of the harmonic disturbance propagating along the positive x axis; ω is the angular frequency, t is the time, k is the wave-number and ε is the initial phase. Let the total phase of the disturbance, φ, be represented by

$$\varphi(x,\varepsilon) = -(kx + \varepsilon) \tag{A-4}$$

then the associated wave may be represented by

$$E(x,t) = E_0 \cos[\omega t + \varphi] \tag{A-5}$$

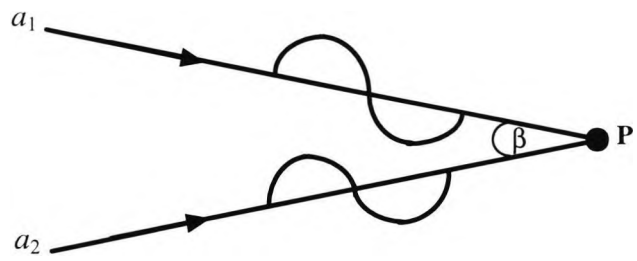

Figure A1.1: Schematic representation of the superposition of two electromagnetic waves, a_1 and a_2, of the same frequency. Solely for the purpose of clarity, the incident waves are shown to have an arbitrary angle, β, between them.

Suppose that two such light waves a_1, a_2,(as shown in Figure A1.1), which interfere with each other at a point P, are defined by their electric fields as

$$\begin{aligned} a_1 &= E_1 \cos(\omega t + \varphi_1) \\ a_2 &= E_2 \cos(\omega t + \varphi_2) \end{aligned} \tag{A-6}$$

having the same frequency and speed and are superimposed at a point in space, where E_1 and E_2 are the amplitudes of the two respective waves and φ_1 and φ_2 are their respective phases. Figure A1.1 illustrates the incident waves having an inclination angle, β, between them, introduced solely for the purpose of enhancing the clarity of this schematic representation. In the following analysis, it is assumed that there are no spatial interference effects present (see section A1.2.2). The resultant field, a_T, at the point, P, will be given by the linear superposition of these waves:

$$\begin{aligned} a_T &= a_1 + a_2 \\ &= E_1 \cos(\omega t + \varphi_1) + E_2 \cos(\omega t + \varphi_2) \end{aligned} \tag{A-7}$$

Using elementary trigonometry, a_T, may be expressed as

$$a_T = E_1[\cos\omega t \cos\varphi_1 - \sin\omega t \sin\varphi_1] + E_2[\cos\omega t \cos\varphi_2 - \sin\omega t \sin\varphi_2] \tag{A-8}$$

By separating out the time dependent terms, this becomes

$$a_T = \left[E_1 \cos\varphi_1 + E_2 \cos\varphi_2\right]\cos\omega t - \left[E_1 \sin\varphi_1 + E_2 \sin\varphi_2\right]\sin\omega t \tag{A-9}$$

Since the bracketed quantities in Equation (A-9) are constant in time, let

$$E_T \cos\varphi_T = \left[E_1 \cos\varphi_1 + E_2 \cos\varphi_2\right] \tag{A-10}$$

and

$$E_T \sin\varphi_T = \left[E_1 \sin\varphi_1 + E_2 \sin\varphi_2\right] \tag{A-11}$$

By squaring and adding Equations (A-10) and (A-11) the following is obtained

$$E_T^2 = E_1^2 + E_2^2 + 2E_1E_2\cos(\varphi_2 - \varphi_1) \tag{A-12}$$

and by dividing Equation (A-11) by Equation (A-10), this gives

$$\tan\varphi_T = \frac{E_1 \sin\varphi_1 + E_2 \sin\varphi_2}{E_1 \cos\varphi_1 + E_2 \cos\varphi_2} \tag{A-13}$$

The total disturbance then becomes

$$\begin{aligned} a_T &= E_T \cos\varphi_T \cos\omega t - E_T \sin\varphi_T \sin\omega t \\ &= E_T \cos(\omega t + \varphi_T) \end{aligned} \tag{A-14}$$

Thus a single disturbance results from the superposition of the sinusoidal waves, a_1 and a_2. The composite wave (Equation (A-14)) is harmonic and of the same frequency as the constituents, although its amplitude and phase are different. The intensity [3] of a light wave is proportional to its amplitude squared. Hence, it follows from Eqn. (A-12) that the resultant flux density is not simply the sum of the component flux densities; there is an additional contribution, $2E_1E_2\cos(\varphi_2-\varphi_1)$, which is known as the interference term.

In the majority of interferometric sensing systems, the incident source intensity is split into two components of equal amplitude [4]. For this very important case where $E_1=E_2=E$, where E is an arbitrary field amplitude assumed to be equivalent to one-half the incident source amplitude, then Equation (A-12) results in

$$E_T^2 = 2E^2\left(1+\cos(\varphi_2-\varphi_1)\right)$$
$$\equiv 4E^2\cos^2\left(\frac{\varphi_2-\varphi_1}{2}\right) \qquad \text{(A-15)}$$

which yields what are usually called cos^2 fringes or 2-beam fringes [5]. Using the half-angle trigonometric identities on Equation (A-15) yields

$$\tan\varphi_T = \tan\left(\frac{\varphi_1+\varphi_2}{2}\right) \qquad \text{(A-16)}$$

The intensity of the wave will be proportional to E_T^2, so that, from Equation (A-15), the intensity will vary from $4E^2$ to zero as $(\varphi_2-\varphi_1)/2$ varies from zero to $\pi/2$.

The crucial factor in the analysis of an interferometric system is the phase difference between the two interfering waves a_1 and a_2, which is denoted by δ, where δ is given by $(\varphi_2-\varphi_1)$. When $\delta=0, \pm2\pi, \pm4\pi, \pm6\pi, \ldots$, the resultant amplitude is a maximum, whereas when $\delta=\pi, \pm3\pi, \pm5\pi, \ldots$, yields a minimum. In the former case, the waves are said to be in phase, while in the latter case, the waves are π out of phase, as shown in Figure A1.2.

The phase difference, δ, may arise from a difference in path length traversed by the two waves, as well as any difference in the initial phase angle. Thus, the phase difference, δ, may be represented as

$$\delta = (kx_2+\varphi_2)-(kx_1+\varphi_1)$$
$$\equiv \frac{2\pi}{\lambda}(x_2-x_1)+(\varphi_2-\varphi_1) \qquad \text{(A-17)}$$

where x_1 and x_2 are the distances from the sources of the two waves to the point of observation, and λ is the wavelength of the source.

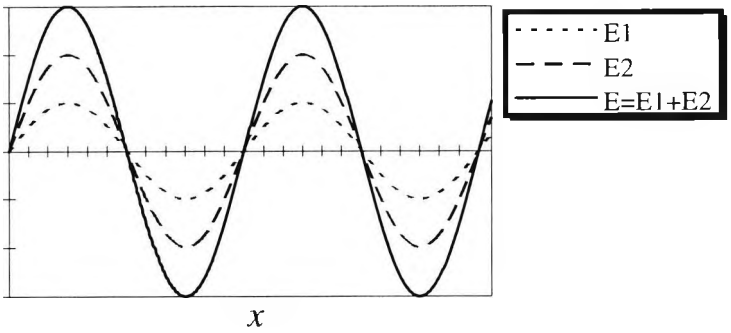

(a)

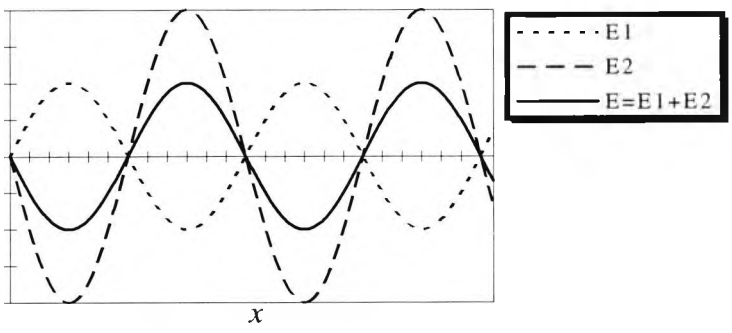

(b)

Figure A1.2: The superposition of two harmonic waves, highlighting the Intensity (arb. units) as a function of the propagation distance, x, (a) in phase; and (b) out of phase

Waves for which $(\varphi_2-\varphi_1)$ is constant, regardless of its value, are said to be coherent [2, 3, 4]. If the waves are initially emitted in phase, then $\varphi_1 \equiv \varphi_2$, and the phase difference, δ, is given by

$$\delta = \frac{2\pi}{\lambda}(x_2 - x_1). \tag{A-18}$$

The refractive index, n, is given by

$$n = \frac{c}{\upsilon} = \frac{\lambda_0}{\lambda} \tag{A-19}$$

where c is the speed of the electromagnetic wave in a vacuum, υ is the speed of the electromagnetic wave in matter; and λ_0 is the wavelength in vacuum. Thus, it follows that the phase difference, δ, is given by

$$\delta = \frac{2\pi}{\lambda} n(x_2 - x_1) \tag{A-20}$$

The quantity, $n(x_2-x_1)$, is known as the optical path difference (OPD).

A1.1. Intensity Considerations

The intensity, I, of light has been defined as the time average of the amount of energy which crosses in unit time a unit area perpendicular to the direction of the energy flow. For a plane wave:

$$I = \frac{c}{4\pi}\sqrt{\frac{\varepsilon}{\mu}}\langle E^2\rangle = \frac{c}{4\pi}\sqrt{\frac{\mu}{\varepsilon}}\langle H^2\rangle \qquad \text{(A-21)}$$

where ε is known as the permittivity, μ is the permeability and H is the magnetic field Since in this work, all intensities will be compared in the same medium, then the quantity, $\langle E^2\rangle$ will be taken as a measure of the intensity. In many texts, intensity and irradiance are described as being one and the same [2,3], they are in fact defined as different quantities. Intensity represents the irradiated power from a point source and irradiance represents the power from a surface. Therefore, they must be distinctly defined whenever the geometry of the source and detector have to be taken into account [4,6]. The intensity may be defined as the absolute square of the field, E;

$$I = \langle E.E^* \rangle \qquad \text{(A-22)}$$

then from equations (A-12) and (A-22), the resultant intensity is given by

$$I = I_1 + I_2 + 2\sqrt{I_1 I_2}\cos\varphi \qquad \text{(A-23)}$$

whereby $I_1=\langle E_1^2\rangle$ and $I_2=\langle E_2^2\rangle$ are the intensities of the two waves (shown in Figure A1.1), and $2\sqrt{I_1 I_2} = 2\langle E_1.E_2\rangle \equiv 2E_1E_2\cos\varphi$ is the interference term [4], where the optical phase difference, φ, is given by $(\varphi_2-\varphi_1)$.

A1.2. Theoretical Background to Coherence considerations

Coherence is sometimes defined as the condition necessary to produce interference, and interference is defined as an interaction of waves that are coherent [4]. However, these circular arguments do not provide any clarity to the situation. Coherence implies that two or more waves in a radiation field are in a fixed and predictable phase relationship to each other. Thus, the time for which the wave-train remains represented by a simple harmonic relationship is called the coherence time and the associated distance travelled is the coherence length [3,4]. The coherence of a wave describes the extent to which it can be represented by a pure sine wave. A practically generated sine wave does not have infinite extension, unlike a theoretically pure sine wave of infinite extent. Perfect coherence is thus unachievable, however waves which can be represented by sine waves for a limited period of time or in a limited region of space are called partially coherent waves.

When an area is illuminated simultaneously by two or more incoherent sources, the resultant, I, from such sources will yield an illumination defined by a simple intensity sum, i.e. the sum of the intensities which would be produced by the individual sources acting separately, as given by

$$I \propto \sum_{i=1}^{N} E_i^2 \tag{A-24}$$

However, if the waves from the different sources maintain constant phase relationships, then they are coherent with each other. Thus, the resultant intensity will vary from point to point, yielding interference fringes. Hence, for in-phase coherent sources, the resultant intensity, I, is given by

$$I = \left(\sum_{i=1}^{N} E_i \right)^2 \tag{A-25}$$

Two classes of coherence are important in this work; spatial coherence and temporal coherence. Temporal coherence for example for waves travelling along the

same path, refers to the constancy, and the predictability, of phase as a function of time. Spatial coherence by comparison is exemplified by the phase relationship between waves travelling side by side, at a certain distance from one another. The farther apart the two waves, the less likely they will be in phase, and the less coherent the light will be [3,4].

A1.2.1. Temporal Coherence

Light wavetrains can be considered to be represented by a length, Δs, termed the coherence length, the product of the number of waves, N, contained in the wavetrain and of their wavelength, λ;

$$\Delta s = N\lambda \tag{A-26}$$

Since it takes a wavetrain of length, Δs, a certain length of time, Δt, to pass a given point then

$$\Delta t = \frac{\Delta s}{c} \tag{A-27}$$

where c is the velocity of light and the associated length of time, Δt, is called the coherence time.

The most convenient method of measuring the degree of temporal coherence of a light source is to use a Michelson interferometer [4, 6, 7]. A schematic representation of which is shown in Figure A1.3. It is simply composed of two mirrors, B and C, and a beamsplitter, A, where the incident beam from the source, S, is incident at an angle of 45° with respect to the beamsplitter, A. This beam is then split into two components by the beamsplitter, A, one of which is incident on and then reflected off mirror C. This beam then travels back along the same path via beamsplitter A, to the detector, D, where the other beam is incident upon mirror, B, where it is reflected back along path BA. This beam is then reflected again off the back face of A, where it is reflected by 90°, and is then incident on the detector, D. If the two paths, ABA and ACA, (as shown in Figure A1.3), are equal in length, the fringes observed at point, D, will have maximum contrast, and hence amounted with that maximum temporal coherence. If

they are not equal in length, the contrast is less pronounced. The degree of temporal coherence is thus inversely proportional to the magnitude of the optical path difference (OPD) and is directly proportional to the length of the wavetrains.

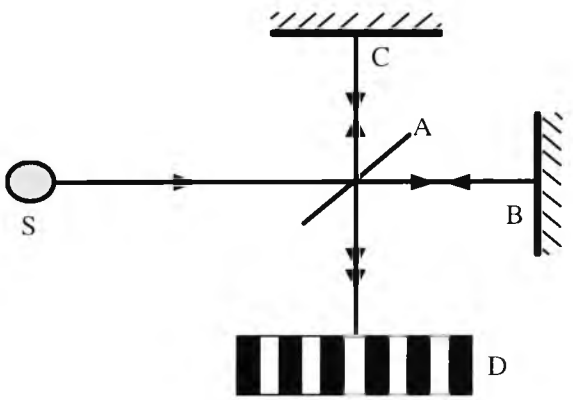

Figure A1.3: Schematic representation of a Michelson interferometer employed for the measurement of the temporal coherence length

A1.2.2. Spatial Coherence

In order to observe the effects of spatial coherence, a simplified schematic representation of Young's interferometer [3] may be employed, as shown in Figure A1.4. Here, the light is incident from a source, S, onto a double slit. On a distant screen, C, a system of interference fringes is observed. With highly spatially coherent light, the fringes contrast (or visibility - see section A1.3) is high. As the two slits, A and B, are moved further apart, the fringes become more closely spaced and the pattern produced will lose contrast. Again, the degree of contrast is a measure of the degree of spatial coherence.

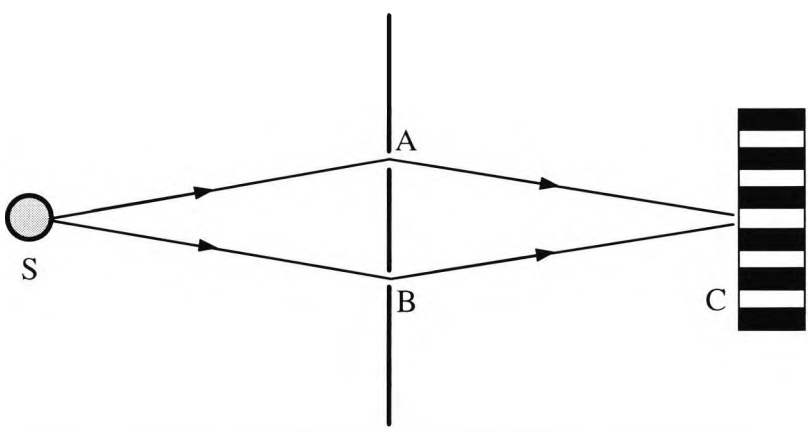

Figure A1.4: Schematic representation of Young's double slits employed for the measurement of spatial coherence

A1.2.3. Coherence time and coherence length

The coherence time, t_c, may then be defined as the time taken for the source to emit a wavetrain of length L_c, such that [3,4]:

$$t_c = \frac{L_c}{c} \tag{A-28}$$

The coherence time may also be related to the linewidth of the source emission, $\Delta\nu$, by the expression [8,9,10]

$$\Delta\nu = \nu_0 - \nu = \frac{1}{t_c} \tag{A-29}$$

whereby, for quasi-monochromatic light, $\Delta\nu << \nu_0$, and ν_0 is the mean frequency. From the uncertainty relationships [2] the inequality relating the average duration of the wave train, Δt_c, and the effective frequency range of the spectrum, $\Delta\nu$, may be given by

$$\Delta t_C \Delta\nu \geq \frac{1}{4\pi} \tag{A-30}$$

In most cases of practical interest, this inequality may be replaced by the order of magnitude sign [2];

$$\Delta t_C \Delta\nu \sim \frac{1}{4\pi} \tag{A-31}$$

From equation (A-31), $$L_c = c\Delta t_c \sim \frac{c}{\Delta\nu} \tag{A-32}$$

and using the relationship

$$\lambda = \frac{c}{\nu} \tag{A-33}$$

then by differentiating both sides, the following is obtained

$$\frac{\Delta\nu}{\Delta\lambda} = \frac{-c}{\lambda^2} \tag{A-34}$$

If λ_0 is the mean wavelength, then

$$\frac{c}{\Delta\nu} = \frac{\lambda_0^2}{\Delta\lambda} \tag{A-35}$$

Substituting Eqn. (A-33) into (A-32) yields

$$L_C = \frac{\lambda_0^2}{\Delta\lambda} \tag{A-36}$$

where $\Delta\lambda$ is the source spectral width [9].

A1.3. Fringe Visibility

The fringe visibility is a very important measure of the quality of the interference fringes. The definition of visibility is based on a matter of comparison, and thus the fringe visibility, V, can be defined as the ratio of the difference between the maximum intensity, I_{max}, and minimum intensity, I_{min}, to the sum of the intensities in a fringe pattern, i.e.

$$V = \frac{I_{max} - I_{min}}{I_{max} + I_{min}} \tag{A-37}$$

Assuming that the minimum intensity, I_{min}, is zero, and the maximum value, I_{max}, takes any arbitrary value, then the visibility, V=1. However, if $I_{max}=I_{min}$, then V=0 and no fringes can be observed. The visibility may vary between 0 and 1 and assume any value in between dependent on the values of I_{max} and I_{min}. The degree of visibility of the fringes produced by the interference of two waves is equal to the degree of coherence between these two waves [11].

For quasi-monochromatic light with a spectral distribution function, $P(\nu)$, that is symmetric about $\nu=\nu_0$, as illustrated in Figure A1.5(a), the corresponding oscillatory term, $I(\tau)$, [8] may be expressed as

$$I(\tau) = C(\tau)\cos 2\pi\nu\tau \qquad \text{(A-38)}$$

where τ is the retardation time between the two beams as introduced by the OPD between them.

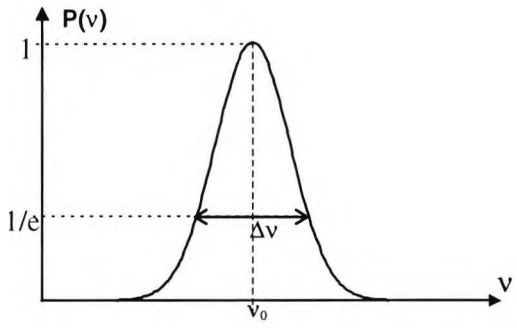

Fig. A1.5(a): A curve that characterises the spectral distribution of energy emitted by the quasi-monochromatic source

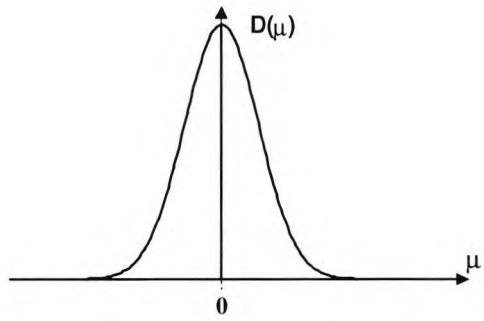

Fig. A1.5(b): The curve of Fig. A1.5(a) with a change of origin

For quasi-monochromatic light (as defined in [2]), the spectral distribution function is peaked about $\nu=\nu_0$, where ν_0 is the mean of a range of frequencies, defined by a function, $P(\nu)$, and tends to zero rather rapidly as ν departs significantly from ν_o. If $\Delta\nu$ is the spectral width of this spectral distribution function, $P(\nu)$, then it follows that $\Delta\nu<<\nu_o$. It is convenient to write $P(\nu)$ in the form

$$P(\nu) = D(\nu - \nu_0) \qquad \text{(A-39)}$$

where $D(\mu)$ is small except for the interval $(-\Delta\nu/2)<\mu<(+\Delta\nu/2)$. Equation (A-39) merely represents a change of origin from ν to $\mu(\equiv\nu-\nu_0)$.

For quasi-monochromatic light with a spectral distribution function in the form of a Gaussian distribution[8]

$$P(\nu) = D(\nu - \nu_0) = \exp\left[-\left(\pi^2(\nu-\nu_0)^2\tau_d^2\right)\right]\sqrt{\pi}\tau_d \qquad \text{(A-40)}$$

The parameter τ_d has dimensions of time and characterizes the width of the distribution, since P(ν) is reduced to *1/e* of its value at $\nu=\nu_0$, when $\nu=\nu_0\pm 1/\pi\tau_d$. Also, for the light to be quasi-monochromatic, it is necessary that $\tau_d\nu>>1$. The normalised oscillatory term, I(τ), that describes the interference pattern is given by [8]

$$I(\tau) = C(\tau)\cos 2\pi\nu_0\tau \tag{A-41}$$

where

$$C(\tau) = \exp\left[-\left(\frac{\tau}{\tau_d}\right)^2\right] \tag{A-42}$$

and

$$I(\tau) = e^{\left[-\left(\frac{\tau}{\tau_d}\right)^2\right]}\cos 2\pi\nu_0\tau \tag{A-43}$$

The relationships between $P(\nu)$ and ν and $I(\tau)$ and τ is shown in Figure A1.5(a) and Figure A1.6 respectively. The visibility function, C(τ), as given by Equation (A-42), has a retardation time factor, τ, which is given by

$$\tau = \frac{\delta}{c} \tag{A-44}$$

where δ is the OPD between the two beams.

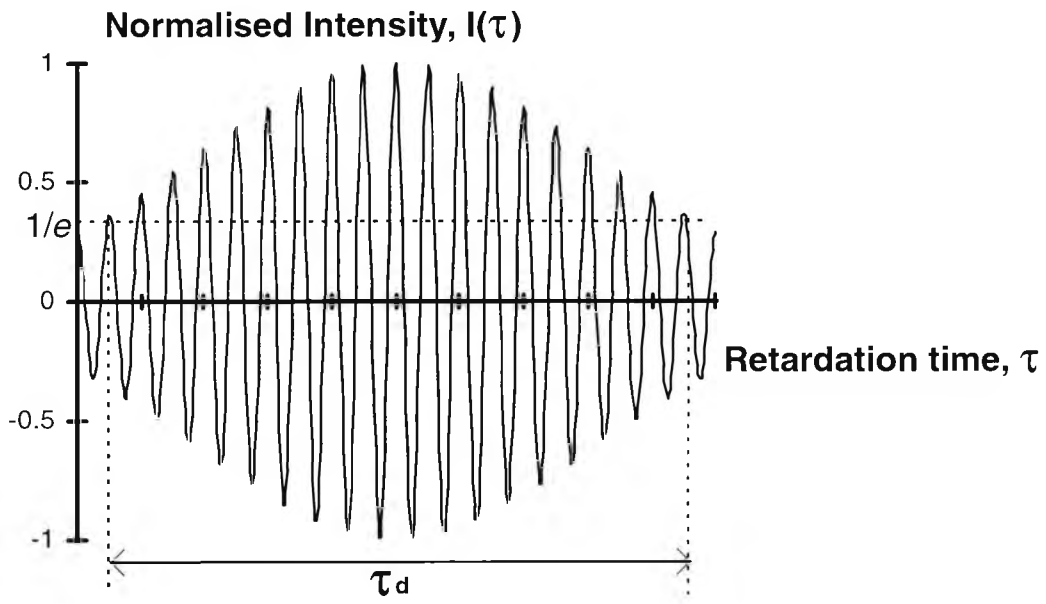

Figure A1.6: Normalised oscillatory term, $I(\tau)$, which corresponds to the general spectral distribution function, for a quasi-monochromatic line with a Gaussian shape (shown in Fig, A1.5(a)) and a coherence time, τ_d.

Substituting equations (A-44) and (A-45) into Equation (A-42) yields a visibility function, $C(\tau)$, as given by

$$C(\tau) = \exp\left[-\left(\frac{\delta}{l_c}\right)^2\right] \tag{A-46}$$

which is the general visibility function for a quasi-monochromatic source [2,8,12].

A1.4. Essential Interferometry

Interference phenomena can readily be observed in interferometers. Most interferometers are composed of the following elements; a light source; an element for splitting the light in two (or more) partial waves; different propagation paths where the partial waves undergo different phase contributions; an element for superposing the partial waves; and a detector for observation of the interference effect.

Depending on how the light is split, interferometers may usually be classified as wavefront-dividing or amplitude-dividing; although there are configurations which fall outside this classification. In a wavefront-splitting interferometer, portions of the primary wavefront are used either directly as sources to emit secondary waves or in conjunction with other optical devices to produce virtual sources of secondary waves. These secondary waves are then brought together, to interfere. However, this scheme is really only useful with sufficiently small sources [2] and utilises only a fraction of the maximum available light source intensity. In the latter case of amplitude splitting, the primary wave itself is divided into two segments, which travel along different paths before recombining and interfering. Amplitude-splitting interferometers can be used with extended sources, and thus the effects may be of greater intensity than with the use of division of wavefront.

From Equation (A-23), the intensity, I, of the superposition of two quasi-monochromatic waves may be expressed as;

$$I = I_1 + I_2 + 2\sqrt{I_1 I_2}\,|\gamma(t)|\cos(\varphi_2 - \varphi_1) \qquad \text{(A-47)}$$

where $\gamma(t)$, is the complex degree of coherence and is a measure of the ability of the two waves to interfere [13]; $I_1 \equiv E_1^2$ and $I_2 \equiv E_2^2$ which are the intensities of each respective beam; $\varphi_1 \equiv$ phase of beam 1; $\varphi_2 \equiv$ phase of beam 2; such that $(\varphi_2 - \varphi_1)$ is the optical phase difference, φ.

Whenever the phase difference, φ, is zero, there will be a maximum amount of light,

$$I_{max} = I_1 + I_2 + 2\sqrt{I_1 I_2}\,|\gamma(t)| \qquad \text{(A-48)}$$

which, when $I_1 = I_2$ and $\gamma(t) = 1$, becomes;

$$I_{max} = 4I_1 \qquad \text{(A-49)}$$

On the other hand, whenever the phase difference is π, there will be a minimum amount of light,

$$I_{min} = I_1 + I_2 - 2\sqrt{I_1 I_2}|\gamma(t)| \tag{A-50}$$

which, when $I_1=I_2$ and $\gamma(t)=1$, becomes $I_{min}=0$.

At points that lie between the maximum and minimum, under the same conditions

$$\begin{aligned} I &= 2I_1(1+\cos\varphi) \\ &= 4I_1\cos^2\left(\tfrac{\varphi}{2}\right) \end{aligned} \tag{A-51}$$

When equations (A-48) and (A-50) are substituted into the general visibility formulae (Equation (A-37)) yields a visibility, V, given by;

$$V = \frac{2\sqrt{I_1 I_2}\,|\gamma(t)|}{I_1 + I_2} \tag{A-52}$$

For two waves of equal intensity, $I_1=I_2$ and Equation (A-52) becomes $V = |\gamma(t)|$, which shows that in this case, $|\gamma(t)|$ is exactly equal to the visibility. If the two contributions are unequal, there will be some excess light (from the more energetic contribution), and the minima will not be completely dark. As a consequence, the light distribution resulting from a superposition of waves will consist of alternating bright and dark bands in the form of interference fringes. Figure A1.7 shows the energy distribution across a few fringes, such as may result when projected on a screen.

If only one beam of light illuminates the screen, the distribution is uniform, as shown by the lower horizontal line labelled I_1 in Figure A1.7. If there are two incoherent beams of light of equal energy, the distribution is once again uniform, however now there is twice as much light (shown by the upper horizontal line labelled $2I_1$). In addition, if the two beams are coherent, then they will produce interference in the form of alternate maxima and minima.

If $I_1=I_2$, then the maxima (from Equation (A-51), will contain four times the energy of each individual beam contribution, and the minima will contain no energy, as shown in Figure A1.7. This results in the familiar $\cos^2$ fringe curve [3], which is

labelled $4I_1$. Here, the areas under the curves $2I_1$ and $4I_1$ are identical, since energy can neither be created nor destroyed, with the interference causing a redistribution of this energy.

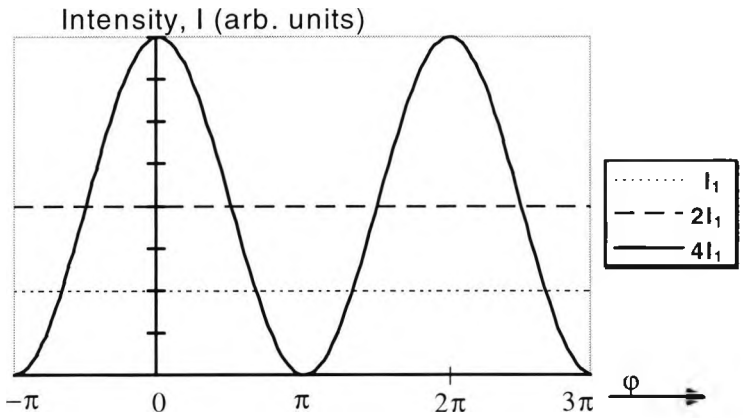

Figure A1.7: Energy distributions produced by 1 source; 2 sources not causing interference; and 2 sources capable of causing interference

A1.5 Summary

The essential principles of interferometry have been introduced in order to serve as an essential pre-requisite to the principles of white-light interferometry. The fundamental theories of interferometry, superposition, intensity, coherence and visibility are essential foundations of white-light interferometry.

A1.6 References

1. Hecht, E and Zajac, A: "Optics", Ch. 2, pp. 12-29, 2nd ed., Addison-Wesley, 1987.
2. Born, M., and Wolf, E.: "Principles of Optics", Ch. 1, pp. 1-70, 4th ed., Pergamon press, 1970.
3. Meyer-Arendt, J.: "Introduction to classical and modern optics", Ch. 2, pp. 173-278, 2nd ed., Prentice-Hall, 1984.

4. Rogers, A. J., "Essential optics", Ch. 3, pp. 25-106, In: "Optical fiber sensors: Principles and components", Eds. Dakin, J. and Culshaw, B., Artech House, Boston, 1988.
5. Welford, W. T.: "Optics", Ch. 3, pp. 37-57, 3rd ed., Oxford University Press,1988.
6. Jackson, D. A., and Jones, J. D. C.: "Fibre Optic Sensors", Opt. Acta, vol. 33, 1469-1503, 1986.
7. Meggitt, B. T.: "Fiber optic white-light interferometric sensors", Ch. 9, pp. 269-312, In: "Optical Fiber Sensor Technology", Eds. Grattan, K. T. V. and Meggitt, B. T., Chapman & Hall, London, 1995.
8. Klein, M. V. and Furtak, T. E.: "Optics", Ch. 8, 2nd ed., Wiley, New York, 1986.
9. Francon, M: "Optical interferometry", Ch.1, pp. 1-34, Academic Press, London, 1966.
10. Hopkins, H. H.: "The theory of coherence and its applications", Ch. 6, In: "Optical electronics", 3rd ed., Ed. Yariv, A., Holt-Sanders, Japan, 1985.
11. Van Cittert, P. H.: "Degree of Coherence," Physica 24, 505-7, 1958.
12. Gerges, A. S., Farahi, F., Newson, T. P., Jones, J. D. C. and Jackson, D. A.: "Fibre-optic interferometric sensors using a low coherence source: dynamic range enhancement", International J. of Optoelectronics, vol. 3, No. 4, 311-322, 1988.
13. Gasvik, K. J.: "Optical Metrology", Ch. 3, pp. 27-50, 2nd ed., John Wiley, England, 1995.

Appendix B

Fizeau Interferometer Analysis

B1.0. Fizeau Interferometer

The configuration of a conventional Fizeau interferometer consists of a wedge with 2 partially reflective surfaces, P1 and P2, as illustrated in Figure B1.1. The collimated incident light (normal to P2) is split into many transmitted (T0, T1,...,) and reflected (R0, R1,...,) beams due to the multiple reflections between the two surfaces. The fringes from the interference between transmitted beams T0 and T1 are detected by a CCD array, and produce the required signal.

B1.1 Analysis of the Fizeau Interferometer

In this Fizeau interferometric configuration, the surfaces P1 and P2 have been separated by an additional distance H, as shown in Figure B1.1. This was done in order to validate the use of this simplified two beam model rather than use a three beam model. This occurs since the effects of any multiple reflections are increasingly subdued with an increase in H, which produces a relatively larger OPD between the beams, which implies that only adjacent beams will be coherent. A spatial offset, d, between the surface P2 and the CCD has also been introduced in order to improve the accuracy of this model (Figure B1.1).

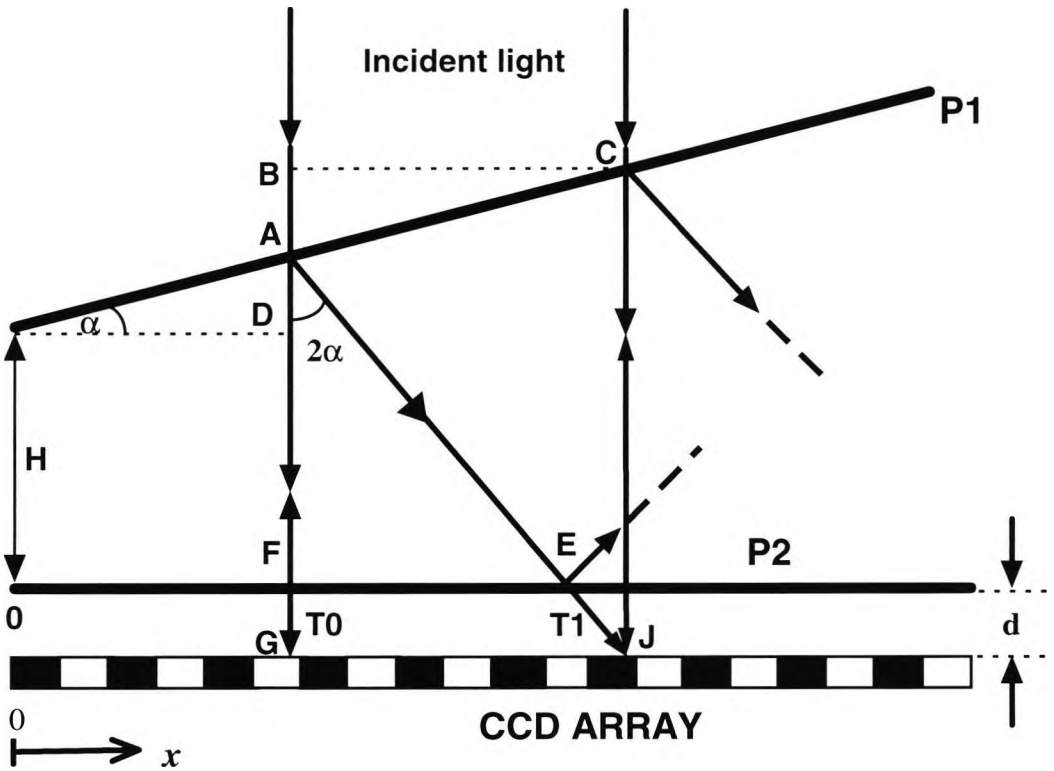

Figure B1.1: Schematic representation of a conventional Fizeau Interferometer producing spatial interference fringes. This configuration shows only 2 significant beams in the interference process. *P1, P2* are mirrors (assumed here to have 50% reflectance and negligible thickness in order to ignore the effects of refraction in this basic model). α is the angle of inclination mirrors P1 and P2.

Before constructing the full analysis that incorporates multiple reflections, it was assumed that the coherence length of the source was initially short enough to enable the effects of the interference between rays T0 and T2, T1 and T3, T2 and T4, etc.., to be negligible. Hence, the analysis could be simplified to a two beam model, which only takes into account the interference between adjacent rays (i.e. T0 and T1, T1 and T2,.. etc.). From the schematic representation of the Fizeau interferometer (shown in Figure B1.1), an arbitrary section of the incident beam is simplified by considering that it is represented by two rays, R1 and R2.

Let the light be incident normal to the mirror P2. Now consider the interference at the point J produced by the ray CJ and the ray BADFDAEJ, which is reflected once at each surface. Ray BADF is isolated through an angle π (at mirror P2) to return to point A, and then through an angle 2α (at mirror P1) to reach point J. Let the path

length taken by ray R1 via BADFDAEJ be denoted by L_1, and the path length taken by ray R2 via CJ be denoted by L_2.

From Figure B1.1, the path length L_1, is given by:

$$\begin{aligned} L_1 &= BA + AD + H + H + DA + AE + EJ \\ &= BA + 2(AD + AH) + AE + EJ \end{aligned} \tag{B-1}$$

Likewise, path length L_2, is given by:

$$L_2 = CJ \tag{B-2}$$

The resultant optical path difference (OPD) is given by:

$$\begin{aligned} OPD &= L_1 - L_2 \\ &= BA + 2(AD + AH) + AE + EH - CJ \end{aligned} \tag{B-3}$$

However, from Figure B1.1,

$$CJ \equiv BA + AD + H + d \tag{B-4}$$

where d is the displacement between the CCD and beamsplitter P1 (as shown in Figure B1.1). Thus, from Equations (B-3) and (B-4), the OPD is given by:

$$OPD = AD + AE + H + EJ - d \tag{B-5}$$

where;

$$\begin{aligned} AD &= x\tan(\alpha) \\ AE &= \frac{AF}{\cos(2\alpha)} \equiv \frac{(AD + H)}{\cos(2\alpha)} \\ EJ &= \frac{d}{\cos(2\alpha)} \end{aligned} \tag{B-6}$$

If the intensity reflection coefficient = R, then the electric field reflection coefficient, r, is given by $\sqrt{R}$. The total electric field, E_J, at an arbitrary point, J, is given by the superposition of the fields E_1 and E_2, which are representative of the respective beams L_1 and L_2. If the electric field at point J, due to rays R1 and R2, are

denoted by E_1 and E_2 respectively, then, from the principle of superposition (see Chapter 2), the electric field, E_J, at point J may be expressed as

$$\begin{aligned} E_J &= E_1 + E_2 \\ &= r_1 r_2 (1-r_1)(1-r_2) E_0 e^{-j(kL_1-\omega t)} + (1-r_1)(1-r_2) E_0 e^{-j(kL_2-\omega t)} \\ &= E_0 \left[r_1 r_2 (1-r_1)(1-r_2) e^{-j(kL_1-\omega t)} + (1-r_1)(1-r_2) e^{-j(kL_2-\omega t)} \right] \end{aligned} \tag{B-7}$$

$$E_J = E_0 e^{+j\omega t} \left[r_1 r_2 (1-r_1)(1-r_2) e^{-j(kL_1)} + (1-r_1)(1-r_2) e^{-j(kL_2)} \right] \tag{B-8}$$

$$E_J^* = E_0 e^{-j\omega t} \left[r_1 r_2 (1-r_1)(1-r_2) e^{+j(kL_1)} + (1-r_1)(1-r_2) e^{+j(kL_2)} \right] \tag{B-9}$$

where E_0 is the initial electric field amplitude; r_1 is the reflectivity of surface P1; r_2 is the reflectivity of surface P2; and k is the wave-number, given by $2\pi/\lambda$, where λ is the source wavelength. The total intensity at point J, I_J, is given by

$$I_J = E_J . E_J^* \equiv (E_1 + E_2).(E_1 + E_2)^* \tag{B-10}$$

where the asterix dentoes the complex conjugate.

From equations (B-8), (B-9) and (B-10), the resultant total intensity may be expressed as:

$$\begin{aligned} I = E_0^2 \left[r_1^2 r_2^2 (1-r_1)^2 (1-r_2)^2 + r_1 r_2 (1-r_1)^2 (1-r_2)^2 e^{-j(k(L_1-L_2))} \right] + \\ E_0^2 \left[r_1 r_2 (1-r_1)^2 (1-r_2)^2 e^{+j(k(L_1-L_2))} + (1-r_1)^2 (1-r_2)^2 \right] \end{aligned} \tag{B-11}$$

By utilising the trigonometric identity;

$$\frac{e^{-jx} + e^{+jx}}{2} = \cos(x) \tag{B-12}$$

equation (B-11) may be re-expressed as

$$I = E_0^2\left[(1-r_1)^2(1-r_2)^2(r_1^2r_2^2+1)+2r_1r_2(1-r_1)^2(1-r_2)^2\cos\left(k(L_1-L_2)\right)\right] \tag{B-13}$$

$$\Rightarrow I = E_0^2\left[A+2B\cos\left(k(L_1-L_2)\right)\right] \tag{B-14}$$

in which the constants A and B are given by;

$$\begin{aligned} A &= (1-r_1)^2(1-r_2)^2(r_1^2r_2^2+1) \\ B &= r_1r_2(1-r_1)^2(1-r_2)^2 \end{aligned} \tag{B-15}$$

However, equation (B-14) implies that the intensity profile distribution has a linear coherence profile. This is unrealistic since most have a Gaussian coherence profile (see Chapter 2), and thus the intensity, I, is now given by

$$I = E_0^2[A+2B\cos(k\delta)]e^{-\left(\delta/L_C\right)^2} \tag{B-16}$$

where L_c is the coherence length of the source, and the OPD between the two beams, δ, is given by (L_1-L_2). Equation (B-16) equates with the standard interferometric equation (Chapter 2) as shown in Equation (B-17):

$$I = A_1 + A_2 + 2V(\delta)\sqrt{A_1A_2}\cos(\delta) \tag{B-17}$$

where δ = OPD and $V(\delta)$ = exponential visibility function. The analogy between equations (B-16) and (B-17) is shown in the identities (B-18).

$$\begin{aligned} \therefore\ A &\equiv A_1 + A_2 \\ &\equiv \left((1-r_1)^2(1-r_2)^2r_1^2r_2^2\right)+\left((1-r_1)^2(1-r_2)^2\right) \\ \therefore\ B &\equiv \sqrt{A_1A_2} \\ &\equiv (1-r_1)^2(1-r_2)^2r_1r_2 \end{aligned} \tag{B-18}$$

Appendix C

ESWLI Processing System
Turbo Pascal Program Listing

The following program was compiled using Borland Turbo Pascal v6.0.

```
program rs232coms;
{$N+}
{$M 65520,0,655360}

{ ***************************************************************
  Version 1.1   Electronically-Scanned White-Light Interferometry Sensing
                System Software

                This program reads in the fringe interferogram from an ESWLI
                which employs a CCD detector. The CCD is interfaced to a Digital
                Storage Adaptor (DSA) which has an inbuilt 8bit A/D C.

                This program interfaces with the DSA (via the RS232 port) to record
                the background beam intensity profile and the fringe interferogram. The
                beam profile is eliminated from the interferogram and the processed
                fringes are stored in a file. The central fringe position of the processed
                fringes is then computed.

                This program eliminates the beam profile from the response, by moving
                the Fabry-Perot mirror until it is out of coherence in order to obtain
                the beam profile. Whereby this profile is divided into the response to
                yield the processed fringes.

  Written on 17 July 1995     (c) Ray Marshall
  ***************************************************************
```

The addresses for the primary RS232 port are $3F8 to $3FE, while the addresses for the secondary RS232 port are $2F8 to $2FE

Code	Primary ADDRESS	Secondary ADDRESS	Register Selected	DLAB State
adrs[1]	$3F8	$2F8	Tx Buffer	0
adrs[1]	$3F8	$2F8	Rx Buffer	0
adrs[1]	$3F8	$2F8	Divisor latch LSB	1
adrs[2]	$3F9	$2F9	Divisor latch MSB	1
adrs[2]	$3F9	$2F9	Interrupt Enable Register	
adrs[3]	$3FA	$2FA	Interrupt Ident. Register	

```
adrs[4] |  $3FB  |  $2FB  | Line Control Register   |
adrs[5] |  $3FC  |  $2FC  | Modem Control Register  |
adrs[6] |  $3FD  |  $2FD  | Line Status Register    |
adrs[7] |  $3FE  |  $2FE  | Modem Status Register   |
```

Thus by control of the data loaded into the array adrs, the port which is to be addressed can be controlled. The value of the variable coms is the flag:-

```
coms = 1   =>   primary serial port
coms = 2   =>   secondary port
```

for this to work the array adrs must be global. }

```
{This program gives the option to store the data in a file in the
 form:-
   point number(integer)  ch1 value(integer)  ch2 value(integer)
         "                "                "
 etc for all the 1024 points then there follows the three strings:-

   Time base details (string)
   channel 1 details (string)
   channel 2 details (string)

}

{ Remember that I have dispensed with the trace2 arrays in order to conserve
  variable space }

uses crt,dos,graph;
type dsa_trace = array [0..1025] of real;


{****** Declare variables ******}
var
  i,j,coms,
  baud_rate,datanum :integer;
  centre_fringe_pixel_position:integer;
  ch,
  yes_no,
  data_age,
  data_source,
  interferogram_choice,
  menu_choice,reference_choice,
  re_scan_choice    :char;
  comstr,repstr,errorstr:string;
  DSR,RLSD,CTS      :boolean;
  adrs              :array [1..7] of integer;
  trace1,trace2, trace1b, trace1c,
```

```
 trace1d, trace1s, ccdnoise     :dsa_trace;

 file_in,file_out              :text;
 time_label,
 f_in_name1,
 f_in_name2,
 f_in_name3,
 root_name,
 f_out_name1,
 f_out_name2,
 f_out_name3,path,
 channel1,channel2,time_base          :string;
 time_base_real,time_factor,
 ch1_gain, ch1_gain_factor,
 ch2_gain, ch2_gain_factor,
 ch3_gain_factor:real;
 time_unit,ch1_gain_unit,ch2_gain_unit,ch3_gain_unit,plot_title:string;
 min1, min2, mean:real;

 {also required for the graphics}
 xcoord   :real;
 xcomax,ycomax,
 xborder,yborder:integer;

 {now define the global variables required by the graphics as I've defined them:-
 xscale - scale factor for the x axis
 xoffset - offset for the x axis
 and similarily for the y axis
 These are needed in the procedures/functions :-
 open_graphic_window,
 xpoint, ypoint. These functions are then used in all graphics}

 xscale,xoffset,
 yscale,yoffset   :real;
 clip          :boolean;

{---------- The line/modem control/status register procedures-------}


procedure set_baud(rate:integer);
const
  clock_rate=1843200;
var
       i:longint;
       divisor:byte;
     {set baud rate and 8 bit words with no parity and one stop bit}
begin
     i:=clock_rate div 16;
     divisor:=i div rate;
```

```
      {set Line Control Register:
       bit 7 high for DLAB high
       bits 6,5,4 low
       bit 3 low for no parity
       bit 2 low for  one stop bit
       bit 1 and 0 high for 8 bits to data}
      port[adrs[4]]:=$83;
      {now set baud rate LSB = divisor LSB}
      port[adrs[1]]:=lo(divisor);
      {now set baud rate MSB = divisor MSB}
      port[adrs[2]]:=hi(divisor);
      {now set DLAB low again - test it is high first}
      if (port[adrs[4]] and $80) = $80 then
          port[adrs[4]]:=(port[adrs[4]] XOR $80);
end;


procedure set_interrupt;
begin
{no interrupts}
    port[adrs[2]]:= $00;
end;


procedure Set_Data_Terminal_Ready;
{set modem control register bit 0 high}
{NOT bit 1 which is RTS}
begin
    port[adrs[5]]:= $01;
end;


procedure Unset_Data_Terminal_Ready;
{set modem control register bit 0 low}
{NOT bit 1 which is RTS}
begin
    if (port[adrs[5]] AND $01) = $01 then
        port[adrs[5]]:=(port[adrs[5]] XOR $01);
end;


procedure Set_Ready_To_Send;
begin
{set modem control register bit 1 High}
          port[adrs[5]]:=(port[adrs[5]] OR $02);
end;


procedure Unset_Ready_To_Send;
```

```
begin
{set modem control register bit 1 low}
     if (port[adrs[5]] and $02) = $02 then
          port[adrs[5]]:=(port[adrs[5]] XOR $02);
end;


function Data_Set_Ready:boolean;
{Test modem status register for bit 5}
begin
    Data_Set_Ready:=((port[adrs[7]] and $20)= $20);
end;


function Receive_Line_Signal_Detect:boolean;
{test modem status register for bit 7}
begin
    Receive_Line_Signal_Detect:=( (port[adrs[7]] and $80) = $80);
end;


function Clear_To_Send:boolean;
{test modem status register for bit 4}
begin
    Clear_To_Send:=((port[adrs[7]] and $10) = $10);
end;

{----------End of the line/modem control/status register procedures-------}


{------------------- Start of graphic procedures -------------------------}

{Including the following procedures...

 the global variables required by the graphics as I've
 defined them are:-
 xscale - scale factor for the x axis
 xoffset - offset for the x axis
       - and similarily for the y axis
 clip   - boolean for clipon or clipoff
 These are needed in the procedures/functions :-
 open_graphic_window,
 xpoint, ypoint. These functions are then used in all graphics


        procedure initializegraphics;
        procedure
open_graph_window(xsize,ysize:integer;xmin,xmax,ymin,ymax:real);
        function int2str(i:longint):string;
```

```
        function real2str(x:real):string;
        procedure clipping(onoff:boolean);
        function xpoint(x:real):integer;
        function ypoint(y:real):integer;
        procedure draw_axes(xcross,ycross,xmin,xmax,ymin,ymax,xtic,ytic:real);
        procedure plot_point(x,y:real);
        procedure label_axes(xlabel,ylabel,title:string;xcross,ycross:real);
                        .....}


procedure initializegraphics;
{.....}

var
grdrive, grmode, errcode :integer;

begin
   { setup graphics }
   clip:=true;
   grdrive:=detect;
   initgraph(grdrive,grmode,'c:\TP\BGI');
   errcode:=graphresult;
   if errcode<>0 then
    begin
        writeln('Graphics Error ',grapherrormsg(errcode));
        writeln('program terminates....');
        halt(1);
    end;
end;


procedure
open_graph_window(xin,yin,xsize,ysize:integer;xmin,xmax,ymin,ymax:real);
{.....}
{xsize, ysize are the size of the window in graphics units,
 it is automatically centred in the screen.
 xmin, xmax, ymin,ymax are the x and y range of values to be plotted}

var
xscmax,yscmax   :integer;

begin
{set limits for the view port to be used-_____}
     xscmax:=xin+xsize;
     yscmax:=yin+ysize;
     {set range of input values to be mapped to screen}
     {calculate scaling and offset factors----------}
     xscale:=(xsize)/(xmax-xmin);
     yscale:=-1.0*(ysize)/(ymax-ymin);
```

```
    xoffset:=(xsize/xscale)-xmax;
    yoffset:=-ymax;
    {now xsc(on screen)=trunc((xin(in range -2,2)+xoffset)*xscale)) and similar for y}
    setcolor(1);                {magenta=5, blue=1}
    setbkcolor(14);             {yellow=14, white=15}
    setviewport(xin,yin,xscmax,yscmax,clipon);
end;


function int2str(i:longint):string;
var s:string;
begin
    str(i,s);
    int2str:=s;
end;


function real2str(x:real):string;
var s:string;
begin
      str(x:5:1,s);
      real2str:=s;
end;


procedure clipping(onoff:boolean);
{.....}
{switches clipping on or off depending on onoff}
var port:viewporttype;
begin
      getviewsettings(port);
      with port do
       setviewport(x1,y1,x2,y2,onoff);
end;


function xpoint(x:real):integer;
begin
      xpoint:=trunc((x+xoffset)*xscale);
end;


function ypoint(y:real):integer;
begin
       ypoint:=trunc((y+yoffset)*yscale);
end;
```

```
procedure draw_axes(xcross,ycross,xmin,xmax,ymin,ymax,xtic,ytic:real);
{.....}
{xcross, ycross are the co-ords of the crossing point of the axes,
 the other constants define the length of the axes}
const ticlength =10;
var x,y :real;

begin
        clipping(clipoff);
        {setcolor(14);}
        moveto(xpoint(xmin),ypoint(ycross));
        lineto(xpoint(xmax),ypoint(ycross));
        moveto(xpoint(xcross),ypoint(ymin));
        lineto(xpoint(xcross),ypoint(ymax));
        settextjustify(centertext,centertext);
        settextstyle(defaultfont,horizdir,1);
        if (xtic<>0.0) AND (ytic<>0.0) then
         begin
            x:=xmin;
            repeat
               moveto(xpoint(x),ypoint(ycross));
               linerel(0,-ticlength);
               moverel(0,2*ticlength);
               outtext(real2str(x));
               x:=x+xtic;
            until x>xmax;
            y:=ymin;
            settextjustify(righttext,centertext);
             repeat
                    moveto(xpoint(xcross),ypoint(y));
                    linerel(ticlength,0);
                    moverel(-ticlength-5,0);
                    outtext(real2str(y));
                    y:=y+ytic;
             until y>ymax;
        end;
        clipping(clipon);
end;


procedure plot_point(x,y:real);
{.....}
const dx=2;
begin
        moveto(xpoint(x),ypoint(y));
        moverel(dx,0);
        linerel(-2*dx,0);
        moverel(dx,dx);
```

```
          linerel(0,-2*dx);
end;


procedure label_axes(xlabel,ylabel,title:string;xcross,ycross:real);
{.....}
const xpixeloffset=30;
    ypixeloffset=20;
var port:viewporttype;

begin
        clipping(clipoff);
        getviewsettings(port);
        with port do
         begin
             moveto(((x2-x1) div 2),-xpixeloffset);
             if length(title)>20 then
               settextstyle(triplexfont,horizdir,1)
             else
               settextstyle(triplexfont,horizdir,2);

             settextjustify(centertext,centertext);
             outtext(title);
         end;
        moveto(xpoint(xcross),ypoint(ycross));
        moverel(270,xpixeloffset);
        settextstyle(Triplexfont,horizdir,1);
        settextjustify(lefttext,bottomtext);
        outtext(xlabel);
        moveto(xpoint(xcross),ypoint(ycross));
        moverel(-50,0);
        settextstyle(Triplexfont,vertdir,1);
        settextjustify(centertext,lefttext);
        outtext(ylabel);
        clipping(clipon);
end;


{--------------------End of (general) Graphic procedures ----------}


procedure writebase(s:string;i,base:integer);
const
  digits : array [0..15] of char='0123456789ABCDEF';
var
 outstr:string;
 dummy,count:integer;
 temp:char;
```

```
begin
        outstr:='';
        dummy:=i;
        count:=0;
        repeat
                outstr:=outstr+digits[dummy MOD base];
                count:=count+1;
                dummy:=dummy DIV base;
        until dummy=0;
        {NOW WE HAVE THE REQUIRED STRING BUT IT IS BACK TO FRONT}
        {count:=length(outstr);}
        dummy:=1;
        repeat
                temp:=outstr[dummy];
                outstr[dummy]:=outstr[count];
                outstr[count]:=temp;
                dummy:=dummy+1;
                count:=count-1;
        until count<=dummy;
        writeln(s,outstr);
end;


procedure report_register_status;
begin
        writeln('Status of registers associated with RS232');
        writebase('Tx/Rx buffer ',port[adrs[1]],16);
        writebase('Interrupt enable r ',port[adrs[2]],16);
        writebase('Interrupt Ident r ',port[adrs[3]],16);
        writebase('Line Control Reg ',port[adrs[4]],16);
        writebase('Modem Control Reg ',port[adrs[5]],16);
        writebase('Line Status Reg ',port[adrs[6]],16);
        writebase('Modem Status Reg ',port[adrs[7]],16);
end;


procedure all_upperc(var s:string);
var i:integer;
begin
          for i:=1 to length(s) do
           s[i]:=upcase(s[i]);
end;
```

```
procedure out_command(cstr:string;var ers:string);
const crcode=$0D;
    countout=100000;

var i,j,
  ercount:integer;
begin
      i:=0;
      j:=0;
      ers:='';
      repeat
           ercount:=0;
           Set_Data_Terminal_Ready;
           repeat
            ercount:=ercount+1;
       until ((port[adrs[7]] and $10) = $10) or (ercount>countout);   {CTS FROM
DSA}
       repeat
            ercount:=ercount+1;
       until ((port[adrs[6]] and $20) = $20) or (ercount>countout);   {Tx EMpty}
       if ((port[adrs[6]] and $20) = $20) and ((port[adrs[7]] and $10) = $10) then
       begin
            i:=i+1;
            port[adrs[1]]:=ord(cstr[i]);
            port[adrs[5]]:=(port[adrs[5]] XOR $01);
            {Unset_Data_Terminal_Ready;  Removes CTS at DSA, in line for
increased speed}
            {output ASCII code to port}
            {writeln(ord(cstr[i]));}
       end
        else
           ers:='ERROR IN ESTABLISHING LINK';
      until (i=length(cstr)) or (ercount>countout);
      i:=0;
      if (ercount<countout) then
      repeat
           Set_Data_Terminal_Ready;
           repeat
            ercount:=ercount+1;
       until ((port[adrs[7]] and $10) = $10);   {CTS FROM DSA}
       repeat
          ercount:=ercount+1;
       until ((port[adrs[6]] and $20) = $20);   {Tx EMpty}
       if ((port[adrs[6]] and $20) = $20) and ((port[adrs[7]] and $10) = $10) then
        begin
            i:=1;
            port[adrs[1]]:=crcode;
            port[adrs[5]]:=(port[adrs[5]] XOR $01);
```

```
            {Unset_Data_Terminal_Ready;  Removes CTS at DSA, in line for
increased speed}
            {writeln(crcode);}
        end;
      until i=1;
end;


procedure read_string(var s:string);
const
 crcode = $0D;
 countout=100000;
var
 ch:char;
 chno,i,ercount:integer;
begin
      s:='';
      i:=0;
      repeat
            ercount:=0;
           { Set CTS at DSA,
            Wait for the  data Holding Register  Flag in line status reg,
            Then Unset CTS at DSA}
            Set_Data_Terminal_Ready;   {Asserts CTS at DSA}
            repeat
                ercount:=ercount+1;
            until ((port[adrs[6]] and $01) = $01) or (ercount>countout);
            port[adrs[5]]:=(port[adrs[5]] XOR $01);
            {Unset_Data_Terminal_Ready;  Removes CTS at DSA, in line for
increased speed}
            if (port[adrs[6]] and $01) = $01 then
            begin
                chno:=port[adrs[1]];
                ch:=chr(chno);
                {read ASCII code from port and apppend to string}
                s:=s+ch;
            end
            else
                s:=s+' ERROR CTS NOT DETECTED';
      until (ord(ch)=crcode) or (ercount>countout);  { or (i>countout);}
      {writeln('This is the read string of length ',length(s),' ',s);}
      s:=copy(s,1,length(s)-1);
      {writeln(s);}
end;
```

```
procedure read_data_stream_bin(var tra:dsa_trace;var s:string);
{read data as binary stream}
const crcode = $0D;
    countout=100000;
var
 chno,i,j,
 ercount:integer;
 ch:char;

begin
      for i:=1 to 1024 do
       tra[i]:=0;
      i:=0;
      s:='';
      repeat
            ercount:=0;
           { Set CTS at DSA,
            Wait for the  data Holding Register  Flag in line status reg,
            Then Unset CTS at DSA}
            Set_Data_Terminal_Ready;   {Asserts CTS at DSA}
            repeat
                ercount:=ercount+1;
            until ((port[adrs[6]] and $01) = $01) or (ercount>countout);
            port[adrs[5]]:=(port[adrs[5]] XOR $01);
            {Unset_Data_Terminal_Ready;  Removes CTS at DSA, in line for
increased speed}
           if ((port[adrs[6]] and $01) = $01) then
           begin
                {IS data to be read so process}
                i:=i+1;
                tra[i]:=port[adrs[1]];
                { writeln('Element ',i,' value ',tra[i]);    test write out}
           end
           else
               s:='ERROR CTS NOT DETECTED';
          until (i=1024) or (tra[i]=crcode) or (ercount>countout);
            {tra[i]=crcode means a reading error}
          if tra[i]=crcode then
           for j:=1 to i do
                s:=s+chr(trunc(tra[j]))  {Changes data read into sting for error report}
          else
           repeat
            Set_Data_Terminal_Ready;   {Asserts CTS at DSA}
             repeat
                ercount:=ercount+1;
            until ((port[adrs[6]] and $01) = $01) or (ercount>countout);
            port[adrs[5]]:=(port[adrs[5]] XOR $01);
```

```
            {Unset_Data_Terminal_Ready;  Removes CTS at DSA, in line for
increased speed}
            if ((port[adrs[6]] and $01) = $01) then
            begin
                {read ASCII code from port and apppend to string}
                chno:=port[adrs[1]];
                ch:=chr(chno);
             s:=s+ch;
            end
            else
                s:=s+'ERROR CTS NOT DETECTED';
       until (ord(ch)=crcode) or (tra[i]=crcode) or (ercount>countout);
end;


function input(t1 :  string) :  string;
begin
      repeat
            writeln(t1);
            t1:='';
            readln(t1);
            while pos(chr(32),t1)=1 do delete (t1,1,1);
      until t1<>'';
      input:=t1;
end;


procedure append_dat(var fname:string);
{this adds the file type '.DAT' to the filename if not already supplied}
var
 len:integer;
 temps1:string;
begin
       len:=length(fname);
       temps1:=copy(fname,len-3,len);
       if (temps1='.dat') or (temps1='.DAT') then
          {do nothing}
       else
          fname:=concat(fname,'.DAT');
end;


procedure readdata2array_new(var F:text;fname:string;
                    var datin1,datin2:dsa_trace;var datnum:integer;
                          var chn1,chn2,tmb:string);
var i,dno,temp:integer;
  s:char;
begin
       assign(F,fname);
```

```
        reset(F);
        readln(F,dno);
        for I:=1 to dno do
         begin
            readln(F,temp,datin1[i],datin2[i]);
         end;
        readln(F,tmb);
        readln(F,chn1);
        readln(F,chn2);
end;


procedure write_data(var F:text;fname:string;
                  var datout1,datout2:dsa_trace;datnum:integer;
                        chn1,chn2,tmb:string);
var i:integer;
begin
        assign(F,fname);
        rewrite(F);
        writeln(F,datnum);
       i:=0;
       while i<datnum do
           { Writing zeroes to trace 2 file since trace 2 is in-active }
           begin
              i:=i+1;
              writeln(F,i,' ',datout1[i],' ',0);
              write('.');
           end;
       writeln('... done');
       writeln(F,tmb);
       writeln(F,chn1);
       writeln(F,chn2);
       close(F);
end;


procedure decode_time_info(tm_bs:string;var tm_bs_rl:real;var tm_ut:string);
var i,j:integer;

begin
       {DECODE TIME BASE INFO.}
       tm_bs_rl:=0.0;
       tm_ut:='';    {Use as dummy string for now}
       i:=1;
       while pos(tm_bs[i],'0123456789')=0 do
         inc(i); {skip to first number}
       while pos(tm_bs[i],'0123456789.')>0 do
        begin      {read the digits of the time base into a string}
             tm_ut:=tm_ut+tm_bs[i];
```

```
            inc(i);
        end;
        val(tm_ut,tm_bs_rl,j);
        tm_ut:='';      {blank before setting to time unit}
        j:=i;
        while tm_bs[j]<>',' do
        begin
            tm_ut:=tm_ut+tm_bs[j];
            inc(j);
        end;
end;


procedure decode_gain(ch_info:string;var ch_gain:real;var gain_unit:string);
var i,j:integer;
begin
        i:=1;
        j:=0;
        ch_gain:=0.0;
        gain_unit:='';
        repeat  {find second comma}
        if pos(ch_info[i],',')>0 then
          inc(j);
        inc(i)
        until j=2;
        while pos(ch_info[i],'0123456789.')>0 do
        begin     {read the digits of the gain into a string}
         gain_unit:=gain_unit+ch_info[i];
         inc(i);
        end;
        val(gain_unit,ch_gain,j);
        gain_unit:='';      {blank before setting to gain unit}
        j:=i;
        while ch_info[j]<>',' do
        begin
            gain_unit:=gain_unit+ch_info[j];
            inc(j);
        end;
end;


procedure find_mxmn(var tra:dsa_trace;datnum:integer);
var
 i:integer;
begin
        tra[0]:=256;     {this element will hold minimum value}
        tra[datnum+1]:=0; {this element will hold maximum value}
        for i:=1 to datnum do
        begin
```

```
                if tra[i]<tra[0] then
                 tra[0]:=tra[i];
                if tra[i]>tra[datnum+1] then
                 tra[datnum+1]:=tra[i];
        end;
end;


procedure scale_data(datin:dsa_trace;var datout:dsa_trace;datnum:integer);
{this is to scale the data into the range +/- 1}
var
 aver,dummy,
 diff,scale,
 max,min   :real;
 i     :integer;

begin
          max:=datin[datnum+1];
          min:=datin[0];
          diff:=(max-min);
          scale:=2/diff;
          aver:=(max+min)/2.0;
          for i:=1 to datnum do
           begin
                  datout[i]:=(datin[i]-aver)*scale;
           end;
           datout[0]:=-1;
           datout[datnum+1]:=1;
end;


procedure offset_data(datin:dsa_trace;var datout:dsa_trace;datnum:integer);
{this is to offset the data without scaling to give a signal symmetric about 0}
var
 aver,dummy,
 max,min   :real;
 i     :integer;
begin
       max:=datin[datnum+1];
       min:=datin[0];
       aver:=(max+min)/2.0;
       for i:=1 to datnum do
        begin
            datout[i]:=(datin[i]-aver);
        end;
       datout[0]:=datin[0]-aver;
       datout[datnum+1]:=datin[datnum+1]-aver;
end;
```

```
procedure find_min(trace1:dsa_trace;datnum:integer; var min:real);

{ *** finds the minimum value from the interferogram data *** }
var
  i    :integer;

begin

    for i:=1 to datnum do
       begin
       if trace1[i]<min then
            min:=trace1[i];
       end;

end;


procedure data_input_from_DSA(var repstr,comstr,errorstr,time_base:string;
                    var time_unit,channel1,channel2:string;
                    var time_base_real:real;
                    var trace1, trace2 : dsa_trace);

{ *** capture data from DSA ***}
var
  i    : integer;
begin
         set_interrupt;
         Set_Ready_To_Send;
         if (NOT Data_Set_Ready) or (NOT Receive_Line_Signal_Detect) then
                repstr:='ERROR IN DSR OR RLSD';
          i:=port[adrs[1]];  {read to flush i/o port}
          i:=0;
         if repstr='' then
          begin
                comstr:='MODE,BIN';
                out_command(comstr,errorstr);
                read_string(repstr);
                writeln('DSA set in ',comstr,repstr);
          end;
         {report_register_status;}
         out_command('CH1?',errorstr);
         read_string(repstr);
         if pos('OK',repstr)>0 then
             channel1:=repstr;
         out_command('CH2?',errorstr);
         read_string(repstr);
         if pos('OK',repstr)>0 then
             channel2:=repstr;
```

```
        out_command('TMB?',errorstr);
        read_string(repstr);
        if pos('OK',repstr)>0 then
            time_base:=repstr;
        writeln('CHANNEL 1 DETAILS ',channel1);
        writeln('CHANNEL 2 DETAILS ',channel2);
        writeln('TIME BASE DETAILS ',time_base);
        decode_time_info(time_base,time_base_real,time_unit);
        out_command('MEM?,TRA',errorstr);
        read_data_stream_bin(trace1,repstr);
        writeln(repstr);
        out_command('MEM?,TRB',errorstr);
        read_data_stream_bin(trace2,repstr);
        writeln(repstr);
end;


procedure store_data(var file_out:text;trace1,trace2:dsa_trace);

{ *** store data in a file ***}
var
  yes_no : char;
  root_name, f_out_name1 : string;
  i : integer;

begin
    writeln('Do you wish to store the data y/n');
    yes_no:=readkey;
    while pos(yes_no,'yYnN')=0 do
        yes_no:=readkey;
    if pos(yes_no,'yY')>0 then
    begin  {data is to be stored}
        root_name:='';
        writeln;
        writeln('Enter output file name for this data set');
        writeln('Please use no digits - File name will be');
        writeln('Truncated at a digit or at 7 characters');
        writeln;
        f_out_name1:=input('Enter Output file name for this data set:');
        i:=1;
        while (i<7) do
        inc(i);
        root_name:=copy(f_out_name1,1,i);
        f_out_name1:=root_name;
        f_out_name1:=concat(path,f_out_name1);
        append_dat(f_out_name1);
        writeln('Attempting to write to output file : ',f_out_name1);

write_data(file_out,f_out_name1,trace1,trace2,datanum,channel1,channel2,time_base);
```

```
    end;
end;


procedure plot_output_from_DSA(datanum:integer; var trace1,trace2:dsa_trace;
                        var time_base,time_label,time_unit,
                           plot_title:string;
                        var time_base_real, time_factor:real);

{ *** Plot interferogram on screen *** }

var
  xorigin, yorigin, xmin, xmax, ymin, ymax, xstep, ystep : real;
  i : integer;
  file_out : text;

begin

        find_mxmn(trace1,datanum);
        find_mxmn(trace2,datanum);
        initializegraphics;
        if time_base='' then
         begin
              {  time_label:='Time'; }
                time_label:='CCD pixel number';
               time_factor:=1.0;
         end
        else
         begin
            {  time_label:='Time ('+time_unit+')'; }
               time_label:='CCD pixel number';
              time_factor:=time_base_real/100.0;
         end;
        xorigin:=0.0;
        yorigin:=0.0;
        xmin:=0.0;
        xmax:=datanum*time_factor;
        if trace1[0]<trace2[0] then
            ymin:=trace1[0]
        else
            ymin:=trace2[0];
        {if trace1[datanum+1]<trace2[datanum+1] then
            ymax:=trace2[datanum+1]
         else
             ymax:=trace1[datanum+1];}

         { omit previous if statement since I am not using trace 2 at the moment }
         ymax:=trace1[datanum+1];
        xstep:=(xmax-xmin)/2.0;
```

```
        ystep:=(ymax-ymin)/2.0;
        open_graph_window(100,100,400,200,xmin,xmax,ymin,ymax);
        draw_axes(xmin,ymin,xmin,xmax,ymin,ymax,xstep,ystep);
        {plot output signals in this window}
        {First signal}
        moveto(xpoint(1*time_factor),ypoint(trace1[1]));
        for i:=2 to datanum do
        begin
              {plot the signals}
              {This is the first signal}
              lineto(xpoint(i*time_factor),ypoint(trace1[i]));
        end;
        {Second signal}
        moveto(xpoint(1*time_factor),ypoint(trace2[1]));
        for i:=2 to datanum do
        begin
              {plot the signals}
              {This is the second signal}
              lineto(xpoint(i*time_factor),ypoint(trace2[i]));
         end;
        label_axes(time_label,'Detected Intensity',plot_title,xmin,ymin);
        readln;
        closegraph;
        store_data(file_out,trace1,trace2);
end;


procedure press_enter_when_ready;
{ *** prompt for user entry of <ENTER> to continue *** }

begin
    writeln;
    writeln('Press <ENTER> when ready.....,');
    readln;
end;


procedure eliminate_spikes(var trace1:dsa_trace;datanum:integer);

{ *** eliminates any noise spikes from data *** }

var
  i          : integer;
  sum, mean    : real;

begin
    sum:=0.0;
    mean:=0.0;
    for i:=1 to datanum do
```

```
      sum:=sum + trace1[i];

   mean:=sum/(datanum*1.0e0);
   for i:= 1 to datanum do
      begin
       if (trace1[i]>(2.1*mean)) OR (trace1[i]<(mean/2.1)) then
          trace1[i]:=mean;
      end;

end;


procedure initialise_settings;

{ *** initialise all DSA settings ***}

begin
    clrscr;
    comstr:='';
    repstr:='';
    time_base:='';
    path:='C:\data\';
    datanum:=1024;      {number of pieces of data}
    baud_rate:=9600;   {Maximum baud rate tested is 19200}
    coms:=2;           {coms equals 1 for primary port and 2 for secondary port}
    for i:=1 to 7 do
     {calculates an array of addresses correct depending on the setting of coms}
      adrs[i]:=($4F7+i)-coms*$100;
 {
 These Initializations should always be carried out irrespective of
 source of data
 }
end;


procedure display_data_from_file;

{ *** displays interferogram from previously saved plot *** }
begin
        f_in_name1:=input('Enter root file name for data set:');
        i:=1;
        while (i<7) do
          inc(i);
        root_name:=copy(f_in_name1,1,i);
        f_in_name1:=root_name;
        f_in_name1:=concat(path,f_in_name1);
        append_dat(f_in_name1);
        writeln('Attempting to read data from ',f_in_name1);
```

```
readdata2array_new(file_in,f_in_name1,trace1,trace2,datanum,channel1,channel2,time
_base);
        decode_time_info(time_base,time_base_real,time_unit);
        decode_gain(channel1,ch1_gain,ch1_gain_unit);
        decode_gain(channel2,ch2_gain,ch2_gain_unit);
        plot_title:='Output Signals';
        plot_output_from_DSA(datanum,trace1,trace2,time_base,time_label,
              time_unit,plot_title,time_base_real,time_factor);
end;


Procedure read_in_beam_profile_from_dsa;

 begin
    { read in and display beam profile }
    writeln('Move Fabry-Perot mirror out of coherence to observe beam profile');
    press_enter_when_ready;
    data_input_from_DSA(repstr,comstr,errorstr,time_base,time_unit,
                    channel1,channel2,time_base_real,trace1b,trace2);
    find_min(trace1b,datanum,min1);
    plot_title:='Beam profile';
    plot_output_from_DSA(datanum,trace1b,trace2,time_base,time_label,
                    time_unit,plot_title,time_base_real,time_factor);

 end;


Procedure read_in_fringes_from_dsa;

 begin {read in interferogram}
      writeln;
      writeln('Please set-up interference fringes on CCD');
      press_enter_when_ready;
      data_input_from_DSA(repstr,comstr,errorstr,time_base,time_unit,
                  channel1,channel2,time_base_real,trace1,trace2);

      find_min(trace1,datanum,min2);
      plot_title:='Interferogram output';
      { plot output interferogram on screen}
      plot_output_from_DSA(datanum,trace1,trace2,time_base,time_label,
                  time_unit,plot_title,time_base_real,time_factor);
end;
```

```
Procedure centre_heading;
{ procedure simply produces 10 writeln satatements in order to position }
{ text at centre of page }

 var
  count:integer;

 Begin
   for count:=1 to 10 do
      writeln;
 end;


Procedure find_centre_fringe_position;

{ *** Computes the centre fringe position using the threshold technique *** }
 var
    count : integer;
    max_value : real;

Begin
    { Find the maximum value in data array 1d }
    max_value:=0.0;
    For count:=1 to datanum do
       Begin
          If (trace1d[count]>max_value) then
            begin
               max_value:=trace1d[count];
               centre_fringe_pixel_position:=count;
            end;
       End;
    centre_heading;
    writeln(' central fringe occurs at pixel number ',centre_fringe_pixel_position);
    press_enter_when_ready;

End;


 Procedure eliminate_beam_profile;

 Begin { eliminates the beam profile using the division method }

       plot_title:='Interferogram output with uniform beam profile';
      { plot new processed response }
      writeln('Eliminating beam profile from response.....,');
      if min1>min2 then
         min1:=min2;

      { Division method }
```

```
        for i:=1 to datanum do
          begin

           if (trace1b[i]=min1) then
             trace1d[i]:=trace1d[i-1]
           else
             trace1d[i]:= (trace1[i] - min1) / (trace1b[i] - min1) ;
          end;

        plot_output_from_DSA(datanum,trace1d,trace2,time_base,time_label,
                    time_unit,plot_title,time_base_real,time_factor);
        find_centre_fringe_position;

        eliminate_spikes(trace1d,datanum);
        writeln('Eliminating spikes from plot...,');
        plot_output_from_DSA(datanum,trace1d,trace2,time_base,time_label,
                    time_unit,plot_title,time_base_real,time_factor);
        find_centre_fringe_position;

end;


{ * * * * * *  S T A R T   O F   M A I N   P R O G R A M  * * * * * * * }

begin

Repeat

    min1:=100000.0;
    min2:=100000.0;

    initialise_settings;
    writeln('         ***********************************************');
    writeln('         ** Fringe Interferogram Processing Software  **');
    writeln('         ***********************************************');
    writeln;
    Writeln('      IS DATA FROM FILE (F) OR DSA (D) CONNECTED VIA
RS232');
    data_source:=readkey;
    while pos(data_source,'dDfF')=0 do
        data_source:=readkey;
    if pos(data_source,'Ff')>0 then
      { You have selected DATA FROM FILE }
      display_data_from_file;

    if pos(data_source,'Dd')>0 then
      { You have selected DATA FROM DSA }
      begin
         writeln('Program Expects DSA at RS232 coms port ',coms);
```

```
          writeln('Baud rate should be set to ',baud_rate);
          press_enter_when_ready;
          set_baud(baud_rate);

          writeln('Do you wish to eliminate the beam profile from the
interferogram(Y/N)?');
          interferogram_choice:=readkey;

          if pos(interferogram_choice, 'Yy') >0 then
            begin
               read_in_beam_profile_from_dsa;
            end
          else
            read_in_fringes_from_dsa;

       end;

{ ***  PROCESSING SECTION  *** }

if (pos(interferogram_choice,'Yy')>0 ) AND (pos(data_source,'Dd')>0) then
       { eliminate the beam profile }
  begin
    Repeat
       read_in_fringes_from_dsa;
       eliminate_beam_profile;
       centre_heading;
       writeln('
**************************************************');
       writeln('          *** Do you wish to re-scan the fringe data (Y/N)? ***');
       writeln('
**************************************************');
       re_scan_choice:=readkey;
       min2:=100000.0;
    Until pos(re_scan_choice, 'Nn')>0
  end;

  centre_heading;
  writeln('          ****************************************');
  writeln('          *** Enter N for New scan or X to eXit ***');
  writeln('          ****************************************');
  menu_choice:=readkey;
  while pos(menu_choice, 'XxNn')=0 do
       menu_choice:=readkey;

until pos(menu_choice, 'Xx')>0
end.
```

Appendix D

Vibration Measurement Processing System 'C' Computer Program Listing

The following program was compiled using the Borland C++ v3.1 compiler.

```
/*****************************************************/
/**** VIBRATION EXPERIMENT A/D CONVERSION PROGRAM  ****/
/*****************************************************/
/**** Removes dark signal from interferogram data  ****/
/**** and stores each processed vibration frame        ****/
/**** in a file. System has the capability to      ****/
/**** sample at upto 125kHz using cascaded samples ****/
/**** CLOCK1=CLOCK2=CLOCK3==2                          ****/
/*****************************************************/
/****          filename: vibrtn8.c                 ****/
/*****************************************************/


#include <dos.h>
#include <stdio.h>
#include <stdlib.h>
#include <conio.h>
#include <math.h>
#include <graphics.h>
#include <string.h>

#define dmanumber  4000
#define FRAME_MAX 25
#define xbegin 50
#define ybegin 70
#define xend xbegin + 550
#define yend ybegin + 350

/* xbegin, ybegin, xend, yend  - sets graph window limits */

void initializead(int base_add);
int getdata(int base_add,int chan_no);

unsigned int huge framedata [FRAME_MAX] [dmanumber];
float huge processed_data [FRAME_MAX] [1000];
unsigned int bpdata[dmanumber];
```

```
unsigned int convdata[16][1024];
//unsigned int dmaarray[2000];
// unsigned int far *arrayptr=dmaarray;
int chans[16];
int arraya1[17];
int x, scan, adppi, timer, dmachannel;
unsigned char samplehi, samplelo;
unsigned int i;
int isr3_called;

int const PORTA = 0;  /* To address portA A0=0 A1=0 */
int const PORTB = 1;  /* To address portA A0=1 A1=0 */
int const PORTC = 2;  /* To address portA A0=0 A1=1 */
int const CNTRL = 3;  /* To address control A0=1 A1=1 */
int const COUN0 = 0;  /* 8253 counter#0 */
int const COUN1 = 1;  /* 8253 counter#1 */
int const COUN2 = 2;  /* 8253 counter#2 */
int const EOA   = 0xFF; /* End of array marker for arraya1 */
int const CLOCK = 0;    /* IRQ number for the IBM PC's clock */
int const OFFSET= 8;    /* offset for interrupt number */
double const PI = 3.1415926536;
enum ubpol {UNI, BIP};

static void enableirq(unsigned char irq);
static void disableirq(unsigned char irq);
static void intrate(unsigned int ratio0, unsigned int ratio1, unsigned int ratio2);
static void interrupt isr1(void);
static void interrupt isr3(void);
static void dmarate(unsigned int ratio0, unsigned int ratio1, unsigned int ratio2);

void    initaddr(int newaddr);
void    setadchans(int numchans);
double  calcvolts(enum ubpol pol, double range, unsigned int dat);
int     adconv(void);
void    softscanad(int numscans);
void    intscanad(int numresults,
          unsigned int ratio0, unsigned int ratio1, unsigned int ratio2,
          unsigned char irq);
int     checkbuffer(unsigned int far *datapointer, unsigned int numelements);
void    initdma(unsigned int far *datapointer,
          unsigned int ratio0, unsigned int ratio1, unsigned int ratio2,
          int dmachan, unsigned int numsamples);
void    dmaad(int anachan);
void    closedma(void);
double  measurefreq(unsigned char irq, unsigned int ratio0);

extern unsigned int convdata[16][1024];
extern int chans[16];
```

```
void main(void);

/*-------------------------------------------------------------------------*
 |Name         enableirq                                                   |
 |-------------------------------------------------------------------------|
 |Description  Enables specified IRQ level in 8259 PIC                    |
 |-------------------------------------------------------------------------|
 |Arguments    irq : unsigned char - IRQ level                             |
 |-------------------------------------------------------------------------|
 |Return Value  none                                                       |
 *-------------------------------------------------------------------------*/
static void enableirq(unsigned char irq)
{
int imr, mask;  /* imr is interrupt mask register */

mask = ~(1 << irq);
imr = inportb(0x21);
imr &= mask;
outportb(0x21,(unsigned char) imr);
}


/*-------------------------------------------------------------------------*
 |Name         disableirq                                                  |
 |-------------------------------------------------------------------------|
 |Description  Disables a specified IRQ level in the 8259 PIC             |
 |-------------------------------------------------------------------------|
 |Arguments    irq : unsigned char - interrupt level                       |
 |-------------------------------------------------------------------------|
 |Return Value  none                                                       |
 *-------------------------------------------------------------------------*/
static void disableirq(unsigned char irq)
{
int imr, mask;  /* imr is interrupt mask register */

mask = 1 << irq;
imr = inportb(0x21);
imr |= mask;
```

```
outportb(0x21,(unsigned char) imr);
}


/*-------------------------------------------------------------------------*
 |Name        intrate                                                      |
 |-------------------------------------------------------------------------|
 |Description  Programmes the Counter/Timer with the three divide ratios   |
 |             provided.  For example, the master clock rate is 1MHz; if   |
 |             ratio1 = 2, ratio2 = 10 and ratio3 = 100, the interrupt     |
 |             rate would be 500Hz.                                        |
 |-------------------------------------------------------------------------|
 |Arguments    ratio0, ratio1, ratio2:unsigned int - counter divide ratios |
 |-------------------------------------------------------------------------|
 |Return Value  none                                                       |
 *-------------------------------------------------------------------------*/
static void intrate(unsigned int ratio0, unsigned int ratio1, unsigned int ratio2)
{
outportb(timer+CNTRL,'\x36');
outportb(timer+COUN0,(unsigned char) (ratio0 & 0xFF));
outportb(timer+COUN0,(unsigned char) (ratio0 >> 8));
outportb(timer+CNTRL,'\x76');
outportb(timer+COUN1,(unsigned char) (ratio1 & 0xFF));
outportb(timer+COUN1,(unsigned char) (ratio1 >> 8));
outportb(timer+CNTRL,'\xB6');
outportb(timer+COUN2,(unsigned char) (ratio2 & 0xFF));
outportb(timer+COUN2,(unsigned char) (ratio2 >> 8));
}


/*-------------------------------------------------------------------------*
 |Name        isr1                                                         |
 |-------------------------------------------------------------------------|
 |Description  ISR for interrupt controlled sampling                       |
 |-------------------------------------------------------------------------|
 |Arguments    none                                                        |
 |-------------------------------------------------------------------------|
 |Return Value  none                                                       |
 *-------------------------------------------------------------------------*/
static void interrupt isr1(void)
{
outportb(adppi+PORTC, (unsigned char) arraya1[i+1]*16 + '\x8');/* select next
channel */
samplelo = inportb(adppi + PORTA);
samplehi = inportb(adppi + PORTB) & 0x0F;          /* get 12 bits of data */
convdata[arraya1[i]][scan] = samplehi*256 + samplelo; /* current data into array */
if (++i==x)  {                    /* check for beginning of next scan */
  i=0;
  scan++;
```

```
  }
outportb(0x20,'\x20');                    /* interrupt clear to 8259 */
}


/*-------------------------------------------------------------------------*
 |Name         isr3                                                        |
 |-------------------------------------------------------------------------|
 |Description   ISR for frequency counter routine                          |
 |-------------------------------------------------------------------------|
 |Arguments     none                                                       |
 |-------------------------------------------------------------------------|
 |Return Value  none                                                       |
 *-------------------------------------------------------------------------*/
static void interrupt isr3(void)
{
samplelo = inportb(timer + COUN2);      /* read final count value */
samplehi = inportb(timer + COUN2);
isr3_called = 1;                    /* set global terminal count flag */
outportb(0x20,'\x20');                /* interrupt clear to 8259 */
}


/*-------------------------------------------------------------------------*
 |Name         dmarate                                                     |
 |-------------------------------------------------------------------------|
 |Description   Programmes the Counter Timers with the supplied Counter    |
 |              Divide Ratios for DMA controlled sampling.  For example, the|
 |              master clock is 1MHz, if ratio1=2, ratio2=10 and ratio3=10,|
 |              the DMA rate would be 5kHz.                                |
 |-------------------------------------------------------------------------|
 |Arguments     ratio0, ratio1, ratio2:unsigned int - counter divide ratios|
 |-------------------------------------------------------------------------|
 |Return Value  none                                                       |
 *-------------------------------------------------------------------------*/
static void dmarate(unsigned int ratio0, unsigned int ratio1, unsigned int ratio2)
{
outportb(timer+CNTRL,'\x34');
outportb(timer+COUN0,(unsigned char) (ratio0 & 0xFF));
outportb(timer+COUN0,(unsigned char) (ratio0 >> 8));
outportb(timer+CNTRL,'\x74');
outportb(timer+COUN1,(unsigned char) (ratio1 & 0xFF));
outportb(timer+COUN1,(unsigned char) (ratio1 >> 8));
outportb(timer+CNTRL,'\xB4');
outportb(timer+COUN2,(unsigned char) (ratio2 & 0xFF));
outportb(timer+COUN2,(unsigned char) (ratio2 >> 8));
}
```

```
/* Callable routines */

/*-------------------------------------------------------------------------*
 |Name         initaddr                                                    |
 |-------------------------------------------------------------------------|
 |Description  Re-defines PC26AT register addresses w.r.t. new base addr.  |
 |-------------------------------------------------------------------------|
 |Arguments    newaddr:integer - new PC26AT base address                   |
 |-------------------------------------------------------------------------|
 |Return Value  none                                                       |
 *-------------------------------------------------------------------------*/
void initaddr(int newaddr)
{
adppi = newaddr;
timer = newaddr + 4;
outportb(adppi + CNTRL,'\x92');
}


/*-------------------------------------------------------------------------*
 |Name         setadchans                                                  |
 |-------------------------------------------------------------------------|
 |Description  The array chans has 16 elements and holds data defining     |
 |             which channels will be sampled.  They will be activated in  |
 |             strict order startimg with chan[0] and finishing with       |
 |             chan[15].                                                   |
 |-------------------------------------------------------------------------|
 |Arguments    numchans:integer - used to place a pseudo EOF marker in the |
 |             array to indicate the end of the scan sequence.             |
 |-------------------------------------------------------------------------|
 |Return Value  none                                                       |
 *-------------------------------------------------------------------------*/
void   setadchans(int numchans)
{
for (i=0; i<numchans; i++)
  arraya1[i] = chans[i];
arraya1[numchans] = EOA;
}


/*-------------------------------------------------------------------------*
 |Name         calcvolts                                                   |
 |-------------------------------------------------------------------------|
 |Description  Converts an A/D sample data word to a voltage reading takes |
 |             into account the voltage range selected on the PC26AT, also |
 |             the polarity and the data format - 2's complement or sign   |
 |             and magnitude.                                              |
 |-------------------------------------------------------------------------|
 |Arguments    pol:ubpol - bip or uni i/p polarity                         |
```

```
|          range:double - maximum voltage reading eg 10 for 10 uni/bip |
|          dat:unsigned int - data word to be converted                  |
|-------------------------------------------------------------------------|
|Return Value  double - voltage reading                                   |
*-------------------------------------------------------------------------*/
double calcvolts(enum ubpol pol, double range, unsigned int dat)
{
dat &= 0xFFF;
if (pol == UNI)
   return((range * dat) / 4095.0);
if (pol == BIP) {
   if (dat < 2048)
         return((range * dat)/2047.0);
   else
         return(-range*(4096-dat)/2048.0);
   }
return 0;
}

/*-------------------------------------------------------------------------*
 |Name        adconv                                                       |
 |-------------------------------------------------------------------------|
 |Description   Performs a single A/D conversion on the channel defined in |
 |          ArrayA1[0]. This must have been already set in SetAdchan.       |
 |-------------------------------------------------------------------------|
 |Arguments     none                                                       |
 |-------------------------------------------------------------------------|
 |Return Value  integer: conversion result                                 |
 *-------------------------------------------------------------------------*/
int adconv(void)
{
outportb(adppi + PORTC,(unsigned char) (arraya1[0]*16 +2));  /* select channel */
delay(1);
outportb(adppi + PORTC,(unsigned char) (arraya1[0]*16 +3));/* start conversion */
outportb(adppi + PORTC,(unsigned char) (arraya1[0]*16 +2));
while ((inportb(adppi+PORTB) & '\x20') == 0);              /* wait for busy */
samplelo = inportb(adppi + PORTA);
samplehi = inportb(adppi + PORTB) & 0x0F;            /* get 12 bits of data */
return ((samplehi << 8) + samplelo);
}

/*-------------------------------------------------------------------------*
 |Name        softscanad                                                   |
 |-------------------------------------------------------------------------|
 |Description   Performs multiple conversions on the channels prescribed in |
 |          ArrayA1. The results are returned in array AdData. The         |
 |          number of scans is defined by "numscans".                      |
 |-------------------------------------------------------------------------|
 |Arguments     numscans : integer - number of scans through the list of   |
```

```
|                          channels in ArrayA1.                          |
|--------------------------------------------------------------------------|
|Return Value  none                                                        |
*--------------------------------------------------------------------------*/
void softscanad(int numscans)
{
int channel;

x=0;
do                          /* find out how many channels are open */
 x++;                       /* x is the number of open channels */
while (arraya1[x] != EOA);
arraya1[x] = arraya1[0];      /* first chan again for selection before next scan */
outportb(adppi + PORTC, (unsigned char)(arraya1[0]*16+2));  /* select first channel */
delay(1);
for (scan=0; scan<numscans; scan++)  {
 for (channel=0; channel<x; channel++) {
   outportb(adppi + PORTC,(unsigned char) (arraya1[channel]*16 +3));
   outportb(adppi + PORTC,(unsigned char) (arraya1[channel+1]*16 +2));
   while ((inportb(adppi + PORTB) & '\x20') == 0);   /* wait for busy */
   samplelo = inportb(adppi + PORTA);
   samplehi = inportb(adppi + PORTB) & 0x0F;         /* get 12 bits of data */
   convdata[arraya1[channel]][scan] = (samplehi << 8) + samplelo;
   }
 }
arraya1[x] = EOA;
}


/*--------------------------------------------------------------------------*
 |Name         intscaad                                                     |
 |--------------------------------------------------------------------------|
 |Description   Performs interrupt controlled AD on multiple channels       |
 |--------------------------------------------------------------------------|
 |Arguments     numresults:integer - number of results per channel req'd    |
 |              ratio1, ratio2, ratio3:unsigned int - counter divide ratios |
 |              irq:unsigned char - interrupt level to use.                 |
 |--------------------------------------------------------------------------|
 |Return Value  none                                                        |
 *--------------------------------------------------------------------------*/
void intscanad(int numresults, unsigned int ratio0, unsigned int ratio1,
                          unsigned int ratio2, unsigned char irq)
{
static void interrupt (*vec)(void);
vec = getvect(irq + OFFSET);    /* save previous IRQ vector */
setvect(irq + OFFSET,isr1);     /* change it to isr1 */
intrate(ratio0, ratio1, ratio2);
outportb(adppi+CNTRL,'\x92');   /* control word for QA11, A&B i/p, C o/p */
outportb(adppi + PORTC, (unsigned char)(arraya1[0]*16+0xC));
```

```
x=0;
do                          /* find out how many channels are open */
  x++;                      /* x is the number of open channels */
while (arraya1[x] != EOA);
arraya1[x] = arraya1[0];      /* first chan again for selection before next scan */

i=scan=0;                   /* initialise for first channel & first scan */
disableirq(CLOCK);
enableirq(irq);             /* enable interrupts */
while (!kbhit() && (scan < numresults));
disableirq(irq);
enableirq(CLOCK);           /* disable interrupts */
setvect(irq + OFFSET,vec);    /* restore previous IRQ vector */
arraya1[x] = EOA;           /* restore EOA marker */
}


/*-------------------------------------------------------------------------*
 |Name        checkbuffer                                                  |
 |-------------------------------------------------------------------------|
 |Description  Checks whether the DMA data array resides totally within a  |
 |          64k physical block.  If not then it cannot be used for DMA.    |
 |-------------------------------------------------------------------------|
 |Arguments    datapointer:unsigned int * - pointer to data array          |
 |          numelements:unsigned integer - size of array                   |
 |-------------------------------------------------------------------------|
 |Return Value  int - non-zero if array can be used for DMA                |
 *-------------------------------------------------------------------------*/
int checkbuffer(unsigned int far *datapointer, unsigned int numelements)
{
unsigned long offset, segment, physical;

segment = FP_SEG(datapointer);
offset  = FP_OFF(datapointer);
physical = segment * 16 + offset;
segment = physical / 65535L;
offset = physical % 65535L;
if (offset + numelements * 2 < 65535)
  return(1);
else
  return(0);
}


/*-------------------------------------------------------------------------*
 |Name        initdma                                                      |
 |-------------------------------------------------------------------------|
 |Description  Sets up the DMA starting address at the beginning of the    |
```

```
|          data array, sets up the DMA mode register to Mode 1 (single |
|          transfer) Increment Address and Auto Initialisation.       |
|          Transfer Direction, DMA channel and Number of transfers are |
|          specified.                                                  |
|----------------------------------------------------------------------|
|Arguments    datapointer:unsigned int * - pointer to DMA data array    |
|          dirn:dmadirn - adc or dac                                   |
|          ratio0, ratio1, ratio2:unsigned int - counter divide ratios |
|          dmachan:int - dma level                                     |
|          numsamples:unsigned - total number of DMA word transfers    |
|----------------------------------------------------------------------|
|Return Value  none                                                    |
*----------------------------------------------------------------------*/
void    initdma(unsigned int far *datapointer,
         unsigned int ratio0, unsigned int ratio1, unsigned int ratio2,
         int dmachan, unsigned int numsamples)
{
unsigned char   load, hiad;
unsigned char   page;
unsigned char   ai, tfr;
unsigned long   segment, offset, physical;

dmachannel = dmachan;
dmarate(ratio0,ratio1,ratio2);
segment = FP_SEG(datapointer);
offset  = FP_OFF(datapointer);
physical = segment * 16 + offset;
load = physical & 0xFF;
hiad = (physical >> 8) & 0xFF;
page = (physical >> 16) & 0xFF;

outportb(adppi+CNTRL,'\x92');   /* control word for QA11, A&B i/p, C o/p */
tfr = '\x04';                   /* transfer type as IO to memory */
ai =  '\x00';                   /* auto initialisation disabled */

if (dmachannel == 1)  {
  outportb(11,'\x41'+tfr+ai);   /* Mode Register loaded with :-
                                   Transfer type = IO to memory
                                   Single transfer
                                   Address increment
                                   No auto initialisation
                                   DMA channel 1. */
  outportb(12,'\x0');           /* Clear first/last flip flop. */
  outportb(2,load);             /* Put starting address into base and */
  outportb(2,hiad);             /* current address registers. */
  outportb(0x83,page);          /* DMA page. */
  outportb(3,(unsigned char)((numsamples*2-1) & '\xFF'));  /* number of samples into
current */
```

```
 outportb(3,(unsigned char)(((numsamples*2-1) >> 8 )& '\xFF'));/* and base word
count registers... */
 }

if (dmachannel == 3) {
 outportb(11,'\x43'+tfr+ai);  /* Same as above, but for DMA channel 3 */
 outportb(12,'\x0');
 outportb(6,load);
 outportb(6,hiad);
 outportb(0x82,page);
 outportb(7,(unsigned char)(numsamples*2-1) & '\xFF');
 outportb(7,(unsigned char)(((numsamples*2-1) >> 8) & '\xFF'));
 }
}


/*-------------------------------------------------------------------------*
 |Name        dmaad                                                        |
 |-------------------------------------------------------------------------|
 |Description  Unmasks the DMA channel for DMA controlled A/D into the     |
 |             array pointed to by DMApointer.  Note that the timer should |
 |             have already been set up in DmaRate, and that InitDMA       |
 |             should have already been set up.                            |
 |-------------------------------------------------------------------------|
 |Arguments    anachan:integer - A/D input channel                          |
 |-------------------------------------------------------------------------|
 |Return Value  none                                                       |
 *-------------------------------------------------------------------------*/
void   dmaad(int anachan)
{
outportb(adppi + PORTC, (unsigned char)(anachan*16+4));  /* select chan & DMA */
delay(1);                  /* allow for channel to settle */
if (dmachannel == 1)          /* unmask DMA channel 1 */
  outportb(10,'\x01');
if (dmachannel == 3)          /* unmask DMA channel 3 */
  outportb(10,'\x03');
}


/*-------------------------------------------------------------------------*
 |Name        closedma                                                     |
 |-------------------------------------------------------------------------|
 |Description  Re-masks the DMA channel to prevent any more DMA action.    |
 |-------------------------------------------------------------------------|
 |Arguments    none                                                        |
 |-------------------------------------------------------------------------|
 |Return Value  none                                                       |
 *-------------------------------------------------------------------------*/
void   closedma(void)
```

```
{
if (dmachannel == 1)
  outportb(10,'\x05');
if (dmachannel == 3)
  outportb(10,'\x07');
outportb(adppi + PORTC, '\x00');
}


/*-------------------------------------------------------------------------*
 |Name         measurefreq                                                 |
 |-------------------------------------------------------------------------|
 |Description   Measures the frequency of the signal on the EXT Freq pin   |
 |-------------------------------------------------------------------------|
 |Arguments     irq:byte - interrupt level to use                          |
 |              ratio0:unsigned int - divisor ratio which determines the   |
 |                gate period of the counter.  The master clock frequency  |
 |                is 1MHz. Hence if ratio0 is 100, the Cntr0 o/p frequency |
 |                will be 10kHz. This would give a gating period of 10ms.  |
 |-------------------------------------------------------------------------|
 |Return Value  double - number of pulses counted in the gating period.    |
 *-------------------------------------------------------------------------*/
double  measurefreq( unsigned char irq, unsigned int ratio0 )
{
static void interrupt (*vec)(void);
vec = getvect(irq + OFFSET);    /* save previous IRQ vector */
setvect(irq + OFFSET,isr3);     /* change it to isr3 */
outportb(adppi+CNTRL,'\x92');   /* A/D PPI Ports A,B input, Port C output */
outportb(adppi+PORTC,'\x08');   /* enable interrupts */
outportb(timer+CNTRL,'\xB0');   /* counter2 in mode0 (terminal count) */
outportb(timer+COUN2,'\xFF');   /* load in 0xFFFF. The clock to this */
outportb(timer+COUN2,'\xFF');   /* counter is the external signal */
outportb(timer+CNTRL,'\x30');   /* counter0 in mode0 (terminal count) */
outportb(timer+COUN0,(unsigned char)(ratio0 & 0xFF));    /* cntr0 divisor */
outportb(timer+COUN0,(unsigned char)(ratio0 >> 8));

isr3_called = 0;
disableirq(CLOCK);
enableirq(irq);                    /* enable interrupts */
while( !isr3_called );               /* wait for isr3 to get called */
disableirq(irq);
enableirq(CLOCK);                     /* disable interrupts */
setvect(irq + OFFSET,vec);             /* restore previous IRQ vector */
return(0xFFFF - 256*samplehi - samplelo);
}


/****************** PC26AT ***********************/
```

```
void initializead(int base_add)
{       outport(base_add+3,0x92);
   /* the control byte and address of the PC26AT AD-convertor*/
}

int getdata(int base_add,int chan_no)
{       int busy,i,out_val,samplelo,samplehi,sum;
        sum=0;
        busy=0;
        outportb(base_add+2,chan_no*16 +2);  /*Select channel*/
        outportb(base_add+2,chan_no*16 +3);  /* start conversion */
        outportb(base_add+2,chan_no*16 +2);
        while (busy==0) { busy = inportb(base_add+1) & 0x20;}
                        /* wait till conversion is flagged*/
        samplelo=inportb(base_add);  /* low byte in base address*/
        samplehi=inportb(base_add+1) & 0x0F;   /* high byte */
        sum=sum+((samplehi*0x100) + samplelo);
        return(sum);
}
/*************************   end   ********************

/*************          MAIN  PROGRAM       *************/

void main(void)
{
/* Use DMA A/D conversion to sample data */

        FILE *file1=NULL, *bpfile=NULL, *file2=NULL;

        int i, j, k,frame_count, sum, trigger, frame;
        int low_trigger=4000, dummy;
        int group_size=6;
        int number_of_groups=dmanumber/group_size;
        int max_value, group, array_pointer;

        unsigned int indata[dmanumber];   /* Array to store the A/D readings */

        file1=fopen("c:\\dma11.dat","w");
        bpfile=fopen("c:\\bpdma11.dat","w");
        file2=fopen("c:\\proces11.dat","w");

        if(file1==NULL || bpfile ==NULL || file2==NULL)

          {     printf("Can not open the file!!!!!");
                exit(0);
           }

/* initialise the input data arrays to zero */
```

```
for (i=0; i<dmanumber; i++) { indata[i]=0; }

for (frame=0; frame<FRAME_MAX; frame++)
  {
     for (i=0; i<dmanumber; i++)
     {   framedata[frame][i]=0;
     }
  }

if (checkbuffer(indata,32768)) printf("Buffer ok\n");
 else {  printf("Bad Buffer");  /* check that the array is */
          exit(0);              /* completely in one segment */
        }
/* initialise DMA with the following...
    destination address as convaddr,
    CDRs = 5, 2 & 2, giving sampling rate of 62.5kHz
         --------> 62.5kHz=1000kHz/(5*2*2)
    if all timers cascaded, DMA channel 1, 5000 samples */

initdma(indata,3,2,2,1,dmanumber);

printf("Input data channel number 3,5,6  \n");
scanf("%d",&j);

initaddr(0x300);          /* set PC26AT base address */
printf("\n Set up beam profile - enter 1 to continue \n");
scanf("%d", &dummy);

/* initially, pre-store beam profile */

        /* Read trigger input from channel 4 */
        chans[0]=4;
        setadchans(1);          /* set up PC26AT base address */
        trigger=0;

        while(trigger<=low_trigger)  /* read trigger input until it goes high */
                trigger = adconv();

printf("\n\n Reading beam profile trigger input from channel 4");

dmaad(j);   /* Read BP from ANALOG channel j to DMA channel 1 */

delay(100);  /* Wait for process to finish.  N.B. You may need to
             increase this value for machines faster than 33MHz */

for (i=0; i<dmanumber; i++)
{
        /* set first 4 bits of input data word to zero - since
```

```
                computer will handle this as 16 bit-word whilst A/D
                card uses only 12 bit words. Thus before conversion
                to volts is done, must ensure that first 4 bits are zero
                to eliminate errors */

                indata[i]=indata[i]&0x0fff;
                bpdata[i]=indata[i];
        }

        /* eliminate CCD dark signal from beam-profile reading */

          for (group=0; group<number_of_groups; group++)
          {
                max_value=0;
                for ((array_pointer = (group*group_size));
                    (array_pointer< ((group*group_size) + group_size));
                    array_pointer++)
                {
                        if (bpdata[array_pointer]>max_value)
                                max_value = bpdata[array_pointer];
                }
                bpdata[group] = max_value;
          }

        /* write beam profile data to file */
        for (i=0; i<number_of_groups; i++)
        {
                fprintf(bpfile,"%d %d \n",i,bpdata[i]);
        }

/* now read interferogram data */
        printf("\n Set up fringes - enter 1 to continue \n");
        scanf("%d", &dummy);

        printf ( "\n Reading data frames. . . \n ");

        for (frame=0;frame<FRAME_MAX;frame++)
        {
                /* Read trigger input from channel 4 */
                chans[0]=4;
                setadchans(1);          /* set up PC26AT base address */
                trigger=0;

                while(trigger<=low_trigger)  /* read trigger input until it goes high */
                {
                        trigger = adconv();
                }

                printf(" %d ", frame);
```

```
                dmaad(j);   /* Read from ANALOG channel j to DMA channel 1 */

                delay(100);  /* Wait for process to finish.  N.B. You may need to
                   increase this value for machines faster than 33MHz */
                scanf("%d", &dummy);

                for (i=0; i<dmanumber; i++)
                {
                /* set first 4 bits of input data word to zero - since
                computer will handle this as 16 bit-word whilst A/D
                card uses only 12 bit words. Thus before conversion
                to volts is done, must ensure that first 4 bits are zero
                to eliminate errors */

                indata[i]=indata[i]&0x0fff;

                /* write new frame data to array framedata */
                framedata[frame][i]=indata[i];

/*      printf("Element %2d : Channel 0 =  %6.3fV\n",i,
                        calcvolts(UNI,10.0,indata[i])); */
                }


        }
    closedma();

   /* Eliminate background noise from data */

    for (frame=0; frame<FRAME_MAX; frame++)
    {
        for (group=0; group<number_of_groups; group++)
        {
            max_value=0;
            for ((array_pointer = (group*group_size));
                (array_pointer< ((group*group_size) + group_size));
                array_pointer++)
            {
                if (framedata[frame][array_pointer]>max_value)
                    max_value = framedata[frame] [array_pointer];
            }
            framedata[frame][group] =max_value;
        }
    }

   /*   Eliminate beam profile from framedata readings */

   for (frame=0; frame<FRAME_MAX; frame++)
   {
```

```
        for (i=0; i<number_of_groups;i++)
        {
                processed_data[frame][i]=(framedata[frame][i]- bpdata[i])/bpdata[i];
        }
    }

    /* write all frame data to files */

        for (i=0; i<number_of_groups;i++)
        {
                for (frame=0;frame<FRAME_MAX;frame++) {
                        if (frame==0) /* write x-data column to file */
                                fprintf(file1, "%d\t", i);

                        fprintf(file1,"%d\t",framedata[frame][i]);
                        }
                fprintf(file1, "\n");
        }

        for (i=0; i<number_of_groups;i++)
        {
                for (frame=0;frame<FRAME_MAX;frame++) {
                        if (frame==0) /* write x-data column to file */
                                fprintf(file2, "%d\t", i);

                        fprintf(file2,"%f\t",processed_data[frame][i]);
                        }
                fprintf(file2, "\n");
        }

        fclose(file1);
        fclose(bpfile);
        fclose(file2);

        printf(" -------PROCESS COMPLETED ----------");
}

/********************** E N D ************************/
```

Appendix E

Author's Publication List

1. Marshall, R.H., Ning Y. N., Jiang, X. Q., Palmer, A. W., Meggitt, B. T. and Grattan K. T. V.: "A novel white-light interferometer using an electronically-scanned Mach-Zehnder interferometer", Proc. SPIE 2594, manuscript number 17, In: "Self-calibrated intelligent optical sensors and systems", Philadelphia, USA, October 1995, Ed. Wang, A., pp.159-167. ISBN 0-8194-1958-3.

2. Marshall, R.H., Ning Y. N., Jiang, X. Q., Palmer, A. W., Meggitt, B. T. and Grattan K. T. V.: "A novel electronically-scanned white-light interferometer using a Mach-Zehnder approach", IEEE J. Lightwave Technol., vol. 14, No. 3, pp. 397-402, March 1996.

3. Marshall, R.H., Ning Y. N., Palmer, A. W. and Grattan K. T. V.: "A novel implementation of a bulk-optical Mach-Zehnder interferometer for enhanced stability in a fibre-optic electronically-scanned white-light interferometric system", Proc. Optical-fibre sensors (OFS-11) Sapporo, Japan, In: "Interferometry and Polarimetry", vol. We3-41, Eds: Y. Ohtsuka, T. Yoshino; 336-339, May 1996, Japan AP961211.

4. Marshall, R.H., Ning Y. N., Palmer, A. W. and Grattan K. T. V.: "Vibration measurement using a novel fibre-optic electronically-scanned white-light interferometer", Proc. Optical Measurements I: Scientific, In: "International conference on Applications of photonic technology (ICAPT '96)", Montreal, Canada; July 1996.

5. Marshall, R.H., Ning Y. N., Palmer, A. W. and Grattan K. T. V.: "High sensitivity displacement measurement using a novel fibre-optic electronically scanned white light interferometer", In: SPIE 1996 International symposium on Optical science, engineering and instrumentation, Denver, USA, Proc: SPIE vol. 2861-08 Laser interferometry VIII : Applications; Ed. Pryputniewicz, R. J., Brown, G. M., Jueptner, W. P.; pp. 52-61, ISBN: 0-8194-2249-5.

6. Extracts from Reference [5] are also published in SPIE, OE Reports, No. 155, In: "Laser interferometry", pp. 7, Ed. Fowler, R. E., Bellingham, USA, November 1996.

7. Marshall, R.H., Sokolov, I., Ning Y. N., Palmer, A. W. and Grattan K. T. V.: "Photo-Electromotive Force Crystals For Interferometric Measurement Of Vibrational Response", IOP: J. Measurement and Science Technol., Vol.7, No.12, pp.1683-1686, 1996.

8. Marshall, R.H., Ning Y. N., Palmer, A. W. and Grattan K. T. V.: "Dispersion in an electronically-scanned dual-wavelength low-coherence interferometer", Optics Communications, vol. 138, pp.136-142, 1997

9. Marshall, R.H., Ning Y. N., Palmer, A. W. and Grattan K. T. V.: "Accurate displacement measurement using a novel fibre-optic electronically-scanned white light interferometer", Proc. XIV IMEKO World Congress, P2: Photonic measurements, Tampere, Finland, 1-6 June 1997.

10. Marshall, R.H., Ning Y. N., Palmer, A. W. and Grattan K. T. V.: "Simultaneous measurement of AC and DC stresses using a fibre-optic electronically scanned white-light interferometer", accepted for publication in Sensors and Actuators in 1997.

11. Marshall, R.H., Ning Y. N., Palmer, A. W. and Grattan K. T. V.: "The measurement of AC and DC stresses using an electronically-scanned white-light interferometer", IOP Sensors and their applications VIII conference, Glasgow 7-10 September 1997.

12.Marshall, R.H., Ning Y. N., Palmer, A. W. and Grattan K. T. V.: "Implementation of a dual wavelength bulk optical electronically-scanned white-light interferometric system", Optics Comms., vol. 145, pp. 43-47, 1998.